Peter Dörfler
Mirjam Sick
André Coutu

Flow-Induced Pulsation and Vibration in Hydroelectric Machinery

Engineer's Guidebook for Planning, Design and Troubleshooting

Springer

Flow-Induced Pulsation and Vibration
in Hydroelectric Machinery

Peter Dörfler · Mirjam Sick
André Coutu

Flow-Induced Pulsation and Vibration in Hydroelectric Machinery

Engineer's Guidebook for Planning, Design and Troubleshooting

Springer

Peter Dörfler
Andritz Hydro Ltd
Zurich
Switzerland

André Coutu
Andritz Hydro Ltd
Pointe-Claire, QC
Canada

Mirjam Sick
Andritz Hydro Ltd
Zurich
Switzerland

Preface

Hydraulic turbomachines have played a prominent role in the procurement of renewable energy for more than a century. Embedded in the context of general technological progress, their design for efficiency and reliability has reached an outstanding level of quality, and no other turbomachines have reached the efficiency levels of Francis turbines, now close to 96 %. To maintain such a level in every project is a permanent engineering challenge because, unlike other types of equipment, the turbines and storage pumps for a hydroelectric power plant are usually 'tailor-made', that is their design is adapted to the flow and head available for a given location. Furthermore, with the fundamental changes in the electricity markets due to the integration of non-dispatchable renewables, such as wind and solar power, the role of hydropower in the electrical grid has dramatically changed from being a contributor of constant energy supply to a highly flexible supplier of ancillary services. Hydraulic turbomachines are nowadays operated in a far more dynamic way thereby requiring substantial progress in technology development.

The main hydraulic performance issues of hydroelectric machinery—output, efficiency, and cavitation—have been in the focus of interest right from the beginning because they are obviously linked with the owner's financial success. Well-established practice and standards for testing these properties of the machines have existed for a long time. It is more difficult to assess in advance the durability of the equipment. Mechanical failure of one or more components after some period of operation is in most cases due to fatigue caused by fluctuating stress added to the steady-state load. These fluctuating stresses are, like the steady-state ones, a consequence of the working principle of the hydraulic machines. To predict them becomes more and more important if the machines should be designed for good hydraulic performance, but at the same time be developed for the lowest possible cost and the most flexible operation.

Apart from issues of mechanical safety, there are other reasons for limiting the unsteady phenomena. For example, spontaneous power swings due to some mechanism of instability are not acceptable for the electrical network. There are also some issues at the border between safety and convenience, phenomena like

pressure shocks, vibrations, and noise where both operators and suppliers may disagree about what is acceptable or not.

To make things even more challenging, the flexibility of modern power plants leads to a remarkable trend toward operating the equipment in off-design conditions for a larger percentage of time. As a consequence, the importance of fluctuating loads increases and the unsteady operational behavior must receive more attention.

The idea for this book was born a few years ago, when a number of researchers in the field, including one of the authors, reached the age of retirement. Engineers who have acquired specific knowledge in the field, both empirical and theoretical, owe a good deal of that knowledge to unforeseen technical mistakes and their correction. The problems that had to be dealt with typically occurred once in every few years, or even over many years. Within a well-governed company, however, such incidents drive a process of rule-making to provide guidelines to avoid similar events. Over the years, the body of rules and guidelines increases and the errors are finally avoided. It is not quite the same in the open literature of the technical community. Paradoxically, the very large number of conference papers seems to assist in the merciless erosion of know-how. In view of this we recognized that we should make this specific knowledge available in a more compact form, some of it being owed to publicly funded research projects, or collected in exchange of experience with colleagues from other companies in working groups organized by IAHR.

In addition, this book is intended as a contribution to help improving the efficiency of collaboration between the buyers and suppliers of hydroelectric machinery. We are faced in many projects with unrealistic or unpractical technical requirements with regard to unsteady performance. This is mainly due to lack of available information about the actual behavior of hydraulic machines. With our book, we want to close this gap of knowledge and contribute to a more rational handling of the subject in future projects.

Zurich, Switzerland, April 2012   Peter Dörfler

Acknowledgments

Notice

This book reflects today's state-of-the-art in the hydropower industry. The authors do not make any warranty, expressed or implied, or assume any legal responsibility for the accuracy of any information or for the completeness or usefulness of any apparatus, product or process disclosed, or accept liability for the use, or damages resulting from the use, thereof. Neither do they represent that their use would not infringe upon privately owned rights.

Furthermore, the authors hereby disclaim any and all warranties, expressed or implied, including the warranties of merchantability and fitness for a particular purpose, whether arising by law, custom, or conduct, with respect to any of the information contained in this book.

In no event shall the authors be liable for incidental or consequential damages because of use or any information contained in this book. Any reference in this book to any specific commercial product, process, or service by trade name, trademark, manufacturer or otherwise does not necessarily constitute or imply its endorsement or recommendation by the authors.

Contents

Nomenclature

Latin Letters

a	Velocity of wave propagation
a_{ij}	Elements of transfer matrix
A	Cross-section area
A	Transfer matrix
A	Amplitude
B_0	Height of wicket gates
c	Flow velocity
c_m	Meridional flow velocity
c_t	Peripheral flow velocity
C_C	Cavitation compliance
C	Damage ratio
C_p	Pressure coefficient
d	Thickness, width
D	Diameter
D(s)	Denominator
E	Energy
E	Modulus of elasticity
f	Frequency
F	Force
g	Gravity acceleration
G	Transfer function
h	Variation of head
h_{dyn}	Velocity head
H	Head
I	Inertance
I, J	Moment of inertia
j	Imaginary unit

k	Friction factor (unsteady)
k	Harmonic of runner blade frequency
k	Polytropic exponent
K	Speed coefficient, relative to $\sqrt{(2E)}$
L	Length
n	Runner speed, frequency of runner rotation
m	Harmonic of stationary blade frequency
m	Swirl ratio
M	Mach number
M	Torque, bending moment
N	Number of samples
N(s)	Numerator
p	Pressure
P	Power
q	Variation of flow
Q	Mean value of flow
R	Radius
R	Resistance
s	Laplace transform parameter
S	Surface tension
St	Strouhal number
t or T	Time
T	Torque
u	Peripheral velocity of runner
u	Radial source velocity
v	Velocity
V_C	Volume of cavity
w	Relative velocity
x	Longitudinal coordinate
X	(general) Variable
X2	Dimensionless relative discharge variable
Y	Hydraulic admittance
Y	Guide vane opening
Z	Hydraulic impedance
Z	Number of blades

Greek letters

α	Void fraction
α	Real part of eigenvalue
α	(Guide vane opening) Angle
β	Inclination angle
β	(Runner blade opening) Angle
χ	Mass flow gain factor
Δ	Fluctuation of .. , difference of ..
γ	Propagation constant
η	Hydraulic efficiency
φ, ϕ	Discharge coefficient
κ	Upstream portion of mass flow gain
λ	Friction factor (steady-state)
Λ or λ	Wave length
μ	Bulk viscosity
ν	Specific speed
ν	Signed number of node diameters
π	3.141592...
ρ	Density
σ	Cavitation number
σ	Mechanical stress
Σ	Sum
ω	Angular velocity
Ω	Angular velocity of runner rotation
ψ	Pressure coefficient
ζ	Damping ratio

Abbreviations

asyn	Asynchronous part of DTPP
CFD	Computational fluid dynamics
DES	Detached eddy simulation (turbulence model)
DNS	Direct numerical simulation (turbulence model)
DOF	Degrees-of-freedom
DTPP	Draft tube pressure pulsation
EPFL	Swiss Federal Institute of Technology (Lausanne, CH)
FEA	Finite element analysis
FFT	Fast Fourier transform
FRR	Frequency reduction ratio
GV	Guide vanes
IEC	International electrotechnical commission
ISO	International organization for standardization
lcm	Lowest common multiple
LES	Large eddy simulation (turbulence model)
LMH	Laboratory of Hydraulic Machines (at EPFL)
MFGF	Mass flow gain factor
MIV	Main inlet valve
ND	(number of) Node diameters
ND	Non-drive
NPSE	Net positive suction energy
NR	Noise rating
p-p	Peak-to-peak
PSS	Power system stabilizer
p.u.	Per unit
rms	Root mean square
RSI	Rotor–stator interaction
SAS	Scale-adaptive simulation
SPL	Sound pressure level
SR	Suction coefficient
SST	Shear stress transport (turbulence model)

sync	Synchronous part of DTPP
TVA	Tennessee Valley Authority
USBR	US Bureau of Reclamation
VoF	Volume of fluid
WG	Wicket gate

Subscripts

B	Barometric
BP	Runner blade passage
c	Related to cm (at runner exit)
C	Cavity
DT	Draft tube
EX	Exciting (forcing)
G	Generator
G	Guide vane
h	Horizontal, hydraulic
HW	Headwater
L	Liquid
max	Minimum
min	Maximum
n	Natural (frequency)
NB	Narrow-band
nom	Nominal = rated
opt	At best efficiency point
r	Rated
r	Rotating cascade
R	Radial at runner
R	Runaway
RF	Risk factor
s	Stationary cascade
sp, SC	Spiral casing
v	Vertical
T	Turbine
TW	Tail water

u	Related to u (at runner exit)
W	Wall
W-B	Wide-band
11	Per unit of reference variables
1, 2	Upstream, downstream
2	Related to runner exit (diameter)

Chapter 1
Basic Concepts

Some basic engineering and physical concepts are introduced and discussed in this chapter. These concepts are important to characterize the performance, pulsations and vibrations, and other related phenomena presented in this book.

First, the representation of an operating point and the operating range by non-dimensional parameters is described. Many different parameters may be defined and these are briefly outlined. The occurrence of many vibration and pulsation phenomena in turbines is restricted to specific operating conditions and the use of non-dimensional parameters allows different machines to be directly compared with each other in a dimensionless hill chart. Second, the quantitative description of an oscillation process in terms of amplitudes or frequency spectra is explained. Third, the fundamentals of hydraulic resonance and stability are briefly outlined as many phenomena, in particular intense low-frequency fluctuations, often concern the whole water conduit and ducting rather than just the interior of the hydraulic machine.

1.1 Hill Charts, Operating Modes, and Parameters

This book considers both pumps and water turbines. Turbines are work-producing machines and extract hydraulic power ρQgH from the working fluid to provide mechanical power $2\pi nT$ at the rotating shaft. Pumps are work-absorbing machines and take mechanical power from the shaft to produce an increase in fluid energy in the flow being pumped. The dimensional parameters describing the duty of the machine are the head H (or potential energy $E = gH$), the flow rate Q, and the rotational speed n. These parameters are absolute measures to define the actual process in a particular machine at a specific operating point and differ from

---

An erratum to this chapter is available at 10.1007/978-1-4471-4252-2_10.

machine to machine. Dimensionless representations of these parameters enable a more simple comparison to be made with other operating conditions, or with other machines, for instance with reduced-scale laboratory models [1], as the effects of speed and size may be removed. This chapter presents some frequently used sets of dimensionless parameters that have established themselves to describe machine performance in the hydraulic community.

Auxiliary variables. The operation of a turbomachine is closely linked with its speed of rotation. Turbomachines are rotor-dynamic devices and the circumferential blade velocity $u = D\pi n$ at some meaningful reference diameter D provides a good scaling parameter for non-dimensionalizing variables like the pressure, head, or energy. The reference pressure obtained from the square of the blade speed is the velocity head $u^2/2\,g$, or dynamic pressure $\rho u^2/2$. Practical conventions for the reference diameter are the runner exit diameter D_2 and the throat diameter D_{th} for reaction turbines, or impeller exit diameter D_1 for pumps or pump-turbines. IEC 60193 [1] stipulates the exit diameter in turbine sense D_2. In this book, we use this convention but shall deviate slightly from this convention whenever this permits better physical insight. In addition to the blade speed, a useful reference velocity $c = \sqrt{(2E)}$ (known as the 'spouting' velocity) may also be derived from the operating head $H = E/g$. The spouting velocity $\sqrt{(2E)}$ is the velocity that would be achieved if all of the potential energy available in the head (H) were to be converted to kinetic energy in a frictionless nozzle. For the non-dimensional work and flow parameters K_u and K_{cm} described below, the spouting velocity $\sqrt{(2E)}$ is used as a reference velocity rather than the blade speed.

A further alternative is to define a dynamic head h_{dyn} based on a meridional velocity $c_m = Q/(D^2\pi/4)$ in the flow, instead of the circumferential blade velocity u. This reference is useful for estimating the steady-state pressure in the draft tube [2]. *Non-dimensional reference parameters based on E and D.* Parameters using the potential energy E and diameter D for reference produce the most frequently used type of hill chart.

Figure 1.1 shows how the IEC 60193 standard explains the hill chart of a Francis model turbine.[1]

The dimensionless discharge Q_{ED} ('discharge factor') is displayed against the dimensionless rotational speed n_{ED} ('speed factor'), both as defined below, for several guide vane settings, with the contours of efficiency (which lead to the name "hill" chart). The advantage of this arrangement with the rotational speed as the abscissa is that it can be used to identify all operating conditions of a turbine, including standstill.

Conventional dimensionless parameters used as measures for the blade speed are

$$K_u = \frac{u}{\sqrt{(2E)}} = \frac{D\pi n}{\sqrt{(2E)}} \tag{1.1}$$

---

[1] Figure 55 from IEC 60193 ed. 20.0 (1999), Ref. [1].

Fig. 1.1 Francis turbine hill chart using references E and D. Reproduced with kind permission © 1999 IEC Geneva, Switzerland (www.iec.ch)
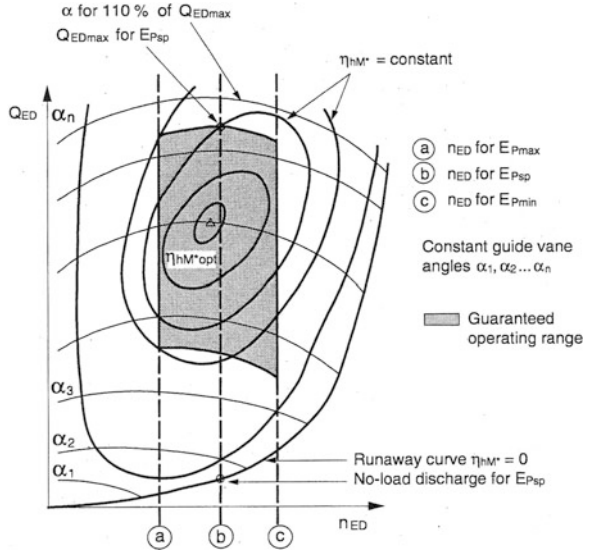
and

$$n_{11} = \frac{Dn}{\sqrt{(H)}}. \tag{1.2}$$

K_u is the blade speed made non-dimensional with the spouting velocity and is widely used by turbine engineers—it is identical with the parameter Φ well known to North American water turbine engineers and u/c_0 used by steam and gas turbine engineers. n_{11} is the blade speed made non-dimensional with the square root of the net head. This is in fact not exactly non-dimensional as the head would have to be multiplied by the acceleration due to gravity, g. Because of this, the parameter bears some risk of inaccuracy due to slight variations of gravity parameter g. A further dimensionless blade speed parameter n_{ED} defined in IEC 60193 avoids this problem

$$n_{ED} = \frac{nD}{\sqrt{(E)}} \tag{1.3}$$

In the same manner, dimensionless parameters for discharge Q have been derived as follows:

$$K_{cm} = \frac{c_m}{\sqrt{(E)}} \tag{1.4}$$

$$Q_{11} = \frac{Q}{(D_2\sqrt{(H)})} \quad \text{and} \tag{1.5}$$

$$Q_{ED} = \frac{Q}{D_2\sqrt{(E)}} \tag{1.6}$$

Table 1.1 Relationships between characteristic parameters for head/energy/speed

	From n_{ED}	From $K_u = \Phi$	From n_{11}
n_{ED} =		$0.45016 \times K_u$	$0.005322 \times n_{11}$
K_u =	$2.22144 \times n_{ED}$		$0.011823 \times n_{11}$
n_{11} (metric) =	$187.89 \times n_{ED}$	$84.582 \times K_u$	
ψ =	$0.20264/n_{ED}^2$	$1/K_u^2$	$7{,}154.1/n_{11}^2$
E_{nD} =	$1/n_{ED}^2$	$4.9348/K_u^2$	$35{,}304/n_{11}^2$

Both n_{11} and Q_{11} may give rise to misunderstanding because their values are different if based on either the metric (SI) or English units. Using metric values and standard gravity 9.80665 m/s^2, the relationships between the non-dimensional variables for blade speed and energy are given in Table 1.1

Another important parameter based on energy E is the cavitation number (Thoma number) σ:

$$\sigma = \frac{\mathrm{NPSE}}{E} \tag{1.7}$$

where NPSE is the net positive suction energy, which is the pressure reserve compared to vapor pressure, at a certain elevation in the machine, as defined in IEC 60193. When NPSE becomes small the pressure approaches that of the vapor pressure and cavitation may occur. For some purposes, e.g., the comparison of cavitation phenomena in a draft tube at different values of prototype operating head, or in turbines with different specific speed, a modified parameter, $\sigma\psi = \sigma/K_u^2$ or equivalent, may provide a better representation of the degree of cavitation; we use this parameter in Fig. 2.3 and also in Chap. 7.2.

Non-dimensional reference parameters based on n and D. The theoretical description of turbomachines often makes use of a non-dimensional parameter for head (or stage pressure) called the pressure coefficient, in which the head is made dimensionless with the square of the blade speed:

$$\psi = \frac{2gH}{u^2} = \frac{1}{K_u^2}, \tag{1.8}$$

The corresponding definition in IEC 60193 is the energy coefficient E_{nD}.

$$E_{nD} = \frac{E}{(nD)^2}. \tag{1.9}$$

The definition of E_{nD} is simpler than that of ψ when expressed in terms of rotational speed n, as the factor $2/\pi^2$ is omitted. Unfortunately, in exchange for this simplicity, the analogy with parameters often used in other (non-hydraulic) turbomachines has been sacrificed, together with a clear physical interpretation.

Table 1.2 Relationships between characteristic parameters for discharge

	From Q_{ED}, n_{ED}	From K_{cm}, K_u	From Q_{11}, n_{11}
Q_{ED} =		$1.11072 \times K_{cm}$	$0.31933 \times Q_{11}$
K_{cm} =	$0.90032 \times Q_{ED}$		$0.2875 \times Q_{11}$
Q_{11} (metric) =	$3.1315 \times Q_{ED}$	$3.4783 \times K_{cm}$	
φ =	$0.4053 \times Q_{ED}/n_{ED}$	K_{cm}/K_u	$24.317 \times Q_{11}/n_{11}$
Q_{nD} =	Q_{ED}/n_{ED}	$2.4674 \times K_{cm}/K_u$	$60 \times Q_{11}/n_{11}$

In an analogous manner to the pressure coefficient, the discharge coefficient can be defined as $\varphi = cm/u$, so that with $cm = Q/(D^2\pi/4)$ and $u = D\pi n$, its successor as defined in IEC 60193 is

$$Q_{nD} = \frac{Q}{(nD^3)}. \qquad (1.10)$$

The use of Q_{nD} plotted against E_{nD} for dimensionless hill charts is also foreseen in IEC 60193, as an alternative to Q_{ED} plotted over n_{ED}. This latter representation has a number of advantages. A machine in the electrical grid operates at constant speed; therefore, the use of a 'speed' parameter (n_{ED}) may at first sight seem an unnecessary complication. If the focus of interest is on normal operation, the version using E_{nD} and Q_{nD} is more descriptive because the axes are directly proportional to the main hydraulic parameters. In particular, operation in pump mode is often represented in this way. Table 1.2 shows the relationships between different parameters for the discharge flow.

Transient operating conditions of turbines may usefully be visualized using the kind of diagram shown in Fig. 1.1. In pumps and pump-turbines, however, a problem of representation arises from the fact that the characteristics $Q_{ED} = f(n_{ED})$ are ambiguous in the two instability regions, as the flow may take on two different values for a given head at a fixed speed, see Chap. 6.4. This problem also occurs in the domain of hydraulic transient simulation where it hampers interpolation. Based on a concept published by Suter [3] for non-regulated pumps, different sets of parameters have been developed that avoid such ambiguity. A description of this technique is given in [4].

In the case of reaction turbines, in particular Francis turbines, the use of Q_{nD} (rather than Q_{ED}) has another positive side effect because the limits between different flow regimes in the draft tube—which are at the same time the boundaries of the occurrence of different kinds of pulsation—are basically lines of constant discharge. Figure 1.2 is an example from a model Francis turbine with a specific speed of $n_{QE} = 0.144$.[2] Using this property of Q_{nD} may be helpful in order to avoid measurements for an unnecessary large number of prototype heads (or n_{ED}). *Specific speed.* The specific speed is a non-dimensional parameter based on both the flow and the head, which can be used to categorize machines into different

---

[2] For definition, see Eq. (1.14).
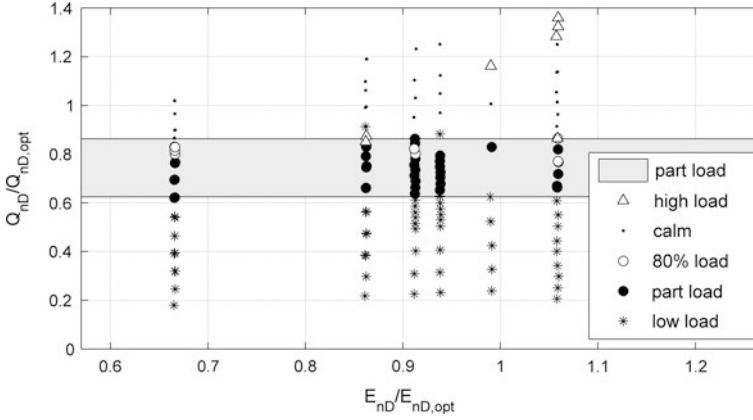
Fig. 1.2 Pulsation types in a Francis hill chart, references n and D

Table 1.3 Relationships between parameters for specific speed

	From v	From n_{QE}	From n_Q	From n_s
$v=$		2.1078 n_{QE}	6.339e−3 n_Q	2.0243e−3 n_{QE}
$n_{QE}=$	0.47443 × v		3.0075e−3 n_Q	0.9604e−3 n_{QE}
$n_Q=$	157.75 × v	332.50 n_{QE}		0.31933 n_{QE}
$n_s=$	494.0 × v × $f(\eta)$	1,041 × n_{QE} × $f(\eta)$	3.1315 × n_Q × $f(\eta)$	

Turbine $f(\eta) = \sqrt{\eta}$ *Pump* $f(\eta) = \sqrt{1/\eta}$

types. Traditional measures for specific speed, or runner speed for a given head and flow, have been, among others,

$$n_Q = 60 \times n \times Q^{1/2} \times H^{-3/4} \tag{1.11}$$

$$n_S = 60 \times n \times P^{1/2} \times H^{-5/4}, \text{ and} \tag{1.12}$$

$$v = \frac{\varphi^{1/2}}{\psi^{3/4}} \tag{1.13}$$

n_Q and n_S are not entirely dimensionless, and are therefore open to misinterpretation between systems using different units. In Eqs. (1.11, 1.12), and Table 1.3, Q is in m³/s, P in kW and net head H is in mwc.

In this book, we use the definition from IEC 60193,

$$n_{QE} = n \times Q^{\frac{1}{2}} \times E^{\frac{-3}{4}} = n_{ED} \times Q_{ED}^{\frac{1}{2}} = Q_{nD}^{\frac{1}{2}} \times E_{nD}^{\frac{-3}{4}} \tag{1.14}$$

All values refer to the best efficiency point in turbine or pump mode, as appropriate. The relationships between the different definitions of specific speed are given in Table 1.3.

1.2 Amplitudes and Spectra

When discussing the amplitude of vibrations and pulsations poor definitions are often a source of confusion. Data on pulsation intensities are of little use if their definition is not clear, and it is normally not possible to compare data from different sources unless truly identical definitions are used. To demonstrate this issue an example is discussed in detail in this section.

The amplitude is the maximum deviation of a pulsating variable from its mean value [5]. This definition is clear in the case of a periodical signal, in reality however, we usually have to deal with random signals, even if they may contain periodic components like a sine wave. For a random signal, one cannot apply the same definition as for a periodic sine wave, because its evaluation would yield either random or arbitrary results. A statistical definition is necessary to obtain unambiguous results.

In IEC 60193 [1], the relevant standard for hydraulic model testing, there is a footnote suggesting to define the amplitude as that variation which contains a certain percentage of the sample, for example 97 % is suggested in the footnote. While the wording in IEC 60193 is rather non-committal at the moment, this proposal for a standardized amplitude would be extremely helpful if practicing engineers were to start adopting it. The question is not purely academic because the apparent amplitude value largely depends on the percentage chosen, as explained below.

The example in Fig. 1.3 compares some possible, and actually used, values of 'peak-to-peak amplitude' based on test results sampled during a Francis turbine model test.[3] The five curves have been computed from the same time series of the same pressure fluctuation signal and represent different definitions of the amplitude. The signals at two specific operation points with typical pulsation characteristics shown as vertical bars are shown in Fig. 1.4. The right-hand side shows a test point with a fairly regular pulsation of the draft tube vortex (at 64 % of design flow) and the left-hand side shows the very stochastic signal from low partial load (at 33 % of design flow).

For these two selected test points marked in the figure, these amplitudes are compared in Fig. 1.4 with a representative time sample from the signal, the mean value being suppressed. The horizontal lines describing the various 'amplitudes' are given the color of the corresponding curve in Fig. 1.3. The differences in apparent amplitude are spectacular, and certainly some results are more plausible than others.

The blue and magenta lines are results from what may be called a *window method*. The definition derives from the literal sense of peak-to-peak amplitude, as the difference between the maximum and minimum value of the signal, within a certain time window, as shown in Fig. 1.5.

---

[3] This test series is also the basis of Figs. 1.4, 1.5, 1.6, 1.7, 1.8, 1.9, 1.10, 1.11, 1.12, 1.13.
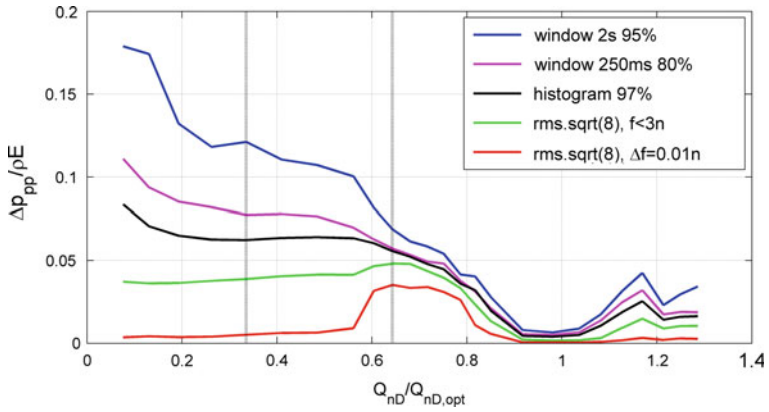
Fig. 1.3 Various measures for amplitude compared (example)
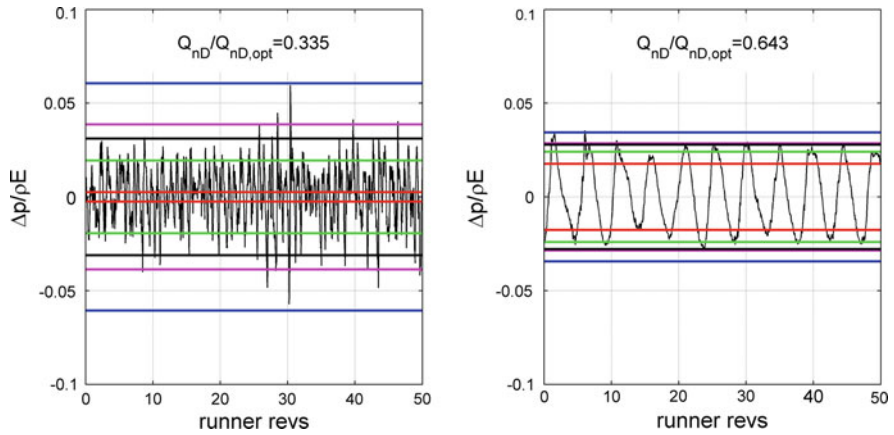
Fig. 1.4 Amplitude measures compared to time-domain data
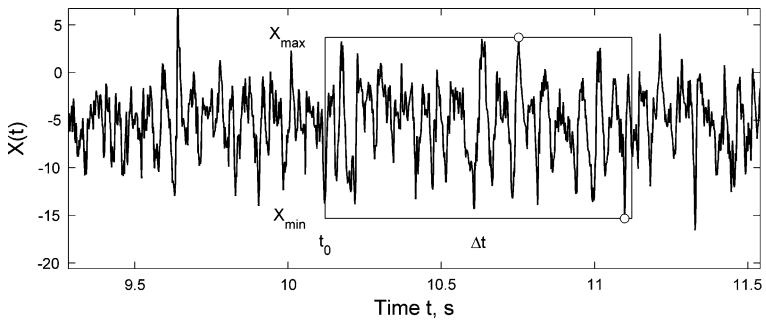
Fig. 1.5 Peak–peak amplitude in a time window
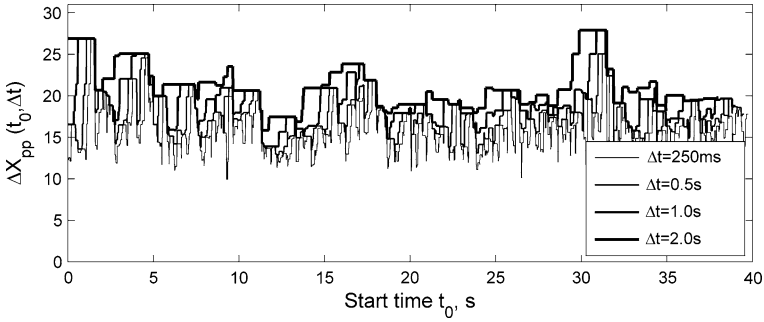
Fig. 1.6 Peak–peak amplitude depends on the time window
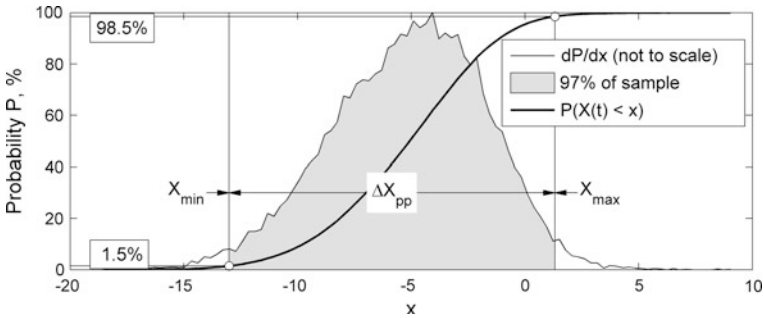
Fig. 1.7 Peak–peak amplitude by the histogram method

It is evident from the figure that the value of $\Delta X_{pp} = X_{max} - X_{min}$ will not be the same if we choose a different start time t_0 or a different length Δt for the window. This is a consequence of the stochastic nature of the signal and, unfortunately, it applies to the vast majority of test results. For the signal represented in Fig. 1.5 (and in the left-hand diagram of Fig. 1.4), this dependency on t_0 and Δt has been visualized in Fig. 1.6. In order to eliminate the uncertainty caused by the random influence of t_0, it is necessary to evaluate ΔX_{pp} for a sufficient number of windows N_W of the recorded data. In addition, a rule is required saying how the N_W values are to be processed to yield the desired amplitude. This could be by simple averaging or, more conservatively, one may sort the results by ascending values and discard a certain percentage of the highest 'outliers', for instance the largest 5 %. The highest value in the remaining 95 % is then used as peak-to-peak amplitude. This has been done for the blue curve in Fig. 1.3. For statistical reasons, there is also an important influence of the window length, as demonstrated in Fig. 1.6. For the blue curve in our example, a window length of $\Delta t = 2$ s has been used.

The choice of window length Δt is as arbitrary as the percentage chosen, and both have a strong positive correlation with the resulting amplitude. A definition

using 80 % of 250 ms windows (magenta curve) would thus yield much lower values. One may argue that Δt should be related to the lowest frequency of interest. In the test series considered, the runner rotation period is 0.0522 s. A typical period of vortex rotation, as will be shown in Sects. 2.2 and 7.1, would be about four runner revolutions, i.e., 200 ms, thus the 250 ms window seems adequate.

The black curve in Fig. 1.3 has been obtained using the method suggested in the IEC 60193 standard. One may call this a *histogram method* because a probability density curve (histogram, Fig. 1.7) of the sampled values is evaluated retaining the 97 % values in the middle and discarding half of the remaining 3 % at the lower as well as the upper limit of the distribution curve.

The double amplitude, denoted ΔX_{pp} in the diagram is then defined as the difference between the values separating the retained and discarded values.

According to Fig. 1.3 the window method used with appropriate parameters may produce roughly the same results compared to a histogram method, depending on the characteristic of the signal.

A further class of possible definitions is based on evaluation of *frequency spectra*. For a sine function, the single (that is zero-to-peak or half of the full peak–peak) amplitude is equal to the standard deviation (rms = root mean square) of the signal times $\sqrt{(2)}$.

$$\Delta X_{0-p} = \Delta X_{\mathrm{rms}} \times \sqrt{2} \qquad \text{for } x(t) = a \text{ sinbt} \tag{1.15}$$

If only a single spectral line of the signal is considered, then such a definition would yield the amplitude of this spectral component (red curve in Fig. 1.3). To obtain a peak-to-peak amplitude, the factor would be $2 \times \sqrt{(2)} \cong 2.828$.

Sometimes the definition is extended to a wider part of the spectrum (green curve in Fig. 1.3); for example using the overall rms value of all frequencies lower than three times runner frequency. In wide-band signals, however, the factor $\sqrt{(8)}$ between the rms and peak-to-peak amplitude is no longer justified. Typically, the 97 % histogram method would yield about 4.0–4.5 times the standard deviation which means up to 60 % higher values.

$$\Delta X_{p-p} \cong \Delta X_{\mathrm{rms}} \times (4.0...4.5) \quad \text{for random } x(t) \tag{1.16}$$

Looking at the red curve in Fig. 1.3, the definition based on a single spectral line seems poorly justified. Nevertheless, there might be some good reason to analyze the data with this method. If the purpose of the test is to assess the risk of a resonance with low damping, then the intensity of such resonance depends indeed on the magnitude of the corresponding spectral line. On the other hand, mechanical fatigue is often a result from many frequencies acting simultaneously (see Sects. 1.6 and 4.2.2).

On the right-hand side of Fig. 1.4 a test point with a fairly regular pulsation of the draft tube vortex is shown. In this case, the scatter between the various definitions is much smaller than that of the very stochastic signal from low partial load, on the left-hand side. The 50 runner revolutions of the selected windows correspond to 2.6 s.
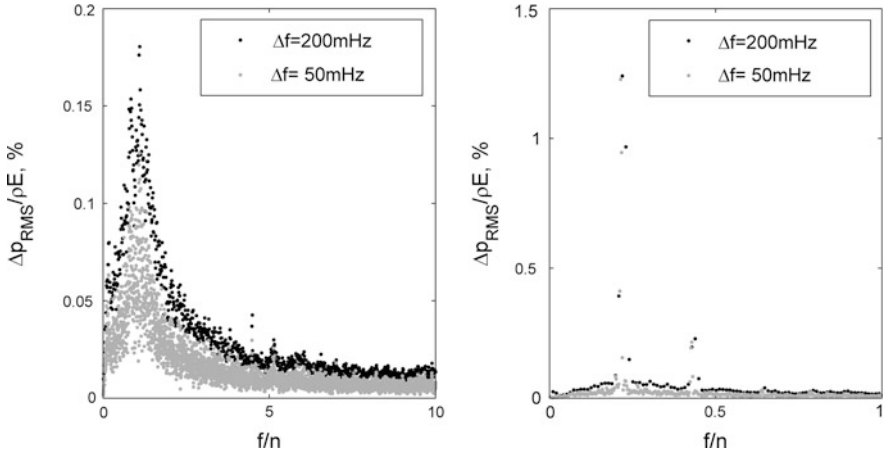
Fig. 1.8 Influence of frequency resolution Δf on spectral results

While amplitudes are obtained by analyzing values directly sampled in a time series (time-domain analysis), many problems require information about the frequency content of a pulsation. In *frequency-domain analysis*, the distribution of signal intensity with regard to frequency, presented as a frequency spectrum, is investigated. Frequency spectra are usually obtained using the fast Fourier transform (FFT) of sampled time series of the signal. Suppose that the pulsating variable is sampled N times in equal time intervals t_s. The Fourier transform in this case will result in an array of $N/2$ spectral values. The frequencies will range from zero to $F = f_s/2 = 1/2t_s$, the frequency spacing or frequency resolution being $\Delta f = f_S/N$. The spectral values are complex numbers, with a real part and an imaginary part of the spectrum, with a phase angle for every frequency.

A common representation is a linear spectrum showing for all frequencies f the amplitude of a sine function with the rms content of the frequency band $f \pm \Delta f/2$, with the phase information discarded. Some evaluations automatically search and display the spectral line f with the highest spectral value, as for example the red curve in Fig. 1.3. If the process analyzed has a continuous spectrum, and the resolution Δf is not known, then this number does not convey any useful information because the spectral values are proportional to the square root of Δf, see the following comments and Fig. 1.8.

Adding the squares of the real and imaginary part of the linear spectrum yields the power spectrum. Note that the power spectrum contains less information as the phase information is lost. This spectrum is not a power density function estimate because it is not divided by bandwidth Δf. The advantage is that truly sinusoidal components of the signal are shown with their real intensity (which has nothing to do with bandwidth). The disadvantage is that the continuous spectrum for any given frequency is a function of bandwidth; for instance, if the increment Δf is widened by a factor of 2, then the continuous power spectrum is lifted by a factor of 2, and the magnitude of the linear spectrum by $\sqrt{(2)}$.

The influence of the frequency resolution Δf on is the resulting spectral values is illustrated by the Fig. 1.8. The two spectra belong to the test points shown in Fig. 1.4. The point with the stochastic pulsation (left-hand side) shows the sensitivity of the continuous spectrum to changes of frequency resolution. This effect may also be noticed in the other point with near-periodic pulsation—note the different scale—but there the important component is the narrow peak contained in a single frequency interval and therefore not depending on the resolution Δf.

The phase information in the linear spectrum may be useful if several signals of an oscillating system are sampled at the same time. In such a case, it is often possible to measure a complex *transfer function* [6] between the signals which may yield better and more reliable insight into the mechanism of pulsation. In order to obtain good accuracy, transfer function measurement must always be based on a sufficient number of separate time windows. As a by-product of this process, the coherence between the signals is obtained. For every frequency, coherence may assume a value between 0 and 1. A value of 0 means that the signals are completely independent at the given frequency, while values close to 1 indicate that there is a strong linear dependency between the two signals, the deviation from 1 being a measure for the relative amount of noise or other deviations from linear relationship. For any measured transfer function, only the frequency intervals with a coherence close to 1 are reliable.

Waterfall diagrams (see Figs. 1.15 and 1.16 for examples) are a common way to concentrate spectra from several tests in a single diagram. Their benefit is to show at a glance the influence of a test variable—very frequently the turbine discharge or the tail water pressure—on the development of a spectrum. Quantitative details are not easy to read in a waterfall diagram, therefore in many cases they are more like a convenient extra aiding comparison of data, and are not a real alternative or replacement for single spectra of important variables.

1.3 Pulsation Phenomena in Pipes and Plants

Many dynamic problems occurring in hydraulic machines can only be properly understood if their interaction with the fluid column in the waterways of the plant is taken into account. Non-steady pressure and flow propagate into the fluid column in the penstock and other pipes connected. Even in plants with short and simple water conduits, there is always some kind of response of the water conduit to excitations from the hydraulic machine. This response may be seen as a dependency between the pressure pulsation and the flow pulsation, a dependency that is basically governed by three types of properties:

- Inertia,
- compressibility (compliance),
- dissipation (friction).

For instance, a simple time-domain model based on the unsteady momentum equation for a frictionless incompressible fluid when applied to a very short uniform piece of pipe with length L and cross-section A leads to

$$p_2 = p_1 - \left(\frac{\mathrm{d}Q}{\mathrm{dt}}\right) \times \frac{\rho L}{A} \tag{1.17}$$

where the pressure p_1, p_2 and the discharge Q are functions of time. The equation indicates that the pressure difference $p_1 - p_2$ divided by the inertia term $\rho L/A$ produces the fluid acceleration $\mathrm{d}Q/\mathrm{dt}$. For a sinusoidal pulsation of the form $e^{\mathrm{j}\omega t}$ at frequency $\omega = 2\pi f$ we may use an equivalent frequency-domain model. This is obtained by replacing the terms in the equation by the equivalent sinusoidal relationship. The derivative d/dt then leads to a multiplication of the discharge with the imaginary factor $\mathrm{j}\omega$, so that the pulsation vectors are given by

$$\tilde{p}_2 = \tilde{p}_1 - \tilde{Q} \times \mathrm{j}\omega \times \frac{\rho L}{A} \tag{1.18}$$

Here $\tilde{p}_1, \tilde{p}_2$ and $\tilde{Q}$ are complex numbers indicating the amplitude and phase of the pulsation vectors at frequency ω. We learn from this that the discharge pulsation $\tilde{Q}$ has a 90° lag (indicated by the imaginary factor $-j$) with respect to the driving pressure difference $\tilde{p}_1 - \tilde{p}_2$.

Our extremely simple model accounts only for the effect of mass (water hammer), as the friction and the compressibility in the short pipe have been neglected. More general models have been defined taking into account these effects. Such models must always jointly consider the pressure and discharge pulsation as these two 'state' variables cannot be treated in a disconnected manner. Transmission of hydraulic pulsation through any linear element is always described by a pair of equations linking the pulsation vectors on either side of the element. The example below shows the outlet pressure and the outlet discharge as a function of the inlet pressure and inlet discharge:

$$\begin{aligned}
\tilde{p}_2 &= a_{11}\tilde{p}_1 + a_{12}\tilde{Q}_1 \\
\tilde{Q}_2 &= a_{21}\tilde{p}_1 + a_{22}\tilde{Q}_1
\end{aligned} \tag{1.19}$$

The coefficients a_{ij} may be arranged in a so-called transfer matrix A. In our simplified example from above, the matrix is

$$A = \begin{pmatrix} 1 & -\mathrm{j}\omega\rho L/A \\ 0 & 1 \end{pmatrix} \tag{1.20}$$

In this case, we could simply write $\tilde{Q}$ instead of $\tilde{Q}_1$ and $\tilde{Q}_2$ and omit the second equation, because we neglected compressibility. In the general case of a uniform pipe element, the coefficients of the transfer matrix including compressibility and friction effects are [7, 8]

$$a_{11} = a_{22} = \cosh(\gamma L)$$
$$a_{12} = -Z_c \times \sinh(\gamma L)$$
$$a_{21} = -\left(\frac{1}{Z_c}\right) \times \sinh(\gamma L)$$

$$(1.21)$$

In this definition, cosh and sinh are hyperbolic functions, the factor Z_c is the characteristic impedance of the fluid column in the pipe, and γ is the propagation constant (which depends on frequency). All of these parameters are normally complex-valued. In case of a circular pipe with diameter D, cross-section $A = D^2\pi/4$, and wall thickness s, two auxiliary variables Z and Y may be introduced that account for the modulus of elasticity of the pipe wall E_W, the compliance of the fluid $1/E_F$, and the friction λ:

$$Z = \left(\frac{\lambda \bar{c}}{D} + j\omega\right) \times \frac{\rho}{A}$$

$$Y = \left(\frac{(D/s)}{E_W} + \frac{1}{E_F}\right) \times A \times j\omega = j\omega \times \rho \times \frac{A}{a^2}$$

$$(1.22)$$

and this allows us to calculate the two parameters as

$$\gamma = \sqrt{Z \times Y}$$

$$(1.23)$$

and

$$Z_c = \sqrt{Z/Y}.$$

$$(1.24)$$

In the equation for Y, viscoelastic dissipation effects have been neglected; if we also neglect the steady-state friction ($\lambda = 0$), then the characteristic impedance is real valued:

$$Z_c = a \times \frac{\rho}{A}$$

$$(1.25)$$

and the transfer coefficients become

$$a_{11} = a_{22} = \cos(\omega L/A)$$
$$a_{12} = -Z_c \times j \times \sin(\omega L/A)$$
$$a_{21} = -\left(\frac{1}{Z_c}\right) \times j \times \sin\left(\frac{\omega L}{A}\right)$$

$$(1.26)$$

For a short pipe, $L < 0.2\, a/\omega$, the coefficients may be further simplified:

$$a_{11} = a_{22} \cong 1$$
$$a_{12} \cong -j\omega \times \frac{\rho L}{A}$$
$$a_{21} \cong -j\omega \times \frac{LA}{(\rho a^2)}$$

$$(1.27)$$

Our starting case would result from the equations above if we neglect the coefficient a_{21} representing compressibility.
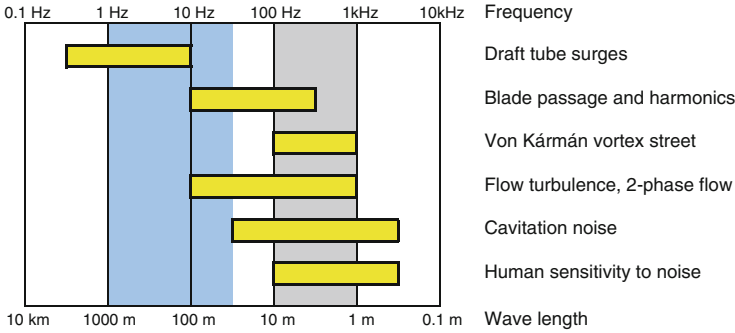
Fig. 1.9 Typical ranges of frequency and wavelength

Frequency-domain models are preferred for many unsteady flow purposes because they provide a much simpler way to formulate the problems, compared to time-domain models. The transfer matrix of a series connection of several pipes or other elements is represented simply by multiplication of the consecutive individual transfer matrices. The complex ratio between the pressure and discharge pulsation in any point of such a linear network of pipes is the local hydraulic impedance Z_h

$$Z_h(j\omega) = \frac{\tilde{p}}{\tilde{Q}} \tag{1.28}$$

A value of the impedance can also be defined for a component of the network whose discharge is the same at both ends, i.e., with negligible compressibility. In this definition, the local pressure is replaced by the pressure difference across the component. An example is the turbine impedance between the spiral casing entry and runner exit for low frequencies (the draft tube is often represented separately)

$$Z_T(j\omega) = \frac{(\tilde{p}_1 - \tilde{p}_2)}{\tilde{Q}} = \frac{\rho g \tilde{H}}{\tilde{Q}} \tag{1.29}$$

For a disturbance propagating in water, the wave speed

$$a = \sqrt{\left(\frac{E_F}{\rho}\right)} \tag{1.30}$$

results as 1,449 m/s from the fluid's modulus of elasticity ($E_F = 2.1\,\mathrm{GPa}$) and the density of water, $\rho = 1{,}000$ kg/m^3. In our context, we will always deal with plane (1D) waves propagating in pipes or ducts whose walls are not rigid. The compliance of the wall acts on the fluid as if it was a reduction of the fluid stiffness E_F. In practice, this is accounted for by using a reduced wave velocity a. For a steel penstock in a medium-head plant, a wave speed of 1,000 m/s would be a common figure to use for the effective wave speed. The compliance of the wall in this case

has about the same quantitative effect as the compressibility of the fluid, as can be understood from Eq. (1.30)

If the pulsation is periodic with frequency f, then its wavelength becomes $\Lambda = a/f$. These simple facts may be used to compare various kinds of pulsation in a frequency graph with logarithmic scale. In the Fig. 1.9, the most common types of hydraulic pulsation are placed roughly in the order of ascending frequency, or decreasing wave length. Note that, this categorization is in the same order that will be used for the descriptive chapters to follow, where each of these types of pulsation is explained in more detail.

A comparison between the wavelength in a fluid-filled pipe and the dimensions of the machine or plant may be useful to adequately approach certain kinds of problems. For instance, detailed mathematical models accounting for the dynamic response of the penstock may simply not make sense if the frequency range of interest is too high. The frequency of runner blade passage, for example, is known for every ordinary hydroelectric machine but nevertheless, the pertinent wavelength has the same relative uncertainty of prediction as the effective wave speed, in typical cases about 5–10 %. If the uncertainty of the reflection time is no longer small compared to the oscillation period $1/f$, then the dynamic response of the penstock becomes very uncertain. Considering this and the uncertainty inherent to dynamic modeling of the machine itself, there is but little chance for a meaningful simulation model including the system response.

On the other hand, the wave length associated with low-frequency phenomena of draft tube pulsation is of the same order of magnitude as the penstock length, or even shorter. For these problems it is sufficiently accurate and therefore useful to consider the dynamic response of the water conduit.

With regard to noise, Fig. 1.9 also explains which phenomena are most likely to be associated with audible noise. The main frequencies of draft tube surges are outside of the audible frequency range. Draft tube surges can only be 'heared' by the modulation of higher frequencies associated with them. On the other hand, the wide-band noise due to flow turbulence or cavitation notoriously coincides with the best sensitivity range of the human ear. These phenomena cannot be handled by 1D transient methods because of their complex 3D structure and their very short wavelength.

A pressure wave traveling through a pipe is always accompanied by a wave of fluid discharge. The characteristic impedance of the fluid-filled pipe can be described by the ratio between the two state variables p and Q of the wave $Z_c = \dfrac{\tilde{p}}{\tilde{Q}}$. With the two flow variables[4] expressed as complex numbers to consider their phase, Z_c becomes a real number if dissipation effects such as friction may be neglected. In this case, the pressure wave and the discharge wave are synchronous, and their amplitude ratio is $Z_c = a\rho/A$, where A is the internal cross-section of the pipe. If the pipe terminates at a boundary with constant pressure such as a

---

[4] $\tilde{p}, \tilde{Q}$ are the state vectors of the traveling wave, not of the resulting pulsation.

reservoir, then an approaching pressure wave is reflected with equal amplitude and negative sign; the resulting wave thus fulfills the boundary condition of constant pressure. Due to the inverted sense of propagation, the reflected discharge wave keeps its phase, and therefore a doubling of discharge pulsation results at the open end. From the superposition of waves traveling in either direction, the pressure and flow inside the pipe exhibit a standing wave pattern. Pressure nodes (i.e., points with minimum pulsation amplitude) will appear if the length of a conduit exceeds half of the wave length at the respective frequency.

The correct modeling of unsteady pipe friction in the context of oscillations is a difficult task. Various unsteady friction models exist and some of them have been shown to work well in selected cases of transient computation; for a survey see Bergant [9]. For single-phase flow in rigid pipes, the main difficulty stems from the 2D structure of pipe flow. Distortion of the velocity profile during variations of discharge causes a rather complex behavior with regard to unsteady friction. Some authors have devised a simplifying approach to modeling of unsteady friction effects in the frequency domain. A frequency-dependent damping effect has been inter-preted as a volume viscosity μ of the fluid (Habán [10]) or as stiffness-proportional damping (Svingen [11]). This type of damping may be modeled by inserting a term containing μ in Eq. (1.22) that stems from the equation of continuity

$$Y = \left(\frac{j\omega Ag}{a^2}\right) \times \left(1 - \frac{j\omega\mu}{\rho a^2}\right) \tag{1.31}$$

In this representation, μ was found to be inversely proportional to the frequency

$$\mu(f) = \frac{\mu_0}{f} \tag{1.32}$$

Experimental values obtained for μ_0 are 7.4 [11], 9.8 [10], and 5.0 GPa [12]. The latter value resulted from a test using sustained stochastic oscillations in a penstock. An alternative way representing the same amount of damping is to change Z instead of Y in Eq. (1.22), introducing an additional friction parameter k in the momentum equation

$$Z = \left(\frac{1}{Ag}\right) \times \left(\frac{\lambda \times c}{D} + k \times |\omega| + j\omega\right) \tag{1.33}$$

k is independent of frequency, and in tests reported by Dörfler [12], k resulted as 0.015 for sustained oscillations and 0.030 for shutdown transients, the latter value being in agreement with Habán's results. Given this friction characteristic, the decay of pulsation following shutdown in any uniform pipe should, in the absence of additional damping effects, normally correspond to a damping ratio near $\zeta = 0.015$.

Using the Eq. (1.26), the behavior of an elastic fluid in a system of pipes is very efficiently represented in the frequency domain. In this model the fluid inertia, compressibility, and friction are assumed to be uniformly distributed along the

pipe length, and therefore this type of model is called a *distributed-parameter* model. Simulation in the time domain is not directly possible with this model. It is necessary to replace the distributed continuum by an alternating arrangement of incompressible stretches of duct and compressible points between them, and this yields a *lumped-parameter* model. The lumped-parameter approximation consists of a finite number of simple elements, and therefore it may be more readily integrated to obtain transient simulations. For the same reason the lumped-parameter models have only a finite number of eigenvalues which may be computed by standard methods if the model is linear or linearized.

1.4 Hydraulic Resonance

To explain some properties of hydraulic resonance, let us consider a single Francis turbine with its penstock and draft tube, as shown schematically in Fig. 1.10, with the technical data influencing the dynamics as shown in Table 1.4. This would be a turbine operating under a head of 100 m, with a synchronous speed of 300 rpm and a rated output of about 50 MW.

Our interest in this case is with the pulsation produced by the draft tube vortex at partial load. The simplest model to reasonably represent this phenomenon is a series connection of five elements as shown in Fig. 1.10, each represented by an equation in the frequency domain:

1. The fluid in the penstock (inertia I_1)

$$\tilde{p}_1 = -\tilde{q}_1 \times j\omega \times \rho \times \frac{L_1}{A_1} = -\tilde{q}_1 \times j\omega \times I_1$$

2. The flow resistance R of the turbine

$$\tilde{p}_C = \tilde{p}_1 - \tilde{q}_1 \times R_\text{T} \times \frac{\rho E}{Q} = \tilde{p}_1 - \tilde{q}_1 \times R$$

3. The compressibility C_C of the draft tube vortex

$$\tilde{q}_2 = \tilde{q}_1 - \tilde{p}_C \times j\omega \times C_C$$

4. The pressure source $\Delta\tilde{p}_\text{EX}$ at the draft tube elbow

$$\tilde{p}_2 = \tilde{p}_C + \Delta\tilde{p}_\text{EX}$$

5. The fluid inertia I_2 in the draft tube

$$\tilde{p}_2 = \frac{\tilde{q}_2 \times j\omega\rho L_2}{A_2} = \tilde{q}_2 \times j\omega I_2 \qquad (1.34)$$
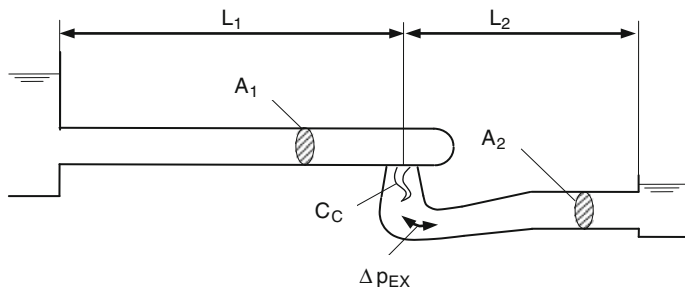
Fig. 1.10 System schematic

Table 1.4 Plant data for partial load pulsation example

L_1	100	m	Equivalent length[a] of penstock plus turbine
A_1	10	m^2	Cross-section of penstock
L_2	6	m	Equivalent length of draft tube
A_2	4.5	m^2	Cross-section of draft tube
R	5.00e + 04	Pa × s × m^{-3}	Hydraulic resistance of turbine $\sim 1.7\rho E/Q$
C_C	7.14e−06	m^3 × Pa^{-1}	Compressibility ('cavitation compliance') of draft tube vortex
f	1.25	Hz	Precession frequency of draft tube vortex = $\omega/2\pi$
ρ	1,000	kg × m^{-3}	Density of working fluid

[a] For non-uniform cross-section $A = f(x)$, equivalent length $L_1 = A_1(\mathrm{d}x/A(x))$

This set of equations defines a mathematical model for the behavior of this system in the frequency domain. The model assumes the fluid in the penstock and draft tube may be treated as incompressible and frictionless, but allows for a compressible spot just downstream of the turbine runner.[5] Due to our assumptions, we have a third order system, the state variables being the discharges $\tilde{q}_1$ and $\tilde{q}_2$, and the pressure $\tilde{p}_C$. The compressibility parameter C_C (cavitation compliance) is defined by

$$C_C = -\frac{\partial V_C}{\partial p_C} \tag{1.35}$$

and represents the change in volume of the system for a given change in pressure. If the 'cavitation compliance' C_C is not zero, then the system will have exactly one natural frequency corresponding to the pair of complex conjugate roots $s_{1,2}$ shown in Eq. (1.39).

Using the transfer matrix method, we may obtain a complex transfer function $G(j\omega)$ [6] between the disturbance (pressure source $\Delta\tilde{p}_{EX}$) and the pressure oscillation at the runner exit ($\tilde{p}_C$):

---

[5] In this model, the turbine impedance according to Eq. (1.29) is $Z_T = R$; some fluid inertia inside the turbine should either be included in $j\omega I_1$ or in Z_T.
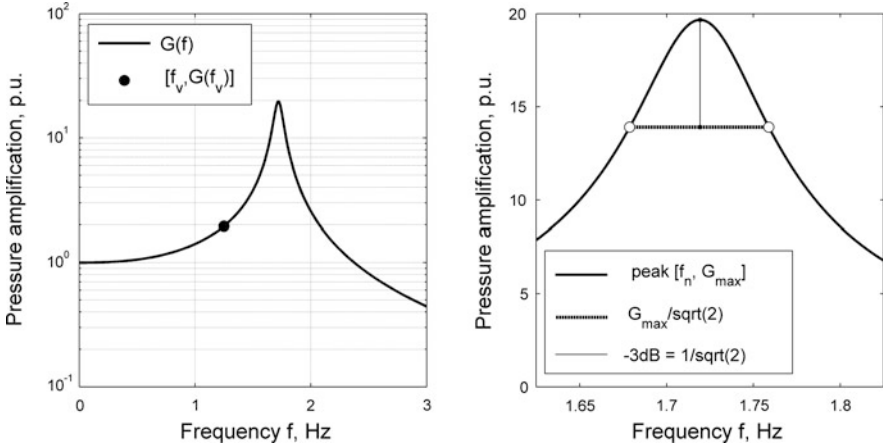
Fig. 1.11 Resonance curve, shape of peak, and damping ratio ζ

$$\frac{\tilde{p}_C}{\Delta \tilde{p}_{\text{EX}}} = G_C(j\omega) \tag{1.36}$$

The magnitude of this transfer function G, shown in Fig. 1.11, shows all the characteristics of the well-known mass-spring oscillator. Indeed the transfer functions of the two systems have the same mathematical structure and are described by the same equations. The oscillator's mass is represented by the fluid inertia

$$I_2 = \rho \times \frac{L_2}{A_2} \tag{1.37}$$

in the draft tube, the cavitation compliance is inversely proportional to what would be the spring stiffness in a mechanical system, and the damping effect originates from the oscillating turbine head $\tilde{q}_1 \times R_T \times \rho \times \frac{E}{Q}$.

We expect that the pulsation will have a frequency near 25 % of runner frequency, or 1.25 Hz if the runner speed is 300 rpm. At this frequency, the gain is 1.85. The maximum gain $|G|_{\text{max}}$ would occur at the frequency of 1.719 Hz, and would be 19.7. As a rule-of-thumb, this gain is an approximate measure of damping ratio ζ according to $|G|_{\text{max}} \approx 1/2\zeta$, which would give an estimated damping ratio $\zeta \approx 2.5$ %.

As a more general alternative to the frequency domain we may determine the transfer function in the Laplacian domain (by replacing $j\omega$ by s)

$$G_C(s) = \frac{N(s)}{D(s)} = \frac{(R + I_1 s)}{(C I_1 I_2 s^3 + R C I_2 s^2 + (I_1 + I_2)\, s + R)} \tag{1.38}$$

and solve the characteristic equation $D(s) = 0$. We then directly obtain the three eigenvalues of this third order system

$s_{1,2} = -0.2515 \pm 10.8055j$ and $s_3 = -2.9691$, the dimension being s^{-1}

$$(1.39)$$

The oscillatory eigenmode is represented by the pair of conjugate complex roots $s_{1,2} = \alpha \pm \omega j$.

The angular frequency $\omega = 10.8055$ rad/s provides the natural frequency

$$f_n = \frac{\omega}{2\pi} = 1.7195 \text{ Hz} \tag{1.40}$$

which agrees well with the frequency of maximum gain, while the exact value of the damping ratio results from

$$\zeta = \frac{-\alpha}{\omega} = \frac{0.2515}{10.8055} = 0.0233 \text{ or } 2.33 \text{ \%.} \tag{1.41}$$

If the damping ratio ζ is low, as in our case, then it may be directly estimated from the shape of the spectral peak. For the two points where the magnitude is lower than the peak value by 3 dB, or a factor of $\sqrt{2}$, the frequency differs from the natural frequency by a factor $1 \pm \zeta$.

If Δf denotes the width of the curve at—3 dB, then we find the damping ratio using

$$\zeta = 0.5 \frac{\Delta f}{f_n} \tag{1.42}$$

in our case to be $0.5 \times (1.7588 - 1.6787)/1.719 = 0.0233$. This relationship is sometimes useful for a quick check of measured data.

The very small value of damping is due to the large incompressible water mass in the penstock resulting in a very low level of the discharge pulsation $\tilde{q}_1$. This pulsation acting together with the turbine resistance is the only sink for oscillation energy in our strongly simplified system, and this then controls the damping. For a shorter penstock length, a larger pulsation of the turbine discharge and an increased damping would result.

The eigenvalues describe the free oscillations of the system. In absence of the forcing action (in our case, if $\Delta p_{EX} = 0$) the movements of all variables (pressures, discharges) are only composed of functions of time

$$Y_k(t) = Y_k(0) \times \exp(s_k t) = Y_k(0) \times \exp((\alpha_k \pm \omega_k j) \times t) \tag{1.43}$$

where k denotes the different eigenvalues.

Every free oscillation may be described as the product of a complex function $\exp(\omega_k j t)$ indicating the oscillating phase, and a real function $Y_k(0) \times \exp(\alpha_k t)$ denoting the time dependency of the amplitude. $T_{1/2} = \text{abs}(\ln 2/\alpha_k)$ is the half-value period of the oscillation amplitude if α_k is negative (i.e., the eigenmode is *stable*), or the doubling time, if it is unstable.

With the oscillation period $T_p = 2\pi/\omega_k$,

Table 1.5 Amplitudes and oscillation power flow

Location x		Pressure amplitude/phase		Discharge amplitude/phase		Power flow	Power balance
		(kPa/dg)		(m³/s)	(dg)	(kW)	(kW)
Headwater	p_{HW}	0.00	0.00	q_1 0.168	−64.3	0.000	
End of penstock	p_1	13.20	−154.3	q_1 0.168	−64.3	0.000	0.000
Runner exit	p_C	15.64	173.2	q_1 0.168	−64.3	−0.706	−0.706
Downstream of cavity	p_C	15.64	173.2	q_2 0.74	76.2	−0.706	0.000
Downstream of pressure source	p_2	7.22	169.0	q_2 0.74	76.2	0.000	+0.706
Draft tube exit	p_{TW}	0.00	0.00	q_2 0.74	76.2	0.000	0.000

$$\frac{T_{1/2}}{T_p} = \ln 2 \times \frac{\omega_k}{(2\pi\alpha_k)} = 0.11/\zeta \qquad (1.44)$$

is the number of oscillations in a half-value period.

Continuing with our example, we may also ask for the energy balance of the pulsation. For this turbine, a likely amplitude of the draft tube pressure source Δp_{EX} would be 8 kPa, pulsating at the frequency of 1.25 Hz. Solution of the system yields the results shown in Table 1.5.

The oscillation power transmitted through any cross-section x ('Power flow' in Table 1.5) with the complex local state variables p_x and q_x may be computed using the scalar product $(p_x \times q_x)$ according to

$$P_{osc} = 0.5 \times (p_x \times q_x) = 0.5 \times |p_x| \times |q_x| \times \cos(\text{phase } (p_x) - \text{phase } (q_x)) \qquad (1.45)$$

The power balance in Table 1.5 concerns the area upstream of the respective cross-section; it is the difference of power flow between the indicated cross-section and the one upstream. The sign of the power balance between two adjacent cross-sections means that net oscillation power is either created (+) or destroyed (−) in the respective element. In our plant model, nonzero power flow occurs only at two cross-sections in the draft tube cone (because we neglected the relatively unimportant friction loss in the penstock and draft tube). The negative sign indicates that power is transmitted upstream. In three areas (penstock, cavity, and diffuser), we have a zero balance of oscillation power, because we have neglected pipe friction and we assumed the vortex cavity to act as a passive 'spring' element. The 'active' regions are the draft tube elbow where oscillation power is supplied and the turbine runner where it is consumed.

A few more things may still be learned from the simple example. The 0.706 kW net power budget of the oscillation is very small compared to the turbine output of 28 MW in this part-load condition. The pulsation amplitude of discharge in the draft tube is much larger than in the penstock and turbine. Although the frequency is just 27 % lower than the natural frequency, the peak–peak amplitude of 3.2 mwc is still

moderate. This natural frequency is mainly defined by draft tube data. It should be noted that the pulsation computed in this example is only the so-called synchronous part of the partial-load pulsation, as explained later in Sects. 2.2.1 and 7.2.1.

1.5 Hydraulic Instability

The pulsation described above is a forced oscillation. In absence of the forcing pressure source $\Delta\tilde{p}_{EX}$ there would be no oscillation at all, because in our system every 'spontaneous' disturbance soon cancels out due to the damping of the free oscillation. By contrast, there may also be flow conditions which lead to oscillatory system eigenvalues $\alpha \pm j\omega$ with a positive α. In such a case, a *self-excited oscillation* with frequency $f = \omega/2\pi$ would arise even in absence of any defined forcing. If α is positive, the amplitude of this pulsation would increase indefinitely over time as indicated by Eq. (1.43). Eigenmodes with positive α, and systems having such eigenvalues, are called *unstable*. In reality, this infinite increase is not possible because physical systems do not remain linear in the case of very large amplitudes. Dissipation effects like friction are present in every real system, and as they always tend to increase the damping ratio of the free oscillation modes, they therefore increase stability. Destabilizing effects are less frequent; they are often caused by delay effects or dead times in a system. Such phenomena producing instability will be discussed in Sect. 2.2.7.

In a practical sense, forced oscillations (like the Francis partial-load surge) and self-excited oscillations differ with regard to their amplitude behavior. The amplitudes of a forced oscillation may be computed, or at least estimated, if the forcing term and the transfer function are known. In a self-excited oscillation, the amplitude may be very hard to predict because it strongly depends on the nonlinear characteristics of the system, which are often not known. In cases with instability it is more realistic to assess the stability limit rather than the amplitudes. The *stability limit* is the condition where an oscillatory eigenvalue becomes purely imaginary, with zero damping term α.

Various effects may result in hydraulic instability. The following description makes use of the frequency-domain representation of the pulsating variables, pressure p and discharge q.[6] Figure 1.12 shows their magnitude and phase at a certain frequency in the complex plane. The system is simple and typical for Francis units with short separate penstocks. The data correspond to the case study reported in Sect. 8.1, considering a steady high-load oscillation with a frequency of 0.72 Hz, which was observe'd in a condition with $H = 143.4$ m and $Q = 241$ m^3/s. The frequency is only 36 % of the lowest natural frequency of the fluid column in the penstock. One may therefore treat the fluid masses in the penstock and turbine, and in the non-cavitating part of the draft tube, indicated in Table 8.1, as incompressible, as

---

[6] For more clarity, it is convenient to reserve capital Q for time-averaged values.
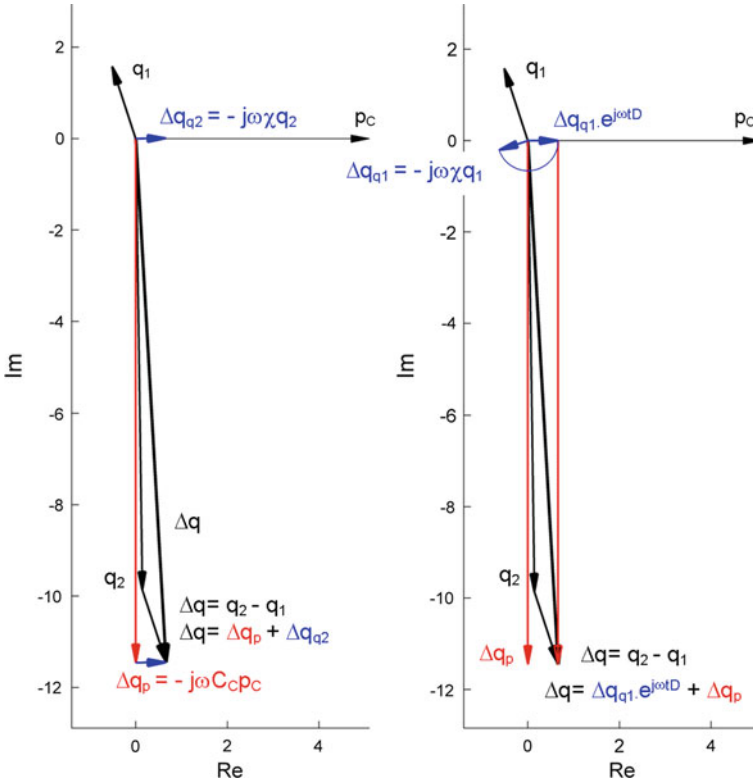
Fig. 1.12 Concepts of cavitation-driven hydraulic instability

in the example at the beginning of Sect. 1.4. The total resistance of the penstock and turbine is $R_1 = 9{,}340$ Pa. s. m^{-3}. We assume that the Eq. (1.34) remain valid except that the source pressure is absent ($\Delta p_{EX} = 0$, therefore $p_2 = p_C$), and we consider an estimated fluid resistance of the draft tube $R_2 = 73.2$ Pa. s. m^{-3}. First, it will be shown that no steady oscillation can exist based on this set of assumptions alone. Figure 1.12 represents the oscillating variables downstream of the turbine runner in the complex plane. As a starting assumption, we use the local pressure fluctuation p_C whose amplitude at $f = 0.72$ Hz is 50 kPa; to provide better proportions in the figure, its magnitude is expressed in mwc, and its phase is deliberately chosen to be 0°. The pulsation of discharge is given in m^3/s.

From Eq. (1.34)/1–2, it follows that $p_C = -q_1 \times (j\omega I_1 + R_1)$. On the other hand, $p_C = p_2 = q_2 \times (j\omega I_2 + R_2)$ (because $\Delta p_{EX} = 0$). The vectors for q_1 and q_2 are drawn such as to fulfill the two conditions. In order to permit a sustained oscillation, corresponding to the limit of stability, the difference between these two discharges has to be made up by a suitable change of the cavity volume. If we would only attribute a compliance C_C to the cavity, as in Sect. 1.4, then the discharge difference $\Delta q = q_2 - q_1$ would have a 90° phase shift against the

pressure, like the red vector Δq_p in the figure; it can only compensate the imaginary part of the required vector but not the real part.

The real part of q_1 indicates that, due to the resistance of the turbine characteristic, the subsystem upstream of p_C consumes oscillation power [see Eq. (1.45)], which has to be restored somehow—but C_C is a neutral element and does not change the oscillation power balance.

Apart from the pressure influence C_C, the cavity volume also depends from the discharge. In analogy to $C_C = -\partial V_C/\partial p$, the derivative

$$\chi = -\frac{\partial V_C}{\partial Q} \quad \text{(mass flow gain factor, or MFGF)} \qquad (1.46)$$

has been introduced by Brennen [13]. Theoretically, both parameters may be derived from V_C values measured or computed in a number of steady states with different pressure and discharge. The discharges q_1 and q_2 are not the same in the context of oscillation; this raises the question which one of the two discharge variables is the proper reference for use with Eq. (1.46).

Considering that X is negative for $Q > Q_{\text{opt}}$, and that the portion for Δq resulting from the Eq. (1.35), $-j\omega\chi q$ is therefore 90° leading over the discharge pulsation q; the easy answer seems to be q_2. Accordingly, most researchers have opted for this assumption [14]. In our example, the stability limit would be at $X = -0.015$ s. This scenario is shown at the left-hand side of Fig. 1.12.

The destabilizing effect can also be explained by a mechanism based on the runner exit discharge q_1. Using Eq. (1.46) literally, the mass flow gain effect from q_1 in this example produces a Δq in the sense of increased damping, Δq_{q1} in the figure. But the runner exit swirl does not act instantaneously on the vortex volume. Assuming a dead time $t_D = 0.76$ s, the delayed effect $-j\omega\chi q_1 \times \exp(j\omega t_D)$ provides the negative damping required to compensate the effects of R_1 and R_2 and thus reach the stability limit. In that case the necessary mass flow gain is $X = -0.088$ s, six times larger than for the other hypothesis, and it would be even larger if the dead time (i.e., phase shift) differs from the critical value. In Fig. 1.12, the phase rotation of Δq_{q1} due to the dead time is indicated by the blue circle.

If there is a mathematical model available for a certain type of oscillation, the stability limit may be visualized as a function of the most important parameters in a *stability diagram*. Figure 1.13 is an example from [15], addressing the importance of using the correct reference discharge for mass flow gain. In addition to the stability limit, shown as a bold line, this graph also displays lines of constant damping ratio (dashed curves) and lines of constant frequency, annotated in Hz. In this example, instability based on discharge q_1 (left side) is possible with sufficiently large negative mass flow gain X, in the absence of a dead time. The frequencies concerned are somewhat higher than the first natural frequency of the penstock, therefore in a diagram like Fig. 1.12, q_1 would be in the lower right quadrant, and the contribution $\Delta q_{q1} = -j\omega\chi q_1$ can directly cause instability.
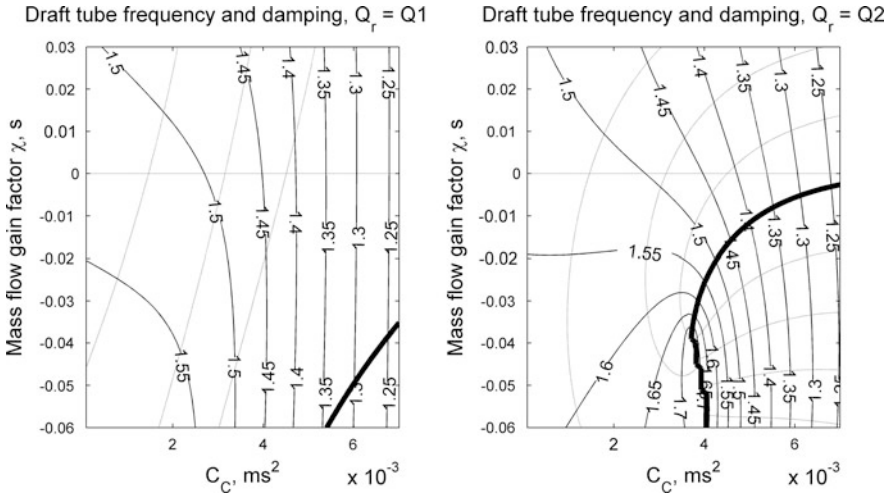
Fig. 1.13 Stability diagram, influence of mass flow gain reference

Theories describing instability are currently not available for all phenomena. Even the Francis high-load pulsation discussed above is still subject to ongoing research [15, 16]. More detailed information may be found in Chap. 2.2.7.

For the example discussed above, we assumed that the turbine impedance may be based on the steady-state turbine characteristic, $R_1 = R_T = \rho g \partial H/\partial Q$. It is not self-evident that this assumption holds for all frequencies, and indeed in the past some authors have suggested that, starting from some frequency, the turbine impedance may deviate from steady-state behavior. Most important in this would be the behavior of the real part. If it becomes negative, then the discharge vector in Fig. 1.12 would point into the upper half plane, and in that case instability could arise even in absence of a mass flow gain. This kind of change of the turbine impedance has remained a matter of speculation; the topic was raised in the 1980s but experiments are scarce. Jacob and Prénat [17] give an account of a systematic experimental study using a pump-turbine model with low specific speed. While the study aims at higher frequencies, the results suggest that, at least for frequencies relevant for draft tube pulsations, the steady-state turbine characteristic plus some inertial term should be an adequate assumption for the hydraulic impedance of a turbine. Apart from hypothetical cases involving a negative real part at some frequency, there are real situations where the impedance of the hydraulic machine is already negative starting from frequency zero. Such cases are described in Sects. 6.4 and 8.3, dealing with the typical instabilities of pumps and pump-turbines.

The explanations in this, and the previous section have been given using lumped parameters. For the same phenomena, some researchers e.g., [18] have proposed to use distributed parameters instead. This approach is more general, it permits additional natural modes for the draft tube pulsation. But the parameters

(such as the wave velocity) are variable in the flow direction; therefore the theoretical benefit can only materialize if the dependency can be identified.

1.6 Mechanical Assessment of Components

Hydraulic phenomena have direct effects on the behavior of mechanical components. An example of a strain gauge signal installed on a runner blade is presented in Fig. 1.14. Both the mean stress and the amplitude are functions of turbine load. In this turbine, the highest amplitudes occur at the so-called speed no-load condition.

Processing of such strain gauge signals are presented in Figs. 1.15 and 1.16 [19] where several kinds of dynamic phenomena varying with power become visible.

Figure 1.15 is a so-called waterfall diagram that concentrates a lot of information on vibration amplitudes at different frequencies and load. From 55 % load upward, the flow is very smooth and only small disturbances from the lowest harmonics of runner frequency n appear; they stem from the unavoidable slight asymmetry of the casing. In the middle load range, the vortex rope contributes some additional variation at low frequency. The frequency seen by the runner is the difference f_v-n, f_v being the precession frequency of the vortex rope. Important random fluctuations of strain occur in the whole lower half of the load range.

In Fig. 1.16, the same test data is represented up to a higher frequency level. The guide vane passing frequency, $Z_s n$ is an important portion of runner strain. In this example, this contribution increases with power because the guide vane opening increases and the guide vane trailing edges come closer to the runner blades. The diagram also shows that the random excitation at low load has an additional maximum at higher frequencies, around 20 times runner frequency n.

The non-dimensional hydraulic parameters (also known as homology parameters) for the transposition of hydraulic characteristics from model to prototype, or from one prototype to another are the key in understanding the machine hydraulic behavior. Nevertheless, one should not forget the transposition of the mechanical characteristics, as these may require different scaling rules. One main concern is to understand how the stress in one machine may be compared with the stress in a homologous one with different diameter, rotating speed, and head.

Several techniques are available to evaluate the damage occurring at various operating conditions, such as Rainflow counting, and material fatigue curves using Miner's damage accumulation rule [20–22]. Rainflow counting is the standard method used to obtain statistics of mean values and amplitudes and numbers of cycles of load variables (forces, stress) for the purpose of fatigue analysis. Time series data of the interesting variable are analyzed using a standard algorithm in such a manner that every maximum and minimum of the record is considered to start a half-cycle of load; the result is a matrix indicating the count for every class of combinations between a mean load and amplitude, as shown in the 2D histogram Fig. 1.17.
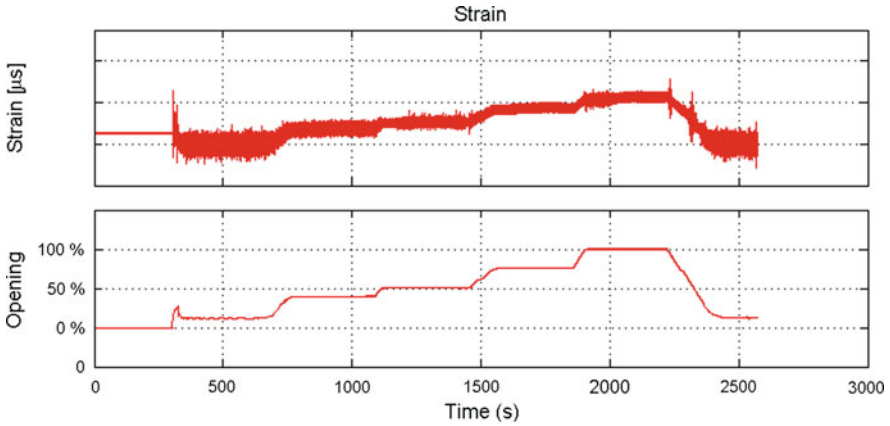
Fig. 1.14 Strain gauge measurements from Francis runner
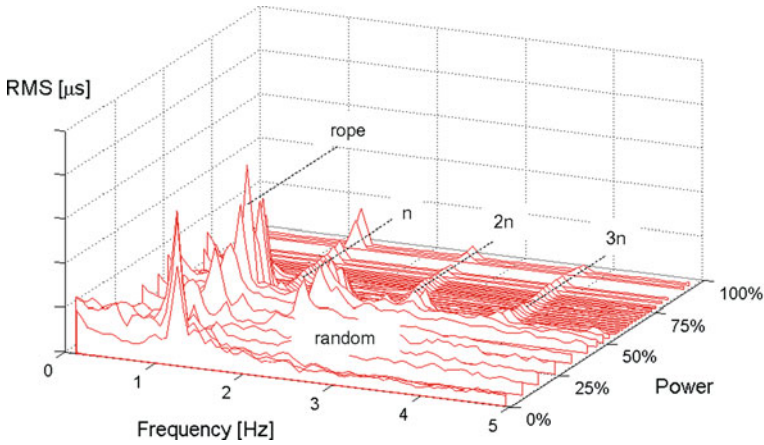
Fig. 1.15 Low-frequency spectra of runner strain

This kind of data, established by estimation, measurement, or simulation, is the input necessary for the assessment of mechanical safety of the component concerned [23].

The damage accumulated in the various stress conditions i considered in the statistics is expressed by the calculated damage C which is computed according to the Palmgren–Miner rule, Eq. (1.47), summing up the damaging effect of all categories i

$$C = \sum_i n_i/N_i \qquad (1.47)$$
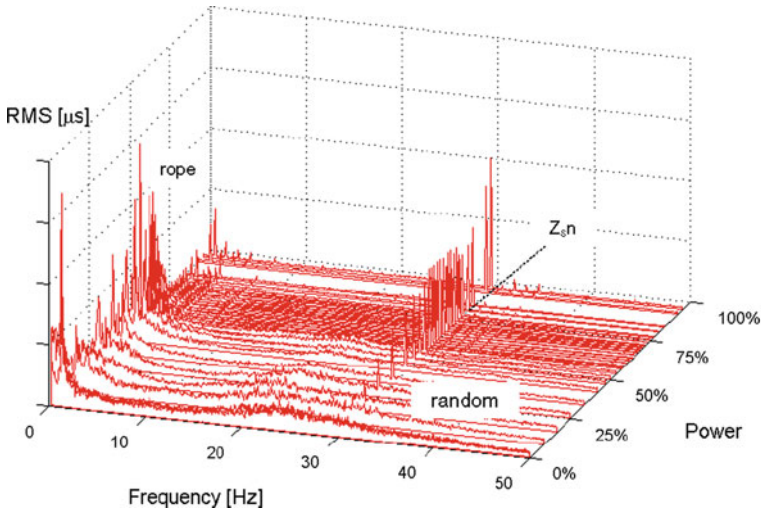
Fig. 1.16 High frequency spectra of runner strain

Fig. 1.17 Rainflow matrix
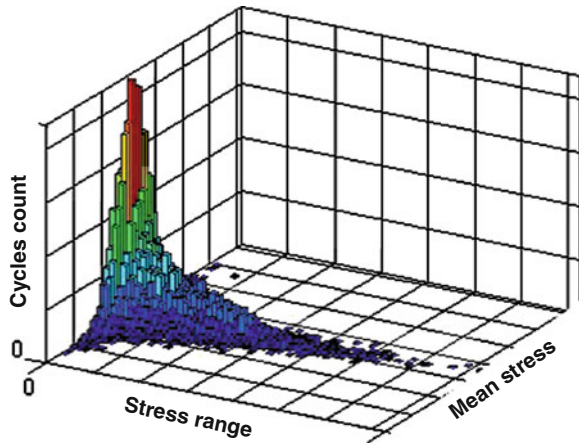
where n_i is the actual number of cycles and N_i the number of cycles leading to damage. This should be done for all relevant conditions of operation; and a relative number C/C_{max} can be derived that indicates the relative distribution of damaging effects of various operating conditions in actual operation, in terms of life reduction, see also Sect. 4.2.3.

Simple homology calculations can show that for two homologous hydraulic machines operating at the same speed coefficient (K_u, n_{11} or n_{ED}), the static stresses in the components are proportional to the head. This conclusion is also valid for dynamic stresses, as long as there is no amplification due to resonance between hydraulic phenomena and mechanical components. The natural frequency
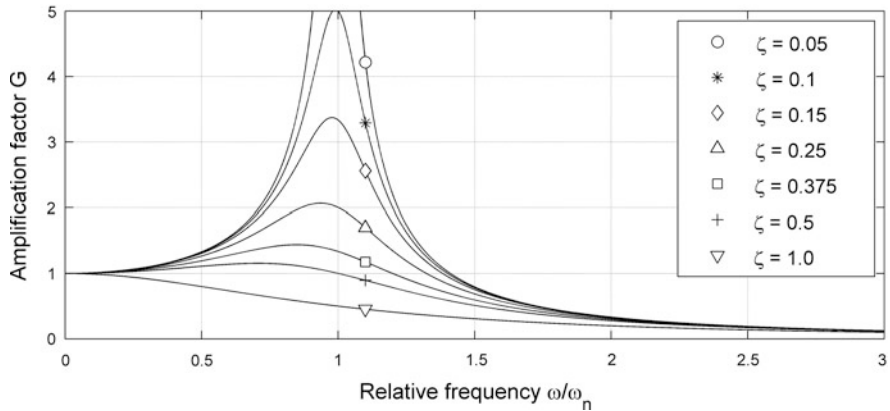
Fig. 1.18 Amplification of a single degree of freedom oscillator

of a mechanical component ω_n is proportional to the inverse of the reference diameter $1/D$ so that the relative frequency of hydraulic pulsations and mechanical response changes with size and needs to be checked. Possible amplification of a pulsation has to be checked based on the ratio of excitation frequency ω to natural frequency of the component ω_n as shown in Fig. 1.18. In addition the natural frequency of a mechanical component in air is different to that when immersed in water due to the effect of the added water mass also becoming involved in the vibration. It is very important in evaluating ω_n, to take this into account and this has only become amenable to computation in the last few years, as described in Sect. 3.3.2. The importance of the damping value ζ increases as the ratio ω/ω_n approaches 1, as demonstrated in Fig. 1.18 for the simplest possible case of a single degree of freedom oscillator.

In some cases, in particular operational transients, the amplification may also depend on the rate of change of the exciting frequency. This will be discussed in Sect. 3.5.4.

References

1. IEC 60193. (1999–2011). *Hydraulic turbines, storage pumps and pump-turbines—Model acceptance tests* (2nd ed.).
2. Doerfler, P. (1986). Design criteria for air admission systems in Francis turbines. In *13th Symposium on IAHR Section Hydraulic Machinery, Equipment, and Cavitation, Montreal* (Vol. I, Paper 8).
3. Suter, P. (1966). Representation of pump characteristics for calculation of water hammer. *Sulzer Technical Review Research Issue*, pp. 45–48.
4. Dörfler, P. K. (2010). 'Neo-Suterian' pump-turbine characteristics and their benefits, In *25th IAHR Symposium on Hydraulic Machinery and Cavitation, Timisoara*.
5. IEC 60994 .(1991).Guide for field measurement of vibrations and pulsations in hydraulic machines (turbines, storage pumps and pump-turbines) (1.0 b ed.).

6. Bendat, J. S., & Piersol, A. G. (2000). *Random data analysis and measurement procedures* (3rd ed.). Hoboken: Wiley.
7. Wylie, E. B., & Streeter, V. L. (1983). *Fluid transients*. Ann Arbor: FEB Press.
8. Chaudhry, M. H. (1987). *Applied Hydraulic Transients* (2nd ed.). New York: Van Nostrand Reinhold.
9. Bergant, A., Simpson, A. R., & Vitkovsky, J. P. (2001) Developments in unsteady pipe flow friction modeling. *Journal of Hydraulic Research, 39*(3), 249–257.
10. Habán, V., Pochylý, F., & Fialová, S. (2009). The second viscosity of fluids. In *Engineering mechanics 2009. Prague, Czech Republic, Institute of Theoretical and Applied Mechanics, v.v.i. 2009* (pp. 349–359).
11. Svingen, B. (1997). *Rayleigh damping as an approximate model for transient hydraulic pipe friction*, Work group on the Behavior of Hydraulic Machinery Under Steady Oscillatory Conditions, 8th meeting, Chatou 1997, Paper F-2.
12. Dörfler, P. K. (2011). Pressure wave propagation and damping in a long penstock: In *Proceedings of the 4th Meeting IAHR Workgroup on Cavitation and Dynamic Problems in Hydraulic Machinery and Systems, Belgrade*.
13. Brennen, C. (1978).The unsteady, dynamic characterization of hydraulic systems with emphasis on cavitation and turbomachines. In *Joint Symposium of ASME/ASCE/IAHR, Ft. Collins* (pp. 97–107).
14. Flemming, F., Foust, J., Koutnik, J., & Fisher, R. K. (2008) Overload surge investigation using CFD data. In *IAHR 24th Symposium on Hydraulic Machinery Systems, Foz do Iguassú*, Oct. 2008.
15. Dörfler, P. K. (2009). Evaluating 1D models for vortex-induced pulsation in Francis turbines. In *Proceedings of 3rd Meeting IAHR Workgroup on Cavitation and Dynamic Problems in Hydraulic Machinery and Systems, Brno 2009, Paper F3*.
16. Dörfler, P. K., Keller, M., & Braun, O. (2010). Full-load vortex dynamics identified by unsteady 2-phase. In *CFD, 25th IAHR Symposium on Hydraulic Machinery and Cavitation, Timisoara*.
17. Jacob, T., Prénat, J.-E. (1991). Identification of a Hydraulic Turbomachine's Hydro-Acoustic Transmsiion Parameters. In: *IAHR Work Group WG1 (The Behavior of Hydraulic Machinery under Steady Oscillatory Conditions) 5th Meeting, Milano*.
18. Philibert, R., Couston, M. (1998). Francis turbines at part load, matrix simulating the gaseous rope. In: *IAHR Section on Hydraulic Machinery and Cavitation, 1*9th S*ymposium*, Singapore, pp. 441–453.
19. Coutu A., Aunemo H., Badding B., Velagandula O. (2005). *Dynamic Behaviour of High Head Francis Turbines*. In *Hydro 2005, Villach, October 17–20, 2005*.
20. Lowys P.-Y., Deniau J.-L., Gaudin E., Leroy P., & Djatout M. (2006). On-Board Model Runner Dynamic Measurements In *Hydrovision 2006, Portland, OR, July 31–August 4, 2006*.
21. Welte T. M., Wormsen A., Harkegard G. (2006) Influence of Different Operating Patterns on the Life of Francis Turbine Runners. In *Hydrovision 2006, Portland, OR, July 31–August 4, 2006*.
22. Coutu A., Monette C., Gagnon M. (2007) Life Assessment of Francis Runners Using Strain Gage Site Measurements. In *Waterpower XV, Chattanooga, TN, July 23–26, 2007*.
23. Sick, M., Michler, W. Weiss, T., Keck, H. (2009). Recent developments in the dynamic analysis of water turbines. *Proceedings of the IMechE Part A: Journal of Power and Energy, 223*, JPE578.

Chapter 2
Low-Frequency Phenomena in Swirling Flow

The presence of swirl is often the cause of separations and pressure fluctuations in the draft tube of hydraulic reaction turbines, in particular Francis turbines. At the design point, water turbines generally operate with little swirl entering the draft tube and no flow separations, but at off-design, at both high and low load, the flow leaving the turbine has a large swirling component. The present chapter describes a number of physical mechanisms that work to produce the pulsation. Their occurrence and impact depend mainly on the actual flow rate of the turbine, but also on the local pressure level, on the exit velocity field of the particular runner, the shape of the draft tube, and the dynamic response of the whole hydraulic circuit. In medium- and large-sized turbines, the frequency of these 'draft tube surges,' which are often approximately periodic, is of the order of 1 Hz, and therefore they may also produce significant electrical power swings.

Given a sufficiently strong vortex flow, comparable phenomena may also occur in other locations, for example in the runner channels, or in penstock manifolds.

2.1 Swirling Flows in Pipes, Vortex Breakdown Phenomena

2.1.1 Basic Observations

Laboratory experiments have shown that swirling flow through a cylindrical pipe tends to separate into two concentric flow regions [1]. Fluid transport basically occurs in the outer region while the inner region may contain a stagnation zone or dead water core. The relative swirl or swirl ratio is the non-dimensional ratio between the swirl momentum and the axial momentum of flow

$$m = \int_0^{R_i} c_m c_t r^2 dr \Big/ \left(R_i \int_0^{R_i} c_m^2 r dr \right) \tag{2.1}$$

(a)   **(b)**   **(c)**
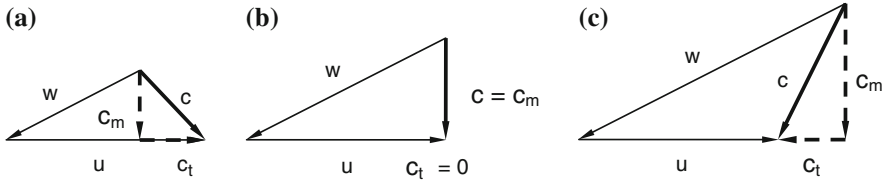
Fig. 2.1 Runner exit velocity triangles **a** partial load **b** zero swirl **c** high load

where R_i is the pipe radius, and c_m and c_t are the axial and tangential components of velocity.

Early measurements supporting the concept of two flow regions were made on a time-averaged basis [1]. The diameter of the dead water core was found to increase with the swirl rate. More detailed observations, which also consider unsteady features of flow, reveal that the boundary between the two regions, is not stable but that its vorticity tends to concentrate in a corkscrew-like vortex filament along the border between the two flow regions [2]. Under some circumstance, in particular in conditions of decelerating flow, the recirculation zone may break down from one flow structure to another, a phenomenon known as vortex breakdown or vortex bursting. The phenomenon of vortex breakdown is associated with an abrupt and drastic change of flow structure. The helical corkscrew vortex at the boundary of the core is one such structure but an alternative structure is an axisymmetric separation bubble on the axis of the vortex.

2.1.2 Early Research

In a Francis turbine, the fixed relative exit angle of the runner blades is designed for a certain water discharge. At this particular discharge, close to the point of best efficiency, the component of the absolute circumferential flow velocity in the outlet is small, leading to a residual swirl close to zero, as shown in part (b) of Fig. 2.1. At lower flows the relative flow angle remains nearly the same, but the absolute flow angle leads to a residual swirl in the direction of the runner rotation, indicated by the tangential velocity component c_t in part (a) of Fig. 2.1. At higher discharge the runner produces a counter swirl against the direction of runner rotation in its exit flow.

The US Bureau of Reclamation (USBR) conducted basic experimental research [2] on the behavior of swirling flow in a reduced-scale draft tube. Instead of a runner, a stationary swirl generating apparatus was used to produce a certain swirl ratio. At very low swirl, the USBR found that the dead water core does not develop, the smooth flow filling the entire cross section of the draft tube. If the swirl ratio exceeds a rather low threshold value, a stagnation point forms in the

Fig. 2.2 Dead water core (*left*, [3]) and corkscrew vortex in a model

flow at the draft tube exit and downstream of this there is a core of separated flow in the draft tube. This stagnation point then moves upstream as the swirl ratio increases. The stagnation point is also the starting point of the corkscrew-like vortex filament. With sufficient swirl, the stagnation point merges with the upstream center of the pipe, and the vortex filament then starts at the 'runner' hub. It is not stationary but rotates about the axis of the draft tube (Fig. 2.2).

The shape and precession frequency of the corkscrew vortex depend on the swirl ratio. This early research was done using air as a working fluid. Cavitation effects were not considered. Starting from the same concept, Nishi et al. [3] studied various aspects of swirling draft tube flow, including the effect of vortex cavitation and the role of the draft tube elbow in the excitation mechanism of pressure pulsations [4].

2.2 Draft Tube Vortex Phenomena

Today, researchers still use reduced-scale models to examine draft tube vortex phenomena, but these days complete turbine models with runner are preferred to stationary swirl generators. While the swirl apparatus can produce the proper amount of swirl, the radial distribution of velocities differs from that in an actual turbine. Several different dynamic flow phenomena due to draft tube swirl may be distinguished by their symptoms and mechanism of origin. The flow rate of the turbine controls the swirl, and has the single most important influence on the occurrence of pulsation. Therefore, it is convenient to use a non-dimensional number for the discharge to quantify this, usually $Q_{nD}/Q_{nD,opt}$. The discharge Q is a good scaling parameter only in the usual case of a turbine operating at constant, synchronous speed. But in other cases such as a model test, the discharge coefficient Q_{nD} should be used because the swirl-free discharge varies with the flow and the runner speed.

Apart from the swirl ratio and the radial velocity distribution, the cavitation number σ also plays an important role. In most cases the high velocities in the core of the draft tube vortex can decrease the static pressure to the vapor pressure, leading to cavitation with a vapor-filled cavity. Some pulsation phenomena are linked to the size and shape of the cavity. The following descriptions are given for modern Francis turbines where the condition of zero swirl normally occurs at, or slightly above, the best efficiency discharge; many of the phenomena are also observed in other reaction turbines with the corresponding draft tube swirl.

2.2.1 Partial-Load Vortex: Forced Oscillation (Half-Load Surge)

In modern Francis turbines, the corkscrew-like flow structure (vortex rope or torch) typically prevails over a range of the relative turbine discharge between approximately 0.5 and 0.85 of the flow at best efficiency. The lower limit of this range is often better developed than the upper limit as it has the character of a boundary between two quite different flow regimes. The common way to measure the effects of the phenomenon is by pressure sensors at the wall of the draft tube cone (draft tube pressure pulsation, DTPP). This pulsation is approximately periodic, the period of the pressure pulsation is the same as that for the rotation (precession) of the corkscrew, which may be observed visually in a laboratory model with a transparent draft tube cone. The relative frequency of precession f/n is between 0.2 and 0.4, whereby values above 0.3 are less likely. First results on this phenomenon, which are still worth reading, can be found in Rheingans [5] who already pointed to problems of generator resonance and proposed a generic estimate f/n $\cong$ 0.278 for the ratio of the precession frequency to the runner speed. For detailed quantitative information on surge parameters, see the Sects. 7.2.1 and 7.3.1.

In a model test, DTPP measurements can be done at different levels of draft tube pressure, or cavitation number σ as described in Sect. 1.1 (other parameters of operation remaining the same). Figure 2.3 shows results from a Francis turbine model with a specific speed of $n_{QE} = 0.113$, and these demonstrate some typical features of the cavitation effect[1] on the part-load pulsation. If the pressure level in the model draft tube is very high, $\psi\sigma \geq 0.3$, the vortex rope becomes invisible because the local pressure drop in its core is not sufficient to produce cavitation. Nevertheless the unsteadiness from the corkscrew vortex still exists in the flow and if the DTPP is measured its frequency remains approximately the same as the draft tube pressure is lowered. It is common to measure the pulsation at several locations around the circumference of the cone simultaneously. The rms values of the fundamental frequency band of the vortex precession in the draft tube cone are

---

[1] In the cavitation number $\psi\sigma$, different from standard σ, the reference pressure is the runner velocity head instead of the net head.
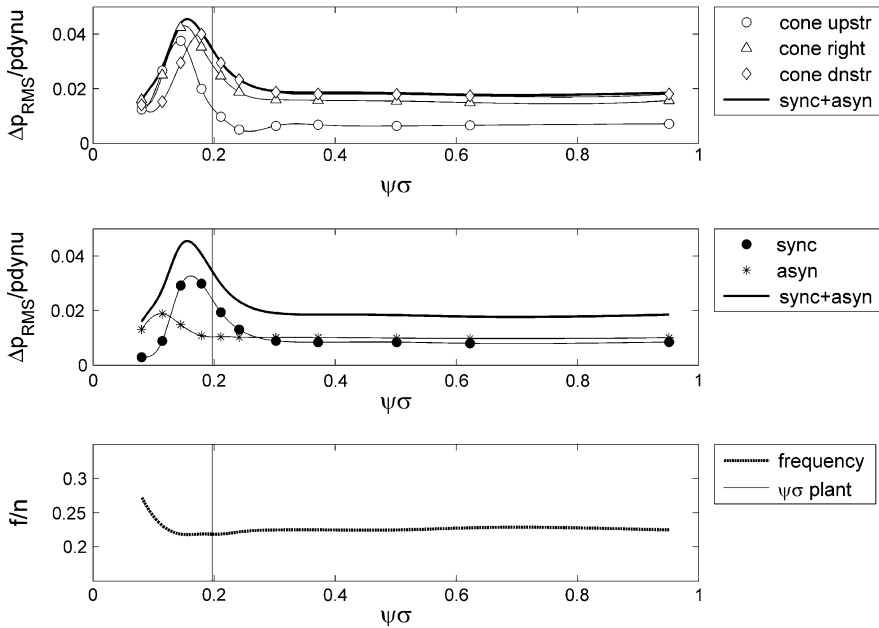
Fig. 2.3 Cavitation effect on half-load surge

shown in the upper graph of Fig. 2.3 for three locations in the draft tube cone.
A maximum of the pressure amplitudes is often observed when the natural frequency of the draft tube fluid associated with the cavitation compliance of the vortex rope coincides with the precession frequency of the rope. In this condition—in our case near $\psi\sigma = 0.16$—the pressure pulsation observed at different circumferential locations becomes approximately synchronous [6]. The reason for the resonance-like behavior, already recognized by Moody [7], is the compressible nature of the flow downstream of the runner, following Brennen's [8] 'cavitation compliance' defined in Eq. (2.2). The correct mechanism of excitation was disclosed in two steps by Dériaz [9] who assumed a periodic variation of flow resistance, and Dörfler [10, 11]. The computation example in Sect. 1.4 and the system response study in Sect. 7.2.3 provide a more detailed description.

The physical properties of half-load surge—that is the amplitude and phase response to changes in cavitation level due to variation in sigma—can only be understood if the compound nature of this phenomenon is accounted for. Nishi [4] showed that the pulsation consists of a synchronous part—a plane wave—and an asynchronous part—the precession movement of the rope, and showed how these components are to be distinguished in an elbow draft tube. He also conducted experiments which demonstrated that the synchronous pulsation does not exist in a straight draft tube—another proof that the excitation source resides in the elbow. The middle graph in Fig. 2.3 presents the synchronous and asynchronous pulsation, which were extracted from the individual pressure signals. It is the

synchronous component, which is involved in a basically one-dimensional system oscillation, that responds to the change of cavitation level. In contrast the asynchronous pulsation as well as the precession frequency (lower graph) do not depend on cavitation except at extremely low draft tube pressure. The maximum possible level of pulsation in any draft tube section may be expressed as the scalar sum of the amplitudes of the two components, therefore this sum forms an envelope for the individual pressure amplitudes versus cavitation number, in the upper graph.

To analyze measurements of draft tube pulsation for its parameters, based on a set of assumptions listed in Sect. 7.2.3, one may use procedures in the frequency domain. The goal is to know in detail the properties of the two main components, asynchronous and synchronous, as well as the forcing term Δp_{EX}.[2] If the test rig has short upstream and downstream pipes as shown in Fig. 1.10, it is particularly easy to identify the pressure source Δp_{EX} by measuring the interesting load points in a reference test at partial load with high cavitation number σ in order to ensure cavitation-free flow in the runner and draft tube. This should normally be the case for $\psi\sigma > 0.5$ but can be checked during the test.

The evaluation should start with a multi-channel FFT analysis of the pressure signals upstream and downstream of the runner; if available, pulsation signals of shaft torque and discharge can also be included. The analysis should concentrate on the frequency band of vortex precession. The magnitude of all spectral lines of the frequency band should be included. The phase angles are required for the analysis; it is recommended to evaluate the coherence as a measure for signal-to-noise ratio. The synchronous pulsation p_{sync} is obtained as the (complex-valued) average of the pressure signals at equally spaced locations in one cross section of the draft tube cone. Four sensors displaced by 90° are recommended, two are minimum. The asynchronous pulsation in every pressure signal p_i results from

$$P_{asyn,i} = p_i - p_{sync} \tag{2.2}$$

always using the complex variables. Note that this procedure can also be used at conditions with cavitating vortex, or at high load. At partial load, it will reveal any cavitation-dependency of the asynchronous component, as shown in Fig. 2.3. At high load, there is often no coherent pulsation, or otherwise there is no significant asynchronous component.

If the system is simple, the pressure source Δp_{EX} is obtained from the measured pressure pulsation p_{SC} in the spiral casing entry and the pressure transfer function $G_{SC}(j\omega)$ between the two pressure variables. $G_{SC}(j\omega)$ differs from G_C in Eqs. (1.36) and (1.38) only in the numerator N which represents the impedance downstream of the runner, and has to be replaced by the impedance at the location of pressure sensor p_{SC}. The compliance C_C is zero in the cavitation-free reference test; therefore there are no more unknowns in the equation

---

[2] We are omitting the tilde; all pressure variables are fluctuations.
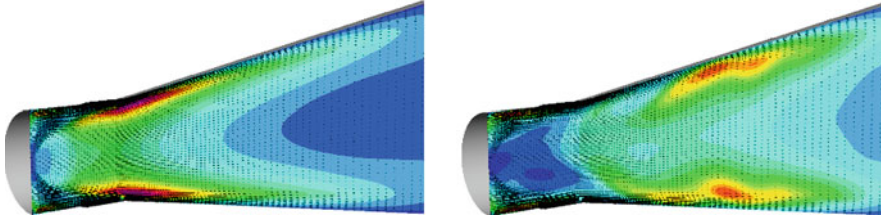
Fig. 2.4 Turbulent kinetic energy of swirling flow in a conical diffuser

$$\Delta p_{EX} \; = \; p_{SC} / \, G_{SC} \qquad\qquad (2.3)$$

Within the accuracy of the one-dimensional system model, the same should result if the synchronous pulsation p_{sync} in the draft tube cone is evaluated first and the equations in Sect. 1.4 are directly used assuming $p_C = p_{sync}$. In theory, the torque signal could also be used but the pertinent transfer function is less accurate.

First attempts to investigate the physical nature of the draft tube vortex at part load by means of Computational Fluid Dynamics (CFD) have steadily been published since 1999. For early examples, see Ruprecht et al. [12] and Sick et al. [13]. Due to the fact that this flow is dominated by vortex structures, the turbulence model has been found to be of high importance for an accurate prediction. A comparison of CFD results obtained with the standard k-ε model and the physically better justified (but more computationally expensive) Reynolds stress model is given in Sick et al. [13] for the swirling flow in a conical diffuser. Differences between the two methods may be seen in the Fig. 2.4.

At the diffuser inlet a circumferentially uniform velocity profile is prescribed which is typical for draft tube inlet flow at part load, including radial variations of the velocity components. As a result of the swirl a strong backflow builds up in the core region of the diffuser, left-hand side of Fig. 2.4. In the shear layer between the inner backflow and the outer swirling flow, small vortices develop into the typical corkscrew-like flow instability. These flow patterns are well predicted both by a laminar flow simulation and a flow simulation with the Reynolds stress turbulence model. In case of the standard k-ε model far too much turbulent dissipation is modeled in the shear layer with the result that the vortices cannot develop. This well-known weakness of the standard k-ε turbulence model can be overcome by a modification which takes into account the stabilizing effect of stream line curvature.

Furthermore, the computational grid is of major importance for a realistic prediction of the vortex and the related pressure drop toward the vortex core, as reported by Stein [14]. A good general rule says that the vortex core should be resolved by at least 20 grid cells. If this condition is not fulfilled both the velocity gradients and the pressure drop are under-predicted.

Validation of predicted DTPP versus experimental data obtained in a model test shows that single-phase flow simulations give very good results of the frequency as well as the amplitude of the pressure pulsations. The CFD simulation reported
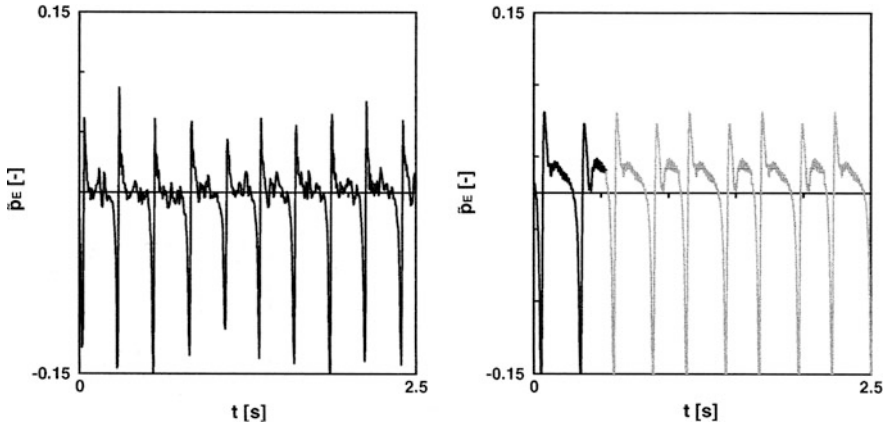
Fig. 2.5 Measured (*left*) and computed (*right*) DT wall pressure pulsation

in [14], shown in Fig. 2.5, gives a frequency prediction within 2 % accuracy compared to the measurements because very high grid resolution was used (overall 35 million nodes). For coarser computational grids, which are more common in industrial applications, the error in frequency prediction may be up to 20 %.

Two phase flow simulations reported in [14] reveal a lack of accuracy of the CFD approach with maximum 35 million grid nodes in the draft tube due to relatively low grid resolution with respect to the cavity: the volume of the cavity was under-predicted leading to a significant error of vortex dynamics prediction [14]. This suggests that numerical flow simulation can be reliably used for predicting frequency and strength of the draft tube vortex with high sigma values but not yet for predicting the effect of varying tail water level or sigma values respectively.

2.2.2 Random pulsation at Very Low Load

If the relative turbine discharge $Q_{nD}/Q_{nD,opt}$ is lower than a certain threshold, usually between 40 and 50 %, the swirl ratio is so high that the vortex rope disintegrates. A large number of unorganized smaller vortices replace the single corkscrew vortex. The DTPP loses its near-periodic behavior and has the character of a wide-band noise. The two pressure samples in Fig. 1.4 demonstrate the different flow regimes very well. While the time-domain pressure amplitude may become larger at lower load, there are often no significant narrow-band fluctuations that may result in an intense resonance.

In the operating range directly below the single-helix vortex rope, there are sometimes vortex flow structures which occur which are not as periodic as the helix but still retain, in a statistical sense, some phase relationships. This may be seen in

Fig. 7.13 in Sect. 7.2.1 where the asynchronous pulsation does not immediately disappear together with the single-helix structure (at $Q_{nD}/Q_{nD,opt} \leq 0.6$) but only gradually. The less regular vortices prevailing in this flow regime correspond to a wider range of frequencies and phase angles in the spectrum.

In addition, Fig. 7.13 shows that the relative amount of hydraulic losses of the turbine, expressed by the ratio $(Q_{ED} - P_{ED})/Q_{ED,opt}$, starts to increase significantly together with the random part of the DTPP, at the limit of the single-vortex zone. At very low load, the entire pulsation consists of random movements only.

2.2.3   Partial-Load Vortex: Two Threads (Twin Vortex)

In some Francis turbines and pump turbines there is an additional draft tube flow regime occurring adjacent to the lower boundary of the single-helix region. If this regime exists, then its range is usually quite small, approximately 5 % of $Q_{nD}/Q_{nD,opt}$. The single helix is replaced by a double helix [15], the two threads being displaced by 180 degrees. In the DTPP, this condition is easily detected due to the discontinuous increase of frequency and change of the phase relationships; the phase relationships resemble the behavior of the 2f component existing in the single-helix flow.

The presence of a central column, or shaft, in the draft tube axis occasionally promotes the formation of the double helix pattern, see [16] for an example. Another example is shown in Fig. 2.6. Pressure signals are shown for three sensors which are equally spaced around the draft tube cone of a model with $n_{QE} = 0.23$. The right-hand side shows the regular behavior with the precession of the low-pressure zone of the single vortex marked with gray arrows. At a slightly lower flow rate, the single-helix pattern is replaced by a flow regime with two vortex threads, the additional thread being indicated by the arrows drawn with broken lines. The central column in this draft tube has 0.30 times the runner exit diameter. The doubling of the vortex does not occur in the model version without a central column.

No practical problems due to the double helix phenomenon have been reported so far.

2.2.4   Low Partial-Load: Self-Excited Oscillation

Other phenomena may also lead to pulsations at partial load. A serious pulsation phenomenon occurred in a large power plant [17] with a rated head of approximately 100 m. Each one of the turbines rated 200 MW has a separate penstock. Intense pressure pulsation was observed around 30 % of the rated output, at a relative discharge $Q_{nD}/Q_{nD,opt}$ between 25 and 40 %. The upper limit approximately coincided with the lower limit of the single-helix range. The relative frequency f/n was between 0.7 and 1.0, and increased with increasing flow.
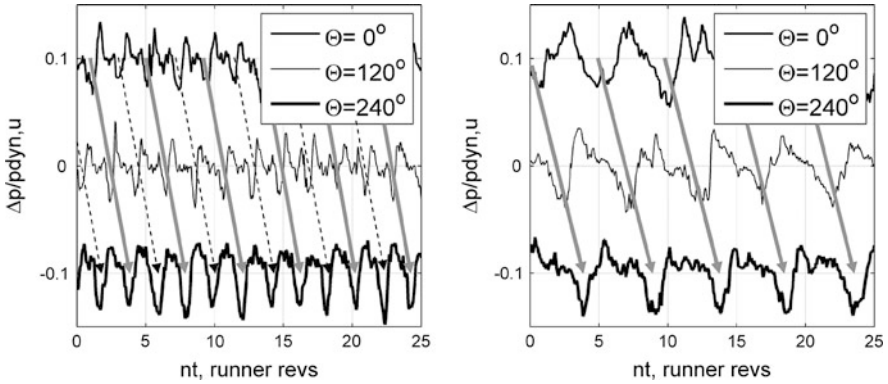
Fig. 2.6 Additional vortex thread due to central column
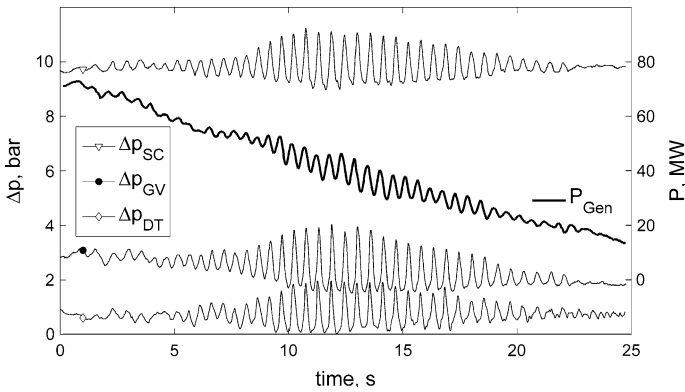
 Fig. 2.7 Slow transient showing self-excited low-load pulsation

The frequency was always somewhat above the lowest natural frequency of the penstock for each one of the three units. The oscillation frequency was found to be dependent on the natural frequency determined by the penstock length (different between the units) and headwater level. The frequency range overlapped with that of the natural frequency of the generator, as a consequence there were large power swings in some situations. Figure 2.7 shows a moderate version of the phenomenon. The magnitude of pressure pulsation is roughly the same upstream and downstream of the turbine, as well as between the wicket gate and runner (Δp_{GV}). In this example, the frequency happens to coincide with the natural frequency of the generator.

   No indication for the phenomenon was found in the model test, and, because of this, the oscillation is classified as self-excited. At maximum head the DTPP attained dramatic peak-to-peak values up to 63 mwc, the amplitude in the penstock being slightly smaller than in the draft tube. A variety of theories have been

proposed to explain the problem. Tentative explanations comprised a hysteresis in the turbine characteristics [18], a dead time in the vaneless space between the guide vanes and runner [18], and some system resonance responding to draft tube pressure fluctuation [17].

In a practical sense, the solution was simple. Injection of a very small air flow (85 l/s, or 0.04 % of nominal turbine discharge) through the runner hub proved to be sufficient to completely suppress the instability.

Gummer [19] described an oscillation with virtually identical properties—specific speed, load range, relative frequency, phase relationships and mode shape. In this paper, a turbine impedance with locally negative real part is supposed to be the cause. Unlike the previous example, this oscillation reportedly does not occur when the unit is ramped up. An explanation could be that the dynamic response of the two-phase flow depends on the partial pressure of the dissolved gas, which requires some time to build up.

2.2.5 Upper Partial-Load Vortex: The "80 % Pulsation"

In the upper partial-load range, usually between 70 and 80 % of $Q_{nD,opt}$, the half-load corkscrew vortex is often accompanied by an additional phenomenon with much higher frequency. Most observations of this phenomenon are from models with high specific speed [20–22]. The frequency spectrum typically consists of several narrow bands whose center frequencies differ by multiples of the vortex precession frequency [23]. Some examples from a Francis turbine model test are presented in Figs. 7.1, 7.2, and 7.6.

The peculiar arrangement of frequencies has been explained by a modulation process. In terms of a mathematical formula, this corresponds to multiplying two periodic functions, each one having a few harmonics:

$$X(t) = \left(A_0 + \sum_{i=1,2,..} (A_i \cos(i\omega_V t) + \ldots + B_i \sin(i\omega_V t)) \right)$$
$$\times \left(C_0 + \sum_{i=1,2,...} (C_i \cos(i\omega_C t) + D_i \sin(i\omega_C t)) \right) \tag{2.4}$$

The lower frequency ω_V represents the vortex precession, while the origin of the higher frequency ω_C is not adequately explained. Arpe et al. [23] found a natural mode of the test rig to be involved; however in some tests [20] the phenomenon could be reproduced at quite different test head and speed. Other authors [24] attribute $\omega_C = 2\pi f_C$ to a precession movement of an elliptical wave shape on the vortex cavity surface. An oscillation mode with elliptical surface of the vortex has been postulated based on theoretical studies [24], and several researchers observed the revolving elliptical deformation by means of high-speed video taken in model turbines [25], and also in a model pump-turbine [26].

Relative frequencies f_C/n between 1 and 5 have been reported [20], with values close to 2.5 being most common [23]. The frequency f_C increases strongly with the draft tube pressure. Other than the pulsation at precession frequency, this component only exists when there is cavitation on the helix. The pressure pulsation may attain amplitudes in excess of the half-load vortex itself; amplitudes in the turbine intake are sometimes higher than at the draft tube cone wall.

While relative amplitudes in the model test have quite often been alarming, the phenomenon usually did not show up at the prototype turbine. Comparable phenomena in prototype units are very rare; pulsation of axial thrust felt at the thrust bearing structure has been tentatively attributed to this category in a few cases. A singular case encountered in the authors' company occurred in a turbine with a straight horizontal draft tube. In this case, the phenomenon was almost perfectly similar between model and prototype. This, and the absence of similarity in other projects, could be a hint that lack of Froude similarity (see Sects. 7.2.1 and 9.2.1) normally prevents the phenomenon from occurring in large prototypes.

In model tests, the pulsation may be suppressed by small quantities of air injected to the draft tube center. In some cases, attempts were made to minimize the 80 % pulsation in the model turbine by design modifications. These can be either changes in the contour of the runner cone (semi-tapered hub, [21]) or adjustment of the runner blade profile [22].

2.2.6 Instability of the Helix Flow Pattern

The corkscrew vortex is a fairly robust flow pattern occurring at partial load in virtually every Francis turbine. At the center of its range at about 2/3 of $Q_{nD,opt}$, it rotates very uniformly and regularly. However, at the limits of its range of occurrence, it may become intermittent with temporary prevalence of other (neighboring) flow patterns. During a transition between different flow regimes the vortex or parts of it may collapse. A sharp pressure shock is produced when the cavitating vortex filament suddenly implodes. Such disturbances have been observed in several model tests [27, 28], in particular near the upper limit of the range of the partial-load vortex, at 80–90 % of $Q_{nD,opt}$. The authors of [28] even called this range the 'shock zone,' when reporting about turbines with rather high specific speed.

This phenomenon has also been observed in prototype turbines where the shocks may become quite unacceptable. Different remedies have proved effective. One possibility is injection or admission of air through the runner hub. In some cases, the problem has been mitigated by adding a cylindrical extension to the runner hub, using a shape similar to the one reported as a remedy against the '80 % pulsation' [21]. For this approach, Strohmer [27], has provided a detailed description from which the content of Fig. 2.8 has been taken. In the upper graph of this figure, the draft tube pulsation in the critical range of load ($Q/Q_{opt} = 0.88$) is compared with the normal behavior at $Q/Q_{opt} = 0.62$.
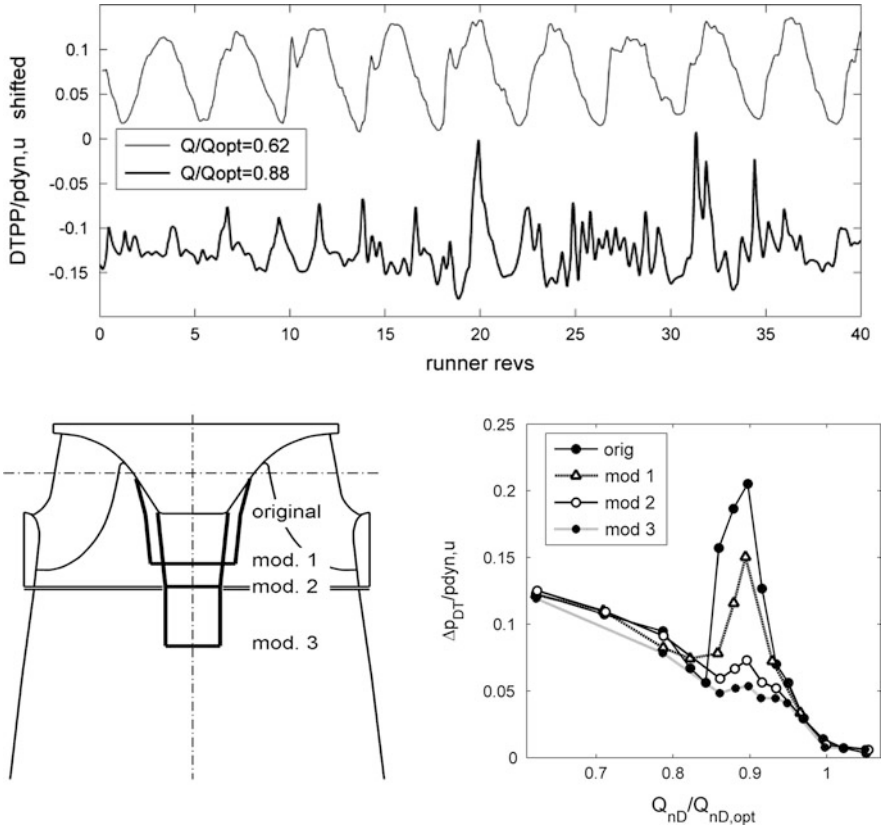
Fig. 2.8 Vortex stability enhanced by extension of hub

At $Q/Q_{opt} = 0.88$, the normal rotation of the vortex rope, with a period of about 4 runner revolutions, is no longer recognizable. Instead, there are less regular fluctuations at higher frequency and occasional pressure spikes that correspond to partial collapse of the rope. This phenomenon causes the high pressure amplitude for the original design in the lower right graph. A series of modifications of the runner hub was examined, showing that a moderate extension of the hub can rectify the problem.

2.2.7 Self-Excited Oscillation at High Load (Full-Load Surge)

In case of negative swirl at high load, the helical vortex shape occurs rather seldom. Here the vortex is usually rotationally symmetric, at least inside the upper cone region of the draft tube. Vortex precession and the accompanying asynchronous pulsation are therefore absent, as well as the forcing term of pulsation.

Nevertheless, some turbines exhibit regular and intense pulsation of pressure and power during high-load operation. This kind of surge has been explained as a self-excited oscillation. While all conventional elements used in one-dimensional fluid transient models have a damping or at least neutral effect on oscillations, the mass flow gain factor (MFGF) $\chi = -\partial V_C/\partial Q$, as explained in Sect. 1.5, has been identified as a potentially destabilizing feature connected with cavitating flows.

In the context of hydraulic turbines, the mass flow gain effect was suspected to play a role in stability for some time. Ideas to apply it to draft tube cavitation were published in the 1980s, either based on upstream flow q_1 [10], or downstream flow q_2 [29]. The latter concept has long been favored because it predicts instability in many cases. Attempts to simulate the full-load vortex were made later with steady-state CFD, in order to get more insight into the fluid dynamics and to obtain quantitative data for the mass flow gain factor (MFGF) and cavitation compliance. Flemming et al. [30] published cavity volumes estimated from single phase as well as two-phase flow simulations. The single-phase simulation estimated the cavity volume from the predicted pressure levels without cavitation (the cavity being assumed to be located in the volume where the pressure was predicted to be less than the vapor pressure), whereas the two-phase simulation calculates the cavity volume based on a certain value of the void fraction. They showed that a two-phase representation is necessary for realistic values of the cavitation parameters. The study reported, for a Francis turbine project, a gross reduction of MFGF due to replacement of single phase by two-phase parameters. It nevertheless predicted instability of the prototype turbine. Unlike many other predictions, this one was made before the turbine was installed. The prototype was commissioned later, and it was stable up to maximum load [31].

As explained in Sect. 1.5 and in [32], the concept of using the downstream flow q_2 as a reference for mass flow gain χ in draft tube flow usually requires much lower magnitude of χ for instability compared to the use of q_1; therefore it overestimates in a systematic manner the destabilizing effect. To close further speculation about the correct approach, a study was conducted in 2009 to directly compute the unsteady behavior of a cavitating, rotationally symmetric vortex [33]. It was confirmed that two-phase computation is indispensable.

As shown in Fig. 2.9, taken from the study [33], the vortex shape resulting from the two-phase model has features known from physical model tests that cannot be reproduced by a single-phase computation. In case of large cavities, it shows a characteristic annular hydraulic jump and an undular structure reminiscent of standing waves.

The transient two-phase computations required a very high spatial resolution. Oscillation of the vortex flow was forced by means of a prescribed time-dependent variation of the draft tube intake velocity field. The response of the draft tube intake pressure, cavity volume, and draft tube exit discharge were simulated for transients with different forcing frequency. The structure and parameter values of a frequency-domain model for the dynamic transmission behavior of the full-load vortex were then identified. A large fraction κ of the mass flow gain effect depends on the runner exit flow q_1 (red curve in Fig. 2.10). The dead time t_d mentioned in
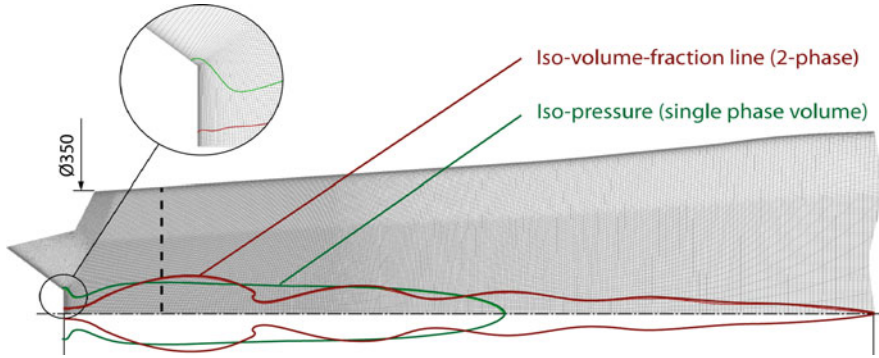
Fig. 2.9 Cavity contour obtained from single-phase and two-phase CFD model
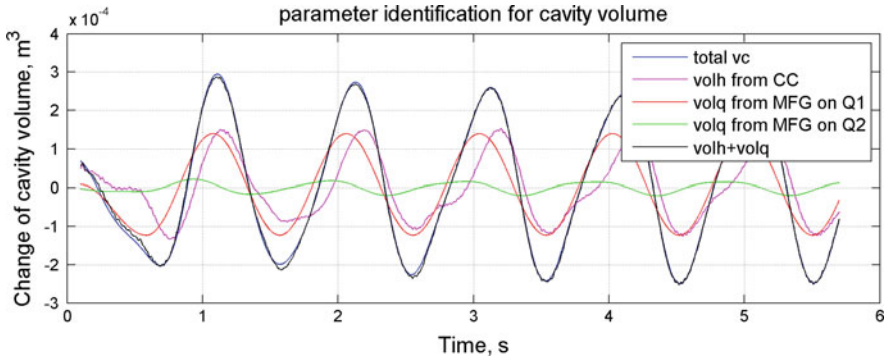
Fig. 2.10 Synthesis of cavity volume in identification procedure

Sect. 1.5 is essential. A small portion $1 - \kappa$ of the mass flow gain effect (between 0 and 4 %) was found to apply to the downstream side; it has only a minor influence on stability (green curve). The resulting lumped parameter model [33] for the cavity volume is

$$V_c = - C_C \cdot p_c - \chi \cdot (\kappa \cdot q_1(t - t_d) + (1 - \kappa) \cdot q_2) \qquad (2.5)$$

Self-excited pulsation at full load has in a number of cases been successfully reduced by air admission to the draft tube center, preferably through the shaft [34, 35], see also Sect. 8.2]. Draft tube fins, which are described below, are not effective because, other than in partial load, at high load the main flow is not concentrated at higher radius.

2.2.8 Full-Load Vortex: Forced Oscillation

In some turbines the helical vortex shape also prevails at full load. It is probably associated with low axial flow velocity in the hub region and can therefore usually be avoided by appropriate runner design. The corkscrew vortex at full load has therefore become quite seldom in modern turbines. There is also an influence of the cavitation number. The corkscrew shape may exist at rather high cavitation number but disappear when the size of the cavitating core increases due to lower pressure. A similar behavior is also known with respect to the partial-load vortex, but due to stronger diffuser effect in the draft tube it is much more important at high load.

The physical properties of the forced full-load surge are similar to the half-load surge. The main difference is that, due to the higher level of flow velocity at comparable swirl number, the frequency is higher than at part load. In a well-documented historical case (reported in Sect. 8.1) the helical shape was observed in the model test, and the DTPP could be measured both at plant sigma and in absence of cavitation. For the successful countermeasure, see Sect. 8.1. In this problem, draft tube fins have also been found ineffective.

2.2.9 System Response

Pressure pulsation in the draft tube is the most common effect caused by the draft tube swirl. Quantitative data may be found in Sect. 7.2.1, some explanations of the hydraulic system response in Sect. 7.2.1 The so-called synchronous part of draft tube pulsation is associated with upstream (i.e., penstock) pressure pulsation, and this in turn can only be produced if the turbine discharge pulsates. The pulsation of turbine discharge (and head), power swing, and in some cases axial vibration (runner, shaft, generator support bracket), are all related to the 'synchronous' pulsation. On the other hand, radial vibration (runner shaft and bearing housing), and some of the low-frequency components of draft tube wall vibration are related to the 'asynchronous' part.

2.2.10 Mechanical Effects

Runner stresses caused by the partial-load vortex have been studied by on-board measurements [36]. A result including the vortex rope effect is shown in Fig. 1.15 in Sect. 1.6.

Although the draft tube rope may not have important effects on the runner [37, 38], long-term operation under rope condition may have more important effects on the draft tube components (cone, door, liner, pier, concrete) as shown in

Fig. 2.11 Crack in concrete
at draft tube door

Fig. 2.12 Crack at junction
of discharge ring to draft tube
liner

Figs. 2.11 and 2.12 for machines operated for extended period of time at low-load
conditions.

The asymmetric pressure distribution created by the helical vortex at partial
load also acts on the runner. This asymmetry results in a rotating radial force
and bending torque acting so that the runner performs a lateral vibration whose
frequency, seen from the stationary system (casing, bearings) is the precession
frequency of the vortex. This rotating radial force, which may also be observed and
measured in model tests (see [39] and Sect. 7.3.3), creates a characteristic feature
in the vibration behavior of the Francis turbines, shown in Fig. 2.13 for a pump
turbine. The shaft vibration also shows a discontinuous change at the lower limit of
vortex stability, in a similar way to the DTPP signals.

The ISO 7919 vibration standard [40] excludes pump turbines, but for Francis
turbines the limits required by the standard are sometimes difficult to fulfill. For a
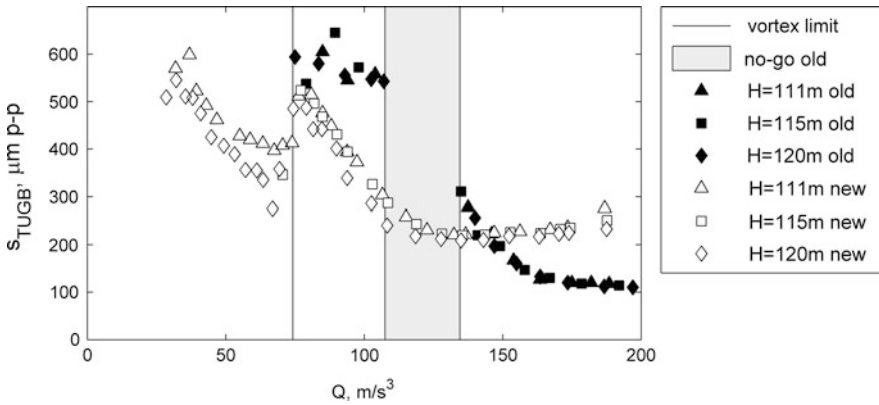
Fig. 2.13 Radial shaft vibration of a pump turbine

machine with the same synchronous speed as the one in Fig. 2.13 (166.7 rpm), the peak-to-peak amplitude of shaft vibration would not be allowed to exceed 250 μm. As the standard does not distinguish between turbine types that develop a part-load vortex (Francis, pump turbines, fixed-blade propeller) and machines that do not (Kaplan, Pelton), it is obvious that the Francis turbines are more critical with regard to fulfillment of vibration standard. Figure 2.13 also shows that even in case of refurbishment, where the draft tube remains the same, the quality of runner exit flow has an important influence on shaft vibration. The black markers in the figure show the behavior of the original runner that could not operate safely in the 'forbidden range' indicated as 'no-go old.' The replacement runner reduced the maximum vibration and eliminated the operational restriction.

In some cases it is likely that flow disturbances connected with the draft tube vortex have excited penstock vibration. Klein et al. [41] reported a case where intense vibration of the penstock shell occurred in the upper partial-load range, at approximately f/n = 1.33. The cure to this problem, likely caused by side effects of the part-load rope (Sect. 2.2.6), was to add stiffener rings to the penstock; the hydraulic cause was apparently not attacked.

In another case [42] the penstock vibration was caused by high-load surge with f/n $\cong$ 0.30, and was mitigated by air injection.

2.2.11 Peculiarities of Francis and Other Turbine Types

The draft tube shape has an important influence of draft tube surging. In early years, the US Bureau of Reclamation [2] even performed research using only the draft tube and no runner but with a swirl generating apparatus. Today, it is clear that the runner is essential for such tests, which makes it useful to compare replacement runners from different suppliers in comparative model tests. It is

known from many rehabilitation projects that a good runner outlet velocity profile may bring significantly better smoothness of operation (see Fig. 2.13 for an example).

2.2.11.1 Shallow Draft Tubes

In turbines with very shallow draft tubes there is often a small radius of curvature radius on the inner side of the elbow. In such cases the part-load vortex comes very close to the elbow contour in every revolution. As a consequence such draft tubes may give rise to high local amplitudes.

2.2.11.2 Straight Conical Draft Tubes

Conical draft tubes are a special case because in the absence of an elbow there is no forced oscillation excited by the usual mechanism. In these machines there is only the asynchronous pulsation. In practice, such turbines can also cause problems. In a turbine with a horizontal axis the vortex precession going through zones of different elevation can still cause periodically variable cavitation and provoke a small synchronous pulsation, in this case of a parameter-excited type. Also, the straight horizontal draft tube hardly responds to aeration because no air is retained in the vortex. By contrast, aeration in turbines with vertical axis is more effective because the air cannot escape easily.

2.2.11.3 Pump Turbines

Draft tube surge in pump turbines is of minor practical importance because pump turbines are designed to frequently pass through transients with much higher pulsation and vibration compared to the part-load surge. Because of this and the higher draft tube pressure level, aeration is seldom necessary. Draft tube surge may nevertheless cause problems if the machine is connected to a long tailrace. In such a case, the high water inertia combined with the small draft tube cavitation compliance may become critical for resonance. For a case example, see [43].

Draft tube inserts such as fins are seldom used, partly because there is a risk of runner damage in pump operation if an insert should fall off. An interesting application has been described in [44]. Model test results from pump-turbine models are shown and discussed in Sect. 7.3.1

2.2.11.4 Kaplan Turbines

In ordinary (double-regulated) Kaplan turbines, draft tube surge is also less important. The available range of runner blade angle adjustment, as defined by the

servomotor, is usually selected in a way as to permit on-cam operation in the foreseen load range. If running on-cam, the turbine produces too little runner exit swirl for a surge. Turbines operating off cam, due to very low load, or fixed-blade propeller turbines, have swirl properties comparable to Francis turbines. A survey of vortex phenomena for various loads has been given by Skotak and Pulpitel [45]. For model test results, see Sect. 7.4

In transient operation however, draft tube surge occurs in every Kaplan turbine. If the unit rejects load, then it has to pass through conditions with large residual swirl; at the instant of maximum speed, the runner torque is zero and the whole swirl generated in the wicket gate is passed through into the draft tube. For that reason large pressure fluctuations at vortex frequency may occur in the draft tube. Sometimes they may give rise to pressure shocks because also the amount of vortex cavitation becomes quite considerable. This is partly due to the deceleration of discharge while the guide vanes are closing. Typically, the resulting pulsation has a frequency of the order of 1 Hz, and fortunately only a few cycles. In some cases it may be necessary to improve the behavior by choosing a more suitable maneuver of the runner blades and wicket gate during load rejection.

2.2.11.5 Valves and Gates

Shutoff devices located downstream of a Francis turbine or pump turbine may also be affected by the draft tube vortex. The precession movement of the vortex continues even downstream of the draft tube elbow. Valves or gates in this environment must be secured absolutely reliably. A singular case has been reported [46] where a spherical valve at the end the draft tube of a high-head Francis turbine started to swing due to the draft tube vortex but was secured in time. Closure of such a valve during turbine operation would entail headwater pressure in the draft tube, with catastrophic consequences.

2.2.12 Prediction and Assessment

Until today, the most reliable source of information about the dynamic behavior of a turbine prior to construction is still the laboratory test with a reduced-scale model. The most important unsteady flow and pressure patterns like the part-load vortex or inter blade vortices may be taken as similar representation of prototype behavior, as far as their local consequences in the draft tube are regarded.

Dynamic similarity is never perfect because many kinds of oscillation phenomena have a global component that depends on system response [47], namely, the water conduit of the installation (test rig, or power plant) and the rotating assembly connected with the runner (brake, generator plus grid). These components of the pulsation may be subject to important distortion, as cautioned in the

IEC 60193 standard. The 'synchronous' component of the ordinary part-load oscillation is a good example [3].

Apart from the system dependency, the representation of cavitation may also cause deviations from similarity. Due to the large draft tube depth in vertical-axis turbines, the gravity component of the pressure distribution has an important influence on the vortex behavior. To correctly represent this influence, the condition of equal Froude number should be fulfilled together with the Thoma cavitation number σ. Equal Froude number means that the ratio between prototype head and model test head should be equal to the geometric scale:

$$H_M/H_P = D_M/D_P \qquad (2.6)$$

In model tests for very large prototypes, this condition results in very high suction head which can often not be realized at the test rig; in such cases the natural frequency of the draft tube cannot be expected to correspond to prototype. For that reason, hydraulic resonance conditions may be shifted to a different load condition or σ value.

The common sense approach to model-based prediction, also incorporated in the standard (Sect. 4.3.7 of [25]), is to expect the frequencies to transform proportional to the runner

$$f_M/f_p = n_M/n_p \qquad (2.7)$$

and the pulsation amplitudes proportional to the net head (or energy)

$$\tilde{p}_M/\tilde{p}_P = E_M/E_P \qquad (2.8)$$

Accordingly, it is common practice to use relative frequencies f/n and relative amplitudes (pressure factor $\tilde{p}_E = \tilde{p}/\rho E$) to characterize the pulsation test results. Other concepts, better adapted to the physical phenomena, have been suggested by the standard ([25], in particular par. 4.3.7.3), and by some authors [11, 48, 49], but apparently have not been adopted in practice. For a discussion, see [32].

Putting aside the issues of transferability, another important question is the admissible amount of pulsation. This matter has not been regulated by an international standard, and it seems that quantitative data have not been published by anybody since the 1980 s. Unrealistic ideas are therefore quite often encountered in technical specifications. One of the goals of this handbook is to provide information to counter this shortcoming. A very simple, unscientific, and yet quite practical limit for a prototype Francis DTPP would be

$$\Delta h_{p-p} < \text{sqrt}(H_r) \qquad (2.9)$$

wherein Δh_{p-p} is the maximum peak–peak amplitude (97 % confidence level) anywhere at the draft tube wall, and H_r is the rated head of the turbine, both figures in mwc at the prototype.

A more sophisticated, and 'scientifically acceptable' limit would be the generic curve presented in Sect. 7.2.1, Figs. 7.7 and 7.9. The authors recommend to no

Fig. 2.14 Draft tube fin shape

DT entry
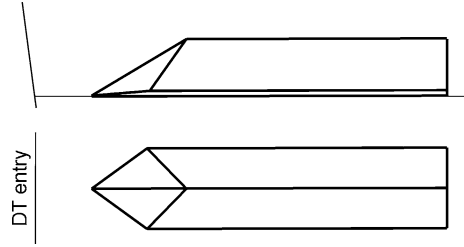
longer define guarantees as constant pressure factor for different values of operating head but as absolute values for pressure pulsation for physical reasons: As the turbine has the same speed and the same draft tube at minimum and maximum head, and as the draft tube vortex does not significantly depend on head, it will also have the same absolute draft tube pulsation.

2.2.13 Countermeasures

In the different types of draft tube surges (Sects. 2.2.1–2.2.8), different physical phenomena are involved. There is no single countermeasure suitable for all types of problems. For instance, draft tube fins are almost certainly useless if the problem is high-load surge.

Therefore, countermeasures have been mentioned as suitable in the pertinent chapters.

2.2.13.1 Draft Tube Fins

Draft tube fins [50, 51] are often a solution to problems caused by the part-load vortex. Depending on the draft tube profile, fins with different proportions have proven effective. Figure 2.14 is a shape that can be successfully used in many draft tube contours. Four fins to be set at 45° against the draft tube symmetry plane. The use of fins requires some caution, see Sects. 2.4.3.

The main effect of draft tube fins on the part-load pulsation is to reduce the amplitude of the pressure source Δp_{EX}, and therefore also the synchronous pulsation. Accordingly, it is the method of choice for suppressing cavitation-related draft tube resonance as well as power swings. Using the analytical procedure described in Sects. 2.2.1, the forcing term Δp_{EX} has been evaluated for a medium-head turbine. As shown on the left-hand side of Fig. 2.15, the excitation is almost completely eliminated. There is less influence on the asynchronous component (not shown). At the same time, the precession frequency is somewhat increased, typically by 10–15 %. As already mentioned, fins are usually ineffective with regard to problems at high load, i.e. flow rates higher than the swirl-free discharge.
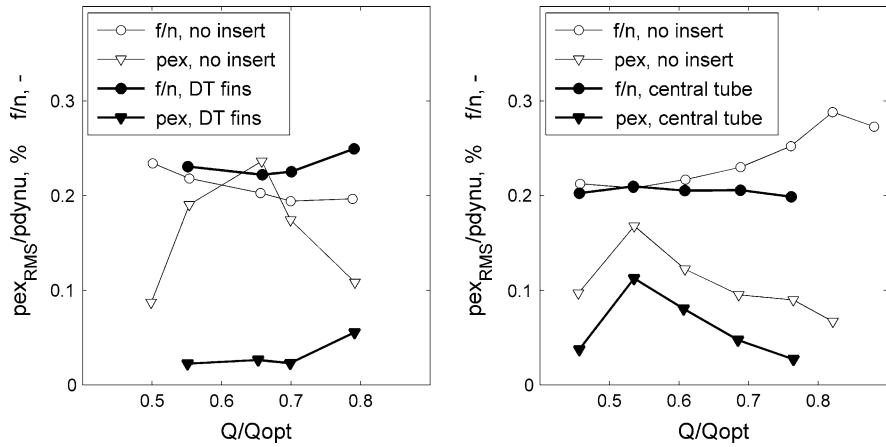
Fig. 2.15 Effect of draft tube inserts on part-load pulsation parameters. **a** $n_{QE} = 0.18$, draft tube fins. **b** $n_{QE} = 0.23$, central column

2.2.13.2 Draft Tube with a Central Column

Draft tube surges can also be reduced by means of other types of draft tube inserts. Placing a central tube in the draft tube axis, between the runner hub and elbow, may also provide smoother operation [52]. This design was probably inspired by the much older Moody cone. As shown on the right-hand side of Fig. 2.15, it also has some effect on the pressure source. The indicated frequency is the precession frequency. For the three test points with $Q/Q_{opt} \leq 0.63$, the vortex has two threads (see Sects. 2.2.3), therefore the actually measured frequency of pressure pulsation for these points was twice the value indicated in the plot. It is likely that this type of insert is also useful for stabilization at high load, however, no reliable results seem to be available.

There is a considerable lateral force of the vortex rope acting on the central tube; therefore sufficient radial support is essential. Stress concentrations at locations where radial struts join the draft tube wall and central tube are possible problem areas to be considered.

2.2.13.3 Air Admission

Air admission or air injection is very often beneficial [53, 56] because it smoothes out the annoying high-frequency components of noise and vibration. In addition, aeration sometimes removes flow instability by manipulating the hydraulic transmission behavior—in particular lowering the draft tube natural frequency. This effect can also be counterproductive in certain cases because a resonance of the synchronous draft tube pulsation may be produced by air injection in a pump-turbine or Francis turbine with rather high submergence.

Little has been published about the effect of flow aeration on turbine efficiency. Losses due to aeration increase with the relative air flow rate. Information about efficiency losses due to aeration has sometimes been collected in connection with tests aiming at increased tail water oxygen content [54, 55].

Depending on design, it is often necessary to add inserts in the draft tube, like tripods or pipes protruding from the draft tube wall. These structures obstruct the flow and cause additional drop in efficiency. Such additional loss may be avoided if air can be admitted through the shaft bore or head cover.

The turbine axis is, because of the radial pressure gradient due to swirling flow, the most suitable location for draft tube aeration by means of atmospheric air. In many cases air can be admitted through the hollow turbine shaft. Self-aspirating aeration may become more difficult or impossible if such an air path is not foreseen. Possible solutions depend on the design applied for axial thrust compensation. Solutions for turbines with external balancing pipes are shown in [56] and in Sect. 8.2 An example for a turbine with axial thrust compensation using a baffle plate is described in [57].

The effect of draft tube aeration on DTPP is often tested during reduced-scale model tests. Such a test demonstrates the possible effects in a purely qualitative manner. Quantitative data, like relative air rate, efficiency drop, or reduction of pulsation amplitude, must not be expected to be transferable.

2.3 Runner Inter Blade Vortex

2.3.1 Physical Mechanism

At part load the flow angle at runner inlet is no more optimally aligned with the blade inlet angle. High incidence occurs especially near hub and shroud which leads to a vortex which is driven through the blade channel toward the runner outlet.

2.3.2 Prediction, Features, Diagnosis

The inter blade vortex phenomenon is amenable to visual observation in the course of a model test, this holds at least in its well-developed form, see also Fig. 5.1.

2.3.2.1 Numerical Simulation

As the flow phenomenon of the inter blade vortices requires extremely high grid resolution (20 grid cells to resolve the vortex core), standard CFD simulations in industry usually reveal inter blade vortices in a coarse way only. There is an
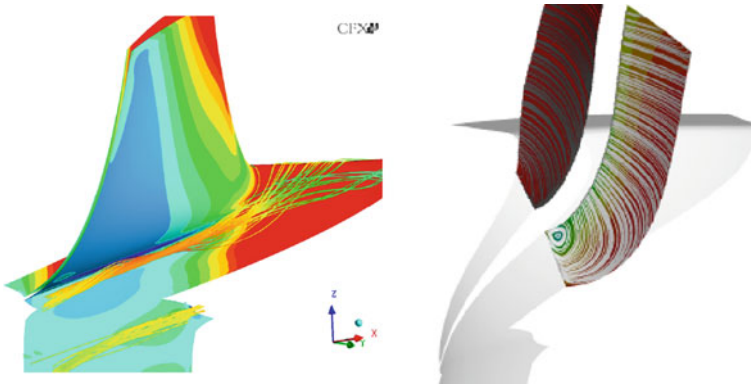
Fig. 2.16 CFD simulation of the inter blade vortex (ANDRITZ internal research, 2008)

example of a CFD simulation published by Stein et al. [14], of inter blade vortices occurring at part load. Another example is given in Fig. 2.16. In the cut-away view on the left-hand side the formation of the inter blade vortex from streamlines originating along the band-side runner entrance is visualized. The streamlines indicating the vortex are colored by velocity magnitude (red: high velocity, green: low velocity).The right-hand side shows the result of a CFD simulation of the inter blade vortex in a Francis runner. The distribution of static pressure on the blade and shroud is also shown from red (high pressure) to blue (low pressure). On the right-hand side the secondary flow patterns in the blade channel are illustrated by lines of the absolute velocity in a cross section showing clearly the center of the inter blade vortex.

To the author's knowledge no attempts have been made so far to predict time-dependent aspects of these vortices.

2.3.3 Operation Range Affected

Typical areas in the turbine hill chart are indicated in Fig. 5.1 (Sect. 5.2—discharge too low/head too high). The limits d and e may combine to form a single limit. Limits f and g in that figure are corresponding phenomena if the incident flow to the runner blades is wrong in the opposite sense (discharge too high/head too low). The example shown below in Fig. 2.18 belongs to the latter category.

2.3.4 Detrimental Effects

Pressure pulsation due to inter blade vortices is of an irregular wide-band nature and may be quite intense. It is not easy to quantify due to its stochastic, wide-band

Fig. 2.17 Cavitation erosion
caused by inter blade vortex
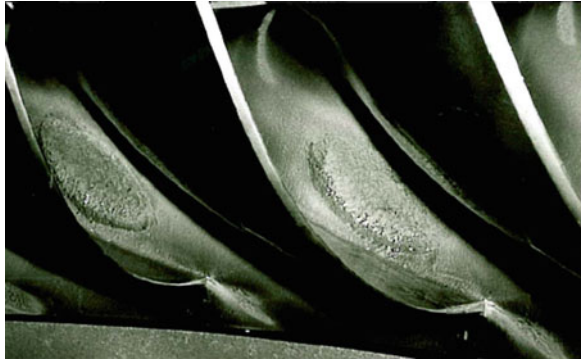
nature. In a Francis turbine with 2.4 m runner diameter, rated 56 MW at 300 rpm,
it was found that maximum intensity at the runner occurred at a higher frequency
(about 250 Hz) compared to the turbine intake (about 50 Hz). Both values cor-
respond to a Strouhal number—using the width of the runner blade channel at the
runner intake and exit, and the pertinent relative velocity—in the range of 0.5–1.0;
however it is not clear if these values are typical.

Inter blade vortices are known to create cavitation in runner blades flow chan-
nels, at the crown and sometimes also at the blades (see Sect. 5.3 on cavitation).
Accordingly, considerable damage by erosion may result in some cases. An
example for erosion by inter blade vortex (in this case due to excessive high
discharge at low head) is shown in Fig. 2.17, another one in Fig. 5.3.

Strong mechanical vibration may be caused by cavitation because the wide-
band excitation spectrum may excite the natural frequencies of many components
of the turbine structure. It is also possible that pressure pulsations travel upstream
into an exposed penstock and cause alarming shell vibration. In one plant, pen-
stock vibrations (Fig. 2.18) near the upstream valve downstream of the surge tank,
were clearly caused by pressure pulsation due to vortex cavitation in the runner.
This could be proven beyond doubt because the pressure signals at the valve
house, upstream (p5) and downstream (p6) of the safety butterfly valve were
sufficiently coherent for several bands of frequency. The phase shift between the
pressures was proportional to frequency, and corresponded to a plausible figure of
wave speed. The distance of sensor locations $\Delta L = 7.54$ m and phase shift of
180 dg (half wavelength) at 58 Hz, together with the definition of wavelength
($\lambda = a/f$), yields a wave speed of $a = 2 \times \Delta L/f = 875$ m/s. This is also an
example for a simple and reliable way of diagnosis, clearly indicating that the
pressure waves are arriving from a source downstream (in this case as far as 350 m
downstream) of the point of interest. It is also interesting that no coherence existed
between the pressure and vibration velocity signal, yet there could be no doubt that
the pressure pulsation excites the shell vibration.
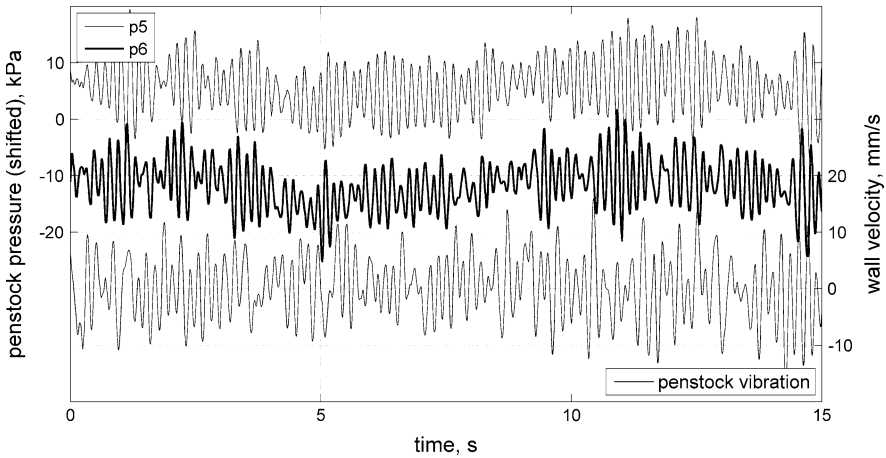
Fig. 2.18 Penstock shell vibration excited by runner cavitation

2.3.5 *Countermeasures*

To some extent, the limits of occurrence can be pushed back by adequate layout of the runner blade profile. If the range of operating heads in a Francis turbine is extreme, the occurrence of inter blade vortex at partial load and high head may become unavoidable.

As an example, in a large plant the maximum head is 2.6 times higher than the minimum head. At very high head—about 125 % of best efficiency head—the operation becomes very rough and extremely noisy. In such a case, air injection upstream of the runner is often highly effective in vibration and noise abatement. In the above-mentioned example air is supplied through a circular manifold above the head cover, connecting to a set of flush air intake holes, one downstream of every guide vane. In this example, the reduction in noise level due to air injection is −8 dB, a remarkable improvement.

An early description of upstream aeration for a low-head Francis turbine has been given by Malamet [58]. In some projects, air injection upstream or inside the runner has also been applied to reduce the erosion rate in runners of water turbines and storage pumps.

2.4 Vortex Breakdown: Other Locations

2.4.1 *Penstock Manifold*

Forceful vortex breakdown phenomena may take place in quite unexpected environment. In a medium-head power plant, the inflow was distributed to the

(a)

(b)
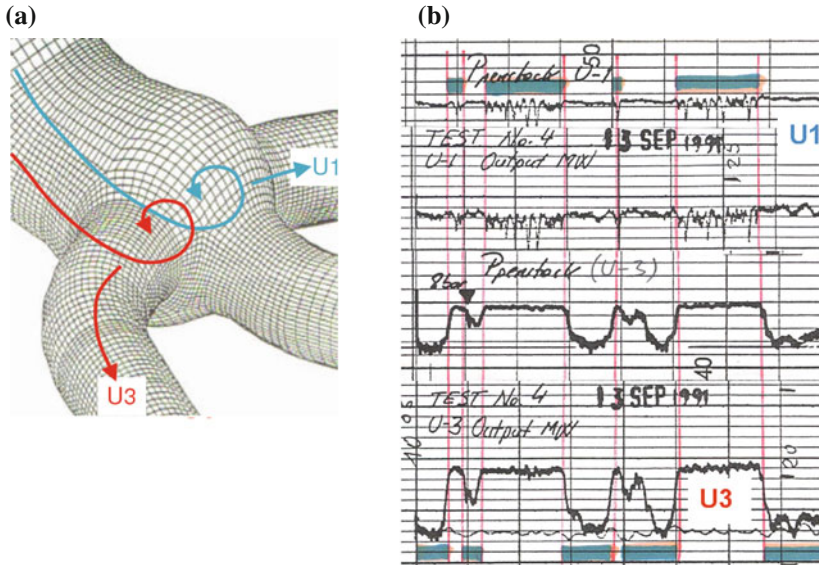
Fig. 2.19 Vortex breakdown in a penstock manifold. **a** Trifurcation with vortex. **b** Pressure and power dropouts

three turbines by a manifold. The manifold was a trifurcation built with a spherical body from which the three branches were fed (Fig. 2.19, left-hand side). The penstock entered the sphere with considerable eccentricity, the lateral branches are connected at an inclination of approximately 70 dg. The design successfully passed standard steady-state performance tests in a hydraulic laboratory, whereby no anomalous behavior was noticed.

A strange problem was detected when plant operation with all three turbines started. Every now and then, the output of unit 3 dropped by as much as 20 % and continued at the reduced level for a few minutes, then recovered to normal. Similar dropout occurred at unit 1 but not at unit 2. Recordings of power and turbine intake pressure of the units (Fig. 2.19, right-hand side) showed that the power variations were caused by a corresponding variation of turbine intake pressure, which in turn needed to be explained.

A closer look into the recordings reveals that the dropout periods at units 1 and 3 are mutually exclusive, as indicated by the green bars in the record. Some phenomenon makes the trifurcation act as a kind of fluidic switch that alternately throttles the inflow to the two lateral branches. The mechanism is comparable to the one acting in a flow device ('vortex throttle') used for one-way throttling in some surge tanks. The very eccentric inflow from the penstock to the spherical chamber obviously produces a strong rotational flow in the sphere with horizontal axis. Entering the side branch, this swirling flow is forced into a much smaller radius, with corresponding increase of tangential velocity. The vortex breakdown in the side branch creates a substantial pressure loss at the turbine intake. The flow

in the sphere is asymmetric. The throttling effect occurs at one lateral branch at a time, while the opposite branch recovers, and vice versa.

Later this problem has been studied by detailed laboratory tests as well as CFD simulations [59]. It was finally cured by inserting a 'roof' plate into the sphere which effectively inhibited the formation of vortices [60].

2.4.2 Kaplan Hub

As an initial step toward understanding the instability phenomena of swirling flows, engineers in the 1930s investigated the disintegration of a concentric pipe flow [1]; it was then that the dead water core was discovered. Later, Eichler [61] made use of this formalism to explain a flow disturbance occurring in axial turbines. A dead water core may form upstream of the runner of a Kaplan or bulb turbine when operating with a small guide vane opening. In the shear zone between this dead water core and the main flow, there are often strong spiraling vortex filaments. The appearance is somewhat similar to a draft tube vortex but there are usual several filaments at the same time. In some turbines there may be one vortex per runner blade that may extend downstream through the runner. In general, dead water core diameter is a function of the wicket gate opening but the intensity is a function of discharge, the phenomena getting stronger at large runner opening.

Pulpitel [62] found between one and four filaments traveling around the hub. He studied critical combinations of the number and precession frequency of those vortices both in a model and the pertinent large prototype of a four-blade Kaplan turbine. Under certain circumstances, the vortices may produce rotor whirling with large lateral shaft displacement. The criterion for an excitation of v cycles (node diameters, see also Sect. 3.1) around the runner circumference is[3]

$$v \; = \; k \times Z_r - m \times Z_D \qquad (2.10)$$

where k and m are low integers and

Z_r = number of runner blades
Z_D = number of disturbances (i.e., vortex filaments).

A whirling movement of the runner is excited if $v = \pm 1$, and the frequency f_s seen in the stationary system (bearings, casing), in the most important case m = k = 1 is

$$f_s \; = \; Z_r \times n \; - \; Z_D \times f_0 \qquad (2.11)$$

n = runner rotation frequency
f_0 = precession frequency of the vortex flow field.

---

[3] Compared to [62], the definitions have been adjusted to comply with Sect. 3.1.

There were quite frequently $Z_D = 3$ vortices rotating at about 60 % of runner speed, thus the four-blade runner was subject to whirling at roughly 2.2 times runner speed.

A typical operational situation where these phenomena become important, is the sluicing maneuver. During sluicing, the turbine is disconnected from the grid but has to discharge as much water as possible. Accordingly, the runner blades are wide open but the wicket gate must be partially closed in order to limit the speed. A peculiarity of the sluicing operation is that the entire swirl produced by the wicket gate is passing through the runner and draft tube. The draft tube flow is therefore also potentially unstable.

2.4.2.1 Numerical Simulation

Similar to the case of the inter blade vortices, the vortices around the Kaplan hub require extremely high grid resolution in order to resolve the vortex cores with 20 grid cells each. Such computational grids are at the limit of today's industrial standard. Nevertheless, an internal CFD study was carried in 2004 out by AND-RITZ Hydro with relatively high grid resolution in order to better understand the flow mechanisms acting near the hub at low part load (30 % of optimum load), see figure. A structured hexahedral computational grid was used with second order accurate spatial discretization. Several operating points were simulated in order to be able to unambiguously identify the cause for the pressure pulsations observed at extreme part load.

At flow rates of 60 % and higher, no vortex structure could be identified between guide vanes and runner blades but at 30 % load strong vortex structures were found near the runner hub. The Fig. 2.20 displays the geometrical proportions of the studied turbine (a) and a simulation result of the flow pattern between guide vanes and runner blades (b).

2.4.3 Draft Tube Fin Tip Vortex

Draft tube fins are often used in Francis turbines because they are a reliable countermeasure against the surge at partial load. If not properly used, they may however cause collateral damage. At reduced discharge, the draft tube flow meets the fins at a considerable angle of attack, giving rise to a secondary vortex starting at the leading edge of every fin, as shown in Fig. 2.21 for a medium-head Francis turbine. In the figure, the appearance of the secondary vortex at one out of four fins, as seen by the test engineer, is shown for various conditions of turbine load, i.e., draft tube swirl.

Cavitation is usually present in the core of the vortices, depending on the runner exit swirl. This measure can therefore produce unwelcome secondary pressure fluctuation at higher frequency, counteracting the desired reduction of pressure

(a)   **(b)**
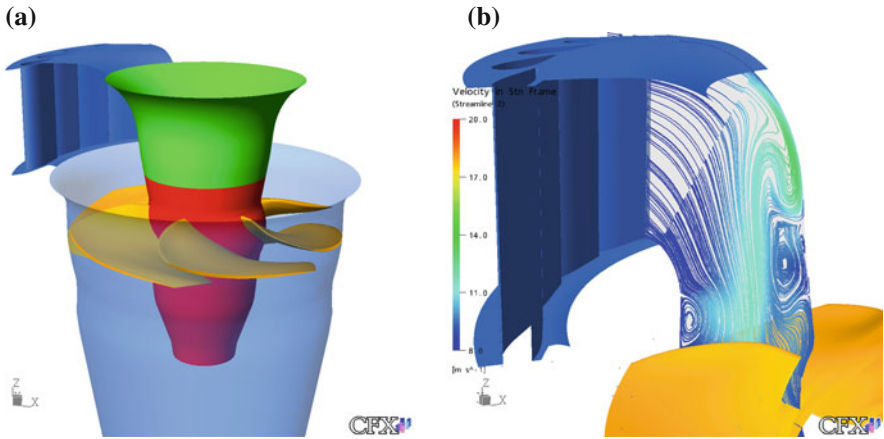
Fig. 2.20 CFD simulation of vortex structure near the Kaplan runner hub. **a** Geometry of the Kaplan runner. **b** Vortex structure at the hub

Fig. 2.21 Draft tube fin tip vortex observed at plant sigma, $n_{QE} = 0.146$
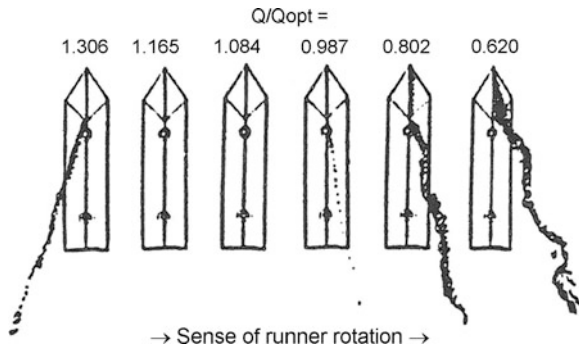
pulsation. In addition, the cavitating tails of the vortices often hit the draft tube wall that, as a consequence, has to be protected against cavitation. Such protection can be made by welding erosion-resistant plates to the draft tube wall in the wake region of the fin.

There is also a more effective means of protection. In case of substantial swirl, the leeward side of the fin tip normally has a small area of very low pressure. By providing a small hole at each one of the fins and connecting the holes to a manifold, it is normally possible to introduce atmospheric air by natural suction [44, 50]. No further protection of the wall is required and, equally important, the parasitic pressure fluctuations are also eliminated. The two references provide some quantitative information concerning the suction effect available at the fins. For more detailed data from ANDRITZ model tests, see Sect. 7.2.2.

References

1. Meldau, E. (1935). *Swirling flow in rotationally symmetric cavity* (in German). PhD thesis, Technical University Hannover.
2. Cassidy, J. J., & Falvey, H. T. (1970). *Frequency and amplitude of pressure surges generated by swirling flows.* IAHR Section Hydraulic Machinery, Equipment, and Cavitation, 5th Symposium (Stockholm, 1970), paper E1.
3. Nishi, M., Kubota, T., Matsunaga, S., & Senoo, Y. (1980). *Study on swirl flow and surge in an elbow type draft tube.* IAHR Section Hydraulic Machinery, Equipment, and Cavitation, 10th Symposium (Tokyo, 1980), Vol. 1, pp. 557–568.
4. Nishi, M., Kubota, T., Matsunaga, S., & Senoo, Y. (1984). *Surging characteristics of conical and elbow-type draft tubes.* IAHR Section Hydraulic Machinery, Equipment, and Cavitation, 12th Symposium (Stirling, 1984), pp. 272–283.
5. Rheingans, W. J. (1940). Power swings in hydroelectric power plants. *Transactions of the ASME, 62*, 171–184.
6. Ulith, P., Jaeger, E. U., & Strscheletzky, M. (1974). *Contribution to clarifying the inception of nonstationary phenomena in the draft tube of high specific speed Francis turbines operating at part load.* IAHR Section Hydraulic Machinery, Equipment, and Cavitation, 7th Symposium (Vienna, 1974), paper III-4.
7. Moody, L. F. discussion of [1].
8. Brennen, C. (1978). *The unsteady, dynamic characterization of hydraulic systems with emphasis on cavitation and turbomachines.* Joint ASME/ASCE/IAHR Symposium, Fort Collins, 1978, pp. 97–107.
9. Dériaz, P. (1960). *A contribution to the understanding of flow in the draft tubes of Francis turbines.* IAHR Section Hydraulic Machinery, Equipment, and Cavitation, 1st Symposium (Nice, 1960), paper B-1.
10. Doerfler, P. (1982). *System oscillations excited by the Francis turbine's part load vortex core: Mathematical modelling and experimental verification* (German text, English summary). Dissertation, Technical University Vienna (Austria), October 1982.
11. Doerfler, P. (1982). *System dynamics of the Francis Turbine Half Load Surge.* IAHR Section Hydraulic Machinery, Equipment, and Cavitation, 11th Symposium (Amsterdam, 1982), Vol. 2, Paper 39.
12. Ruprecht, A., Helmrich, Th., Aschenbrenner, Th., & Scherer, Th. (2001). *Simulation of pressure surge in a hydro power plant caused by an elbow draft tube.* 10th International Meeting of the work group on the behaviour of hydraulic machinery under steady oscillatory condition, Trondheim, Norway.
13. Sick, M., Dörfler, P., Lohmberg, A., & Casey, M. (2002). *Numerical simulations of vortical flows in draft tubes.* WCCM V, Vienna, Austria, 2002.
14. Stein, P., Sick M., Doerfler P., White, P., & Braune, A. (2006). *Numerical simulation of the cavitating draft tube vortex in a Francis turbine.* IAHR Section Hydraulic Machinery, Equipment, and Cavitation, 23rd Symposium, Yokohama, Japan, 2006.
15. Wahl, T. L., Skinner, M. M., Falvey, H. T. (1991). *The Twin Vortex Draft Tube Surge.* Waterpower'91, pp. 2011–2020.
16. Dörfler, P., Bloch, R., Mayr, W., & Hasler, O. (1988). *Vibration tests on a high-head (740 m) Francis turbine: Field tests from Häusling.* IAHR Section Hydraulic Machinery, Equipment, and Cavitation, 14th Symposium (Trondheim, 1988), Vol. 2, Paper D1.
17. Guarga, R., Hiriart, G., Torres, J. J. (1983). *Oscillatory problems at Mexico's La Angostura plant.* Water Power & Dam Construction, October 1983, pp. 33–36.
18. Glattfelder, A. H., Grein, H., & Huser, L. (1980). Self-excited oscillations in a hydroelectric unit. IAHR/IUTAM Symposium, Karlsruhe, 1979, Paper B11. In E. Naudascher & D. Rockwell (Ed.), *Practical experiences with flow-induced vibrations*. Berlin: Springer.
19. Gummer, J. H. (2007). Penstock resonance resulting from unstable turbine characteristics, Paper 21.01, Hydro 2007, Granada.

20. Doerfler, P. (1994). *Observation of pressure pulsations at high partial load on a Francis model turbine with high specific speed.* IAHR Work Group WG1 (The Behaviour of Hydraulic Machinery under Steady Oscillatory Conditions) 6th Meeting, Lausanne 1993, also in: Hydro-power & Dams, January 1994.

21. Billdal, J. T., & Holt, B. G. (2000). *Three Gorges project: Review of GE energy Norway's hydraulic design.* Proceedings of the Hydraulic Machinery and Systems 20th IAHR Symposium (Charlotte, 2000).

22. Shi, Q. (2008). *Experimental investigation of upper part load pressure pulsations for Three Gorges model turbine.* IAHR 24th Symposium on Hydraulic Machinery Systems, Foz do Iguassú, October 2008.

23. Arpe, J., & Avellan, F. (2002). *Pressure wall measurements in the whole draft tube: steady and unsteady analysis.* Proceedings of the 21st IAHR Symposium on Hydraulic Machinery and Systems, Lausanne, Switzerland, September 2002, pp. 593–602.

24. Rudolf, P., Pochyly, F., Hábán, V., & Koutnik, J. (2007). *Collapse of cylindrical cavitating region and conditions for existence of elliptical form on cavitating vortex rope.* IAHR WG (Cavitation and Dynamic Problems in Hydraulic Machinery and Systems) 2nd Meeting, Timisoara Romania, October 24–26, 2007.

25. Nicolet, C., Zobeiri, A., Maruzewski, P., & Avellan, F. (2010). *On the upper part load vortex rope in Francis turbine: Experimental investigation.* 25th IAHR Symposium on Hydraulic Machinery and Cavitation, Timisoara 2010.

26. Kirschner, O., Ruprecht, A., & Göde, E. (2009). *Experimental investigation of pressure pulsation in a simplified draft tube, Proceedings of the 3rd Meeting IAHR Workgroup on Cavitation and Dynamic Problems in Hydraulic Machinery and Systems,* Brno 2009, Paper B1.

27. Strohmer, F. (1975). *Investigation of the operational behaviour of a Francis turbine with high specific speed below best efficiency point* (in German). Dissertation, Technical University Vienna (Austria), April 1975.

28. Fisher, R. K., Palde, U., & Ulith, P. (1980). *Comparison of draft tube surging of homologous scale models and prototype Francis turbines.* IAHR Section Hydraulic Machinery, Equipment, and Cavitation, 10th Symposium (Tokyo, 1980), Vol. 1, pp. 541–556.

29. Pulpitel, L. (1985). *Low frequency pressure oscillations in hydraulic systems with a pump turbine.* IAHR Work Group WG1 (The Behavior of Hydraulic Machinery under Steady Oscillatory Conditions) 2nd Meeting, Mexico City, 1985.

30. Flemming, F., Foust, J., Koutnik, J., & Fisher, R. K. (2008). *Overload surge investigation using CFD data.* IAHR 24th Symposium on Hydraulic Machinery Systems, Foz do Iguassú, October 2008.

31. Dörfler, P., Braun, O., & Sick, M. (2001). Hydraulic stability in high-load operation: a new model and its use in Francis turbine refurbishment. *Hydropower and Dams*, (4), 84–88.

32. Dörfler, P. K. (2009). *Evaluating 1D models for vortex-induced pulsation in Francis turbines. Proceedings of the 3rd Meeting IAHR Workgroup on Cavitation and Dynamic Problems in Hydraulic Machinery and Systems,* Brno 2009, Paper F3.

33. Dörfler, P. K., Keller, M., & Braun, O. (2010). *Full-load vortex dynamics identified by unsteady 2-phase CFD.* 25th IAHR Symposium on Hydraulic Machinery and Cavitation, Timisoara 2010.

34. Purdy, C. C. (1979). *Reducing power swings at Tarbela's turbines.* Water Power and Dam Construction, April 1979, pp. 23–27.

35. Arzola, F., Azuaje, Z., Zambrano, P., & Gulbrandsen, G. (2006). *Undesired power oscillations at high load in large Francis Turbines. Experimental study and solution.* IAHR Section Hydraulic Machinery, Equipment, and Cavitation, 23rd Symposium, Yokohama, Japan, 2006.

36. Lowys P. Y., Doyon J., Couston M., & Vuillerod G. (2001). *Dynamic behaviour of low head Francis turbines.* 10th International Meeting of the Work Group on the Behaviour of Hydraulic Machinery Under Steady Oscillatory Conditions, Trondheim, Norway, June 26–28, 2001.

37. Lowys P.-Y., Deniau J.-L., Gaudin E., Leroy P., Djatout M., (2006) On-Board Model Runner Dynamic Measurements, Hydrovision, Portland.
38. Coutu A., Monette C., Gagnon M., (2007) Life Assessment of Francis Runners Using Strain Gage Site Measurements, Waterpower XV, Chattanooga, TN, July 23-26, 2007.
39. Doerfler, P., Lohmberg, A., et al. (2003). *Investigation of pressure pulsation and runner forces in a single-stage reversible pump turbine model*. IAHR Work Group WG1 (The Behavior of Hydraulic Machinery under Steady Oscillatory Conditions) 11th Meeting, Stuttgart 2003.
40. ISO 7919 Mechanical vibration—Evaluation of machine vibration by measurements on rotating shafts Part 1: General guidelines Part 5: Machine sets in hydraulic power generating and pumping plants.
41. Klein, J., et al. (1976). *Investigation on vibrations of a large penstock, on the sources of their excitation and on getting them under control*. IAHR Section Hydraulic Machinery, Equipment, and Cavitation, 8th Symposium (Leningrad, 1976), paper I-3.
42. Gibberd, J. J. (1997). *Diagnosis and solution of severe hydro-mechanical vibrations following the upgrading of a 30 MW UK hydro station*. Conference on Refurbishment and Upgrading of Hydro Plants, October 1997, pp. 25–38.
43. Koutník, J., Nicolet, Ch., Schohl, G. A., & Avellan, F. (2006). *Overload event in a pumped-storage power plant*. IAHR Section Hydraulic Machinery, Equipment, and Cavitation, 23rd Symposium (Yokohama, 2006).
44. Pulpitel, L., Koutnik, J., & Skotak, A. (1998). *Natural air admission of a deep submerged pump turbine*. IAHR Work Group WG1 (The Behavior of Hydraulic Machinery under Steady Oscillatory Conditions) 9th Meeting, Brno 1999, paper A5, also in: Hydro Vision'98.
45. Skotak, A., & Pulpitel, L. (1997). *Behaviour of a Kaplan turbine model operating under off-cam conditions for a wide range of load*. IAHR Work Group WG1 (The Behavior of Hydraulic Machinery under Steady Oscillatory Conditions) 8th Meeting, Chatou 1997, paper G-1.
46. Wobornik, A. (1967). Observations downstream of Francis turbines with back pressure (in German). *EuM*, *84*(12), 488–493.
47. IEC 60193 Hydraulic turbines, storage pumps and pump-turbines—Model acceptance tests, Ed. 2.0, 1999–11.
48. Jacob, T., Prénat, J.-E. (1996). *Francis turbine surge: discussion and data base*. IAHR Section Hydraulic Machinery, Equipment, and Cavitation, 18th Symposium (Valencia, 1996), pp. 855–864.
49. Tadel, J., Maria, D. (1986). *Analysis of dynamic behaviour of a hydroelectric installation with a Francis turbine*. 5th International Conference on Pressure Surges, BHRA (Hannover, 1986), Paper G1, pp. 169–176.
50. Biela, V. (1998). *Draft tube fins*. IAHR Section on Hydraulic Machinery and Cavitation, 19th Symposium (Singapore, 1998), pp. 454–461.
51. Rocha, G., Sillos, A. (1982). *Power swing produced by hydropower units*. IAHR Section Hydraulic Machinery, Equipment, and Cavitation, 11th Symposium (Amsterdam, 1982), Vol. 2, Paper 44.
52. Lecher, W., Baumann, K. (1968). *Francis turbines at part-load with high back-pressure*. IAHR Section Hydraulic Machinery, Equipment, and Cavitation, 4th Symposium (Lausanne, 1968), Paper B-4.
53. Nakanishi, K., Ueda, T. (1964). Air supply into draft tube of Francis turbine. *Fuji Electric Review,* 10(3), pp. 81–91.
54. Harshbarger, E. D., March, P. A., Vigander, S. (1984). *The effect of hydro turbine air venting on generating efficiency, dissolved oxygen uptake, and turbine vibrations*. Tennessee Valley Authority, Water Systems Development Branch, Rept. WR28-1-600-107, March 1984.
55. Papillon, B., Sabourin, M., Couston, M., Deschênes, C. (2002). *Methods for air admission in hydroturbines*. 21th IAHR Symposium on Hydraulic Machinery and Systems, Lausanne, September 9–12, 2002.

56. Doerfler, P. (1986). *Design criteria for air admission systems in Francis turbines*. IAHR Section Hydraulic Machinery, Equipment, and Cavitation, 13th Symposium (Montreal, 1986), Vol. I, Paper 8.
57. Papillon, B., St.-Hilaire, A., Lindstrom, M., Sabourin, M. (2004). *Analysis of Francis head cover pressure and flow behavior inside runner cone.* Hydro Vision 2004, Montréal, QC, August 15–18, 2004.
58. Malamet, S. (1962). *Aeration of the turbines in the pumped storage plant Geesthacht* (in German). Elektrizitätswirtschaft 61, No. 8, 20-03-1962.
59. Ruprecht, A., Helmrich, Th., Buntic, I. (2003). *Very large eddy simulation for the prediction of unsteady vortex motion*. Conference on Modelling Fluid Flow (CMFF'03). 12th International Conference on Fluid Flow Technologies, Budapest, September 2003.
60. Hoffmann, H., Roswora, R. R., Egger, A. (2000). *Rectification of the Marsyangdi Trifurcation*. HydroVision 2000 (Charlotte, 2000).
61. Eichler, O. (1980). Vibration phenomena on hydraulic axial turbines. IAHR/IUTAM Symposium Karlsruhe, 1979, Paper B3. In E. Naudascher & D. Rockwell (Ed.), *Practical experiences with flow-induced vibrations*. Berlin: Springer.
62. Pulpitel, L. (1993). *The dynamic behaviour of a Kaplan turbine operating under non-standard conditions*. IAHR Work Group WG1 (The Behaviour of Hydraulic Machinery under Steady Oscillatory Conditions) 6th Meeting, Lausanne 1993.

Chapter 3
Periodic Effects of Runner-Casing Interaction

The rotation of the runner relative to the casing produces a number of periodic phenomena which are superimposed on the average fluid motion and pressure in the water passages. Due to the periodic nature, caused by any small variation of rotational speed, they appear in the pressure spectra as single frequencies. Undesired resonant vibration becomes possible if the frequency of the exactly periodic excitation coincides with a suitable natural mode of the structure.

Those phenomena linked to the blade passage often have sufficiently high frequency to be perceived as noise. Depending on the blade numbers in the stationary and rotating cascades, various modes of vibration may be excited directly in these structures. Radial reaction machines, in particular Francis turbines and pumps, may sometimes exhibit additional features which are due to unfavorable wave timing in the spiral casing duct.

Blade-frequency vibration plays an important role in the vibration signature [1] of all types of hydraulic turbo-machines, and is used for vibration diagnosis. Due to the small variation of runner speed, frequency analysis with sufficient resolution permits the effects of rotor–stator interaction to be clearly separated from flow instabilities.

3.1 General Properties of Unsteady Blade Row Interaction

The periodic effects of a runner revolving at constant speed inside a casing or stator have some general properties that are described first, as a guide for better understanding of the particular phenomena discussed later in this chapter. The periodic nature of the rotating and stationary blade cascades of a hydraulic turbo machine needs to be accounted for; however, asymmetric features of their

---

An erratum to this chapter is available at 10.1007/978-1-4471-4252-2_10.

Fig. 3.1 Vibration modes
with 0, 1, and 2 nodal
diameters
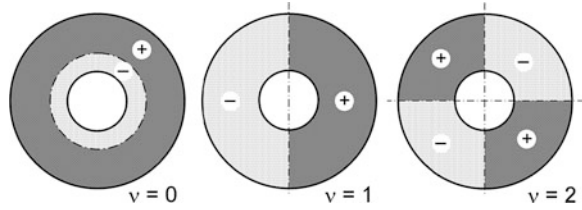
geometry may be also understood if they are described as the limit case of just one
period per rotation, such as the influence of the nose vane in a spiral casing.

Following a customary use by CFD engineers, we will use the term 'rotor–
stator interaction' or RSI, as a synonym for the unsteady interaction between the
rotating and stationary blade rows; the interaction of the same name occurring in
an electric machine is not subject of this book.

The combination of a runner having Z_r blades with a stationary cascade (wicket
gate, or pump diffuser) of Z_s vanes is essential to cause the excitation of a par-
ticular mode shape of runner vibration. Interaction of the two cascades involved
may be represented by an exchange of periodic reaction forces whose variation in
time consists of a fundamental frequency and some harmonics related to the
rotational speed and the blades numbers in each cascade [2]. Using n for the
rotational speed of the runner (in revolutions per second), the effect of the runner
blades on any particular point in the stationary system (i.e., wicket gate and casing)
consists of the frequencies

$$f_{s,k} = n \times Z_r \times k \quad (k = 1, 2, 3, \ldots). \tag{3.1}$$

The lowest of these, $n \cdot Z_r$, is usually referred to as the blade passing frequency and
k is known as the harmonic number. Likewise, every part (for instance, every
individual blade tip) at the runner experiences a periodic force from the stationary
guide vanes with the frequencies

$$f_{r,m} = n \times Z_s \times m \quad (m = 1, 2, 3, \ldots) \tag{3.2}$$

The phase of these impacts on the runner from the ensemble of guide vanes is in
general not the same around the runner circumference. Depending on which
harmonics (k, m) of the interaction are considered, the runner is subject to a
pressure pattern of sectors with equal phase, separated by ND = $|v|$ nodal diam-
eters as shown in Fig. 3.1, fulfilling the condition

$$m \times Z_s + v = k \times Z_r \quad v = \ldots -2, -1, 0, 1, 2, \ldots \tag{3.3}$$

Observed in the stationary system, i.e., the casing, the excitation pattern (the
'mode shape') rotates in the sense of runner rotation if v in Eq. (3.3) is positive.
For negative v, it rotates against the runner rotation. The speed of rotation of
the mode pattern, observed from the casing, is $f_{s,k}/v$, or $n \cdot (kZ_r/v)$. With respect to
the runner, it rotates at a speed $f_{r,m}/v$, or $n \cdot (m \cdot Z_s/v)$. A detailed description of the
kinetics of such interactions may be found in H. Tanaka (1990, [2]).

For the influence of the guide vane on the runner, only the effects of the fundamental frequency $m = 1$ are normally observed [2].[1] In addition, only nodal diameter numbers ND between 0 and $Z_r/2$ are observed in runners with even blade numbers Z_r, and between 0 and $(Z_r-1)/1$ if Z_r is an odd number [3, 4].

Normally, the intensity of the exciting pressure pulsation decreases with increasing orders k and m of the harmonics. Low numbers v indicate simple mode shapes, with high speeds of mode rotation and low natural frequencies of the water passages. An experimental verification of this theory in a large pump-turbine has been published by Fisher et al. [5]. The natural frequencies of the structures are of the same order of magnitude as the exciting frequencies f_s and f_r, and, for that reason, proper consideration of rotor–stator interaction is essential for the design of mechanically safe machines.

3.2   Oscillation at Runner Frequency

Real hydraulic machines always deviate to some extent from the theoretical perfect symmetry of the runner and stator. Based on Eq. (3.3), the effects may be understood by formally replacing the blade number of the asymmetric component by 1. This represents a single pulsation on a once per revolution basis.

3.2.1   Unbalance of Runner

A hydraulic unbalance of a runner would be caused by an uneven partition of water in the blade flow channels. The most probable cause of such a situation would be blades that have been wrongly positioned during runner assembly. Modern designs, supplied by well established suppliers, are very unlikely to present such characteristics.

In very small turbines, hydraulic unbalance may sometimes be caused by foreign parts from upstream caught in a runner channel. In a reaction turbine, the result would be a pressure pulsation at runner frequency n in the water conduit and, at the same time, a significant increase of synchronous shaft vibration.

Some hydraulic unbalance of the runner also explains why the runner frequency appears in the pressure pulsations measured during model tests in the hydraulic laboratory. This disturbance has been much reduced due to modern manufacturing techniques, but may increase if a model runner is modified during testing.

Mechanical unbalance is not a very difficult issue in hydraulic machines. Due to their relatively low speed, recognized mechanical balancing requirements are based on static balancing ISO 1940/1 standard grade G6.3 [6]. Although technical

---

[1] For an exception, see the Francis example with $v = 0$ in chapter 3.3.1.

Fig. 3.2 Severely cracked
Francis runner
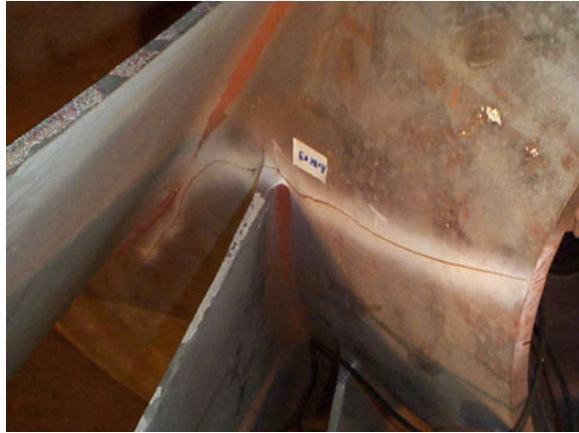
specifications may be more severe and even ask for dynamic balancing, there is no indication of adverse effects related to the mechanical unbalance of modern runners with the G6.3 grade.

Runners have been found to be very tolerant to unbalance caused by deteriorating mechanical condition. Frequent welding repairs for cavitation damage, for instance, are not known to significantly influence runner balance. In addition, severely cracked runners have been reported to show only slight mechanical vibrations. For instance, the runner presented in Fig. 3.2 had several major cracks such as the one shown, but was still in operation. The owner stopped the machine to have a look, because the unit 'displayed a bit more vibrations' than the other ones in the powerhouse. The example demonstrates that mechanical damages actually may be detected based on mechanical vibration properties, but may not show in the initial stage.

3.2.2 Asymmetry of Casing

The flow contour of spiral or semi-spiral casings, in particular those in older machines, is sometimes not well-designed and may not produce a symmetric in- or outflow for the runner. Seen from the runner, the asymmetric boundary condition translates to a periodical disturbance through which the runner rotates. The flow and pressure at a given region of the runner, for instance the exterior edge of every blade, is faced with an alternating load that may in extreme cases be high enough to cause fatigue problems.

Figure 3.3 is an example from a high-head pump-turbine. The diagram shows the pressure variation measured by a pressure transducer rotating with the impeller. The cross section at the narrow end of the scroll case was obviously too small, so that in pump mode the runner outflow was partly blocked in the area behind the nose vane. The peak–peak pressure variation seen by the runner was

Fig. 3.3 Fluctuation of pressure and strain observed at runner, pump operation
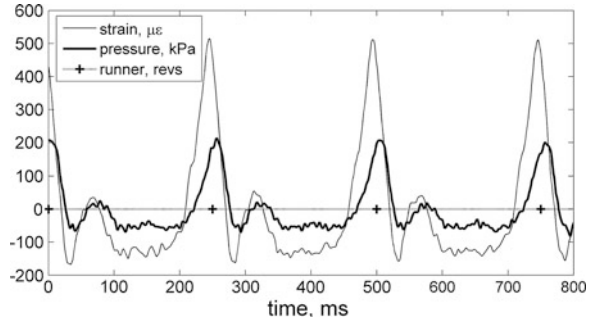

**Fig. 3.4** Strain gauge measurement performed on a Francis runner blade
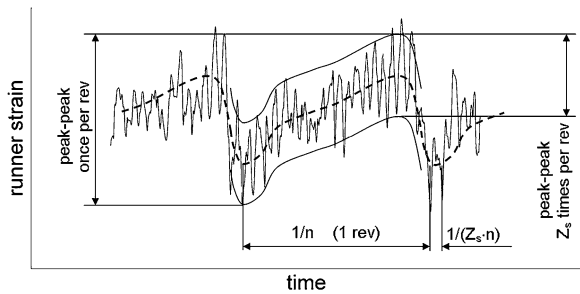
about 18 % of the pump head, much higher than the variation caused by the guide vanes. In a CFD study representing both the entire casing and the impeller [7], it was possible to reproduce these findings.

   As shown by this example, asymmetric flow in the spiral case due to inadequate spiral case design may have some effects on the mechanical behavior of the runner. This can also happen in turbine operation, also shown in Fig. 3.4, which presents the strain measurements performed on a runner blade in a different turbine. The dashed curve indicates the effect of the asymmetric inflow condition. Usually, this effect would not be noticeable. In the case shown in Fig. 3.4, however, fatigue analysis would have to account for this effect together with the effect of the Z_s guide vane wakes.

   An example with more drastic consequences has been observed when a unit in a remotely controlled powerhouse experienced the closure of four wicket gates due to shear pin failures. The unit was not equipped with protective devices to detect shear pin failure and operation continued. Due to the strongly unbalanced flow, the runner was pushed toward the low pressure side of the spiral case and strong contact with the bottom ring occurred at the runner band seal. At the end, the unit failed with major damages to the runner and the wicket gates requiring extensive repairs [8] An example of inhomogeneous inflow from a semi-spiral casing of a Kaplan turbine, refers to Sect. 8.5.

   Flow phenomena in the side chambers adjacent to the runner may also produce similar effects. Inhomogeneous pressure distribution around the circumference may result from secondary flow due to runner rotation. With such a boundary condition,

Fig. 3.5 Alternating runner blade stress due to runner band pressure
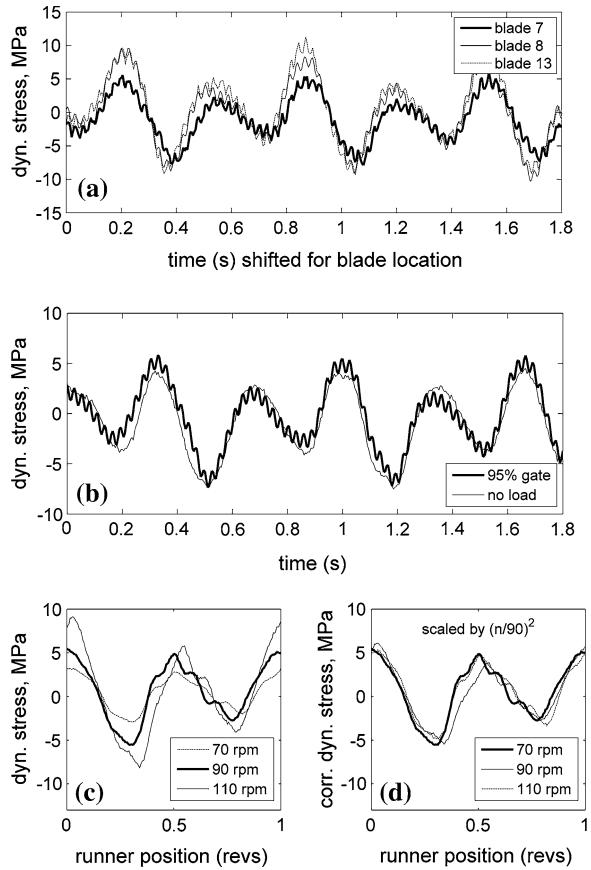
the runner may experience one or several external load cycles during each revolution. The resulting alternating stresses may suffice to produce cracks in highly loaded runners. For example, the low-head Francis turbines in a plant with a maximum head of 56 m frequently developed cracks in the hot spot with high stresses at the blade foot. On-board stress measurements revealed the quite unexpected origin of the problem. The case is also a good example for the kind of 'differential diagnosis' examining each possible cause of vibration that is often required to sort out the root cause of vibration problems.

Strain gages were mounted in the critical locations on several runner blades, and recordings of the stress variation under different conditions of operation were made. Figure 3.5 gives a survey of the main results.

It was found that alternating stress amounted to ±1,000 psi, or ±7 MPa as shown in parts (a) and (c).

In diagram (a), the time scale for the three blades numbered 7, 8, and 13 has been shifted to compensate for their different angular position. In such a representation, the three stress signals approximately collapse into one single function,

if the high-frequency portions are neglected. It became clear from this that there must be a stationary disturbance seen by every blade as to the runner it appears to travel around at runner speed. Looking for a stationary asymmetric load, the disturbance of runner inflow due to poor design of the nose vane region in the spiral casing would be the 'usual suspect.' This effect was, therefore, assumed to be the cause of the alternating load on the runner.

Given the results of the next comparison, diagram (b), this explanation becomes quite unlikely. The inhomogeneous pressure distribution in the runner inflow should certainly depend on the turbine load, as pressure differences scale with the square of the velocity, as is well known from the characteristic load-dependence of radial thrust. But in the case of this turbine, the variation of stress over one revolution was hardly different when full load compared with speed-no load. The small spikes superimposed on the full-load curve, corresponding to the disturbances from the 24 guide vanes, disappeared at no load. However, the two important low harmonics (1.5 Hz and 3 Hz) should respond much more to such a large variation of opening and discharge, but they remained almost the same. Inhomogeneous inflow from the spiral casing could, therefore, not be the reason of the alternating load.

The likely reason was finally clarified by comparing speed-no load tests at different speeds. During testing at 70, 90, and 110 rpm, the period of stress variation changed as expected among 0.85, 0.67, and 0.55 s, that is inversely proportional with the speed. Diagram (c) is, therefore, drawn using the runner revolutions as abscissa instead of time. The important result was, however, that the stress amplitude changed proportionally to the square of speed. If the alternating part of stress is scaled with a factor of $(n/90)^2$ for comparison, then the variation versus the turning angle becomes the same for all three speeds, as shown in diagram (d). According to this finding, the likely cause of the vibration was diagnosed as a secondary flow in the side chamber produced by the runner rotation. This disturbance fulfills all the observed aspects: it stands still in the stationary system, has runner frequency when seen from the runner, has the observed phase shift with regard to the runner blades, and increases with the square of speed.

3.3 Blade Interaction in Reaction Machines

3.3.1 Flow Phenomena Involved

The pressure distribution on the runner blades varies from one side of the blade channel to the other, the so-called pressure and suction sides of the blade, to produce the working torque of the machine. This pressure field rotates with the runner so that in a rotationally symmetric environment, a stationary observer would, therefore, see a periodic variation of pressure and velocity due to runner blade passage. In a turbo machine, the environment is not a rotationally symmetric
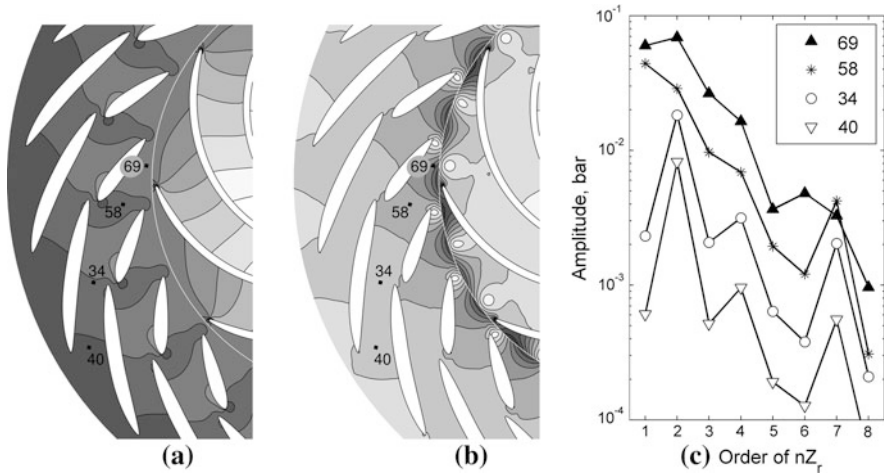
Fig. 3.6 Rotor-stator interaction in a pump-turbine, generating mode (**a**) Time-averaged static pressure (**b**) Pressure amplitude of $v = -2$ mode (**c**) Spectral components inside stator channel

one, but the likewise periodic contour of the stationary cascade (wicket gate, or diffuser vanes in a pump). This fact causes a periodic disturbance for the runner flow by the wicket gate, and vice versa. This is generally referred to as rotor–stator interaction, and may be interpreted as a periodic excitation for the two cascades; it also generates a wave train in every channel of the stationary and runner cascades. For the runner, the excitation follows the rules explained above in Sect. 3.1 above. Wave propagation around the spiral casing of a reaction machine may give rise to wave interference as described in Sect. 3.6. In addition to the dynamic load on the runner, the pulsation of head cover pressure, casing pressure, and guide vane torque has some influence and must be taken into account.

The highest amplitude of pressure variations occurs in the region of the gap between the stationary and rotary cascades; it decreases quite strongly with the distance from that area, as shown at the right-hand side of Fig. 3.6 for the locations numbered as shown on the left-hand side. This figure is based on data from the Hydrodyna joint research project [9]. The graph also shows the decrease of amplitude towards the high-order harmonics, except that in this case the harmonic $2 \cdot Z_r$, however, is almost as strong as the fundamental component; it plays an important role in the combination with the $Z_s = 20$ stator cascade.

With regard to the spatial rate of decay of the pulsation intensity, as a function of the blade spacing and of the order of harmonic order k, an interesting estimation formula may be found in [10]. In Chap. 2 of this reference, Greitzer et al. show that the decay distance of pressure pulsation upstream of a cascade is proportional to the spacing, and proportional to $1/k$. This implies that with increasing distance the harmonics $k > 1$ become more and more unimportant compared to the fundamental pulsation $k = 1$. In a free flow field, the axial variation of pressure amplitude would be approximately

$$\tilde{p}_k = b_k e^{(2\pi kx/W)} e^{(2\pi iky/W)} \tag{3.4}$$

wherein x and y are the axial and circumferential coordinates, and W is the blade spacing. According to this equation, the pressure amplitude should decay exponentially with the relative distance x/W, and in a distance of one half spacing from the cascade $(x = W/2)$, the fundamental component $k = 1$ should already be reduced by a factor of $e^\pi = 23.1$.

The generation of various modes of periodically oscillating load in the casing and runner has been described in a general form in Sect. 3.1. Depending on the number of nodal diameters, v, the interaction produces different kinds of effects.

A mode shape with $v = 0$ means that the whole circumference is excited with the same phase. For the runner, this means an oscillation of torque at the shaft with $k \cdot Z_r$ $(= m \cdot Z_s)$ times the frequency of rotation. If the inflow to the runner is not symmetric with regard to the guide vane centerline, then there is also a pulsation of axial thrust at the same frequency.

For Francis turbines, usually with $Z_r \geq 12$, this condition does normally not occur at low orders. An example would be $Z_r = 15$, $Z_s = 20$, producing vibration at a frequency of $60 \cdot n$. This frequency is much higher than the basic torsional and axial natural frequencies of the runner compound; on the other hand, mechanical resonance due to a natural frequency of the runner may occur. There are several examples for the occurrence of this high-order interaction, as described in the following section.

In Kaplan turbines, the wicket gate number is quite frequently an integer multiple of the runner blade number. A usual combination would be, for example, $Z_s = 20$ and $Z_r = 4$. In such a case, the interaction may already have a noticeable effect, in particular at high load when the runner blades come relatively close to the wakes of the guide vanes. It is possible to hit a circular (torsion or umbrella type) mode where all runner blades vibrate synchronously at frequency $20 \cdot n$, in case of resonance [11]. The same possibility is also present with five runner blades.

A mode shape with one nodal diameter $(|v| = 1)$ results in a non-zero rotating radial force and bending moment acting on the shaft line. This may occur, for instance, in case of a pump turbine with $Z_r = 7$ and $Z_s = 20$, a combination which is used quite often. The condition will be fulfilled at the 3rd harmonic of runner blade frequency

$$k \times Z_r - 1 = 3 \times 7 - 1 = 20 = m \times Z_s \tag{3.5}$$

In such machines, the order 20 may appear with a slightly increased peak in the spectra of bearing vibration or even shaft vibration [12]. The same may happen with $k = m = 1$ in a Francis turbine with $Z_r = 15$, $Z_s = 16$–but this combination is not to be recommended for other reasons, as will be shown in Sect. 3.6.

Mode shapes with higher numbers of diametrical nodes v, between 2 and 6, may also play an important role, in particular in high-head machines where the clearing between guide vanes and runner blades becomes small and the interaction more

intense. In such cases, the important issue is not torque oscillation or lateral vibration but runner safety [1, 2, 13, 14] as will be discussed in Sect. 3.3.2.

A blade passing phenomenon is also involved if the casing is not simply periodic with blade number Z_s but has some symmetry error; this would typically occur due to unfavorable design of the nose vane region. In such a case there is a condition analog to $Z_s = 1$.

A similar condition arises if some guide vanes are brought to an opening angle different from the rest of the wicket gate. This is deliberately done during start and synchronization in a small number of plants with Francis type pump turbines. Without this, some pump turbines exhibit hydraulic instability when operating in the speed-no load condition (see also Sects. 6.4.2 and 8.3.2). Setting a few guide vanes–usually 2–to a strongly increased opening angle has been shown to provide stable operation. This advantage comes with a side effect because the misaligned guide vanes create an intense flow disturbance interacting with the runner blades. An obvious choice would be open up two guide vanes separated by 180°. This means that a periodicity $Z_s = 2$ is created. Most pump turbine runners have an odd number of blades, for example $Z_r = 7$. In this case, the 3rd harmonic of the asynchronous vanes together with the fundamental blade passing excites the runner in the lateral direction with a single node diameter $v = k \times Z_r - m \times Z_s = 1 \times 7 - 3 \times 2 = 1$, and causes a lateral force oscillating at blade passing frequency $7n$ as well as a shaft vibration whirling at frequency $7n$ in the sense of runner rotation. This phenomenon may be avoided if a different relative location of the two guide vanes is chosen. If the runner blade number is even (typically, $Z_r = 6$), then this situation does not occur.

3.3.2 Mechanical Effects

Mechanical effects due to rotor–stator interaction (RSI) between runner blades and wicket gates have been known for many years on pump turbines where they may cause runner failures at the runner blade inlet [15] or structural vibrations [16]. Both the low number of blades and the disk-like shape of the crown and band of high-head machines contribute to the necessity of careful study of dynamic stresses in pump-turbine runners [2, 5, 17].

It is now known that, the risk of high dynamic stress due to RSI also exists in high-head Francis machines. In recent years, major issues have been reported where very high RSI amplitudes with a runner natural frequency very close to wicket gate excitation frequency caused major runner failure within hours of operation [14, 18].

Such damages, shown in Fig. 3.7, comprised long cracks starting at the runner blade near the junction with the hub (left picture) as well as along the band (right-hand side). Root cause analysis performed for this runner indicated some possibility of resonance between a runner vibration mode with $|v| = 5$ nodal diameters and the corresponding disturbance from RSI.

Fig. 3.7 Effects of RSI on a Francis runner
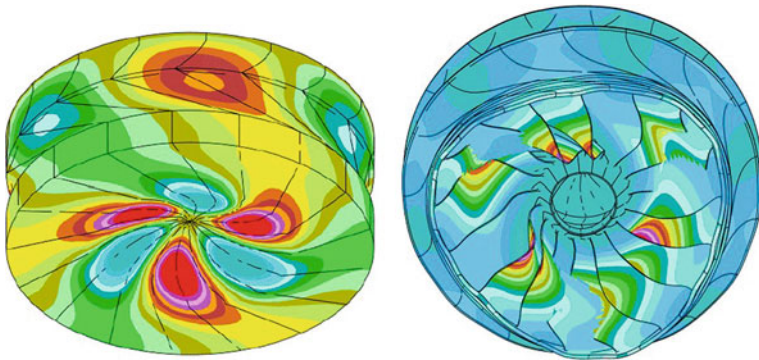
Fig. 3.8 Mode shape ND $= 3$ of water pressure (*left*) and runner displacement (*right*)

This mode results from the fundamental interaction $v = k{\cdot}Z_r - m{\cdot}Z_s = 1{\cdot}15 - 1{\cdot}20 = -5$ of the 15 blade runner with the 20 guide vanes. On-board strain gauge measurements at the runner confirmed the vibration frequency of $Z_s{\cdot}n$ with a phase shift of 120° among neighboring blades.

For a comparable situation but with 17 runner blades ($v = -3$), the distribution of unsteady pressure and runner deformations, simulated for a runner immersed in a cylindrical tank, is demonstrated in Fig. 3.8. For better clarity, the pressure pattern shown at the left-hand side concerns the walls of the tank, not the runner blades.

Resonance must be avoided between the possible modes of pressure excitation due to RSI and the corresponding vibration modes of the runner. The consequences of resonance are most severe if the interaction occurs at a low order of the runner harmonic k, as in the above-mentioned case.

Based on research in pump turbines with low specific speed, Tanaka [2] established specific criteria for the level of dynamic stress. Comparing various combinations of Z_s and Z_r, the maximum resonant stress level at the hot spot with
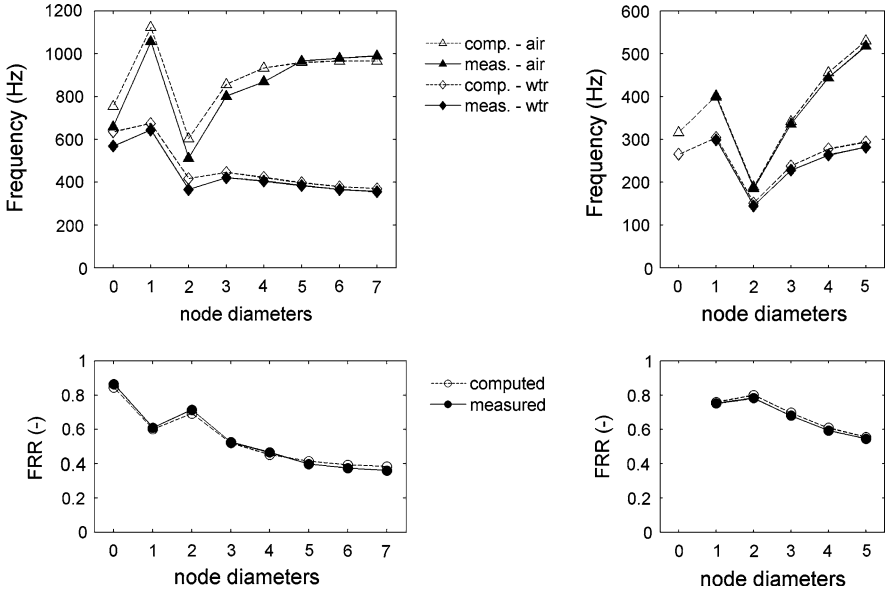
Fig. 3.9 Natural frequencies and frequency reduction ratio of Francis runners

maximum stress at the outward runner blade edges was examined. This occurred where neighboring blades were forced with a phase shift of π, while combinations with synchronous forcing at adjacent blades produced very low dynamic stress. Accordingly, the maximum dynamic stress level is estimated to be proportional to $\sin[(Z_s/Z_r)\pi]$.

The same reference explains how, for an even blade number Z_r, a counter-phase deflection mode of the runner shroud and crown with Z_r node radii is excited by a combined forcing mechanism with two successive runner harmonics k_1 and $k_2 = k_1 + 1$, with $k_1 Z_r \leq Z_s \leq k_2 Z_r$. The two interactions have v_1 and v_2 node diameters with $v_1 - v_2 = Z_r$, and propagate in opposite directions. Contributions from both interactions with equal amplitude A can be shown to add up to an interference pattern ΣX with Z_r node radii:

$$\Sigma X = X_1 + X_2 = A \times \sin(2\pi z_s nt + V_1 \times \varphi) + A \times \sin(2\pi z_s nt + V_2 \times \varphi) \tag{3.6}$$

$$\Sigma X = 2A \times \cos(Z_r \times \varphi/2) \times \sin[2\pi z_s nt + (V_1 + V_2) \times \varphi/2] \tag{3.7}$$

Due to the cosine term in Eq. (3.7), this function is zero for Z_r values of the peripheral angle φ on the runner. Among these Z_r node radii, the structure is forced by a modulated pressure wave with guide vane passing frequency $f_r = Z_s n$, with the peak 2A of this 'beat' traveling around the runner at the frequency $2f_r/(v_1 + v_2)$. Test results in [2] suggest that this concept also holds for odd blade numbers Z_r, despite the noninteger number of node diameters for Z_r node radii.

For combinations with relatively high common factor in the blade numbers, such as $Z_s = 20, Z_r = 15$, the mode shape $v = Z_r–Z_s$ is not the only factor to be taken into account. As already mentioned in Sect. 3.3.1, the rotationally symmetric mode $v = 0$ may also cause increased dynamic stress if the high frequency $n \cdot \text{lcm} (Z_s, Z_r)$ hits a suitable natural frequency of the runner. This condition corresponds to $v = 0$ by definition. In one particular case, cracks developed at the majority of runner blades within a few hours of operation. During a field test conducted for root cause analysis, it was found that the frequency $60 \cdot n$ could clearly be measured in the draft tube pressure—which is very uncommon. An analog observation about draft tube pressure has been made in a study performed by TVA [19, 20] at some turbines with $Z_s = 20, Z_r = 15$, and also with $Z_s = 24, Z_r = 16$ ($f = 48 \cdot n$).

Simulations of forced response computation of the runner structure under RSI, including realistic added-mass effect have now become state-of-the-art [4] due to spectacular advances in combined unsteady CFD with FEM. Good agreement between CFD computation results for dynamic pressures in the runner and measured data from on-board measurements in a model turbine can now be attained [21]. In addition, fluid–structure coupled computation of the natural frequencies of immersed structures may be made. These simulations have replaced the uncertain 'rules of thumb' factors for the added mass effect, and have revealed surprisingly large differences between the traditional estimates for frequency reduction factors and the real behavior. This is certainly one of the most important achievements of simulation techniques for hydropower engineering over the last few years.

With regard to Francis runners, it was shown that frequency reduction ratio

$$\text{FRR} = f_{n,\text{water}}/f_{n,\text{air}} \tag{3.8}$$

which strongly depends on the mode shape, as shown in Fig. 3.9, and can be predicted for the most important natural frequencies with an uncertainty of the order of $\pm 3\%$ [22].

3.3.3 Influence of Design, Countermeasures

The combination of blade numbers Z_r and Z_s has to be selected carefully. Depending on this combination, different mode shapes of vibration will occur. Inadequate blade number selection can lead to unwelcome pulsation, vibration, and noise. In some cases, the consequences may go as far as to necessitate replacement of the runner by another one with different blade number Z_r.

Resonance must be avoided between the possible modes of pressure excitation due to blade row interaction and the corresponding vibration modes of the runner. The consequences of resonance are most severe if the interaction occurs at a low order of the runner harmonic k, as in the above-mentioned case.

The options for troubleshooting in case of such a serious problem are rather limited. In order to keep the machine operating on a temporary basis, reinforcements

may be introduced. For instance, on the turbine described above, the response of the runner was provisionally corrected by applying struts among the downstream ends of the runner blades [14]. The increased local stiffness indeed curbed the resonance but the resulting flow obstruction could not qualify for a final solution. The runner had to be replaced by a newly designed one.

In some exceptional cases, it may be possible to correct the runner response sufficiently by altering the contour of the runner blades. This approach could work if the trailing edges of the runner blades form a lobe projecting between the runner hub and band. Such a shape may be chosen to obtain additional blade length and cavitation safety, but may not actually be necessary.

The radial clearance between the wicket gate (or diffuser vanes) and runner blade exterior edge has important influence on the disturbances created by RSI. This explains the particular importance of RSI in pump turbines and high-head Francis turbines. In nonregulated machines—storage pumps and multistage pump turbines–it may be possible to increase the radial gap between the runner and diffuser. For an example, see Sect. 3.6.2.

Some reduction of the intensity of interaction may be obtained by increasing the runner blade lean angle, as recommended in [23]. The impact of the runner pressure pulse with the stator is then distributed over a longer time interval as the rotor–stator blades are not exactly aligned. At the same time, the magnitude of the disturbance averaged across the height of the flow channel is reduced. The lean of the blade also has an influence on steady-state performance that has to be taken into account.

Other measures which also mitigate the so-called phase resonance effect are listed in Sect. 3.6 below.

3.3.4 Numerical Simulation

The interaction between guide vane wakes and the stagnation point at runner blade inlet can be well investigated by CFD [14, 21, 24, 25]. A typical CFD setup is shown in Fig. 3.10 for a pump-turbine simulation in turbine mode.

The maximum practical size of a hexahedral computational grid for such a 360° simulation is around 10 million nodes. The grid used for the computations in Fig. 3.11 and 3.6, of which Fig. 3.10 shows only a small portion of the grid for demonstration, has a total size of 2.5 million nodes. In order to limit the effort of computation, the computational domain often comprises sections only of the stator and the runner with periodic boundary conditions. The interface between guide vane region and runner region is modeled as a time-dependent sliding interface which allows the complete flow information to be transferred from the stationary to the rotating domain and vice versa without any circumferential averaging. A numerical simulation delivers both the time-dependent pressure field on the runner blades which are important for fatigue analysis but also the upstream wave propagation in case of inappropriate ratio of blade numbers.
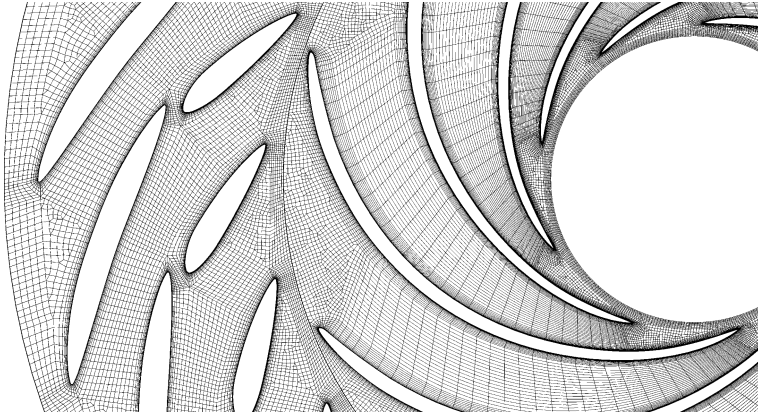
**Fig. 3.10** Computational grid of stay vanes, guide vanes and runner
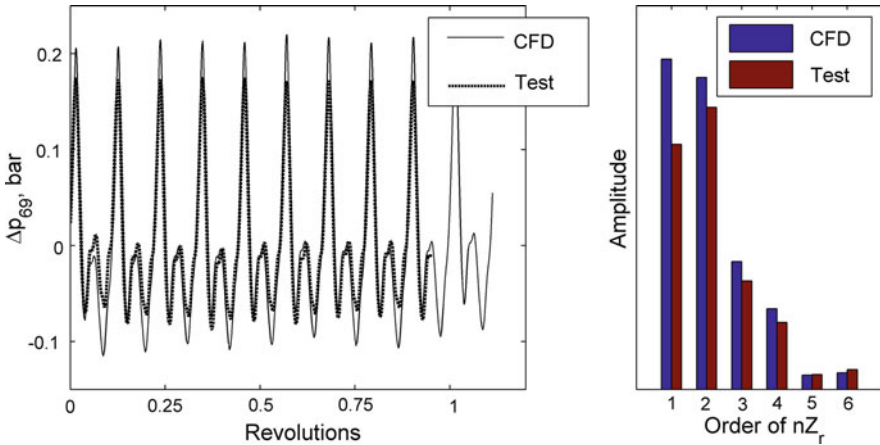
Fig. 3.11 Pressure variation at the wicket gate of a pump turbine **a** Pressure fluctuation **b** Spectral components

Comparison of the simulations with pressure measurements made among the guide vanes shows the good accuracy of the CFD methods and validates the approach. This is demonstrated in Fig. 3.11 using data from the Hydrodyna project. For a test point at high load in turbine mode, the fluctuation of static pressure at location 69 obtained by CFD simulation agrees very well with the corresponding model test result. The test condition and location are those represented in Fig. 3.6.

During the past few years, CFD simulations of the time-dependent pressure field between rotating and stationary blade rows have become the standard tool on which the forced response analysis of turbine runners is based. A more detailed

description of these developments and methods can be found in Sick et al. 2009 [26]. At the same time, comparable progress has also been made in multistage pumps for purposes other than hydropower [27].

3.4 Axial Machines

3.4.1 Wake Effects from Wicket Gates

In some Kaplan turbines with rather small guide vane pin circle diameter, relative to the runner diameter, the wake of the guide vanes at very large opening may noticeably interfere with the rotating flow field of the runner blades. The curvature of the meridional contour and also the guide vane shape has an influence. In some cases, the pressure drop due to the guide vane wake is sufficient to cause intermittent wall cavitation at every time a runner blade passes. For an illustration, see Fig. 5.5. The location of cavitation in this particular example is quite far downstream; in other cases, interaction occurred closer to the torus-shaped part of the discharge ring contour (see the case study in Sect. 8.5).

The effect of guide vane wakes on the pressure field in a Kaplan runner can be simulated in a similar way to the interaction of the pressure field in the runner of a pump turbine or Francis turbine, with the pressure field in the guide vane region. Due to the fact that the space between guide vanes and runner blades is far larger than in radial turbines, numerical dissipation has a stronger effect on the accuracy of the CFD prediction. To the authors' knowledge there are very few publications of serious and accurate CFD simulations of the effect of guide vane wake on the Kaplan runner [28]. Research on this topic is going on, as shown Fig. 3.12. The computational domain is represented in part (a). It consists of a 90° section of the wicket gate (blue colored) and a 90° section of the runner (red colored) with periodic boundary conditions, connected by a transient sliding interface which allows all unsteady effects to be simulated. As the focus of this numerical simulation lies on the flow features in the wake of the guide vane, the computational grid needs to be fine and of high quality in this region as shown in part (b) of the figure. At this opening angle, the guide vanes reach over the bottom ring (so-called overhanging guide vanes) thereby causing additional wake flow.

The streamlines in the guide vane wake are displayed in part (d) of Fig. 3.12. A distinct vortex develops from the bottom part of the guide vane with some pressure drop in the vortex core indicated by the color of the streamlines. Thus, the effect of the guide vane wake on the runner flow is two-fold: firstly, the flow angle is locally disturbed thereby causing local incidence in the tip region of the runner blade leading edge. Secondly, the static pressure field is disturbed by a local pressure drop in each wake. As the runner blade moves through the guide vane wakes the pressure at the blade tip briefly drops and then recovers. This leads to a moving pattern of spots of low pressure on the suction side of the runner blade in
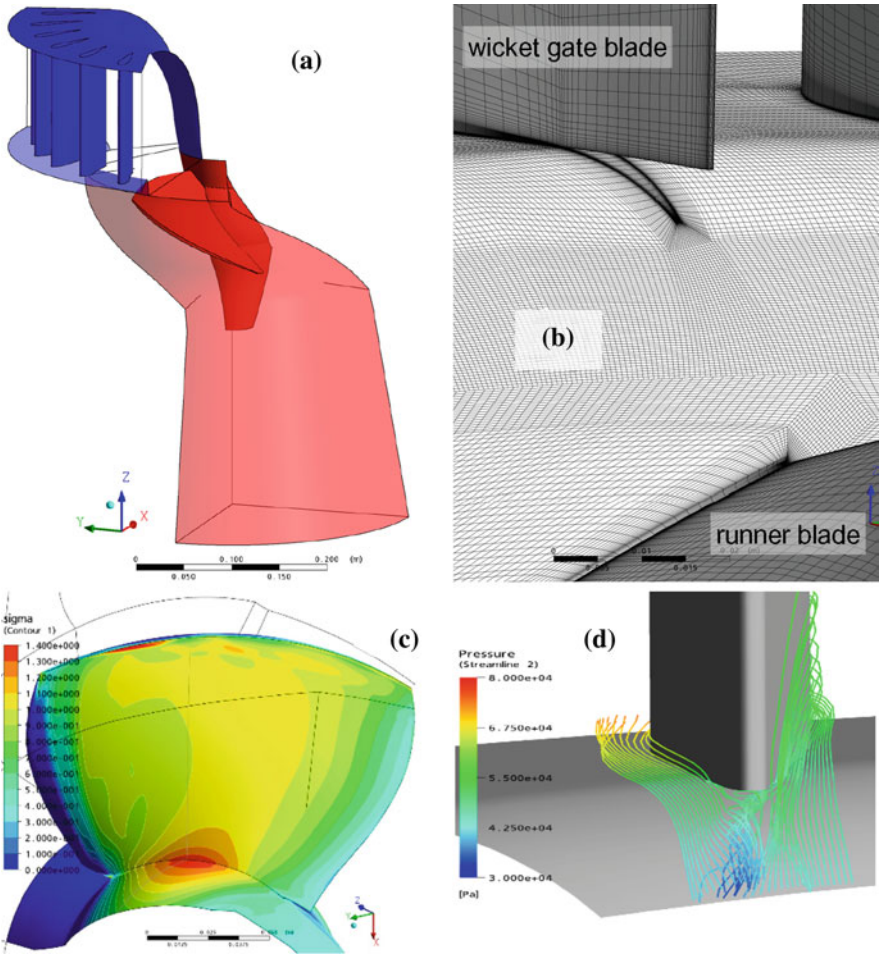
Fig. 3.12 CFD simulation of wake flow from Kaplan guide vanes

its tip area. Figure 3.12 part (c) shows a snapshot of the pressure distribution on the suction side of the runner blade near blade tip. Such spots of low pressure can be observed on the test rig as small clouds of cavitation moving along the blade tip. The fundamental frequency of the resulting pressure pulsation equals the number of guide vanes times rotational speed, $Z_s \cdot n$.

3.4.2 Excitation of Axial Vibration

Compared to their size, the distance between the stationary vanes and the blades of the runner in axial machines is larger than in radial machines. The risk of interference
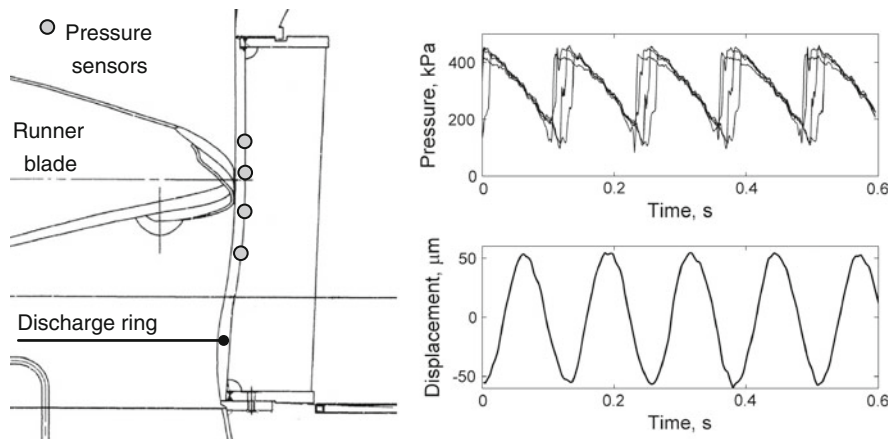
Fig. 3.13 Blade passing effect on Kaplan turbine discharge ring

is thus reduced, but not eliminated. The majority of Kaplan turbines have either four or five runner blades, and many turbines have 20 guide vanes. With these combinations, there is a possibility to excite an umbrella-shaped mode of the rotating parts with $v = 0$ nodal diameters according to Eq. (3.3). The fundamental frequency of this interaction is $Z_s \cdot n$, and this frequency may sometimes coincide with a natural frequency of the runner assembly or of the axial suspension of the rotating parts. In Kaplan turbines, the intensity of excitation increases towards high load, due to the adjustment of runner blade angle.

3.4.3 Runner Blade Passage on Axial Machine Discharge Ring

Each time a Kaplan or propeller blade passes a given location of the discharge ring, it creates a pressure fluctuation due to the difference of pressure between the pressure and suction sides of the blade. These pressure fluctuations create a dynamic radial displacement at the discharge ring which has to be taken into account during design. For a large vertical 5-blade Kaplan turbine, Fig. 3.13 shows a field test result for the periodic lateral displacement measured at the discharge ring, as well as a characteristic saw-tooth shape of the pressure variation acting at the wall. The four pressure signals are displaced in time according to their streamwise arrangement along the meridional contour.

The peak–peak pressure amplitude at the portion of the discharge ring close to the runner, as shown in the upper right graph of Fig. 3.13, and also in Fig. 3.14, is the same order of magnitude as the working head of the turbine.

This is quite unavoidable because the pressure difference across the blade provides the driving torque. Both upstream and downstream of the runner, the
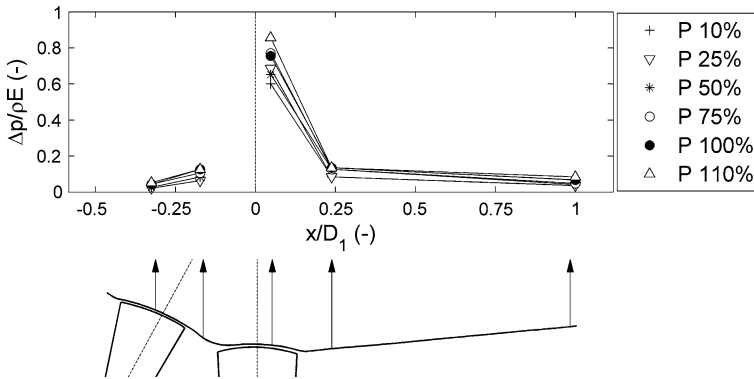
Fig. 3.14 Pressure amplitudes in a bulb turbine along meridional contour

amplitude decreases steeply with increasing distance. This strong variation of wall pressure amplitude in axial direction is demonstrated in Fig. 3.14. For an explanation of this rapid decay, refer to Eq. (3.4) mentioned earlier.

The data of this example have been measured in a Kaplan-type bulb turbine with four blades, rated 24 MW, at a head of 9.26 m. The influence of axial position on the amplitude exceeded the influence of load (i.e., runner blade opening). All amplitudes in Fig. 3.14 are from the same meridional contour (6 o'clock).

3.5 Bucket Passage in Pelton Turbines

3.5.1 Physical Background

The unsteady process taking place in the buckets of a Pelton runner fundamentally differs from the one in a reaction turbine as it is a highly unsteady free-surface flow. The circumferential speed of the bucket is approximately half of the water velocity in the jet. When a bucket enters the jet, it starts to cut out a section of the jet which is decelerated inside the bucket. A separate sheet of water is being cut out by a bucket from every jet, this travels along the bucket's surface and leaves at the bucket exit, to be replaced by water from the next jet. This implies that the resulting force on the bucket undergoes a much bigger relative variation compared to reaction turbines. Figure 3.15 illustrates the filling and emptying process in a bucket when passing through a jet, as determined from a CFD simulation.

In this sequence, the observer rotates with the bucket, and in this frame of reference the jet axis seems to travel around the bucket. Contact with the jet has just begun in the first picture; for a short while there is pressure on the back side of the bucket. In the second frame, the jet has partially filled the bucket, and the jet is not yet cut off by the next bucket. This happens in the next frame; part of the jet is still entering the bucket while some fluid is already leaving. In the last picture,
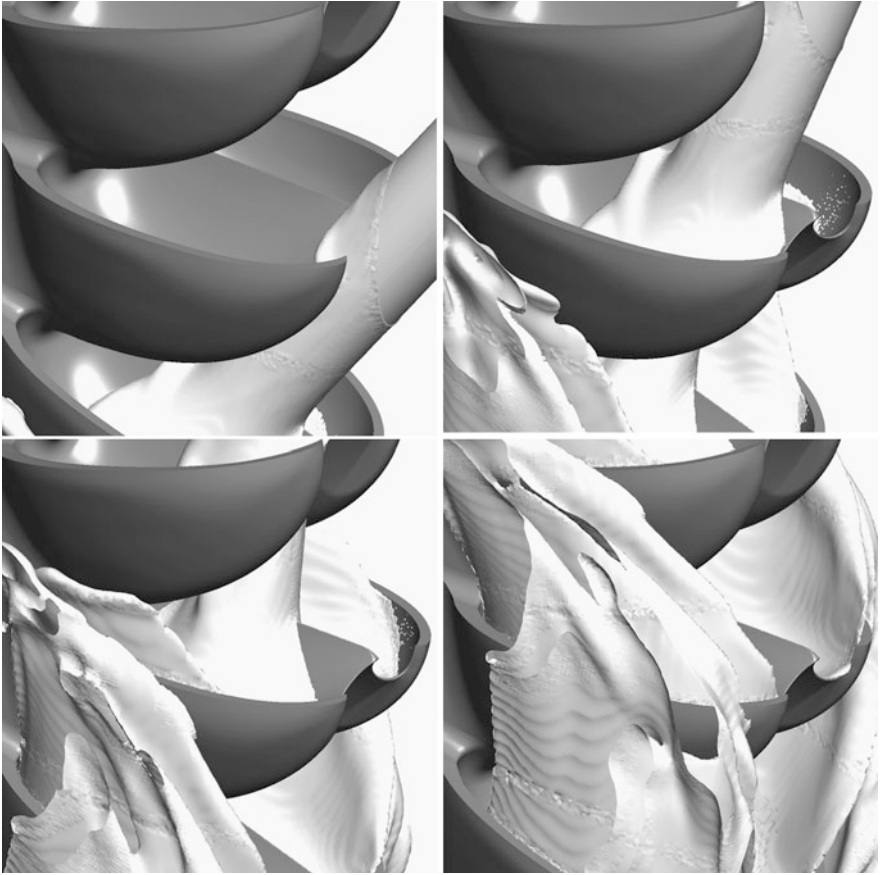
Fig. 3.15 Stages of jet impingement in a Pelton bucket

the inflow has stopped and most of the water is now leaving the bucket as a sheet. The sheets from the preceding buckets are also visible.

Seen from the bucket, the relative movement of the incoming water is reversed, thus transferring momentum from the jet to the runner. The transfer occurs by means of a temporary build up of water pressure on the surfaces of the bucket. The distribution of pressure is not only time dependent but also quite nonuniform across the bucket. Figure 3.17 displays a snapshot of the pressure field from the simulation during the period of maximum force. The maximum pressure can be recognized in the hollow of the bucket. The time dependency of pressure at various locations of the bucket surface is shown in Fig. 3.16. The static pressure is expressed as a dimensionless coefficient

$$C_p = (p - p_{\mathrm{atm}})/\rho E \tag{3.9}$$
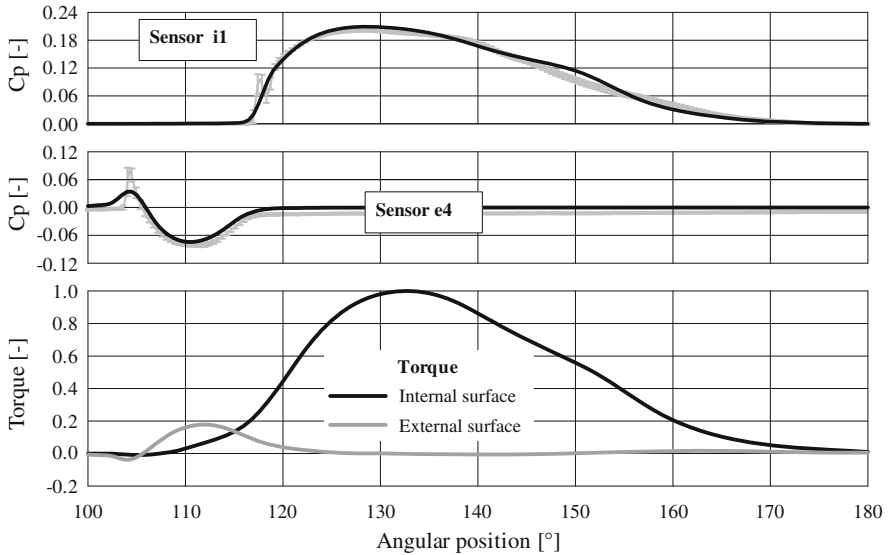
Fig. 3.16 Development of jet force from single interaction
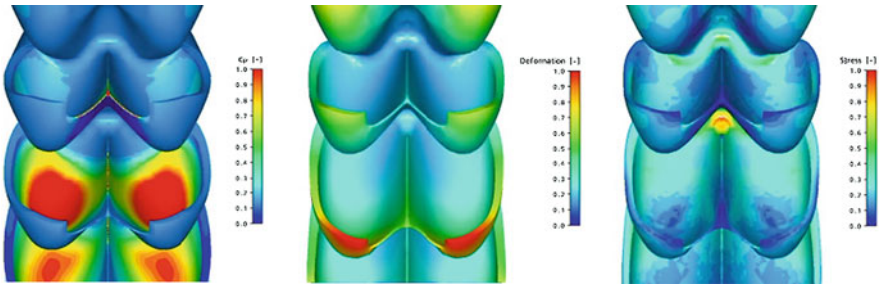
Fig. 3.17 Distribution of pressure (*left*), deformation (*middle*), and resulting stress (*right*)

In the beginning of the interaction, the jet contacts the back side of the bucket producing a small negative force. This can be seen from the trace of the simulated pressure signal at the location of sensor e4 as shown in Fig. 3.16. In accordance with the deceleration of the water jet, the maximum C_p values inside the bucket are typically around 0.2, see the pressure signal in sensor i1. The graphs for e4 and i1 also indicate the good agreement between the simulation result (black curves) and the measured data (grey curves).

The total force acting on the bucket and the corresponding contribution to shaft torque results from the integral of the pressure over the whole bucket surface. In the lower part of Fig. 3.16, the contributions of the inside and outside pressure distribution on the bucket to the torque are displayed separately for a single jet impact.
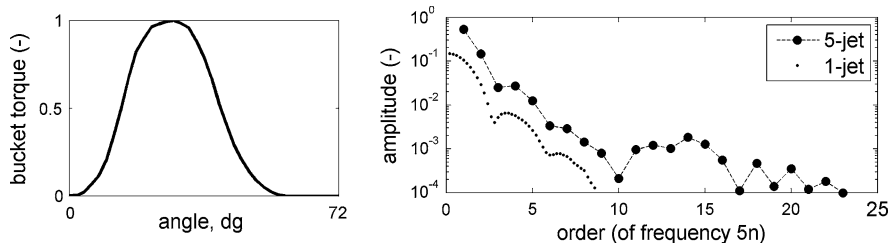
**Fig. 3.18** Jet force acting on a bucket—time and frequency domain

3.5.2 Mechanical Effects

During jet impact, the bucket is loaded with a time-dependent pressure distribution as shown in the left-hand side of Fig. 3.18. Applying this pressure distribution to the FEM model of the bucket yields the deflection shape in the middle of the same figure, and the instantaneous stress distribution (right-hand side). Typically, there is a hot spot of high stress in the root region of the bucket.

The interaction between jet and the moving bucket leads to a short transient pulse of force. The shape of this impact is reflected by the transient torque displayed in Fig. 3.18, left-hand side [29]. A near-periodic jet force acting on each bucket of the runner results from the sequence of interactions with the active jets. The spectrum of this force contains many harmonics, with gradually decreasing intensity. For a 5-jet turbine, this spectrum is shown in Fig. 3.18, right-hand side, for both single-jet and 5-jet operations. The fundamental frequencies are the frequency of runner rotation n in case of single-jet operation, and $n \cdot z_0$ in case of operation with all $z_0 = 5$ jets.

For corresponding frequencies, the amplitudes in case of operation with all z_0 jets are z_0 times larger than in case of single-jet operation. In both cases, the maximum amplitude occurs at the fundamental frequency. As the jet force varies rather smoothly with angle, i.e., close to a sine curve, the amplitudes decrease rapidly with the order of the harmonics. Accordingly, the force amplitude of high harmonics is about three orders of magnitude less than for the fundamental frequency. Nevertheless, high harmonics may play an important role in the actual dynamic stresses. This is because the natural oscillations of the runner/bucket assembly have a very low degree of damping. From vibration observation damping values of $\zeta = 0.05$ % could be deduced. As the maximum amplification of a resonant oscillation equals $1/2\zeta$ the drop in the force amplitude may be compensated by this dynamic gain in case of resonance. For this reason, the dynamic stress in the critical root area of the bucket shown in Figure 3.19 has, superimposed on the lowest harmonics of jet frequency $\Delta\sigma_J$, a high-frequency component $\Delta\sigma_B$ that is not negligible with regard to fatigue analysis.
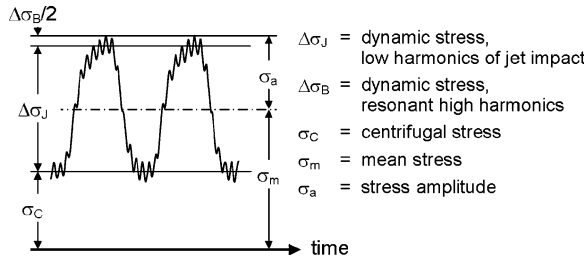
Fig. 3.19 Time history of stress in the root zone of a Pelton bucket

**(a)**   **(b)**   **(c)**
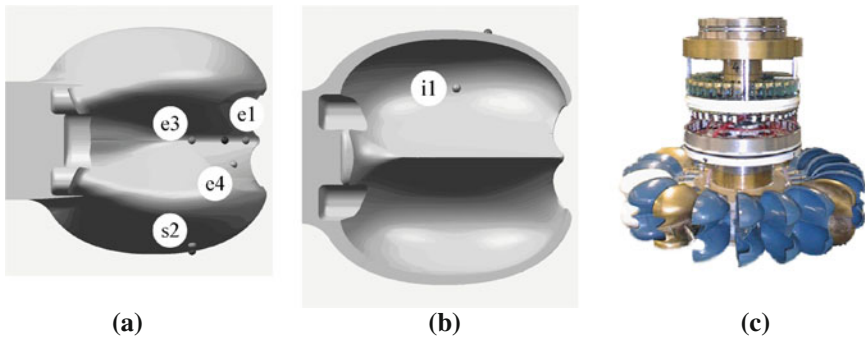
Fig. 3.20 Pressure sensor locations (*left*) in dynamic test model (*right*) **a** back side **b** inner side **c** instrumented shaft

In some cases, there are only narrow windows of 'acceptable' natural frequency bands of the Pelton buckets among the frequency bands of those harmonics which are relevant for resonance, and therefore to be excluded. Despite the use of modern and accurate methods of runner fabrication, the actual natural frequencies always have some degree of variation which creates an important risk of resonance for some of the buckets. A technology of 'detuning' has been developed that comprises selective machining of certain buckets of a runner in order to correct the natural frequencies and remove the risk of resonance. This is explained in detail, for a Pelton turbine with very high head, by Angehrn et al. in [29].

The transient water sheet in the buckets has been found to influence the natural frequencies of the runner due to the added mass effect. This influence is small but cannot be neglected, because the frequency window among relevant harmonics may be very small, and the added mass effect may jeopardize the detuning.

With regard to overall vibration of a Pelton unit, in particular the bearing vibrations which are subject to guarantee, the fundamental frequency of bucket passage is most important. The vibration behavior with regard to this frequency is discussed in Sect. 3.5.4 below.
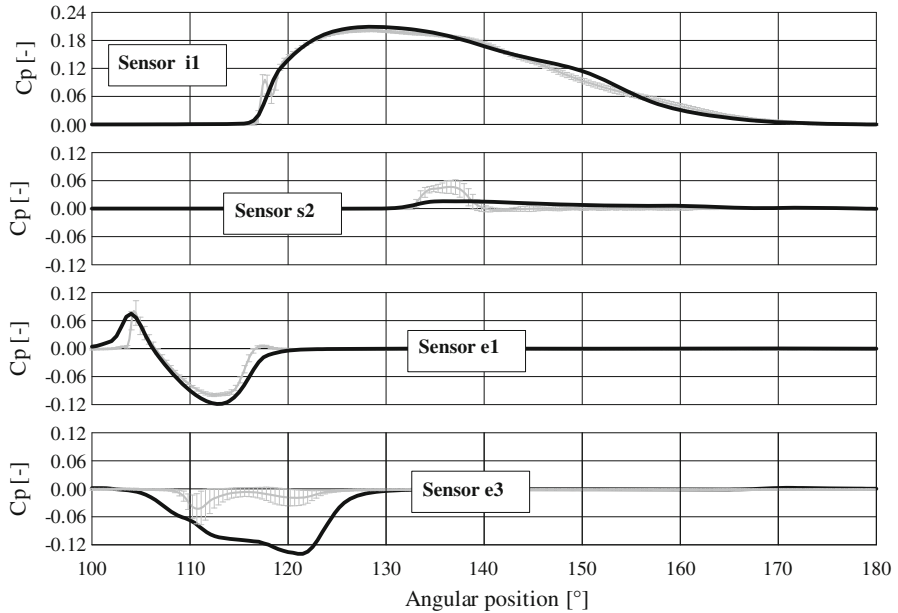
Fig. 3.21 Simulated versus measured local pressures (see also Figure 3.16)

3.5.3 Numerical Simulation of Jet Impact

Until a few years ago, the unsteady free-surface flow passing the Pelton buckets posed insurmountable problems to the numerical handling of the phenomena involved. In the meantime, numerical simulation of the unsteady flow phenomena has become possible due to advanced CFD simulations. Based on the computed variations of the pressure distribution in the bucket, the dynamic stresses are now also amenable to computation [30].

Thorough validation of the hydraulic results has been achieved in a number of cases [30–32], showing that the numerical computation of the process yields reliable results. An example is given in Fig. 3.16 and 3.21.

A reduced-scale model of a 6-jet turbine with rather low head, and consequently large bucket size, was equipped with pressure sensors measuring the surface pressure at various points of interest on either side of the bucket. These locations, and the model turbine, are shown in Fig. 3.20.

Figure 3.21 shows the comparison between the measurement data of the time-dependent pressure in these locations and the CFD prediction [30]. For the purpose of static and dynamic stress analysis, the accuracy of computations is already satisfactory.

Small local effects of flow detachment both on the inner and outer surface of the Pelton bucket which may cause small disturbances in the load as well as cavitation are still a challenge. This can be seen, for example, in pressure signal e3 on the

outer bucket surface. Here, the considerable deviation between measurement data and numerical prediction would not allow a reliable hydraulic optimization to be done. Still, despite the fact that CFD simulations are not yet revealing all flow details on the Pelton bucket with sufficient accuracy, the CFD prediction of time-dependent pressure distribution in the rotating bucket has been proven to be a reliable and a valuable precondition for the lifetime assessment of Pelton runners by strain gage measurements on several prototype runners. The measurement data were compared to the FEA prediction of mechanical stress based on CFD predicted pressure distribution. In all cases, the agreement between numerical simulation and measured values was excellent.

Currently, there are still some uncertainties regarding the prediction of the natural frequencies of the Pelton runner. Firstly, the added mass effect of water on the natural frequencies of Pelton runners; and secondly, slight inaccuracies of the runner geometry due to manufacturing may lead to some deviation between numerical prediction of natural frequencies and their real values. Nevertheless, the numerical methods of CFD and FEA have become an essential tool in the design of Pelton runners withstanding the enormous dynamic excitation by jet–bucket interaction.

### 3.5.4 Influence of Design Parameters

From a mathematical point of view, the same kind of interference phenomena described in the earlier chapters is also present in Pelton turbines. The major difference in the case of Pelton turbines is the fact that Pelton turbines have a significantly lower number of 'stator vanes', i.e., nozzles, corresponding to a higher concentration of the impact. Furthermore, in case of 2-jet or 3-jet Pelton units the jets are usually not equally distributed over the circumference of the runner. This creates a variety of possible interference patterns.

The following examples are focused on the fundamental frequency of blade passage. To assess the excitation of lateral and torsional vibration occurring at this frequency, the jet force variation can be assumed to act in the direction of the jet axis. The resulting force on the runner is computed considering the jet impact of all active nozzles. In a graphical representation of the vector of the resulting force, the vector tip describes an elliptical curve whereby the shape and size of this curve depend on the number of buckets Z_r, the number of nozzles Z_s and the angular position of the nozzles.

We assume equal angular spacing $2\pi/Z_r$ of the buckets and use the inclination angle $\beta(i)$ for the direction of jet (i) in a plane perpendicular to the runner axis, as shown in Fig. 3.22. The pulsating force produced by each individual jet may, then, be expressed by its components:

$$\begin{aligned} f_x(i) &= f(i) \cdot \cos(Z_r \cdot (\Omega \cdot t + \beta(i))) \cdot \cos\beta(i) \\ f_y(i) &= f(i) \cdot \cos(Z_r \cdot (\Omega \cdot t + \beta(i))) \cdot \sin\beta(i) \end{aligned} \tag{3.10}$$

Fig. 3.22 Definition of jet
location in a 2-jet Pelton
turbine
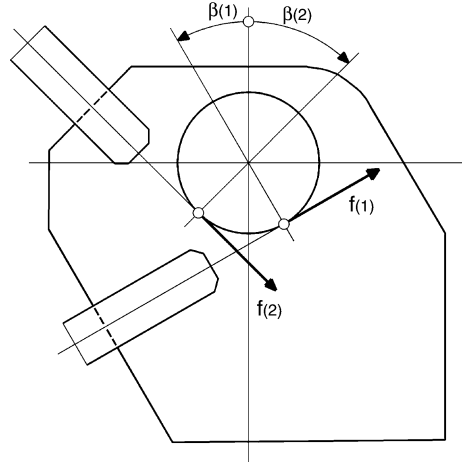
where $Z_r \cdot \Omega = 2\pi n Z_r$ is the angular frequency of bucket passage, and $f(i)$ indicates the amplitude of the single jet force at this frequency. To obtain the total lateral force, it is convenient to express the phase of the components by vectors in the complex plane, at time zero:

$$
\begin{aligned}
F_{0x} &= \sum_{i=1}^{Zs} f(i) \cdot \cos \beta(i) \cdot \exp(j\beta(i)Z_r) \\
F_{0y} &= \sum_{i=1}^{Zs} f(i) \cdot \sin \beta(i) \cdot \exp(j\beta(i)Z_r)
\end{aligned}
\tag{3.11}
$$

Multiplication with the phase vector $\exp(jZ_r\Omega t)$ yields the time dependency of the x and y components of the total lateral force as the real part of the product:

$$
\begin{aligned}
F_x(t) &= \cos(Z_r\Omega t) \times \mathrm{Re}(F_{0x}) - \sin(Z_r\Omega t) \times \mathrm{Im}(F_{0x}) \\
F_y(t) &= \cos(Z_r\Omega t) \times \mathrm{Re}(F_{0y}) - \sin(Z_r\Omega t) \times \mathrm{Im}(F_{0y})
\end{aligned}
\tag{3.12}
$$

The total fluctuation of shaft torque is derived by using the same definitions as before and R for the radius of jet attack. Then, the amplitude is:

$$
\begin{aligned}
T &= R \cdot \left| \sum_{i=1}^{Zs} f(i) \cdot \exp(j\beta(i)Z_r)) \right| = \\
&= R \cdot \sqrt{\left(\sum_{i=1}^{Zs} f(i) \cdot \cos(Z_r\beta(i)) \right)^2 + \left(\sum_{i=1}^{Zs} f(i) \cdot \sin(Z_r\beta(i)) \right)^2}
\end{aligned}
\tag{3.13}
$$

In the first example, a 2-jet turbine with horizontal axis will be considered. The inclination β of the nozzle axes, according to the schematic in Fig. 3.22, is 30° and –35° against horizontal, respectively. The orbit of the pulsating component of the runner force has been computed for runners with a bucket number between 18 and 26. In order to assess the runner force, it is convenient to express its
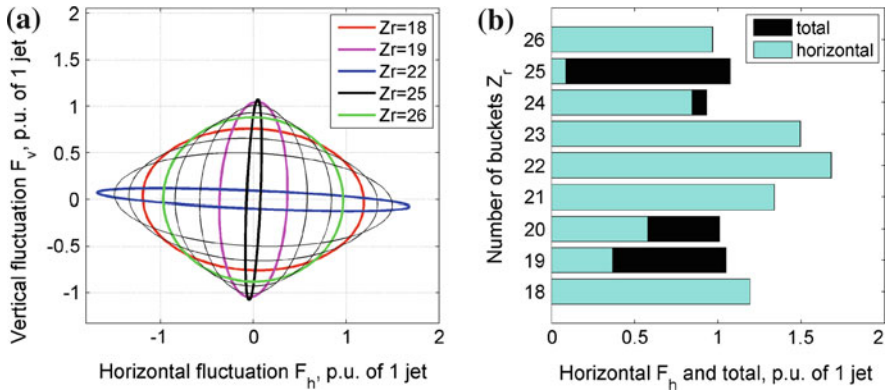
Fig. 3.23 Variation of lateral force in 2-jet Pelton turbine **a** Radial force orbits at bucket frequency **b** Total and horizontal amplitude

magnitude as a multiple of the amplitude for a single jet, setting $f(1) = f(2) = 1$ in Eq. (3.13).

The trajectories of the force are shown in Fig. 3.23 with their correct inclination. As the bearing stiffness of a machine with horizontal axis is normally smaller in the horizontal direction than in the vertical direction, a high amplitude of force in the horizontal direction may produce large vibrations. The figure indicates that a runner with 19 or 25 buckets will produce only small horizontal vibrations when operating with both jets, while for a runner with 18 or 22 buckets one may expect a higher level of horizontal vibration. It is worth noting that consecutive numbers of buckets Z_r do not correspond to consecutive shapes of the orbit. For example, the 19-bucket runner would behave rather like the 25-bucket runner, than the 18-bucket runner. It should also be noted that the result is sensitive to the difference between the inclination angles, $\beta_2 - \beta_1$.

The case of multi-jet turbines is more complex, because the number of jets in operation needs to be taken into account as an additional parameter. Results for 5-jet and 6-jet turbines are shown in the Figs. 3.24 and 3.25, respectively. These diagrams show the relative amplitudes of shaft torque (left-hand side) and of the resulting lateral force (right-hand side) at bucket frequency $n \cdot Z_r$, with the amplitude for single-jet operation as reference.

Runners with 20 or 25 buckets experience synchronous jet impact at all nozzles in a 5-jet turbine; hence, they would fulfill the condition for $v = 0$ nodal diameters. Accordingly, they would cumulate the torque oscillation from all nozzles. These blade numbers should, therefore, be avoided, which is the same for 18 or 24 buckets in the case of 6-jet turbine. Bucket numbers resulting in $|v| = 1$ and $|v| = 2$ nodal diameters avoid this condition. When a choice between $|v| = 1$ and $|v| = 2$ is possible, the latter may be preferred, because it results in a smaller lateral force at bucket frequency.

Usually, in normal operation, the fluctuation of torque does not lead to torsion resonance of the shaft and runner, because the bucket passing frequency is much
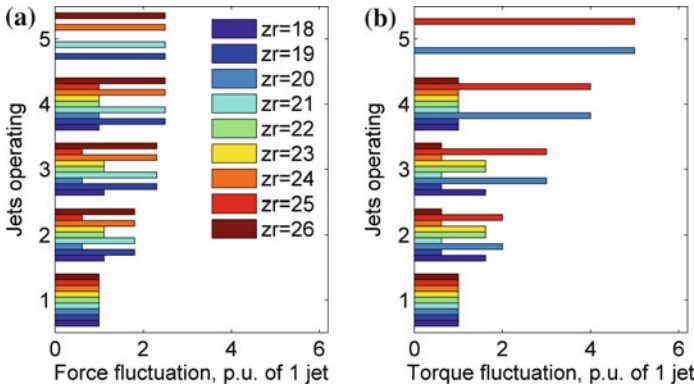
Fig. 3.24 Jet force pulsation versus bucket number, 5-jet turbine **a** Amplitude of force **b** Amplitude of torque
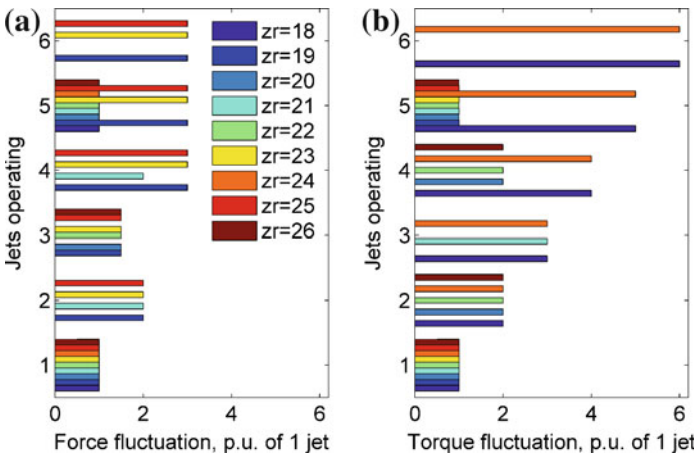
Fig. 3.25 Jet force pulsation versus bucket number, 6-jet turbine **a** Amplitude of force **b** Amplitude of torque

higher than the respective natural frequencies. During startup, however, transient resonances are possible and should not be neglected.

The periodic jet force is capable of exciting torsional vibration, if not compensated by a particular combination of nozzles. The system subject to this excitation consists of generator rotor, shaft, and turbine wheel. The natural angular frequency ω_n [rad/s] of this simple system is:

$$\omega_n = \sqrt{C/I} \tag{3.14}$$

where C [Nm/rad] is the torsional stiffness of the shaft and I [kg·m²] is the effective moment of inertia. Let I_T denotes the inertia of the turbine wheel without
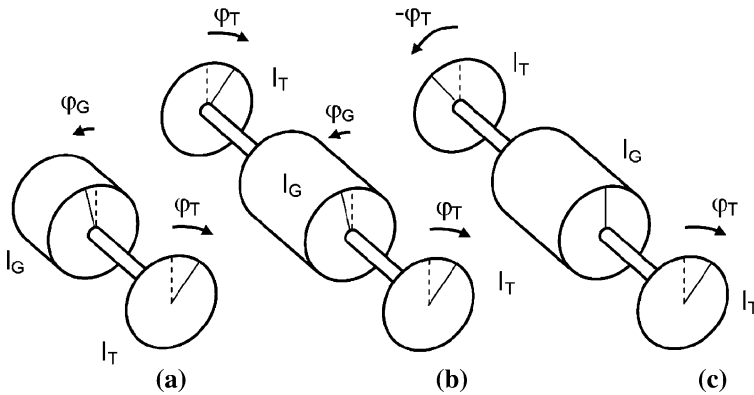
Fig. 3.26 Torsion modes of sets with 1 or 2 wheels **a** single wheel **b** 2 wheels, fast mode **c** 2 wheels, slow mode

the shaft, and I_G for the rest of the rotating masses including the shaft. For the unit with a single Pelton wheel, an estimate for the effective moment of inertia is:

$$I = I_T/(1 - I_T/I_G) \tag{3.15}$$

Many horizontal Pelton units have two wheels; in such a case, there are two natural frequencies of torsion whose ratio depends on the ratio I_T/I_G. If the set is symmetric, then the two natural frequencies are easily derived from the single-wheel case. For the slower mode, I in Eq. (3.1) is equal to I_T, and the torsional oscillation is in counter phase between the two turbine wheels, and zero for the generator, as in Fig. 3.26c.

For the other mode, the effective moment of inertia is $I_T/(1–I_T/I_G)$. The two turbine wheels oscillate in phase with each other, and in counter phase to the generator rotor, as shown in Fig. 3.26b.

Resonance between the bucket passing frequency and these torsion modes would not be acceptable at synchronous speed, but normally the bucket passing frequency is much higher than the natural frequency. However, resonance occurs temporarily during start-up of the unit. During this transient resonance, an oscillation of shaft torque may build up with considerable amplitude, which has to be kept within safe limits. Dynamic overloading due to this mechanism of resonance puts the safety of the runner shaft or coupling at risk if it is not recognized in time.

For simple conditions (single wheel, single jet) the main parameter influencing this risk is the nozzle opening during start up. There are two counteracting effects on the maximum amplitude of torque. With increasing opening, the time for build up of resonance becomes shorter, thus reducing the transient dynamic gain. On the other hand, it means higher jet force and therefore higher amplitude of the exciting torque. The maximum amplitude of the shaft torque is the product of the two influences. As shown below, the influence of the exciting amplitude is dominant, resulting in a limit for possible acceleration in the speed range of resonance. By
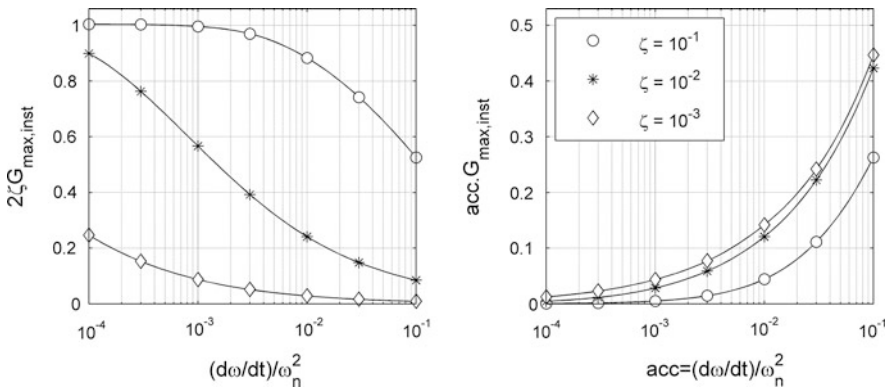
Fig. 3.27 Amplification in a transient resonance

Fig. 3.28 Transient
resonance of a single-degree-
of-freedom oscillator
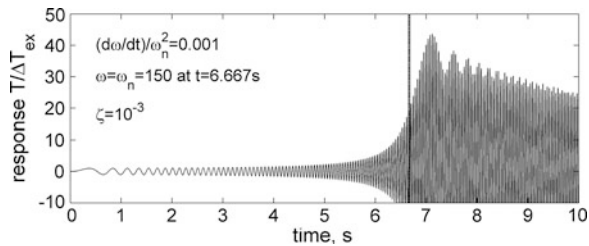
choosing a suitable opening law for the nozzle during start up, it should still be
possible to keep the total run-up time acceptably short.

The first effect is represented in the left-hand graph of Fig. 3.27, the X-axis is a
dimensionless measure for acceleration, the Y-axis is the maximum attained
amplitude as a fraction of the resonance amplitude in case of excitation at constant
frequency. For low damping ratio ζ the resonance gain becomes much smaller than
the stationary gain $1/2\zeta$. The right-hand graph considers also the second effect, i.e.,
the higher excitation level linked to the faster acceleration. This graph shows the
true influence of both accelerating torque and damping.

Figure 3.28 displays the development of the torque oscillation for a single-wheel
unit. The maximum amplitude occurs when the forcing frequency is already larger
than the natural frequency ω_n. The low damping ratio may be seen only from the
slow decay of the oscillation. Evaluation of field tests showed damping ratios in the
range 0.05–0.1 %; in this range the transient gain is already independent of ζ. The
beat comes from the difference between forcing and natural frequency.

In case of units with two wheels, the torsion resonance may have a more
pronounced beat, because the two modes have similar frequency and damping. If
the wheels have equal numbers of buckets, then there is some slight influence of
the relative angular spacing among the runners. The faster mode is more prone to

be excited if the runners are mounted without angular offset, the slower one, with slightly higher amplitude, if they are offset by a half bucket spacing.

3.6 Pressure Wave Interference in the Spiral Casing

In reaction turbines and pumps, pressure waves caused by blade row interactions propagate through the wicket gate and stay vanes into the spiral casing. These waves starting at every single guide vane channel interfere with each other in the spiral conduit.

This process of superposition is governed by laws, which are different from the direct impact on the runner, because the propagation of waves along the spiral duct at finite wave speed is involved. While there is a clear-cut condition for the existence of excitation of a given mode shape in direct interaction [2], a continuous range of degrees of interference exists for the spiral case interference.

Starting from early work by Den Hartog [33], the physical mechanism has been described by Y.N. Chen in [34] by the following assumptions:

A1 Pressure waves of equal intensity are generated at every stator channel. The timing of these interactions is defined by the blade numbers Z_s and Z_r, and by the angular velocity of the runner
A2 Pressure waves entering the spiral casing from every stationary blade channel propagate along the spiral duct, in either direction, at wave velocity a
A3 The effects of spiral taper are neglected, i.e., the volute is treated as a uniform pipe
A4 Reflection of waves at the spiral exit is neglected
A5 Reflection of waves at the narrow end of the spiral duct is neglected
A6 No effect of attenuation of waves is considered. This assumption corresponds to modeling the source of pulsation by volume-type sources, and neglecting friction effects

Under these assumptions, the superposition of waves from all Z_s stationary channels for the kth harmonic of the blade passing frequency $Z_r \cdot n$ results in a gain [35]:

$$\frac{P_k}{p_k} = \frac{\sin(k\pi(1 \pm D_{sp}\pi n/a)Z_r)}{\sin(k\pi(1 \pm D_{sp}\pi n/a)Z_r/Z_s)} \tag{3.16}$$

where P_k is the amplitude of the resulting wave of frequency $k \cdot Z_r \cdot n$ at the (inner or outer) end of the scroll case and p_k is the amplitude of the individual waves created at the Z_s stationary channels. D_{sp} is the diameter of the circumferential flow path in the simplified spiral duct, and a is the wave propagation velocity. As usual, n is the frequency of runner rotation.

The positive signs in Eq. (3.16) apply for waves traveling against the sense of rotation. In turbine rotation, it holds for the waves traveling toward the penstock, and in pump rotation for the waves traveling to the narrowest section of the scroll

Fig. 3.29 Distribution of the phase resonance risk factor
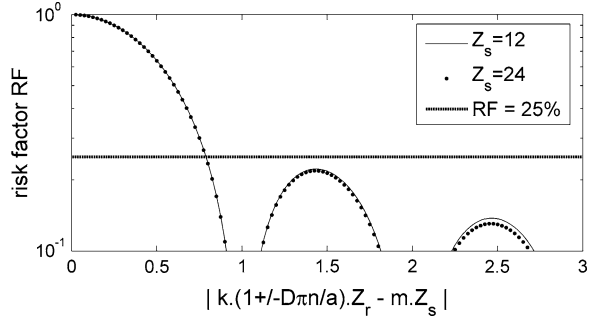
case. The opposite direction is described by the negative signs. The magnitude of the gain function Eq. (3.16) can be any value between 0 and Z_s.

Equation (3.16) is a useful quantitative model for the risk of phase resonance. As an empirical rule, the risk factor [36]

$$RF = (P_k/p_k)/Z_s \qquad (3.17)$$

should not exceed 25 % in order to avoid such problems. This definition restricts the problem to the 'main lobe' of interference as shown in [36], see Fig. 3.29.

It is recommended that the sensitivity of the phase resonance risk factor RF to the wave velocity a in the spiral casing be checked because its value is uncertain. As the wave velocity appears only in the expression n/a, sensitivity to errors in wave speed a becomes visible if the rotational speed is varied relative to the nominal value, see Fig. 3.30 which shows the risk factor for the first three harmonics ($k = 1, 2, 3$) over the relative speed $(n/n_{syn})/(a/a_{theor})$, with a_{theor} being the estimated or computed wave velocity in the spiral casing.

The example shown in Fig. 3.30 is based on a medium-head pump turbine with nine impeller blades and 20 guide vanes which is a common combination. The circumferential Mach number is estimated to be $M = D_{sp}\pi n/a = 0.118$, the diagram shows a significant risk for the second harmonic which corresponds to a mode $v = 2$, with the disturbance mode rotating against the runner rotation. Increased vibration has been found in some plants due to this mode, [16] and [13]. For the blade passing frequency ($k = 1$) the waves in the scroll case almost cancel out.

The intensity of harmonics in the pressure and force fluctuations decreases strongly with the order k. Therefore, the first priority is to avoid phase resonance at the fundamental frequency $Z_r \cdot n$, i.e., $k = 1$ in Eq. (3.16). In case of a Francis turbine with 17 runner blades and 18 guide vanes, for instance, there is a considerable risk for increased vibration and noise in the penstock [33, 37], in particular if the penstock is above ground. The same holds for 15 runner blades and 16 guide vanes.

For the second harmonic $k = 2$ problems are less frequent, however, in pump turbines and storage pumps, serious trouble has been reported in a number of cases. All the factors contributing to intense vibration are small radial clearance
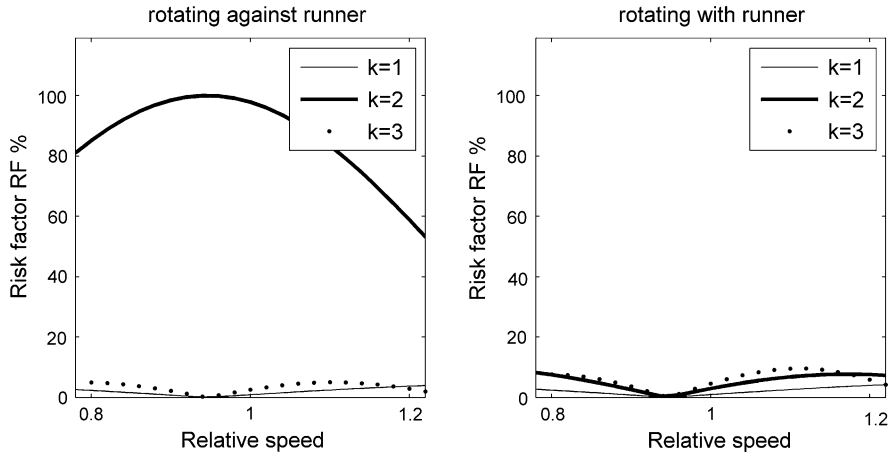
Fig. 3.30 Sensitivity of phase resonance risk to runner speed or wave velocity

among the cascades, in particular between the impeller blade tips and the diffuser vanes of a pump, and a relatively small number of runner blades.

Despite the strongly simplifying assumptions listed above, the model expressed in Eq. (3.16) correctly explains a large number of problems that have been encountered in practice. However, a more accurate representation of the wave phenomena emanating from the spiral casing is to be expected if the assumptions A1 to A6 or some of them are replaced by more realistic ones.

A model which permits additional insight into the mechanism has been devised by Nishiyama et al. in [38]. Their model is equally simple but differs from Chen's model by two features:

B1   Instead of the Z_s discrete sources of oscillation, a continuous source is placed along the whole spiral duct. The distribution of phase angles of this source has an integer number of v periods corresponding to Eq. (3.3)

B2   At the narrow end of the spiral duct, the boundary condition is replaced by assuming zero flow pulsation, i.e., reflection of the pressure waves

Using a continuous representation of the disturbance (A 1) permits an analytical solution of the wave equation, and thus yields much more detailed results compared to Eq. (3.16) which only holds for the ends of the spiral duct. As derived in [38], the pulsation u of flow velocity in the spiral duct has three components:

$$u = \frac{F\lambda^2}{1-\mu^2}\left[-\exp(j(Ut-x)/\lambda) + A \cdot \exp(j(Ut-\mu x)/\lambda) + B \cdot \exp(j(Ut+\mu x)/\lambda)\right]$$

$$(3.18)$$

The first component in the square bracket of Eq. (3.18) is the particular solution of the inhomogeneous wave equation, with wave length corresponding to the source mode,

Table 3.1 Definitions used with equations (3.18) through (3.21)

F	Magnitude of disturbance
U	$=D_{sp}\pi nkZ_r/v$, phase velocity of disturbance
a	velocity of pressure wave in the spiral duct
μ	$=U/a$, 'Mach number' of disturbance
λ	$=L/(2\pi v)$, length per radians of disturbance
x	length coordinate, starting at narrow end of spiral duct
L	$=\pi D_{sp}$, developed length of spiral duct
t	time

the other two terms represent the forward and backward traveling waves of the homogeneous solution. The parameters in Eq. (3.18) are as follows[2]: (Table 3.1)

The coefficients A and B are chosen to fulfill the boundary conditions:

Boundary condition at $x = 0$	Forward wave	Backward wave	
A5	$A = (1 + \mu)/2$		(3.19)
B5	$A = 1-(1-\mu)\cdot\exp(-j2\pi\mu v)/2$		(3.20)
B5, A5		$B = (1-\mu)\cdot\exp(-j2\pi\mu v)/2$	(3.21)

With the continuous disturbance model B1, Eq. (3.18) holds for both sets of boundary conditions, A5 or B5. Therefore, the two basic models may be directly compared. Such a comparison, shown in Fig. 3.31, presents the source mode with $v = 2$ circumferential waves. This would apply, for instance, for machines with $Z_r = 6$ and $Z_s = 20$, ($k = 3$, as in [16]), or with $Z_r = 9$ and $Z_s = 20$, ($k = 2$, as in [13]).

The left-hand side diagram in Fig. 3.31 shows the predicted risk factor, applied to the spiral exit ($x/L = 1$). For this particular location, there is also a result from the summation formula (3.16). The horizontal coordinate is the disturbance Mach number μ that is proportional to rotational speed. It is positive for outward traveling waves. For the pump turbine examples mentioned above, this would be the case in pump operation. All three models predict high risk of phase resonance if μ is close to unity, no matter if a discrete or continuous disturbance model is used.

The boundary condition at $x = 0$ makes a significant difference only in case of the inward traveling disturbance. For $\mu = -1$, the different boundary condition causes completely different results. No pulsation appears at the spiral exit if A5 (nonreflecting boundary condition at the narrow end) holds, but high risk is predicted with the other model and the boundary condition B5, 100 % reflection. The development of pressure amplitudes along the spiral duct is shown at the right-hand side of Fig. 3.31. Only the result for $\mu = -1$ and $\mu = 1$ is shown. In these

---

[2] To maintain consistency within the present chapter, some of the parameter names have been changed compared to [38].
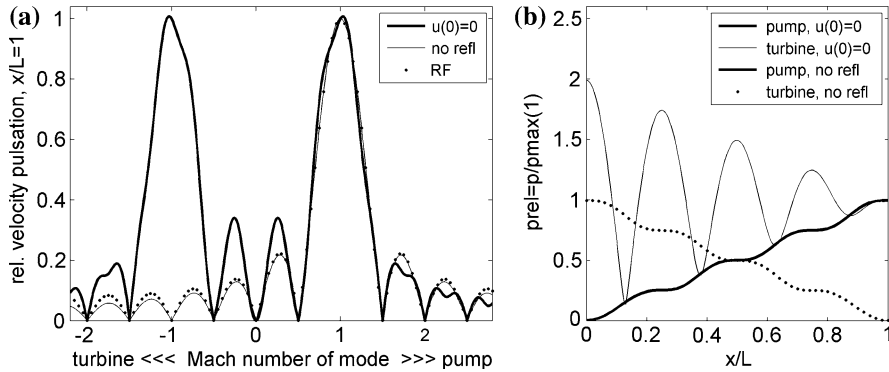
**Fig. 3.31** Risk factor and pressure amplitudes for $v = 2$ mode, basic models
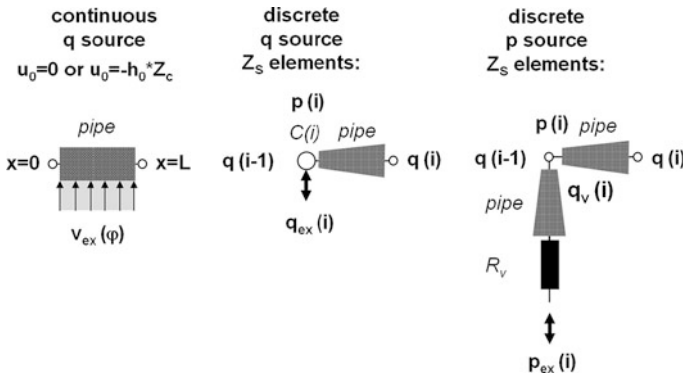
Fig. 3.32 Schematic of 1D model using Z_s pressure sources

cases, the wavelength of the traveling waves times the mode number v (2 in this case) is equal to the length of the spiral, $va/(nkZ_r) = L$.

It is not too difficult to realize a slightly more complex 1-D model which comes fairly close to the real behavior. Numerical 1-D models have been proposed repeatedly [24, 36]. Such a model must be constructed as a network of pipe elements representing the Z_s stator channels and the sections of the volute connecting them. The structure of one element (out of Z_S) is represented on the right-hand side of Fig. 3.32, with the pressure source p_{EX} at the bottom connected to the model of the diffuser channel, shown vertically, and the horizontal pipe indicating the pertinent portion of the spiral duct. The resistance R_V represents the throttling effect of the runner. For comparison, a similar model with discrete volume-type sources is shown in the middle; it is less different from the continuous model at the left-hand side which also uses a volume-type source. The continuous model is the one used in the analytical theory [38].
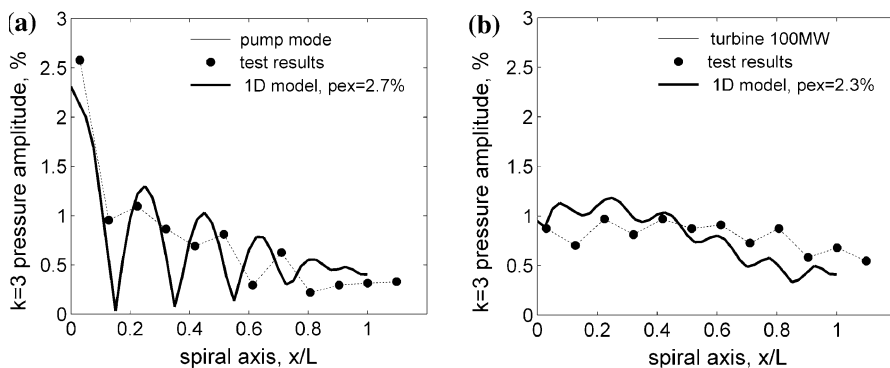
Fig. 3.33 Casing pressure amplitude in a pump-turbine **a** pump mode **b** turbine mode

Ohura et al. 1990 [16] have published field test results of spiral casing pressure pulsation in a high-head pump turbine. Because of the blade numbers $Z_r = 6$ and $Z_s = 20$, the dominating pulsation is the $v = 2$ mode, corresponding to the $k = 3$ harmonic of the blade passing frequency.

Results obtained from a 1-D model as shown on the right-hand side of Fig. 3.32 agree fairly well with the test results published in [16], taking into account that linear interpolation among the test locations may not quite reproduce the real wave pattern, see Fig. 3.33. The result for pump operation suggests that some reflection of pressure waves actually occurs at the inner end.

In a recent study by Tsujimoto and co-workers [39], the reflection at the inner end of the spiral casing according to the theory in [38] has been experimentally proven. Tsujimoto extended his theoretical model from which we quoted the Eqs. (3.18) through (3.21), to include also effects from pressure wave reflection in the pipe connected to the machine.

Virtually, all reported problems have occurred due to the outward traveling wave only ($\mu \cong +1$) where both models are equivalent. Accordingly, one may suspect that the result based on assumption B5 is too pessimistic—otherwise there should be at least some evidence of problem cases with $\mu \cong -1$. Most likely, the actual behavior is between the two extreme assumptions. Analysis of the 1-D models shows that, contrary to Chen's assumption A5, the spiral duct itself cannot absorb the inward going pressure waves. But some dissipation seems to occur at the first place of interaction due to feedback of discharge through the runner on the local pressure pulsation. This effect should depend on the specific speed of the machine, because the reflection of waves is a function of the ratio between the terminal hydraulic impedance and the characteristic impedance of the pipe elements involved. No systematic appraisal of such conditions could be found so far in the hydro literature.

In recent years, it has become possible to simulate pulsations caused by blade passage using compressible 3-D models. Several researchers have successfully applied compressible CFD, [40] and [38]. The computational effort will, however,

normally not be justified. For regular engineering practice, the risk factor concept [36] can be considered sufficiently reliable.

3.6.1 Mechanical Effects

Many cases are documented in the literature where phase resonance produced a high level of noise or vibration at the hydraulic machine [41], in the vicinity of the high-pressure conduit [33, 37, 42–45], or even in the powerhouse structure [46].

Quite frequently, the vibration and noise is not restricted to the powerhouse. Exposed penstocks are highly sensitive to periodic pressure pulsation, because the shell has many possible modes of vibration [42, 44] with low damping and, in addition, these gradually vary along the penstock due to the change of internal pressure and wall thickness. As a consequence, vibration of the penstock shell may sometimes attain unacceptable levels. Also, the single-frequency noise radiated to the environment [44] may be extremely annoying.

Looking for the root cause of these problems, it is normally straightforward to assign it to the runner blade passing frequency and its harmonics, in rare cases also subharmonics. But the reason for the high amplitudes is not always recognized. Sometimes the penstock vibration is attributed to runner blade frequency, but it is not clear if phase resonance is involved because the number of wicket gates and its role are not considered [47].

3.6.2 Possibilities for Mitigation

In case of operation problems due to wave interference in the spiral casing, there are various possible ways to improve the situation.

Increase the radial clearance gap between runner and diffuser

In case of pumps, it is sometimes possible to increase the radial clearance gap between runner and diffuser in order to eliminate phase resonance. An example has been described by Parmakian [42]. Care must be taken to maintain an acceptable pump characteristic: Typically, cutting back the guide vanes may result in a reduction of the maximum pressure coefficient which translates into a reduction in maximum available pump head.

Another example for mitigating pressure pulsation and noise is given by the following test results obtained on a 90 MW single-stage storage pump. This machine has seven impeller blades and 12 diffuser vanes. The speed is 750 rpm and the operating head during the commissioning tests was between 375 m and 405 m (the latter value produced by partial throttling of the spherical valve). To provide up to the maximum specified head of 460 m, the pump was originally designed with a radial gap between the impeller and the diffuser of 1.93 % only. This small gap, together with phase resonance at the harmonics $k = 2$ and $k = 4$
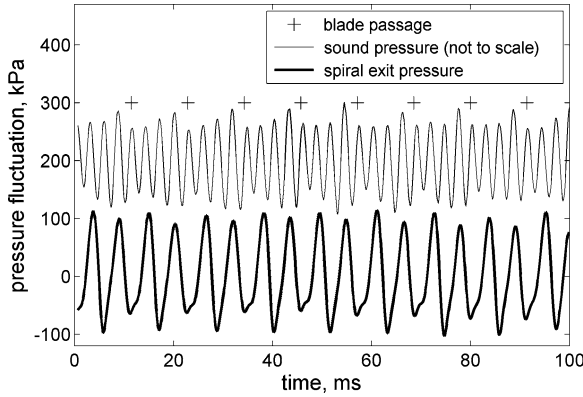
**Fig. 3.34** Manifold pressure and sound pressure
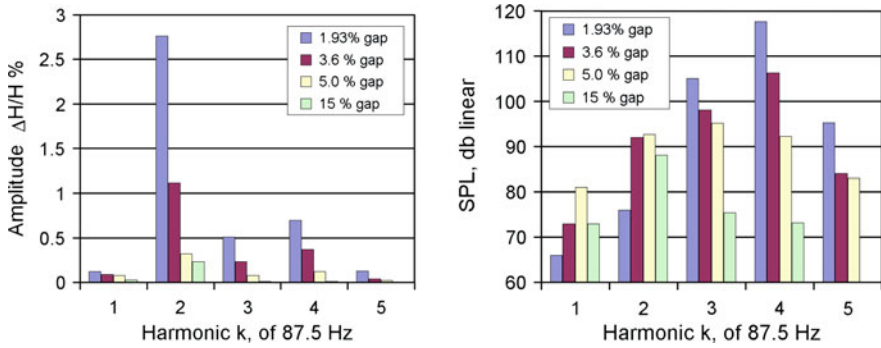
Fig. 3.35 Mitigation by means of increased radial gap

produced excessive pressure pulsation at 175 Hz and noise at 350 Hz, as shown in Fig. 3.34.

It should be noted that, the amplitude at the fundamental frequency (87.5 Hz) was only small in this case, despite the narrow radial clearance. Hence, a combination of the two features (narrow gap and bad combination of blade numbers) was at the root of the problem. In this design, a removable annular insert forms the leading edges of the diffuser vanes. For that reason, it was relatively simple to change the radial gap between the impeller and diffuser.

The gap was increased stepwise to 5 % and, while the phase resonance condition persisted, the vibration behavior and noise were effectively corrected due to a reduction of the amplitude at the source. The resulting pressure amplitude at the spiral casing exit is shown in Fig, 3.35, together with the sound pressure level in 1 m distance from the casing. By completely removing the annular insert, it was also possible to test a purely experimental version with 15 % radial gap. The vibration and noise level with the final gap of 5 % is satisfactory.

Fig. 3.36 Effect of perforated nose vane
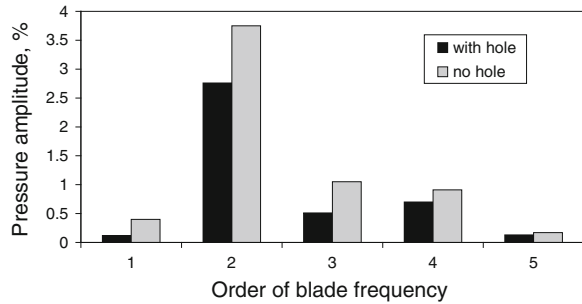
Provide skewed blade tips at the impeller

In order to distribute the rotor–stator interaction over a longer time interval and, at the same time, reduce the content of higher harmonics, the runner blade edge facing the diffuser vanes may be skewed. This is a suitable design strategy for obtaining low vibration level in the design at the outset; for the purpose of troubleshooting in a completed machine without skew it will usually not be applicable.

Perforated nose vane

The ends of the spiral duct may be connected by a sufficiently large hole in the nose vane to allow wave interference between both ends. From the viewpoint of casing strength, there is normally no problem with this artifice. Being a purely empirical measure, it has been successful in a number of cases but is not entirely fool proof. In some cases it did not provide any improvement. The storage pump discussed above may also serve as an example for the effect of the perforated nose vane. As shown in Fig. 3.36, the hole in the nose vane actually reduced the level of nose and pressure pulsation, but not sufficiently, and not as much as an increase of radial runner gap.

Change the wave speed in the spiral duct

Equation (3.16) indicates an important influence of a, the velocity of wave propagation in the scroll case. Therefore, actions which change the wave velocity appear to be an elegant idea to detune the resonance, as described in [37]. The wave velocity may be significantly reduced by inserting a compressible element, like a hose filled with pressurized air, in the spiral casing along its circumference.

This feature has been implemented in practice, in a turbine with 17 runner blades and 18 guide vanes, and reported to be successful. According to background information obtained later, the durability of the compressible hose used for reducing the wave speed was not entirely satisfactory.

Insert a pressure wave absorber in the penstock.

If the objectionable behavior—noise or vibration—occurs at the penstock, then it may be easier to just cure the symptom instead of the root cause. Such a case has been reported by Alming [43] where a damping device was inserted between the turbine and penstock. High-frequency pulsation entering the pipe-like component is absorbed at the wall.

Exchange the runner by another one with a more suitable number of blades

Runner exchange is the most expensive option, a solution of last resort. In some cases, an acceptable level of vibration could only be obtained by replacing the runner.

References

1. Egusquiza, E., Mateos, B., & Escaler, X. (2002). Analysis of runner stator interaction in operating pump-turbines. *21th IAHR Symposium on Hydraulic Machinery and Systems*, Lausanne
2. Tanaka, H. (1990). *Vibration behaviour and dynamic stress of runners of very high head reversible pump turbines. IAHR Section Hydraulic Machinery, Equipment, and Cavitation, 15th Symposium*, Belgrade
3. Thomas, D. L. (1979). Dynamics of rotationally symmetric structures, Internat. *Journal for Numerical Methods in Engineering, 14*, 81–12.
4. Coutu, A., Velagandula, O., & Nennemann, B. (2005) *Francis Runner Forced Response Technology*, Waterpower XIV, Austin
5. Fisher, R. K., Powell, C., Franke, G., Seidel, U., & Koutnik, J. (2004) *Contributions to the improved understanding of the dynamic behavior of pump turbines and use thereof in dynamic design.* 22nd IAHR Symposium on Hydraulic Machinery and Systems, Stockholm, Sweden
6. ISO 1940/1 Mechanical vibrations - Balance quality requirements of rigid rotors—Part 1: Determining of residual unbalance, First edition, 1986-09-01.
7. Gentner, C., Staehle, M., & Sallaberger, M. (2002) *Unsteady numerical analysis of pressure pulsations in the spiral casing and runner of a pump turbine: Proceeding Hydraulic Machinery and Systems 21st IAHR Symposium,* Lausanne
8. Bartkowiak, J., Deslandes, L., & Finnegan, P. (2009). *Repair of the Unit 3 GM Shrum Francis Turbine After a Major Runner Failure* (pp. 27–30). Spokane: Waterpower XVI.
9. Zobeiri, A., Kueny, J.L., Farhat, M., & Avellan, F. (2006) *Pump-Turbines Rotor-Stator Interactions in Generating Mode: Pressure Fluctuation in Distribution Channel, 23rd IAHR Symposium,* Yokohama
10. Greitzer, E. M., Tan, Ch. S., & Graf, M. B. (2004). *Internal Flow*, Cambridge University Press, Cambridge
11. Benkö, G. B., & Holmén, E. K. (1996*) Parametric resonances in umbrella-type generating units.* Symposium on vibrations in hydraulic pumps and turbines, Manchester, England, 14–16 Sept 1966
12. Koutnik, J., Lazar, L. (2002) *Achievements of Rotor Vibration Monitoring at Pumped Storage Power Plant Dlouhé Strán?.* 12th International Seminar on Hydro Power Plants, Vienna
13. Franke, G., Powell, C., Seidel, U., Koutnik, J., & Fisher R. (2003) *On pressure mode shapes arising from rotor stator interactions.* 11th IAHR International Meeting of the Work Group on the Behavior of Hydraulic Machinery Under Steady Oscillatory Conditions, Stuttgart
14. Coutu A., Roy M., Monette C., & Nennemann B. (2008). *Experience with rotor-stator interactions in high head Francis runner.* IAHR 24th Symposium on Hydraulic Machinery Systems, Foz do Iguassú
15. Kaspar, K., & Weisser, H. (1989). *Damage to hydropower plants of modern construction, Upgrading and Refurbishing Hydropower Plants II Water Power & Dams Construction.* Switzerland: Zurich.
16. Ohura Y., Fujii, M., Sugimoto, O., Tanaka, H., & Yamagata, I. (1990) *Vibrations of the powerhouse structure of a pumped storage power plant.* 15th Symposium of IAHR, Belgrade

17. Tamasukuri T., Kikuchi K., & Satch J. (1992). Progress in ultra high head single-stage pump-turbines, Water Power & Dam Construction

18. Coutu A., Proulx D., Coulson S., & Demers A. (2004). Dynamic assessment of hydraulic turbines- high head francis, Hydro Vision 2004, Montréal, QC, Aug 15–18, 2004.

19. Jones, R. K., & March, P. A. (1987). Blade-gate interaction frequency in hydroturbines, (T.V.A Report No. WR28-4-640-103, Aug 30)

20. O'Kelly, F. (1990). Blade/Gate interaction, machine dynamics notebook, Hydro Review

21. Nennemann, B., Vu, T. C., & Farhat, M. (2005). CFD prediction of unsteady wicket gate-runner interaction in Francis turbines: A new standard hydraulic design procedure. Hydro 2005, Villach, paper 2.05, October 17–20

22. Lais, St., Liang, Q., Henggeler, U., Weiss, Th., Escaler, X., & Egusquiza, E. (2008) *Dynamic Analysis of Francis Runners: Experiment and Numerical Simulation*. IAHR 24th Symposium on Hydraulic Machinery Systems, Foz do Iguassú

23. Gülich, J. F. (2008). Centrifugal Pumps, Springer, Switzerland

24. Nicolet, C., Ruchonnet, N., & Avellan, F. (2006). *One-Dimensional Modeling of Rotor-Stator Interaction in Francis Pump-Turbine*. 23rd IAHR Symposium, Yokohama

25. Keller, M., & Sallaberger, M. (2006). Modern design of pump turbines. 14th International Seminar Hydropower Plants, Vienna

26. Sick, M., Michler, W. Weiss, T., Keck, H (2009). Recent developments in the dynamic analysis of water turbines. Proceeding IMechE Vol. 223 Part A: J. Power and Energy, JPE578

27. Fritz, J. (2002). *Investigation of the dynamic loads acting on the diffusers of multistage pumps: A comparison of theoretical and experimental methods*. 21th IAHR Symposium on Hydraulic Machinery and Systems, Lausanne, Switzerland, Sept 9–12, 2002

28. Nennemann B., & Vu T. C. (2007). Kaplan turbine blade and discharge ring cavitation prediction using unsteady CFD, IAHR WG (Cavitation and Dynamic Problems in Hydraulic Machinery and Systems) 2nd Meeting, Timisoara, Oct 24–26 2007.

29. Schmied J., Weiss T., & Angehrn R. (2006). *Detuning of pelton runners. 7th IFToMM Conference on Rotor Dynamics,* Vienna, 25–28 Sept 2006.

30. Parkinson, E., Neury, C., Garcin, H., Vuilloud, G., & Weiss, Th. (2006). Unsteady analysis of a Pelton runner with flow and mechanical simulations. *Hydropower & Dams*, (2), 101–105

31. Kvicinsky, S., Kueny, J.L., Avellan, F. & Parkinson, E. (2002). *Experimental and numerical analysis of free surface flow in a rotating bucket, Proceeding Hydraulic Machinery and Systems 21st IAHR Symposium* Lausanne,

32. Perrig, A., Farhat, A., Parkinson, E., Avellan, F., Garcin, H., Bissel, C., Valle, M., & Favre, J. (2004). *Numerical flow analysis in a Pelton turbine bucket, 22nd IAHR Symposium on Hydraulic Machinery and Systems*, Stockholm, Sweden

33. Den Hartog, J. P. (1929). Mechanical Vibrations in Penstocks of Hydroelectric Turbine Installations. *Trans ASME 51,* 101–110 (and discussion thereof)

34. Chen, Y. N. (1961). Oscillations of water pressure in spiral casings of storage pumps. *Technical Review Sulzer*, Research Issue (Turbo-machinery), 21–34

35. Nechleba, M. (1972). Oscillations of water pressure in pressurized pipes of hydraulic machines, especially pumps (in German). *Maschinenbautechnik 21* 113–116

36. Doerfler, P. (1984). *On the role of phase resonance in vibrations caused by blade passage in radial hydraulic turbomachines. IAHR Section Hydraulic Machinery, Equipment, and Cavitation, 12th Symposium* (Stirling, 1984)

37. Rovaro Brizzi M. (1993). Steady oscillatory conditions originating from the hydraulic machines. Experimentation upon the attenuation possibilities on the Gallicano powerplant. IAHRWork Group 1, 6th meeting, Lausanne, paper 3–2.

38. Nishiyama, Y., Suzuki, T., Yonezawa K., Tanaka H., Doerfler P., & Tsujimoto Y. (2011). Phase resonance in a centrifugal compressor. *International Journal of Fluid Machinery and Systems, 4,* 3,

39. Tsujimoto, Y., Tanaka, H., Doerfler, P., Yonezawa, K., Suzuki, T., & Makikawa, K. (2010). *Effects of Acoustic Resonance and Volute Geometry on Phase Resonance in a Centrifugal Fan, 26th IAHR Symposium on Hydraulic Machinery and Systems*, Beijing, China

40. Yan, J., Koutnik, J., Seidel, U., & Hübner, B. (2010). *Compressible simulation of rotor-stator interaction in pump-turbines. IAHR 25th Symposium on Hydraulic Machinery and Systems*, Timisoara
41. Netsch, H., Giacometti, A. (1982). Axial flow-induced vibrations in large high-head machines. *Water Power & Dam Construction, 34,* 8, 21–27
42. Parmakian, J. (1954). Vibration of the grand coulee pump-discharge lines. *Trans ASME, 76,* 783–790.
43. Alming, K. (1966). *Damping of pressure pulsations from a turbine by an energy-absorber in the pipeline. Proceeding IME* 181, part 3A, 125–133
44. Ruud, F. O. (1987). Vibration of penstocks in hydroelectric installations. *Waterpower 87,* 2214–2223
45. Makay, E., Cooper, P., Sloteman, D. P., & Gibson, R. (1993). *Investigation of pressure pulsations arising from impeller/diffuser interaction in a large centrifugal pump. Proceeding Rotating Machinery Conference.* Somerset
46. Tee T. K. (2001). Noise reduction at the Dinorwig power station. Hydro'01, 259–268
47. Todd R.V. (2000). Vibrations of the Upper Nevada Penstock at Hoover Dam, Hydrovision 2000, Charlotte, NC, 8–11 Aug 2000

Chapter 4
High-Frequency Vortex Phenomena

As a straightforward consequence of dimensional analysis, the frequency of vortex phenomena increases proportionally with the flow velocity, and is inversely proportional to its size. Thus, while draft tube surges are in the Hertz range—the characteristic length being the runner diameter, Von Kármán eddies are basically determined by a trailing edge thickness, and due to the smaller size their frequency is well in the audible range. The Von Kármán eddies have to be minimized by using particular profiles for the trailing edges, in particular in the stay vanes and runner blades, or otherwise the lock-in effect and the narrow-band character of the phenomenon may put the structural safety at risk.

By contrast, wide-band fluctuations result when large flow regions are filled with decaying eddies as a result of large hydraulic losses. Such fluctuations typically occur in reaction machines in far off-design operating conditions, at very low load or during start-up, or load rejection, or runaway. Their nature is highly stochastic, and their impact on the components and the hydraulic circuit is difficult to assess because of the large local amplitudes which are largely incoherent with neighboring regions.

4.1 Von Kármán Vortex Street

4.1.1 Basic Flow Mechanism

Von Kármán vortices are formed in connection with the wake downstream of a bluff body located in a perpendicular flow. The classical example of a cylinder with circular cross-section has been described by Theodore von Kármán as early as 1911 but there are fifteenth century sketches of the phenomenon drawn by Leonardo. In fluid-dynamic terms, each individual vortex is initiated at the separation point between the attached flow and the stalled downstream region. The vorticity contained in this area of flow concentrates in a vortex filament which

detaches from the body and starts traveling downstream. During eddy formation on one side of the body, the separation point on the other side moves downstream along the contour until a separation occurs. Following the detachment of the second eddy the situation returns to begin formation of a counter-rotating eddy on the other side. The sequence of eddies with alternating rotation may be understood as a lumped version of the overall vorticity between the wake and the main flow, the distributed version being hydrodynamically unstable.

As a consequence of the alternating eddy formation, the body—a rod, a plate, or in case of water turbines, distributor vanes, or runner blades—causing the vortex street is subject to a periodical reaction force pulsating with the frequency of eddy detachment. Equation (4.1) is a similarity law which permits this frequency to be computed

$$f \ = \ St.v/L \tag{4.1}$$

where L is a characteristic lateral dimension of the body, v is the velocity component of the main flow relative to the body, and St is a dimensionless coefficient referred to as Strouhal number. This coefficient depends on the shape of the body and on the Reynolds number. Other influences exist but are less important in hydraulic machines; in particular, recent studies have shown an influence of cavitation on the frequency and on the resulting vibration behavior [1], but in stationary cascades a sufficiently low pressure level for this influence is not very likely to occur. There is also a Mach number influence in high-speed gaseous media (not in hydraulic machinery).

In the case of simple objects like a cylinder the characteristic length L determining the vortex shedding frequency would be the diameter. In case of turbine blades, the trailing edge thickness is the appropriate characteristic length, as the thickness of the trailing edge determines the scale of the eddies.

Due to its periodic nature the Von Kármán vortex street holds a considerable risk potential. The frequency of vortex shedding may coincide with a natural frequency of the body producing it, resulting in a *resonant vibration* and this may assume large amplitudes. Resonant vibration is obviously more likely if the flow velocity v is variable. In addition, the frequency is generally high and as a result a large number of cycles may occur leading to mechanical damage from high-cycle fatigue.

If the vibrating structure is sufficiently flexible, then its displacement due to the forces from the alternating eddies may feedback on the vortex shedding process creating more intense and better synchronized vortices and, hence, an increased vibration intensity. On the other hand, once the structure vibrates, the frequency of vortex shedding is no longer controlled entirely by Eq. (4.1) but by the natural frequency of the structure. A typical situation would be the increase of velocity v due to slow loading of the machine, with vibration remaining negligible until v approaches a critical value where a resonant frequency is reached. Vibration ensues and, if the velocity continues to rise, the frequency remains '*locked-in*', with high vibration, until the deviation between the frequency from Eq. (4.1) and
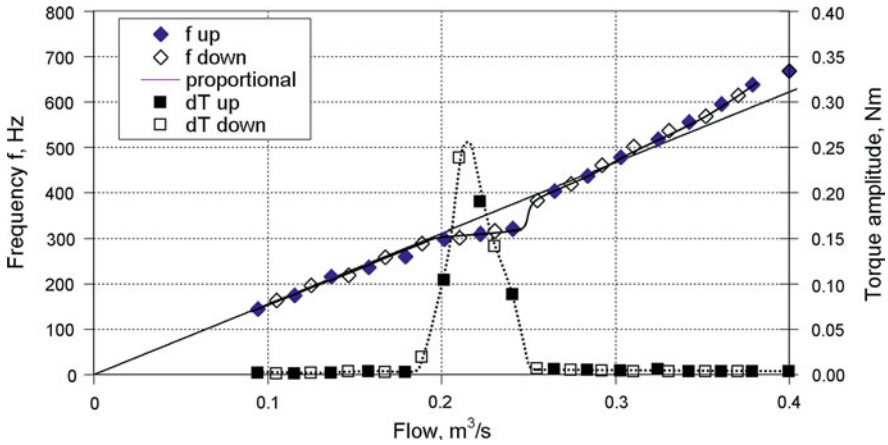
Fig. 4.1 Frequency lock-in in a laboratory test

the natural frequency becomes too large. At this point, the vibration breaks down and the frequency follows again Eq. (4.1), with small amplitude.

Figure 4.1, which has been taken from a laboratory test, demonstrates the lock-in effect. The test object is the oscillating reaction torque of a flexibly mounted stay-vane profile in a water channel. The only condition with noticeable vibrations is near the resonance between vortex-shedding frequency and a natural frequency of the blade. In this condition, the actual vibration is locked in at the natural frequency close to 300 Hz. The straight line indicates the theoretical vortex shedding frequency with a given Strouhal number. Note that the lock-in effect occurs over a fairly wide range of the flow ($\pm$20 %) so that the effect covers a range of possible discharges.

4.1.2 Turbine Components Affected by Vortex Streets

In large hydraulic machines, increased vibration due to vortex streets has occurred quite often. Among the undesired effects are alternating stresses causing mechanical fatigue and sometimes cracking of vital components and, on the other hand, annoying noise centered at the resonant frequency.

Much experience with vibrating stay vanes is documented in the literature. An actual wave of problems occurred in the 1970s when for the first time many large Francis and Kaplan turbines were built, often with fragile profiles not much different from a flat plate with very simple trailing edges. In the meantime, manufacturers are more cautious and this kind of problem has become rare although not exterminated. Figure 4.2 is a graphical summary from Chen's survey [2] combining results from several sources [3–5]. The relative vibration intensity, expressed as a percentage of the result for the blunt edge, is shown versus the
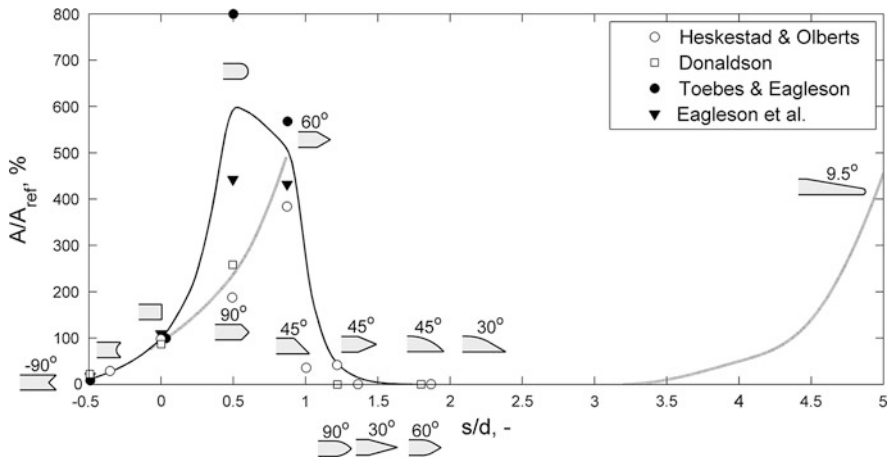
Fig. 4.2 Vortex excitation intensity for simple shapes of trailing edge

relative length of the tail protruding from the parallel faces, considering also indented shapes ('negative protrusion'). With his curve, Chen successfully brought some understanding into the large variety of possible shapes. The y-axis in Fig. 4.2 is a relative intensity of the pulsation reaction force, expressed as percent of the blunt rectangular edge serving as reference. Starting from the reference, indented shapes have reduced intensity, see left-hand side of the diagram. Very high amplitudes result in case of protrusions between 50 and 100 % of the blade thickness. If the edge is more acute-angled, then the intensity becomes very low, and the preferable shapes for water turbines belong to this group.

The 9.5° profile on the right-hand side of Fig. 4.2, added by Chen, seems to indicate that for very low angles the amplitudes rise again; however, this is rather a consequence of the long trailing edge behaving as a extension of the blade with a smaller half-cylinder added in order to retain a reasonable thickness.

Von Kármán vortices causing excessive *stay vane* vibration or failures are well documented in the literature for many cases [6–20]. The situation may be described as "singing stay vanes", with a clear noise occurring, under certain load conditions, at the very specific frequency of the natural frequency of the stay vanes [19]. While prediction of the phenomenon is well developed through CFD, natural frequency calculation of the stay vane has to take into account the added mass effect of water.

Wicket gates may also be excited through Von Kármán vortices [21] but fewer problems have been reported.

Von Kármán excitation of Francis *runner blades* is also presented in the literature [8, 18, 19, 22–24]. The frequency recorded is not that well defined and varies with flow conditions. The issue is solved through proper modification of the outflow edge [19]. Fisher et al. [24] reported an uncommon case where Von Kármán excitation caused runner blade vibration in a condition with closed wicket gate, during coastdown of a large unit.
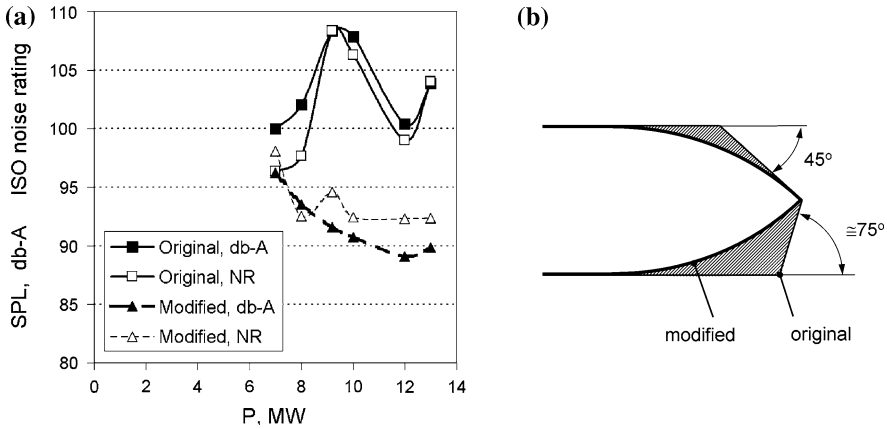
Fig. 4.3 Correction of noise from singing runner blades (**a**) Noise reduction (**b**) Correction of trailing edge

It is not really difficult to avoid the 'singing' of *runner blades* by choosing appropriate profiles, but problems may still be caused by inaccurate manufacturing. The simple chamfered shape—which is perfectly adequate if properly manufactured—already becomes dangerous if it is only slightly tilted. Figure 4.3 is an example from a Francis turbine with runner diameter of 2.75 m, operating under a head of 29 m. A tilt of the correct trailing edge chamfer by about 15° in the finish of this small runner was sufficient to create a problem with extremely annoying howling noise at 400 Hz plus harmonics. The actually manufactured shape was, due to the tilt, roughly equivalent to the worst possible edges located at s/D = 0.5 in Fig. 4.2. Based on the influence of profile parameters shown in Fig. 4.2, the cure was not difficult to find. The final profile in Fig. 4.3, selected from Fig. 4.2, required only slight modification of the runner in place. A very large reduction in sound pressure level by up to 15 dB and reduced noise rating resulted from this simple correction.

Von Kármán-induced vibration of guide vanes is more seldom but has also been observed in some machines. In high-head turbines, high frequencies may result in an extremely annoying whistling tone. Guide vanes may have many modes of vibration, some of them prone to excitation by Von Kármán vortices.

Similar to stay vanes, the trash rack as well is prone to vortex-excited vibration and therefore it has become routine to design it properly, to ensure no resonance with all possible velocity levels. Nowadays, sometimes the unspectacular components are causing troubles, probably because they are not so frequently used and designers are unaware that rather unimportant items are not automatically fool-proof. Examples are flow-straightening fins in a pipe bend, or a fin supporting the flow-measuring device of a butterfly safety valve.

pressure side

suction side

30°
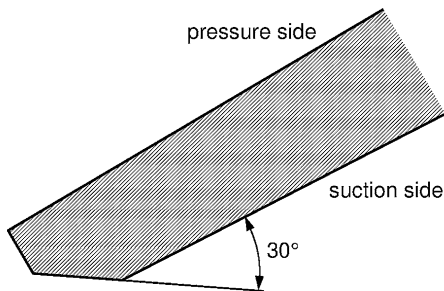
4.1.3 Related Design Practice

Avoidance of vortex-related problems is based on the following rules:

1. Use trailing edge shapes which produce only low-intensity vortex streets.
2. Provide sufficient stiffness to exclude resonance.
3. Provide sufficient damping if resonance cannot be avoided.

In practice rule 1 means that one must not use shapes that proved to be equal or worse than the blunt edge. A Donaldson-type edge is easy to realize and good enough in most cases. Figure 4.4 shows its application for runner blades. Proper execution is crucial, as demonstrated in an example in Fig. 4.3.

Other more general shapes are possible. Combining results from many experiments and publications, an empirical rule may be given which provides more freedom for designers striving to minimize hydraulic losses in the stay vanes. This can be done by setting appropriate limits to the angles α_1 through α_4, and the ratio d_F/d_K in a definition according to Fig. 4.5.

Providing sufficient stiffness according to rule 2 requires the designer to make a comparison between the maximum expected Von Kármán frequency with the minimum natural frequency of the blade. For stay vanes, the frequency is proportional to the turbine discharge, hence the maximum discharge is critical. The lowest natural frequency usually belongs to a simple bending mode. It is necessary to account for the added mass effect reducing the natural frequency. A few years ago, before fluid–structure interaction could be simulated, designers typically used a 30 % reduction of the natural frequency computed in air as a guide to the added-mass effect. In case of stay vanes and guide vanes, it is always possible to avoid resonance with the lower natural modes of vibration. Problems may still occur for the rare cases where vortex shedding is sensitive to the conditions of flow incidence. Such problems can normally be solved by modifying the thickness or shape of the trailing edge.

Providing sufficient damping according to rule 3 is not applicable for stay vanes or runner blades but may be the solution of rare issues with whistling of guide vanes. Publications on this subject are scarce but one example of a high-head Francis turbine is given in Fig. 4.6.
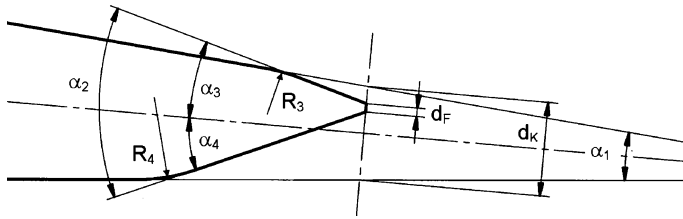
**Fig. 4.5** Generalized trailing edge shape for stay vanes
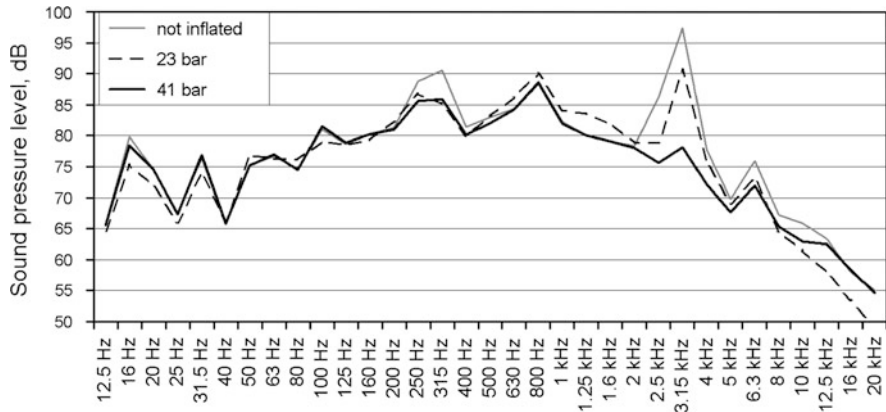
Fig. 4.6 Guide vane whistling suppressed by seal friction

The turbine is rated 24.8 MW at a head of 430 m. To reduce leakage losses, the guide vanes have a water-operated inflatable seal at the front side. The turbine produced a nasty 3.2 kHz whistling noise at high load after the guide vane bearing material had been changed during refurbishment. It was found that the operating pressure of the seal had an influence on the intensity of this noise peak. This fact proved helpful because it clarified the source of noise and, more important, raising the pressure by using water with turbine intake pressure at the same time solved the problem.

As demonstrated in Fig. 4.7, guide vanes in Francis turbines usually have a number of natural frequencies with mode shapes that could easily be subject to vibration excited at the trailing edge. Typically, the lowest natural frequency pertains to the torsion mode. The Von Kármán frequency depends on the point of operation and would lie among the lower bending modes. The figure shows a selection of modes which are susceptible to lateral excitation at the trailing edge for three turbines with significantly different specific speed as indicated by the ratio between blade height B_0 and chord length L. The modes are represented by their natural frequency in air, multiplied by chord length L to eliminate the effect of scale. Obviously, friction must usually be effective in suppressing vibrations, otherwise whistling phenomena would occur much more frequently.
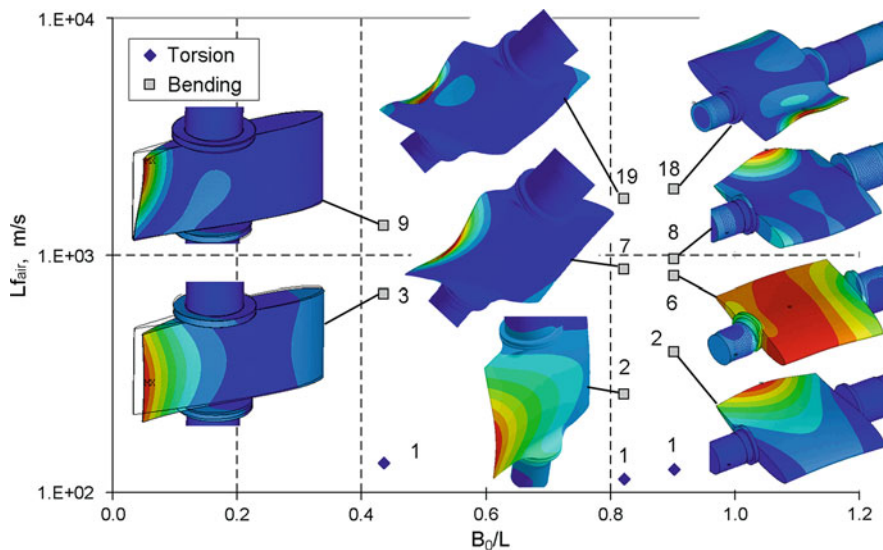
Fig. 4.7 Francis turbine guide vane vibration modes

4.1.4 Numerical Flow Simulation

Traditional practice based on the experience distilled from experimental findings is perfectly sufficient to avoid problems for general use. In certain cases, however, more insight can be gained by an up-to-date CFD technique, which may provide more understanding thus permitting better solutions. A striking example is the more accurate prediction of the added mass effect and hence the natural frequencies of the vane. CFD also permits specific studies concerning the very process of vortex shedding from a given contour.

As an example, a detailed numerical study was carried out for a Canadian utility in order to analyze the root cause of stay vane cracking in an existing plant. The target of the study was a design improvement of the stay vanes. Therefore, a quantitatively reliable CFD study was required. This case is described in more detail as a case study in Sect. 8.4.

According to the rule that at least 20 grid cells are needed to sufficiently resolve a vortex core a CFD simulation of a Von Kármán vortex street requires a very fine grid. Validation of the CFD method was done regarding grid dependency and turbulence modeling. As vortex structures are 3D in nature the simulations were carried out three-dimensionally.

First, an elementary test case of a blade profile in a water channel from the EPFL served as validation case, see Fig. 4.8 which displays the computational grid (left), the vorticity prediction with the standard k-ε turbulence model (middle) and with the SAS turbulence model (right), ref. Lockey et al. [25]. The key results of this investigation were
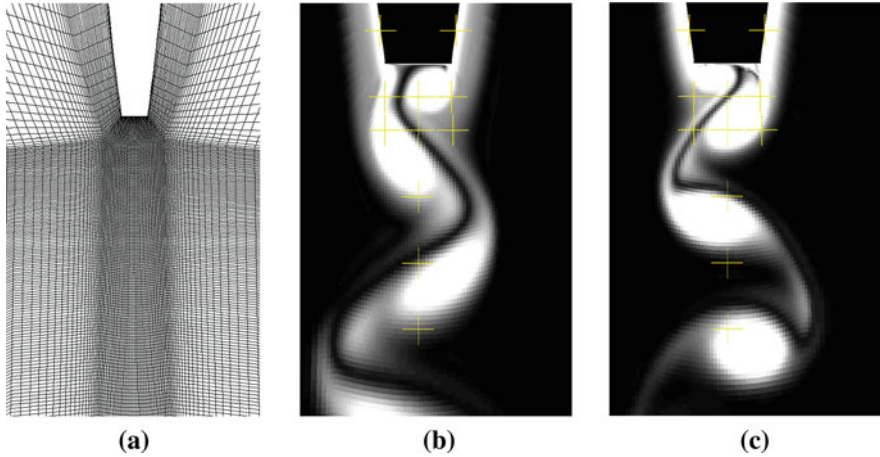
Fig. 4.8 CFD simulation of Von Kármán street downstream of a vane (**a**) computational grid (**b**) standard k-ε model (**c**) SAS model

1. Computational grid: The frequency prediction does not depend very much on the computational grid, but the prediction of amplitude is strongly grid dependent.
2. Turbulence model: The frequency prediction is not strongly influenced by the choice of the turbulence model but the CFD prediction of the amplitude strongly depends on the turbulence model. Furthermore, as shown in Fig. 4.8, the shape of the vortex patterns as well as the degree of dissipation are strongly influenced by the turbulence model. The standard k-ε turbulence model is found to be not a good choice for simulating such vortex-dominated flow features owing to its highly dissipative nature.

Second, the CFD method was used to analyze the frequency and the amplitude of vortex shedding on a range of different trailing edge geometries. The CFD results for the relative amplitude ΔF of the exciting force were compared to measurement results from literature [4] in a qualitative way and showed good agreement. Most importantly, CFD results revealed a mechanism for partial elimination of the alternating vortices which leads to a considerable damping of the shedding amplitude in case of the dove tail trailing edge as well as the Donaldson-type trailing edge, see Fig. 4.9.

The prediction of vortex shedding on round trailing edges has been found to be beyond the limits of industrial CFD so far. In this case, there is no geometrically predefined separation point, and as the turbulence models are inherently weak at predicting the separation location and strength, the vortex shedding prediction usually fails.
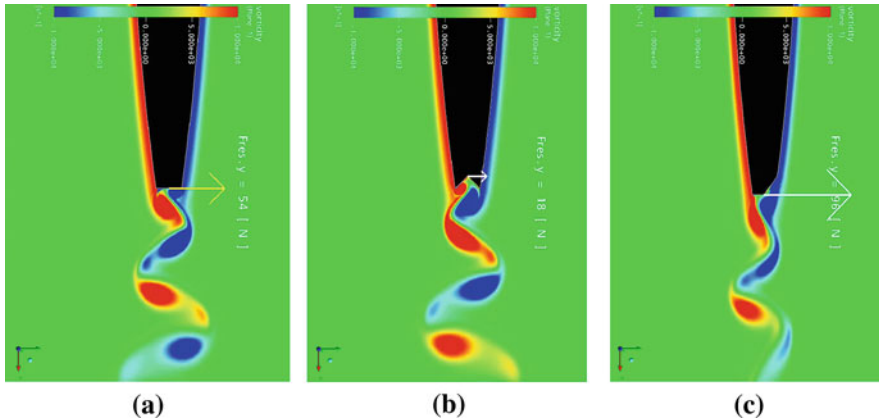
Fig. 4.9 CFD simulation of vortex shedding at different trailing edge shapes (**a**) blunt edge $\Delta F = 1.0$ (**b**) dovetail $\Delta F = 0.6$ (**c**) Donaldson $\Delta F = 0.43$

Countermeasures

Careful design using trailing edges with low excitation level is fundamental for avoidance of problems.

Increasing the stiffness of the structure may also be possible, and suitable to sufficiently increase the relevant natural frequency to prevent resonance.

4.2 Flow Turbulence

4.2.1 Physical Background and Properties

Strong turbulent fluctuations of velocity and pressure occur whenever significant amounts of energy are dissipated. An important feature of turbulent flow is its irregularity. While the details of flow are irregular and random, there are, however, overall features of the turbulence which may be described in terms of probability. For example, the distribution of sizes of eddies in the flow patterns, the kinetic energy of the fluctuations, or the typical frequencies of flow variations, may be analyzed on the basis of their probability of occurrence. While the magnitude of pulsation may become very large, its description has not been an issue of much interest to hydropower engineers. There is apparently no way to influence the stochastic pulsation caused by turbulence and the large hydraulic losses at partial loads and thus this kind of excitation is basically a by-product of the inherently poor efficiency characteristic at off-design operation.

The frequency spectrum of turbulent pressure pulsation is of a quite uniform wide-band nature, and is therefore not interesting in itself. On the other hand, it has the potential to excite many possible resonators in the system. As the existence of
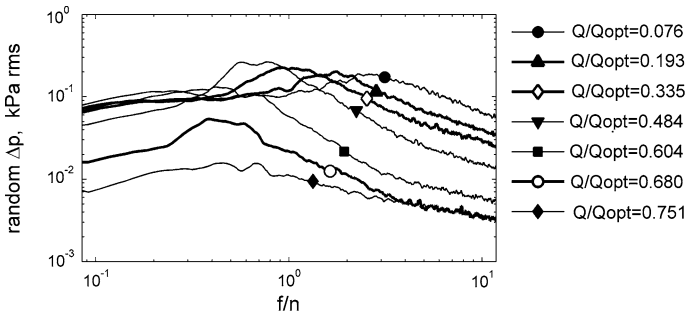
Fig. 4.10 Random part of pressure pulsation spectra

natural frequencies in the surrounding structure is unavoidable, the proper way to deal with this kind of excitation is to ensure a sufficiently robust design.

An example showing the character of turbulent pulsation is the irregular pulsation of Francis draft tube pressure given in the left hand diagram of Fig. 1.4. A histogram of the values sampled from such a pulsation would typically be bell-shaped (see Fig. 1.7), very much like the probability distribution of a white noise signal. In cases, where amplitudes have to be guaranteed, this feature may give rise to difficult discussions because, unlike a sine wave or other near-periodic phenomena, the amplitude of turbulent fluctuation depends a lot on definition (Fig. 1.3), and other definitions than statistical ones make but little sense.

4.2.2 Operating Conditions and Turbulence Level

In the model test evaluation shown in Fig. 7.13, an attempt has been made to separate the 'turbulent' part of pressure pulsation and show how it depends on load. Turbulent fluctuations are quite small in the range of normal operation, and remain small even at those partial loads where most of the pressure pulsation occurs in the well-organized form of the corkscrew vortex. Only where the helix-type vortex structure decays due to excessive swirl (typically at a flow below 0.5 times best efficiency flow) large amounts of turbulent pulsation persist. This is in accordance with the distribution of flow regimes visualized in Fig. 1.2. In the waterfall diagrams of runner stress presented in Figs. 1.15 and 1.16, it is reflected by the marked increase of wide-band noise below 50 % power.

Using statistical methods, the random part of the pressure pulsation spectrum, linked with turbulence, downstream of a Francis runner may be separated from the regular synchronous and asynchronous phenomena [26]. In the model test of a Francis turbine with specific speed $n_{QE} = 0.325$, all spectra obtained by such a procedure were of a wide-band nature, with no particular maxima. Figure 4.10 is a log–log representation of selected spectra for the same test series as Fig. 7.13. For sufficiently high frequencies, they may be represented by a power law.
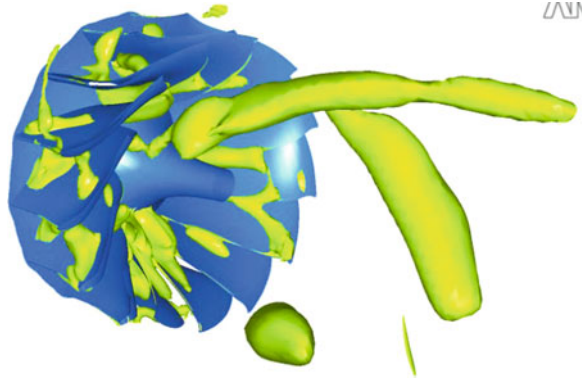
From the frequencies in the spectra, one may estimate the size of eddies. Taking
into account that the eddies travel with the mean velocity of flow c, a rough
estimate of eddy diameter $d_e(f)$ pertaining to frequency f is $d_e(f) \cong$ c/f. In the test
for Fig. 4.10, the runner exit diameter of the model is $D_2 = 0.352$ m, the cir-
cumferential runner speed was $u = 21.2$ m/s, and the flow velocity at the draft
tube wall was between 5 and 15 m/s, depending on the relative discharge. At low
load, the highest amplitudes occurred between 5 and 20 Hz, or 25–100 % of
runner frequency. This corresponds to an eddy size roughly equal to the runner
diameter.

The lowest flow rate shown in the figure, $Q/Q_{opt} = 0.076$, belongs to the
condition of speed-no load, where all of the potential energy E is dissipated in the
turbine. Similar flow conditions, but with higher flow and higher amplitudes of
pulsation, are present in a condition of runaway. From a CFD study performed by
ANDRITZ Hydro, the Fig. 4.11 shows the random fluctuation and irregular vortex
pattern in this case, represented by a surface of constant pressure.

In other types of machines and operating modes, turbulent pulsation is also linked
with dissipation, in other words, energy losses. Large-scale vortex structures are
formed in case of flow separation; these structures then decay successively, forming a
continuous spectrum of smaller and smaller eddies accompanied by correspondingly
higher frequencies of velocity and pressure pulsation. Section 7.3.2 shows examples
from pump turbine operation, using guide vane torque instead of pressure to identify
these properties. Reaction forces like guide vane torque, or hydraulic thrust on the
runner, are also influenced by turbulent fluctuations, and the corresponding time
histories and frequency spectra have characteristics similar to the pressure pulsation.
Examples are shown in Fig. 7.27 (pump operation, at less than 10° guide vane
opening), and Fig. 7.29 (turbine operation, at less than 5 ° guide vane opening).
Figure 7.30 is a survey diagram showing the behavior at 22 ° guide vane setting
(roughly best efficiency opening) opening in all quadrants. The high turbulent por-
tions are basically the spectral components that are not due to blade passing fre-
quencies. The regions where this part of the pulsation (black dots) dominates are
those with very small discharge in the pump and pump brake quadrant. Other

quadrants have blade-passage components with at least the same magnitude as the turbulent ones.

4.2.3 Transient Operation

In phases of transition between different modes of operation (standstill—generating—pumping), pulsation phenomena are more intense than in normal operation. The machines have to pass, at least for short time intervals, through conditions where much of the hydraulic energy is dissipated due to adverse flow conditions. It is usual to study these transient conditions by means of a model test reproducing the instantaneous combinations of the operating parameters, e.g. guide vane opening α, n_{ED}, Q_{ED}, σ, in a steady-state test.

Start-Up and Speed-No Load

Start-up operation creates intense stochastic flow variations due to the runner speed being much too low and due to transient pressure changes in the runner and other components such as the head cover. The number of cycles may not be that high, but the dynamic amplitudes are much higher than the ones observed during normal operating conditions. For runners, it has been found that, in terms of actual damage, one start-up operation is equivalent to years of operation under normal operating conditions [20, 27]. Similar conclusions can be drawn for other components such as head covers.

Until recently, operation at very low load was regarded as something exceptional and, due to the associated low hydraulic efficiency, also unattractive. Motivated by requirements for enhanced capabilities of network regulation, a trend exists to operate turbines more frequently at low load and for extended times. For Francis turbines, this has some relevance with regard to durability. Figure 4.12 shows the relative importance of low-load operation for a turbine whose runner stresses have been examined in a field test. In this turbine, the highest pressure pulsation level occurs in the part load vortex zone (close to 60 % power) but is not relevant with regard to runner fatigue.

However, fatigue calculations will need to be performed for runners of various specific speed before this finding can be regarded as a generally valid. Some field tests including runner strain measurement [28] showed high dynamic stress caused by the part load vortex.

Quick Shutdown and Load Rejection

Machines have to be designed for load rejections. As far as fatigue is concerned, however, the number of cycles which occur in this operational mode generally
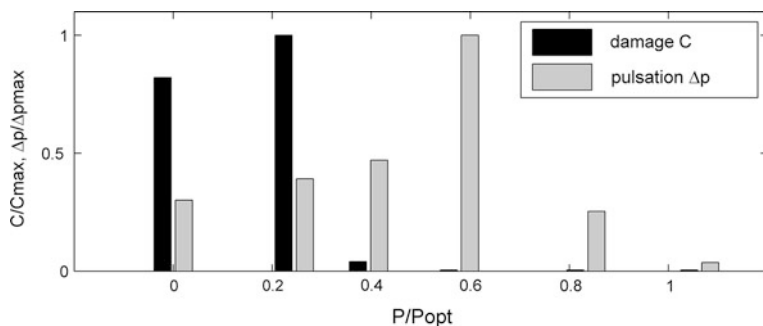
Fig. 4.12 Relative damage from operating conditions of a Francis runner

remains low compared to those occurring in start-up operations. In a normal shutdown the machines are first brought to low load in a gentle manner before they are disconnected, and thus the rough no-load condition is passed at a low level of speed and flow only. By contrast, there is no way to avoid the pulsations during the start.

During load rejection, a turbine inevitably passes through conditions of zero and negative torque, at elevated speed. High stochastic pulsation of pressure and mechanical stresses combines with elevated centrifugal load. In pump-turbines and Francis turbines with very low specific speed, the machine may even temporarily enter a condition of reverse pumping.

For pumps and pump turbines operating in pump mode, similar conditions far from best efficiency exist. In case of a loss of input power, the pump speed decelerates and the pump enters the unstable range with increased vibrations, until the guide vanes or main valves are closed. The high level of pulsation may be seen in the pump brake quadrant of Fig. 7.30. Very high levels of stochastic pulsation and stress occur in the direct transition from pump operation to generation, where the reversal of discharge and speed happens at some intermediate guide vane opening.

4.2.4 Numerical Flow Simulation

Details of the turbulent flow linked to the individual eddies are normally not simulated in CFD, because of the high computational effort. Figure 4.13 is an exception where individual unsteady eddies in the wake of a cascade have been simulated.

Turbulence fluctuations are irregular and unsteady. Direct simulation of turbulent flow requires enormous computational resources far beyond that which is possible for industrial applications. The computational effort scales with $\sim \mathrm{Re}^3$ which make such simulations not suitable for large-scale industrial cases with high Reynolds number. As performance targets in turbo-machinery are related to time-
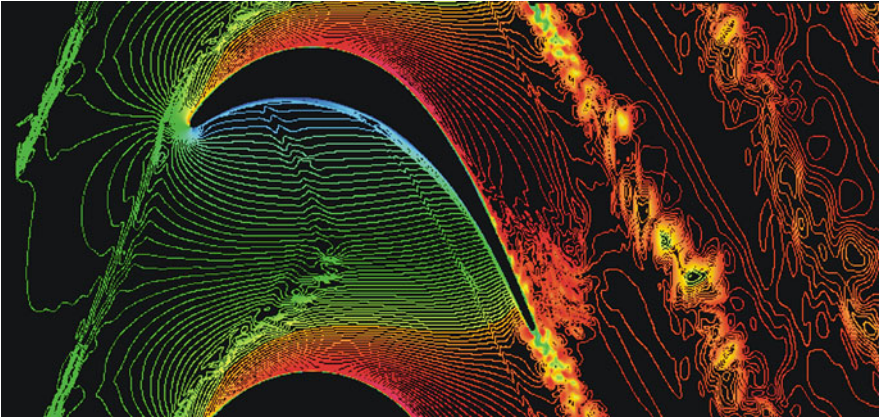
Fig. 4.13 Direct numerical simulation (DNS) of turbulent flow in a turbine runner (courtesy: Center for turbulence research (CTR), University of Stanford, USA, 2009)

averaged values the usual way to overcome this problem is application of time averaged turbulence models such as the two equation k-ε and k-ω models. In these models, the effective viscosity of the turbulent flow is characterized by the statistical nature of its kinetic energy k, its frequency ω, and the rate of decay of the eddies ε. More sophisticated turbulence models such as the Reynolds stress model dispense with the notion of turbulent viscosity, and determine the turbulent stresses directly by solving a transport equation for each turbulence stress component. A compromise between turbulence modeling and full DNS simulations which might become very interesting for the analysis of time dependent features in water turbines is the application of large eddy simulation (LES) or a detached eddy simulation (DES) which is a blend of LES with a two-equation model in the region of boundary layers near the walls.

An example of a rare direct numerical simulation (DNS) of turbulent flow in a turbine blade channel is presented in Fig. 4.13. All scales of motion down to the Kolmogorov scale at which vortices dissipate are resolved in this simulation. The lines and colors in this figure indicate conditions of equal velocity.

References

1. Ausoni, P., Farhat, M., Escaler, X., Egusquiza, E., & Avellan, F. (2007). Cavitation influence on Von Kármán vortex shedding and induced hydrofoil vibrations. *Journal of Fluid Engineering, 129*, 966–973.
2. Chen, Y. N. (1973). Durch die Nebensysteme erregte Schwingungen an den Kreiselpumpenanlagen, Teil 3: Strömungserregte Schwingungen an Platten infolge der Kármánschen Wirbelstrasse (in German), *Pumpentagung Karlsruhe*.
3. Donaldson, R. M. (1956). Hydraulic-turbine runner vibration. *Transaction ASME*, Paper No. 55-A-130, 1141–1144.

4. Heskestad, G., & Olberts, D. R. (1960). Influence of trailing-edge geometry on hydraulic-turbine-blade vibration resulting from vortex excitation. *Journal of Engineering for Power, Transaction of ASME*, Paper No. 59-Hyd-7, 103–110.

5. Toebes, G. H., & Eagleson, P. S. (1961). Hydroelastic vibrations of flat plates related to trailing edge geometry. *ASME Journal of Basic Engineering*, 83, 671–678.

6. Goldwag, E., & Berry, D. G. (1967). Von Karman hydraulic vortexes causes stay vane cracking on propeller turbines at the little long generating station of ontario hydro. *ASME Journal of Engineering of Power*, 89, 213–217

7. Grein, H., & Staehle, M. (1978). Fatigue cracking in stay vanes of large Francis turbines. *Escher Wyss News*, *51*(1), 33–37.

8. Wright, R. A. (1984).Vibration problems in Hydraulic generating units. *Vibrations im Pumps and Hydraulic Turbines*.

9. Aronson, A., Zabelkin, V. M., & Pylev, I. M. (1986). Causes of cracking in stay vanes of Francis Turbines. *Hydrotechnical Construction*, *20*(4), 241–247.

10. Liess, C., Fischer, G., Hilgendorf, J., & Lux, M. (1986). Causes and remedy of fatigue cracks in runners. *ASME International Symposium on Fluid Machinery Troubleshooting*, Anaheim, FED-Vol. 46.

11. Tadeu, M., & Netto, A. R. (1987). Hydroelastic vibrations of stay-vanes of hydraulic turbines. Work group on behaviour of hydraulic machinery under steady oscillatory conditions, Lille, France.

12. Carlson L. (1989). Stay vane vibration caused by vortex shedding at the Nipawin hydro station. CEA meeting, Toronto.

13. Gajic, A., Predic, Z., Muskatirovic, J., Pejovic, S., & Manzalovic, P. (1990). Investigation of cracks on the Kaplan Turbine Stay Vanes. *15th IAHR Symposium*, Belgrade Yugoslavia.

14. Gummer, J. H., & Hensman, P. C. (1992). A review of stay vane cracking in hydraulic turbines, *Water Power & Dam Construction 44*:32–42.

15. Fisher, R. K., Gummer, J. H., & Liess, C. (1994). Stay vane vibrations in the Nukula Falls turbines. *Hydropower & Dams*, 15–20.

16. Gajic, A., Risaburo, O., Ikohagi, T., Ignjatovic, B., & Muskatirovic, J. (1994). Flow induced vibrations and cracks on stay vanes of a large hydraulic turbine. *17th IAHR Symposium*, Beijing, China.

17. Danisovic, I., & Erlach, J. (1995). Stay vane cracking in Aswan I turbines No. 3 and 4. Hydro '95, Nice, Oct. 1995.

18. Shi, Q. (2004). Abnormal noise and runner cracks caused by Von Karman vortex shedding: A case study in Dachaoshan H.E.P. *IAHR Section Hydraulic Machinery, Equipment, and Cavitation*, *22nd Symposium,* Stockholm.

19. Coutu, A., Proulx, D., & Coulson, S. (2003) Dynamic assessment of hydraulic turbines. *Waterpower XIII*, Buffalo, NY.

20. Coutu, A., Monette, C., & Gagnon, M. (2007) Life assessment of francis runners using strain gage site measurements. *Waterpower XV*, Chattanooga, TN.

21. Papillon, B., Brooks, J., Deniau, J.-L., & Sabourin, M. (2006). Solving the guide vanes vibration problem at shasta. *Hydrovision 2006*, Portland, OR.

22. Gongwer C. A. (1952). A Study of Vanes Singing in Water. *Journal of Applied Mechanics, Transaction of ASME*, Paper No. 52-APM-33, 432–438.

23. Oliveira, B. M., Doyon, J., Micotti, F., Ferretti, A., Couston, M., & Lowys, P.-Y. (2002). Fatigue problems on low head francis turbines: The search for the causes and the solutions. *Hydrovision 2002*, Portland, OR.

24. Fisher, R. K., Seidel, U., Grosse, G., Gfeller, W., & Klinger, R. (2002). A case study in resonant hydroelastic vibration: The causes of runner cracks and the solutions implemented for the Xiaolangdi hydroelectric project. *21th IAHR Symposium on Hydraulic Machinery and Systems*, Lausanne, Switzerland.

25. Lockey, K. J., Keller, M., Sick, M., Staehle, M. H., & Gehrer, A. (2006). Flow induced vibrations at stay vanes: Experience at site and FD simulation of von Kármán vortex shedding. *Hydro '06*, Porto Carras, Greece.

26. Doerfler, P. K. (2012). A statistical method for draft tube pressure pulsation analysis. *26th IAHR Symposium on Hydraulic Machinery and Systems*, Beijing, China.
27. Coutu, A. (2008). Francis runner reliability. *Hydropower Africa*, Johannesburg, South Africa.
28. Sabourin, M., Gagné, J.-L. et al (2004). Mechanical loads and fatigue analysis of a francis runner. *Hydro Vision 2004*, Montréal, QC.

Chapter 5
Cavitation-Related Phenomena

In hydroelectric equipment, there are many flow situations where the static pressure drops far enough to reach the vapor pressure of the fluid. Vapor- or gas-filled cavities, or clouds of vapor bubbles develop in the regions concerned, and their dynamics has a strong influence on the vibration behavior and flow stability. Due to the wide range of bubble sizes involved, their oscillation and collapse create a wide band spectrum of intense vibration and noise. Sheet cavitation or high-speed vortex cavitation attached to hydrofoils like runner blades also gives rise to intense vibration.

Due to the compressibility of the vapor-filled zones, the dynamic transmission behavior of the water conduit may change considerably. In particular, cavitation of the draft tube vortex typically reduces the important lowest natural frequency of the fluid column. This may result in hydraulic instability and, following the collapse of large cavities, in strong pressure shocks.

5.1 Dynamics of Cavitation Bubbles and Clouds

When the pressure in a flowing liquid locally drops below the vapor pressure, cavitation nuclei present in every real fluid act as the starting points of tiny bubbles which may grow or collapse depending on the further development of the ambient pressure. For the ideal case of a single spherical bubble, the equilibrium radius R_E fulfills a condition involving the surface tension S and the pressure difference between the bubble's internal pressure $p_B = p_V + p_{GE}$, and the ambient pressure p_∞

$$p_V - p_\infty + p_{GE} - \frac{2S}{R_E} = 0 \tag{5.1}$$

p_v is the vapor pressure and p_{GE} the partial pressure of the non-condensable gas content. Variations of the bubble size due to changing pressure are described by the Rayleigh–Plesset equation

$$\frac{p_B(t) - p_\infty}{\rho_L} = R\frac{d^2R}{dt^2} + \frac{3}{2}\left(\frac{dR}{dt}\right)^2 + \frac{4v_L}{R}\frac{dR}{dt} + \frac{2S}{\rho_L R} = 0 \tag{5.2}$$

of which Eq. (5.1) is the steady-state version. Real flow situations are much more complex; but, in a qualitative manner, theoretical models as described by Brennen [1] are helpful for understanding many features of cavitating flows. Depending on the bubble size and ambient pressure, bubbles may explode and form large vapor-filled cavities. For the ideal spherical bubble, this is the case if the equilibrium bubble radius R_E exceeds a stability limit called the Blake critical radius:

$$R_E > R_C = \frac{2S}{3kp_{GE}} \tag{5.3}$$

In Eq. (5.3), k denotes the polytropic exponent during the changes in the volume of the bubble with changes in pressure. After some expansion the bubble may move with the flow into a region of higher pressure and the bubble may then collapse again. Bubbles with a certain gas content (typically of air) may perform oscillations of size, for which a natural frequency may be estimated. With the fluid density ρ_L, this natural frequency is

$$\omega_N = \left[\frac{1}{\rho_L R_E^2}\left\{3k(\bar{p}_\infty - p_V) + 2(3k-1)\frac{S}{R_E}\right\}\right]^{\frac{1}{2}} \tag{5.4}$$

For bubble radii between 0.1–1 mm, $f_N = \omega_N/2\pi$ for the single bubble is of the order of 1–10 kHz. In real flows, bubbles very often occur in clouds having different dynamics which, under strongly simplifying assumptions, are also amenable to theory. A spherical cloud of homogeneously distributed small uniform bubbles has many natural frequencies which are lower compared to that of an individual bubble. Due to damping effects, only the first and lowest frequency ω_1 is of interest

$$\omega_1 = \omega_N/\sqrt{1 + \frac{4}{3\pi^2}\frac{A_0^2}{R_0^2}\frac{\alpha_0}{1-\alpha_0}} \tag{5.5}$$

In this equation, R_0 and A_0 are the radii of the individual bubble and of the cloud, and α_0 is the void fraction in the undisturbed cloud. Significant reductions of the natural frequency occur if the cloud interaction parameter $\beta = \alpha_0 A_0^2/R_0^2 \gg 1$. In that case, the resulting natural frequency is roughly proportional to $1/A_0$. This is in line with the experimental frequency characteristics described below in Eq. (5.6).

The collapse of a bubble is a highly nonlinear event which generates a wide spectrum of high frequencies. Many such events occurring randomly in a short sequence of time produce the high-frequency pressure fluctuation and intense crackling noise typical of cavitating flows. Pressure spectra measured in experimental situations with simplified flow geometry display features that are also encountered in cavitating hydraulic machinery. Typically, the amplitude spectrum

of pressure follows a power law approximately proportional to $1/f$ at high frequencies. At low frequencies, there is a power law proportional to f^2. In between, there is a spectral peak whose frequency may be estimated by various criteria. In experiments with a cavitating jet, reported by Jorgensen [2] and evaluated by Blake and Sevik [3], the spectral peak is somewhat smaller than their reference frequency

$$f_R = \left(p_\infty / \rho_L D^2\right)^{1/2} \tag{5.6}$$

In experiments by Franklin and McMillan, 1984 [4], also with a cavitating jet, the reduced frequency (Strouhal number) fD/u, based on the jet diameter D and velocity u (as in Eq. (5.6)) was found to be approximately proportional to σ^2. Assuming $u = (2p_\infty/\rho_L)^{1/2}$, fD/u is equivalent to $f/f_R/2^{1/2}$, and the resulting frequencies are roughly the same, with the σ influence explained, in a qualitative manner, by the variation of average bubble size.

In cavitation research, the cavitation number σ is based on the velocity head and pressure of the ambient flow is often used, as follows

$$\sigma = 2(p_\infty - p_V)/\rho_L u_\infty{}^2 \tag{5.7}$$

Frequencies linked with cavitation have also been measured on hydrofoils. Arndt et al. 1995 [5] found an approximate law for the dimensionless frequency based on cavity length l and σ

$$fl/U = 0.25\sqrt{1 + \sigma} \tag{5.8}$$

5.2 Flow Situations Prone to Cavitation

Cavitation occurs whenever the static pressure drops below the vapor pressure. Accordingly, high local flow velocity and low ambient pressure are factors that increase the risk of cavitation. In hydroelectric machinery, the most important component with regard to cavitation is the runner, in particular in reaction machines (Francis, Kaplan, and pumps). Typical areas affected by cavitation may be seen from the damages shown in Sect. 5.3.

Depending on the point of operation, the regions with very low pressure occur in different locations. An instructive survey of typical cavitation phenomena in Francis runners with rather high specific speed has been given by Ulith [6], see Fig. 5.1.

In the center of a vortex with a swirling flow it is also possible to get cavitation. The most typical example is the draft tube vortex occurring in reaction turbines. Other swirl phenomena producing cavitation are the interblade vortex occurring in Francis turbines. The stabilizing fins used in the draft tubes of Francis or the tip leakage flows of propeller turbines also give rise to vortex phenomena.
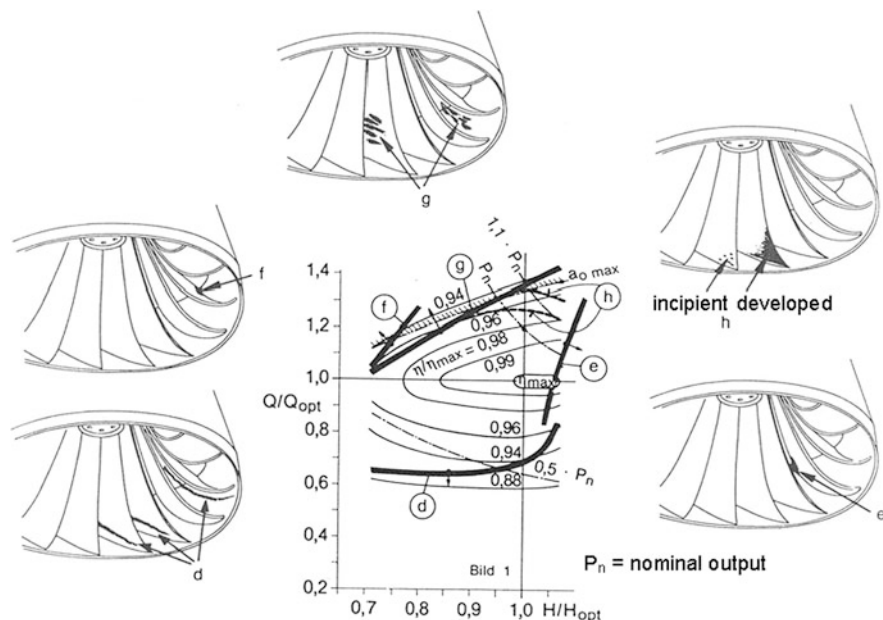
Fig. 5.1 Typical cavitation phenomena in low-head Francis runners [6] Reproduced with kind permission. © Voith Hydro Holding GmbH, Heidenheim(D)

Other inserts projecting into the flow in low pressure areas, such as the draft tube, may also cause local cavitation due to local pressure minima, for instance due to shedding of Von Kármán vortices.

5.3 Cavitation Damage

Cavitation damage may occur at different locations. Examples are presented in the following pictures. Before the advent of CFD and modern runner design tools, cavitation was often considered as necessary evil on Francis runners. Without the simulation tools it was simply not possible to avoid many poor design features in the turbine flow, such as a hydraulic contour which was not well aligned to the flow leading to high local incidence on to the blade leading edges or to non-uniform velocity distributions into the draft tube.

Figure 5.2 presents a classic Francis runner with cavitation erosion damage on the suction side of the blade, at the trailing edge and along the band junction. These types of cavitation damage were quite common and required regular re-welding of the damaged areas. The use of modern Francis blade geometries greatly improved the situation and cavitation damage of this type is less of an issue on runners of modern design.
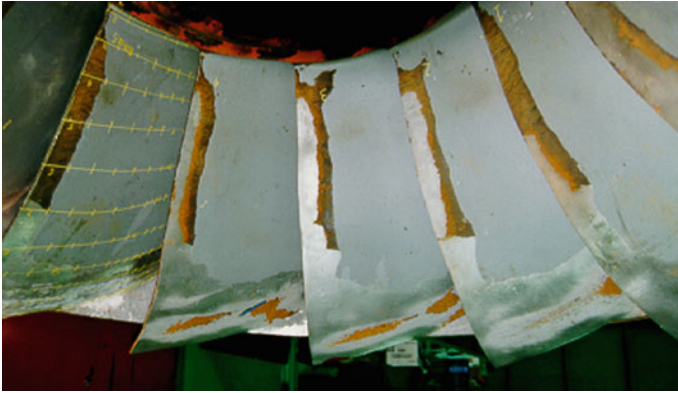
Fig. 5.2 Cavitation damage on suction side of Francis runner blades—outflow and band locations

Fig. 5.3 Cavitation damage on runner crown due to interblade vortices

On the other hand, cavitation damage such as that presented in Fig. 5.3, is more related to the mode of operation. The part load interblade vortices are attached to the crown and are driven through the blade channel toward runner outlet. Cavitation may be observed at the originating location of these vortices, on the crown.

Cavitation damage may also be observed on other components. Figure 5.4 shows cavitation erosion occurring on a wicket gate, at the discontinuity due to junction with the stem.

In Kaplan turbines there is a zone of low local pressure at the torus-shaped surface just downstream of the bottom of the wicket gate. In that area, the small radius of curvature in the meridional contour causes high velocities at high discharge. Cavitation in the undisturbed flow is not normal in that area, but the additional depression caused by the passing runner blades at maximum opening may suffice to create periodic cavitation. This phenomenon explains the erosion

Fig. 5.4 Cavitation damage
on wicket gate at stem
junction

Fig. 5.5 Cavitation damage
on discharge ring due to
interaction between wicket
gate wake and blade tip gap

marks shown in Fig. 5.5. It is also related with the shock phenomena described in
the case study in Sect. 8.5.

   In Fig. 5.5, cavitation damage on a discharge ring is caused by the blade tip gap
of the Kaplan blade interacting with wicket gate wakes [7]. As shown in Fig. 5.6,
Kaplan blades may suffer cavitation at the blade tip, on the suction side, due to the
tip clearance vortex which is driven by the pressure differential between both
pressure and suction sides.

   For another example of the tip clearance vortex in a Kaplan runner, refer to
Fig. 5.9.

Fig. 5.6 Cavitation at the tip
of Kaplan blade
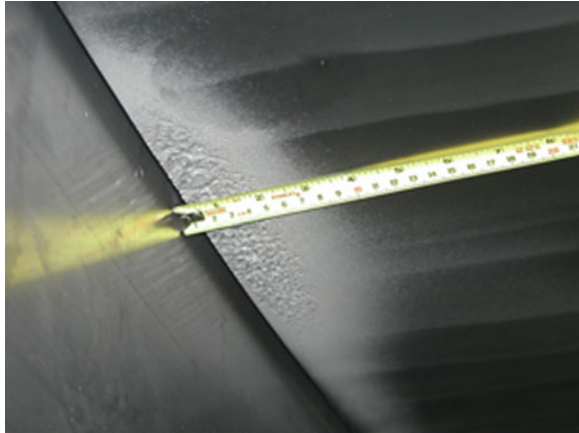
5.4 Other Mechanical Effects

5.4.1 Vibration and Noise

Cavitation normally produces stochastic pulsation of pressure with very large
bandwidth, covering several decades of frequency. It has been found that the
frequency spectrum may even extend into the ultrasonic range. Apart from erosion
damage, mechanical vibrations are also often found unacceptable. Due to the high
frequencies vibrations in the kHz range, where the human ear is most sensitive,
typically cause high perceived noise levels. Cavitation inception may sometimes
produce more noise than developed cavitation.

   In tests with cavitating airfoils [8], oscillations of lift have been recorded whose
main frequency corresponded to a Strouhal number of 0.2–0.8, defined with the
chord length -, increasing together with the cavitation number σ. This corresponds
approximately to our finding with the cavitating interblade vortex, described in
Chap. 2.3.4. Boehm et al. [9] tested a different flow contour and, using the cavity
length as reference, they reported Strouhal numbers between 0.20 and 0.23.

5.4.2 Increased Compressibility of Flow

The presence of a cavitation zone makes a fluid body much more compressible
than without cavitation. As long as the gaseous phase is not present, the fluid
quantity displaced in response to a change in local pressure is very small. The flow
is nearly incompressible with compressibility being limited by the bulk modulus of
the fluid plus some elasticity of the surrounding structure. This changes when
cavitation occurs. The additional fluid volume displaced per unit pressure change
is called the cavitation compliance. This has an important effect on the natural

frequencies of the hydraulic system. For instance, a certain degree of vortex cavitation may produce hydraulic resonance in partial-load operation of a reaction turbine, see Sect. 1.4. (theory) and Fig. 2.3. (experiment).

5.4.3 Pressure Shocks

Pressure shocks due to collapse of cavitation cavities is quite frequent in flows with intense vortex formation. In some occasions pressure shocks may occur in a stochastic way, but there are also examples where pressure shocks occur in a more or less periodic manner.

A typical situation for the occurrence of erratic shocks is when the flow leaving the turbine runner has a very large swirl rate. If the swirl rate is too high, a regular corkscrew vortex with one or two threads is not supported. As a consequence, the swirl disintegrates into an irregular sequence of individual vortex elements which sometimes have a cavitating core. As these flow elements travel to a region with higher average pressure, the cavity element is compressed. If the cavity volume is rapidly reduced to zero, an intense pressure wave is created because the fluid inflow to the cavity is stopped instantaneously. It is in fact such intense pressure waves that may contribute to the mechanism of erosion damage due to cavitation.

A sequence of shocks may be produced when a periodic cavitating flow is subject to a variation or pulsation of sufficient amplitude to temporarily close the cavity. This may occur sometimes in connection with the part-load pulsation of a Francis turbine. At some tail water level it is possible that the cavitation compliance tunes the natural frequency of the draft tube to the vortex precession frequency. If that happens, then the pulsation gets quite intensive, and the cavity may collapse with a loud bang in every rotation of the vortex. This phenomenon is truly alarming, in particular in a turbine with horizontal axis.

On some occasions, a similar phenomenon may also occur in absence of resonance if the turbine operates at the edge of vortex cavitation. An example for this phenomenon is presented in Fig. 5.7. The period of vortex rotation, about 2.3 s, is visible in the draft tube pressure Δp_{DT}. In this condition of operation, at $Q/Q_{opt} = 0.7$, a pressure shock is produced in a certain phase of the rotation cycle and passes through the spiral casing (Δp_{SC}) with the equal intensity. A low-pressure wave follows due to reflection at the headwater which leads to growth and subsequent collapse of the vortex cavity. The nonlinear behavior of the cavity seems to be the reason why this process is chaotic rather than periodic.

Growth and subsequent collapse of a vapor-filled cavity, accompanied by a pressure shock, is also at the root of the reverse water hammer phenomenon. The typical context is the load rejection of a reaction turbine.

In Kaplan turbines, the high amount of residual swirl during load rejection may in some cases produce severe transient pressure pulsation. The local pressure minimum due to the high swirl is aggravated by a transient pressure drop when the discharge is decelerated. The water column in the draft tube separates near the
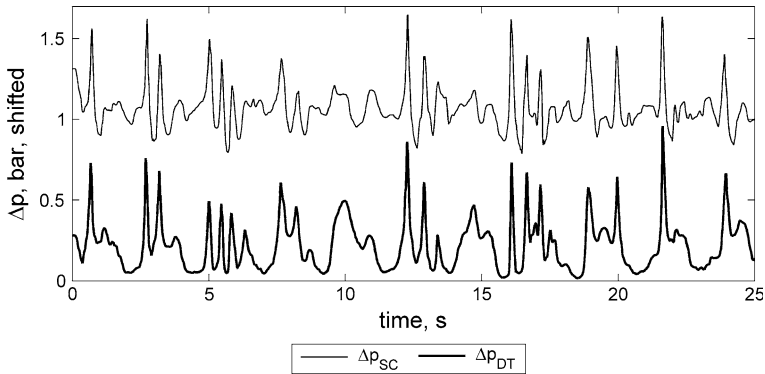
Fig. 5.7 Repeated collapse of the part load vortex causing pressure shocks

runner—actually this starts as a strong increase of the already existing vortex cavity. An additional effect comes from the runner. After passing the zero-torque condition, the turbine remains in the turbine braking mode. The negative torque translates into an axial force exchanged with the water column near the blades; water is pumped away from the space above the blades.

Due to the back pressure from the tail water, the deceleration phase is terminated by a re-closure of the cavity, sometimes a rapid collapse—referred to as reverse water hammer—that may produce dangerous pressure spikes. In some cases, a severe upward blows acting on the runner and shaft line results. Several cases of runner blade fracture have been reported in the literature due to this phenomenon. In addition, the transient upward thrust may exceed the weight of the rotating parts and lift the entire rotor from the thrust bearing for a short instant.

In classical Kaplan turbine design, the dangers resulting from vacuum formation near the runner hub have been countered by putting large self-acting aeration ('vacuum breaker') valves on the head cover. Without such valves, it is also possible to keep the adverse effects within tolerable limits by selecting a suitable maneuver of the wicket gates and runner blades during load rejection. Some authors have recommended to avoid the water column separation altogether. This is possible only in theory, i.e., in one-dimensional water hammer calculation. Field measurements of hub pressure in several Kaplan turbines have shown that in a load rejection from high load, the formation of a cavity at the runner hub can by no means be avoided, but remains harmless with a suitable closing maneuver of the wicket gate. In Francis turbines, the phenomenon of reverse water hammer is less typical but has occurred in some plants [10].

5.4.4 Cavitation-Induced Instability

Apart from changing the natural frequencies of the hydraulic system, cavitation may also actively create spontaneous pulsations in the whole power plant. This is the case when the mass flow gain effect of a cavitating vortex flow is sufficient to destabilize the system, as in the typical high-load surge of the Francis turbines.

5.5 Countermeasures

The best way to combat cavitation damage is, of course, by avoiding the cavitation itself by means of proper design. In that regard, the introduction of CFD has improved the situation very much. It is now possible to reliably design machines with a wider cavitation-free range of operation. On the other hand, the improved possibilities have already been taken up by the operators by pushing the limits of operation.

Much of the erosion, vibration and noise caused by cavitation may be mitigated if it is possible to introduce small quantities of air into the cavitation zone. The presence of air in the cavities leads to less severe bubble implosion when the pressure levels increase and reduces the intensity of the shock wave formed.

As most cavitation problems occur in the runner, this implies that we need to get the air into the runner cavitation zones. This can be done either by releasing air through channels prepared in the runner structure [11], or by injecting air through an arrangement of holes just downstream of the wicket gate [12].

Acting at the source of the problem, the method of high-pressure air injection is very effective, but also expensive in terms of equipment and energy consumption as a high pressure air supply is needed. For noise abatement, it is often sufficient to inject air at much lower pressure at the draft tube wall, directly downstream of the runner. This creates a layer with increased compressibility and reduced velocity of wave propagation, thereby locally mitigating the high-frequency fluctuations emitted by the runner [13]. A volumetric air content of 0.2 %, measured at atmospheric pressure, is already effective for the purpose, as demonstrated in Fig. 5.8. The figure compares the octave spectra of sound pressure measured at the draft tube of a horizontal Francis turbine at full load under a head of 625 mwc, with and without aeration. Aeration achieves, in this case, a significant reduction of the ISO noise rating by 4 dB.

5.6 Numerical Flow Simulation

Water flow with cavitating zones consists of two phases, the fluid phase and the vapor phase. The transition from fluid to vapor and vice versa can be modeled by the Rayleigh–Plesset equation which describes the dynamics of growth and decay
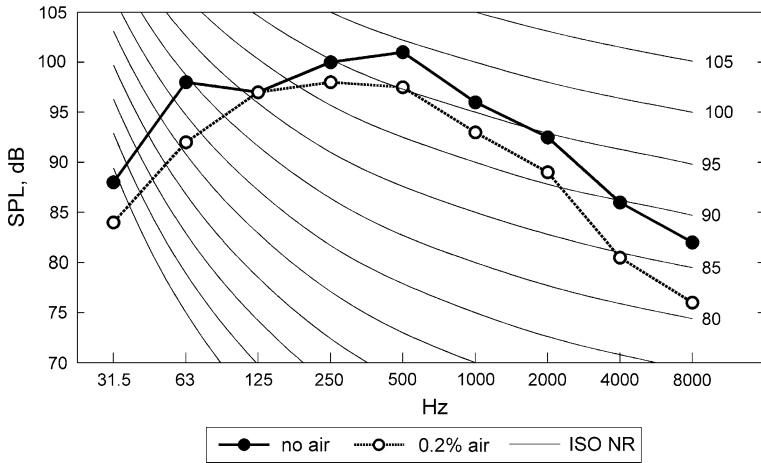
Fig. 5.8 Noise reduction by aeration through draft tube wall

of bubbles in a fluid. Yet, for optimization of the hydraulic design a calculation with a single phase flow usually delivers sufficient information for assessing the risk of cavitation. Zones where the pressure drops below vapor pressure are identified as zones of possible cavitation production. The hydraulic design is then altered such that the static pressure stays above the vapor pressure in order to avoid cavitation.

Still, a small amount of cavitation will normally occur in all types of turbines especially in off-design operation when the flow is no longer optimally aligned with the hydraulic contour.

5.6.1 Cavtitation Modeling

As the density of vapor is orders of magnitude smaller than density of water the occurrence of cavitation bubbles affects the flow of the surrounding water. A CFD simulation which gives a realistic picture of such a flow needs to include a cavitation model or to be a two-phase flow simulation. Apart from the simulations of the cavitating draft tube vortex discussed above [14, 15], there are no such simulations for Francis turbines published. Cavitation prediction with a two-phase simulation is given for the example of a Kaplan runner with special focus on the cavitation tip clearance vortex. It should be mentioned that time-dependent effects of cavitation are beyond the scope of these simulations.

In Kaplan turbines, there is a gap between runner blade tip and casing allowing a leakage flow from pressure side to suction side which rolls up to the so-called tip clearance vortex on the suction side of the blade. In most cases, the pressure in the vortex core drops below vapor pressure leading to a cavitation. A CFD simulation

| CFD | Observed | CFD |
| no cavitation model | in model test | with cavitation model |
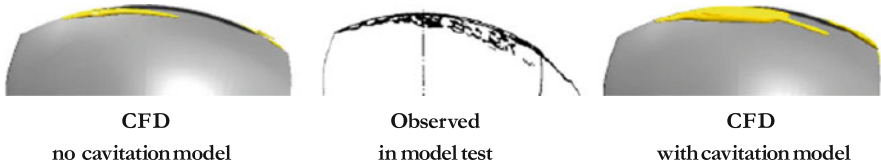
Fig. 5.9 Cavitation due to tip clearance vortex in a Kaplan runner [16]

requires high-grid resolution in the area of this vortex in order to capture the pressure drop within the vortex core. Three CFD simulations were carried out with different approaches to simulate position and size of the cavitation bubble. Apart from the cavitation model used, these simulations are identical regarding discretization in time and space as well as boundary conditions and turbulence modeling. A single-phase simulation is compared to a two-phase simulation. As shown in Fig. 5.9, the two-phase simulation catches the size and position of the cavitation bubble best in comparison to observations in the test rig.

The technology and computational power available for two-phase simulations are rapidly evolving and even during the preparation of this manuscript new results have been published. The unsteady two-phase simulation by ANDRITZ HYDRO concerned with Francis turbine full-load surge, reported in 2010 [15] was deliberately restrained to a rotationally symmetric domain, in order to reduce the computational effort. Meanwhile, other researchers have disposed of such a restriction. As an example of advanced application, Sato and Tanaka [17] presented the unsteady computation of various cavitation phenomena occurring in a volute pump. Like the ANDRITZ HYDRO team simulating the Francis full-load vortex [15], they also used the so-called Volume-of-Fluid (VoF) method. An extremely simplified version of the Rayleigh–Plesset Eq. (5.2)

$$\frac{dR}{dt} = \sqrt{\frac{2}{3}\frac{p_V - p}{\rho}} \tag{5.9}$$

is used, assuming a uniform population of n_0 bubbles with radius R, and solved together with the continuity equation and the Navier–Stokes equations. The void fraction α

$$\alpha = \frac{n_0 \frac{4}{3}\pi R^3}{1 + n_0 \frac{4}{3}\pi R^3} \tag{5.10}$$

thus appears as an additional variable together with the pressure and velocity. The surfaces with values of the void fraction at 50 % are regarded as the boundaries between the liquid and gaseous phases. The unsteady development of the baffle vortex cavitation, backflow vortex cavitation, and sheet cavitation was simulated for various conditions of discharge and cavitation number, typically for periods of three runner revolutions. The pressure pulsations due to the dynamic properties of the aggregate cavitation volume were compared, resulting in an

interesting statistical description. The pulsation frequency in the given installation was found to follow an equation

$$f = 0.22/\sqrt{V_C} \tag{5.11}$$

As the natural frequency in a simple system may be assumed to be inversely proportional to $\sqrt{C_C I}$, it follows that the cavitation compliance is roughly proportional to the volume of the cavities, V_C, or, considering Eqs. (1.35), depends on the pressure by an exponential law.

While such promising results have been possible with the VoF method, more sophisticated methods will probably permit more realistic simulations in the future. The VoF method can only discriminate bubbles as big as the cells of the computational grid or larger. In Ref. [18], Vallier et al. describe a computation method that combines two possible descriptions dedicated to small and large bubbles, separately. The Eulerian grid used for large bubbles according to the VoF method is complemented by a somewhat coarser grid where individual bubbles of small size are described by a Lagrangian particle tracking method. The two methods are coupled by a scheme managing the transition of objects between the two descriptions.

References

1. Brennen, C. E. (1995). *Cavitation and Bubble Dynamics*. Oxford: Oxford University Press.
2. Jorgensen, D. W. (1961). Noise from cavitating submerged jets. *Journal of the Acoustical Society of America, 33*, 1334–1338.
3. Blake, W. K., & Sevik, M. M. (1982). Recent developments in cavitation noise research. *Proc. ASME International Symposium on Cavitation Noise* (pp. 1–10).
4. Franklin, R. E., & McMillan, J. (1984). Noise generation in cavitating flows, the submerged jet. *ASME Journal of Fluids Engineering, 106*, 336–341.
5. Arndt, R. E. A., Ellis, C. R., & Paul, S. (1995). Preliminary investigation of the use of air injection to mitigate cavitation erosion. *Journal of Fluids Engineering, 117*, 498–504.
6. Ulith, P. (1981). Cavitation limits in Francis turbines. *Voith Research and Construction, 3*.
7. Nennemann, B., & Vu, T. C. (2007). *Kaplan turbine blade and discharge ring cavitation prediction using unsteady CFD, IAHR WG (Cavitation and Dynamic Problems in Hydraulic Machinery and Systems) 2nd Meeting*, Timisoara Romania, October 24–26.
8. Arndt, R. E. A., Keller, A., & Kjeldsen, M. (2000). Unsteady Operation due to Cavitation. *Proceedings* Hydraulic Machinery and Systems 20th IAHR *Symposium*, Charlotte.
9. Boehm, R., Stoffel, B., & Ludwig, G. (1997). Investigations on the unsteady behaviour of cavitation and the corresponding pressure field. *La Houille Blanche 4/5* (pp. 84–88).
10. Dahlbäck, N. (2000). Analysis of a structural failure of a large draft tube. *Proceedings Hydraulic Machinery and Systems 20th IAHR Symposium*, Charlotte.
11. Sotnikov, A. A., & Pylayev, N. I. (1976). Some design means of reducing cavitation damage in hydraulic turbines in service. *IAHR Section Hydraulic Machinery, Equipment, and Cavitation, 8th Symposium, paper II-3*, Leningrad.
12. Malamet, S. (1962). Aeration of the turbines in the pumped storage plant Geesthacht (in German). *Elektrizitätswirtschaft 61*(8), 20 March 1962.

13. Doerfler, P. (1986). Design criteria for air admission systems in Francis turbines. *IAHR Section Hydraulic Machinery, Equipment, and Cavitation, 13th Symposium*, Paper 8 (Vol. 1), Montréal.
14. Stein, P., Sick M., Doerfler P., White, P., Braune, A. (2006). Numerical simulation of the cavitating draft tube vortex in a Francis turbine. *IAHR Section Hydraulic Machinery, Equipment, and Cavitation, 23rd Symposium*, Yokohama, Japan.
15. Dörfler, P. K., Keller, M. & Braun, O. (2010). Full-load vortex dynamics identified by unsteady 2-phase *CFD. 25th IAHR Symposium on Hydraulic Machinery and Cavitation*, Timisoara.
16. Keck, H., Grunder, R., Parkinson, E., Sallaberger, M., & Sick, M. (2004). *Examples of recent CFD developments and their applications in practical turbine design, hydropower—renewable and sustainable* (pp. 24–26). Austria: Vienna.
17. Tanaka, K, Sato, T., Inoue, A., Nagahara, T., Shimizu, F., Fuchiwaki, M. (2011). Numerical Study of Cavitating flows and Cavitation Surge in a Double-Suction Volute Pump System. *Proceedings 4th Meeting IAHR Workgroup on Cavitation and Dynamic Problems in Hydraulic Machinery and Systems*, Belgrade.
18. Vallier, A., Revsted, J., & Nilsson, H. (2011). Numerical procedure for simulating the break-up of cavitation sheet. *Proceedings 4th Meeting IAHR Workgroup on Cavitation and Dynamic Problems in Hydraulic Machinery and Systems*, Belgrade.

Chapter 6
Stability-Related Unsteady Phenomena

This chapter presents a number of common oscillation phenomena which are not due to a direct external force but due to a feedback mechanism which may depend on the response of a larger system. Accordingly, the frequency of this kind of fluctuation is dictated by a natural frequency rather than a forcing frequency. For example, if a small displacement in a turbine runner creates a labyrinth force that tends to increase the displacement, then this may suddenly start a whirling motion at a natural bending frequency of the shaft line.

Another example is the hydraulic circuit instability occurring when a pump turbine operates in the so-called S region where an increase of discharge is associated with a drop in head. Another case is a leaking seal in a closed shutoff device which may produce dramatic auto-oscillations in the water conduit if the leakage flow is reduced by increasing pressure.

In some cases, the instability does not fully develop but the reduced damping results in a resonant increase of an existing forced oscillation, as described here for a small turbine with inadequate labyrinth design.

6.1 Gap Flow Effects

6.1.1 Basic Mechanism

Gap flows not only in labyrinths and runner side chambers, but also in between the blades of a cascade, sometimes responding to displacement of the adjacent bodies in an unexpected way. In this chapter, we will show few examples where flow phenomena in the runner labyrinths, in particular of radial machines, produce an important interaction between the runner movement relative to the stationary parts, and the resulting pressure distribution in the labyrinth gaps. This pressure distribution produces a hydraulic reaction force that feeds back into the runner displacement. Depending on the design of the labyrinth, as well as the radial stiffness of the rotating
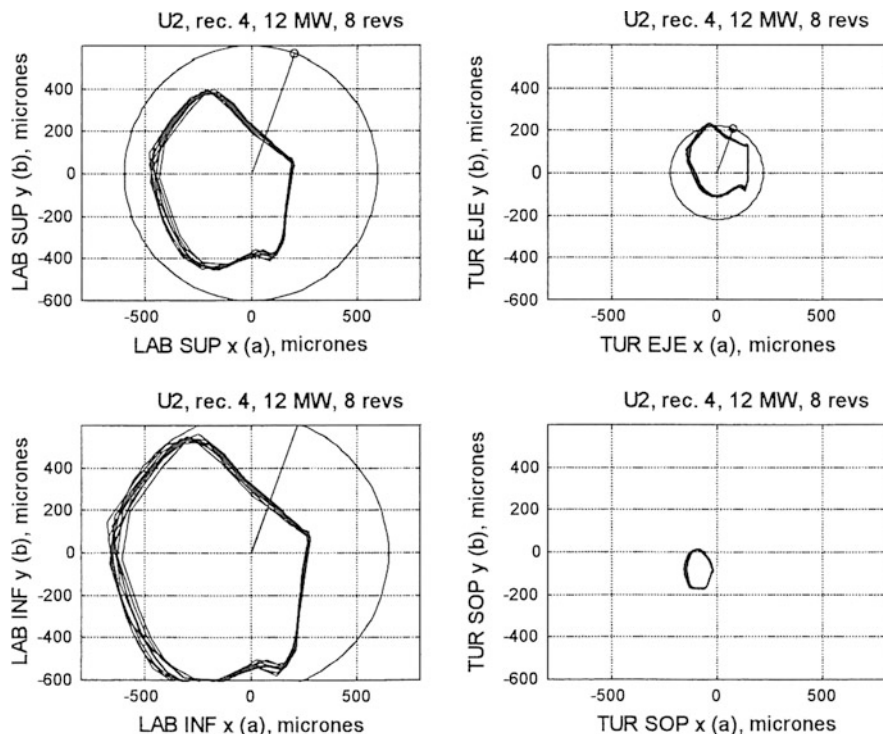
Fig. 6.1 Radial displacement affected by poor labyrinth design

parts, the feedback mechanism may drastically reduce the damping of the radial movement of the runner, or even provoke instability.

The destabilizing effect arises if a positive radial deflection of the runner is accompanied by a change in labyrinth force that tends to increase the deflection. In properly designed labyrinths, the opposite happens, just as in a stable journal bearing. The responding force acts in a sense that reduces the deflection and therefore stabilizes the radial oscillation of the rotating parts.

Figure 6.1 is an example for this destabilizing effect measured in a small vertical-axis Francis turbine with a rated speed of 720 rpm. Orbits of lateral movement are displayed for eight consecutive revolutions. The four graphs represent the following locations (Table 6.1).

The runner of this turbine has a relatively large overhang, and a standard guide bearing mounted atop of the head cover with rather poor radial stiffness. Deteriorating shaft vibration and bearing damages were encountered in the first year of operation. Scratch marks on the runner and lower labyrinth showed that mechanical contact had occurred at the labyrinth. Shaft vibration strongly increases with load. Figure 6.1 is the worst condition, measured at rated load. The circles shown in the graphs indicate the clearance of the respective seal or bearing. From the test results, it may be concluded that the radial vibration amplitude is

Table 6.1 Orbits of displacement shown in Fig. 6.1

Lower right	Guide bearing housing, relative to head cover
Upper right	Turbine shaft, relative to guide bearing
Upper left	Turbine runner hub, relative to upper labyrinth
Lower left	Turbine runner crown, relative to lower labyrinth

basically limited by the lower labyrinth ('LAB INF'), which explains the observations of wear as well as the bearing problems.

6.1.2 Destabilizing Labyrinth

The large overhang and soft guide bearing suspension was only part of the problem in the turbine illustrated by Fig. 6.1. An equally important ingredient was the use of a double-sided upper labyrinth. The nominal clearance of two gaps of the labyrinth was the same.

Figure 6.2 shows the original contour of the labyrinth on the head cover side, with a slight displacement of the runner to the right-hand side. The runner is at the bottom of the figure, the axis at the left-hand side—the runner exit diameter is only 1.0 m. In the original design, all four gaps of the labyrinth (1, 3, 5, 7) have the same radial clearance. In such an arrangement, the labyrinth produces a radial reaction force on the runner which has the same direction as the displacement. This force results from the different pressure development in the gaps at either side, as explained on the right-hand side of Fig. 6.2. If the runner is displaced toward side A, as shown in the left figure, then on this side the width of the outer gap (1, 5) gets smaller and the inner gap (3, 7) gets wider. The average local pressure in the outer gap drops on side A, see the right-hand side of Fig. 6.2. At the other side of the runner circumference (middle of right-hand diagram), the opposite effect occurs. Both sides contribute pressure forces acting on the runner in the same direction A, in a sense to increase the initial displacement.

The mechanism described above comprises several simplifying assumptions but was found to explain shaft instabilities in turbines and centrifugal pumps with double-acting labyrinth seals like the one shown above.

A more detailed model would have to replace some simplifications and, for instance, take account of the compensating flow in the annual gaps or the Lomakin effect [1].

6.1.3 Crown/Band Chamber Effects

Similar problems may occur in relation with the lower labyrinth. A highly instructive comparison between favorable and potentially unstable configurations has been given by Henry [2].
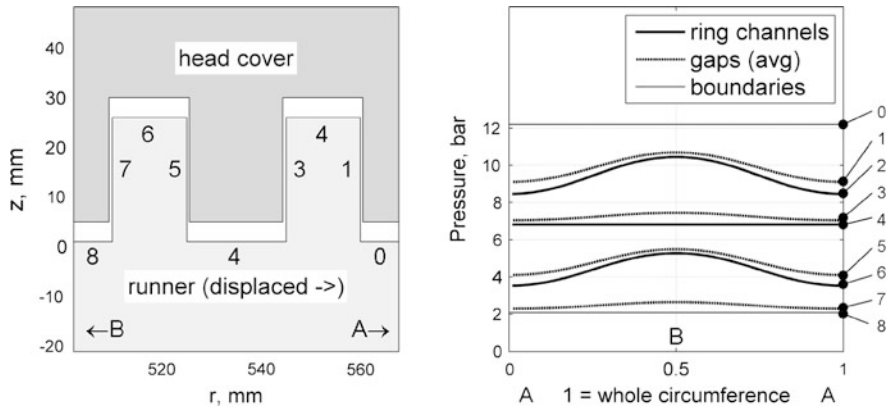
**Fig. 6.2** Contours (*right*) and pressure distribution (*right*) of *upper* labyrinth
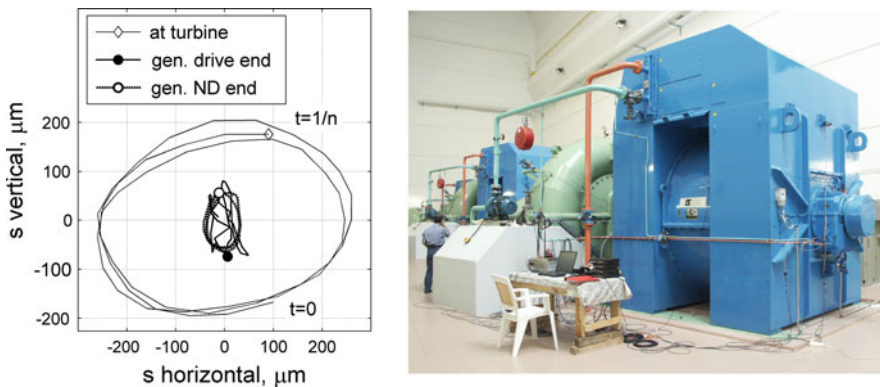
Fig. 6.3 Radial shaft displacement, view of generating set

If the chamber between the runner band and discharge ring is only a narrow gap, then the location of the lower labyrinth may become very important. An experience with a Francis unit with horizontal axis provides a typical example of this. The unit, shown in Fig. 6.3, is rated 9 MW at 600 rpm nominal speed. During commissioning, large radial vibration was found at all loads except speed no load. The dominating vibration frequency was almost constant near 26 Hz, or 2.6 times the runner frequency. This frequency represents the lowest natural bending frequency of the shaft line, thus indicating a condition of radial instability. The 2.6 orbits in Fig. 6.3, recorded at 6 MW, correspond to one revolution of the runner. The end markers indicate the phase among the three signals; the whirling motion occurs in the direction of runner rotation. The very large vibration at the turbine guide bearing is almost entirely composed of the 26 Hz component.

The band-side labyrinth in this turbine is located at the intake side, and there is only a very small clearance between the band and the bottom ring. It was
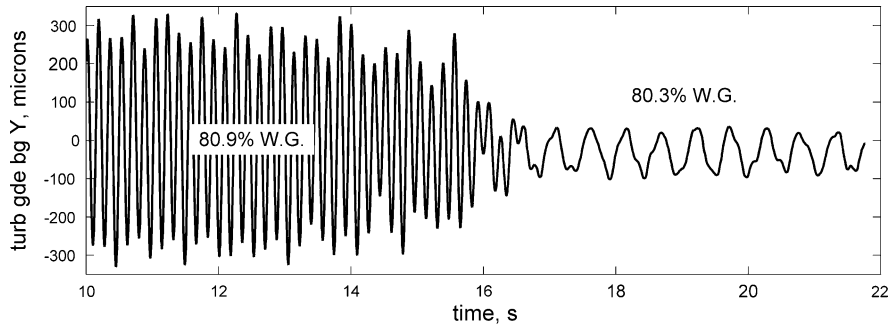
Fig. 6.4 Unstable and stable shaft displacement at the limit of stability

recognized that these features were responsible for the stability problem, and an additional labyrinth was placed at the downstream end of the runner band. As a consequence, the problem disappeared. The remaining shaft vibration at the turbine guide bearing was only $\pm 65\mu m$, composed almost entirely of the usual 10 Hz runner frequency component.

The underlying mechanism is quite similar to the one described in the previous section. A radial displacement of the runner toward side A reduces the labyrinth at side A, thus locally throttling the leakage flow at this side and causing a pressure drop in the narrow band chamber, together with the contrary effect on the opposite side of the runner. The result is a radial force which amplifies the displacement and reduces radial stability.

This effect is also possible in large units, depending on the design of the runner side chambers. Figure 6.4 demonstrates the sharp limit between stable and unstable behavior measured on a very large Francis unit. The radial shaft displacement at the turbine guide bearing normally occurs at the unit's frequency of revolution, with moderate amplitude as shown on the right-hand side of the figure. At slightly higher load, the stability limit is surpassed and an additional oscillation at the natural bending frequency of the shaft line prevails.

As usual with oscillations caused by instability, it is some nonlinear effect that defines the amplitude. In the case of unstable radial displacement, the critical nonlinearity is often the clearance of a guide bearing or labyrinth, whatever comes first.

Just as the side chamber adjacent to the band may cause instability, the side chamber adjacent to the *runner crown* may also cause instability if it is too narrow. Crawford and Ruud [3] reported a case of shaft whirl concerning a Francis turbine with medium specific speed. In this turbine, the problem was linked with the gap between the baffle plate used for axial thrust compensation, and the runner. Accordingly, admission of air into the gap below the baffle proved effective to restore stability. In the paper, the authors attribute the destabilizing feedback to the gyroscopic effect occurring due to deflection of the shaft and the runner.
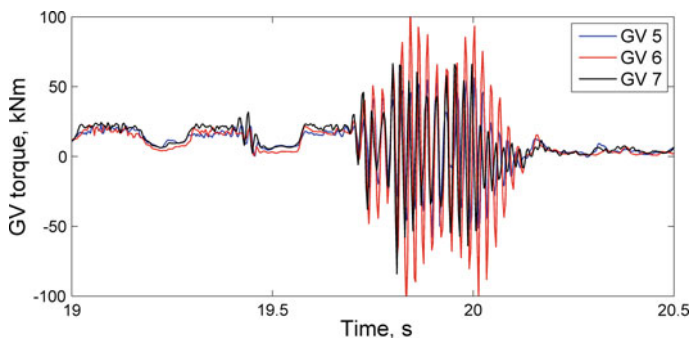
Fig. 6.5 Guide vane flutter at very small GV opening

The dynamic phenomena occurring in the crown and band chambers are not well understood, but some failures on the attachment of secondary devices located in these cavities indicate that these attachments should be carefully designed.

It appears that the concept of stability is not yet very well understood and that conditions of unstable shaft vibration are often misinterpreted. In some plants, the onset of instability depends on particular conditions of load, or tail water level. Thus, the true cause may be masked and too often effort is wasted on remedies that do not solve the problem.

6.2 Flutter of Guide Vanes

Even without a Von Kármán vortex street shed from the trailing edge, guide vane vibration may be caused by torque variation fed back from an oscillation of the vane. In some pump urbines, intense guide vane vibration with high frequency has been observed when the guide vane opening angle was very small and discharge was in the sense of pumping. The frequency of vibration is the natural frequency of the guide vane's torsion mode.

An example for this kind of instability, observed at a low-head pump turbine, is shown in Fig. 6.5. In the figure, the guide vane torque measured on three adjacent guide vanes is plotted. The flutter episode was observed during pump shutdown, at a very small guide vane opening of 1.5 degrees and below.

An early description and analysis of this phenomenon was given by Pulpitel [4] who also established a stability criterion. The main result of his study was that increasing the ratio of radii R_2/R_1 improves stability. R_2 and R_1 are the radii between the guide vane axis and the point of contact with the outer and inner neighboring vane, respectively. The study also included a hydro-elastic model test and this demonstrated additional influences which are well in line with intuition: the region of unstable behavior can be reduced or suppressed by increasing the

torsional stiffness, the friction torque, or by reducing the effective length of the gaps between adjacent vanes.

More recently, a detailed investigation into this phenomenon has been made combining unsteady CFD computation with variable geometry, with the flow contour changing due to the guide vane vibration [5]. This work revealed some additional effects which can play a role in the oscillation mechanism. One mechanism is called bi-stable flow by the authors of the paper. The meaning of this term is that the jet produced between neighboring vanes alternately attaches to either of the vane. Depending on the guide vane design, this phenomenon could also occur at slightly larger guide vane openings, between 4.5° and 5°.

Another effect discovered in this CFD study was the shedding of Von Kármán vortices triggered by the vibration and feeding back due to the pressure variation produced on the neighboring vane.

6.3 Penstock Auto-Oscillation: The 'Leaking Seal' Effect

6.3.1 Basic Mechanism

Pressure oscillations occurring in penstocks may attain dangerous amplitudes if they are caused by phenomena with little or no damping. In normal operation, the occurrence of extreme pressure amplitudes is usually prevented by dissipation effects. The most effective damping device is the hydraulic machine itself whose flow characteristic normally acts as a throttle inserted in the hydraulic conduit. In addition, friction effects in the moving water column also tend to reduce the amplitudes in case of hydraulic resonance.

By contrast, the damping effect associated with oscillations of the enclosed water column at little or no discharge is extremely small. Given some kind of periodic excitation, very high amplitudes of pressure are possible. While forced oscillations are not likely in such a condition, the possibility of self-excited oscillations is quite real. The 'usual suspect' is a closed valve at the downstream end of the penstock. Some types of valves, for instance spherical valves, have a movable seal which is engaged after the rotating part of the valve is in closed position. The closing of the seal is performed using pressurized water. If the seal always remains tight, then no problem may arise. If the sealing effect is not perfect, for instance if the filter used for the operating fluid is clogged, stability depends on the leakage characteristic. If the sealing effect is improved by rising penstock pressure, and lower penstock pressure leads to more leakage, then a feedback between the leakage flow and the penstock pressure starts because even the smallest pressure disturbance travels up the penstock and is reflected at the surge tank or intake. Taking into account the very small damping ratio, a resonant oscillation becomes very likely. An incident of this kind, caused by deteriorated pressure of the service seal, has been described by Ehrhart [6], a similar one by Pérez [7].

Based on field test results reported by Habán [8] and Dörfler [9], a typical damping ratio of the first natural mode of fluid oscillation in a closed, fairly uniform penstock would be about 1.5 %. For the purpose of illustration, let us consider a 300 m long penstock with a cross section of 5 m^2. The velocity of wave propagation is assumed to be 1,200 m/s, corresponding to an oscillation period of one second. At the first natural frequency (1 Hz), the hydraulic impedance at the downstream end of the pipe is $Z_{max} = 1{,}040$ s·m^{-2}. If a valve at this location would have a negative discharge characteristic $dQ/dH = -1/Z_{max} = -0.00096$ m^2/s, then the damping effect due to unsteady pipe friction would be just cancelled; the system would be at the stability limit. If the negative slope was to become larger, then the destabilizing effect would increase further and an auto-oscillation with a frequency of 1 Hz would set in. A doubling of this negative slope of the seal characteristic would mean a negative damping $\zeta = -0.015$. According to the explanations in Sect. 1.4, this would mean a doubling of the pressure auto-oscillation amplitude in the penstock every $0.11/\zeta = 7.3$ cycles, so that the oscillation would grow very fast.

Apart from effects of wear or insufficient actuating pressure, defective control of the service seal can also cause auto-oscillation. A near accident caused by failure to actuate the seal has been reported in [10].

An imperfectly sealing valve is probably not the only possible kind of exciter. Under certain conditions, the guide vanes in a turbine or pump turbine could theoretically produce a similar effect. For instance, if the guide vanes are near to the closed position in pump operation, and the priming pressure from the impeller tends to close the wicket gate, then this tendency, together with some elasticity in the wicket gates and operating mechanism may temporarily create a behavior similar to the leaking seal. It is not clear if this mechanism actually occurs in reality, as no actual cases are known to the authors. Such a case would differ from the mechanism described in Sect. 6.2 by having a much lower frequency.

6.3.2 Characteristic Features

As usual, the item limiting the amplitude in such pulsations is nonlinearity. The typical limiting nonlinear effect in this kind of oscillation would be cavitation occurring somewhere in the conduit. The pressure in any part of the water conduit cannot drop below the vapor pressure. If the conduit has no 'high point', and the auto-oscillation occurs with the simplest possible mode shape (one half-wave), then it is conceivable that cavitation starts at the location of highest amplitude, i.e., at the downstream end of the penstock. In such a case, one may expect that the maximum pressure caused by the auto-oscillation becomes roughly 200 % of the normal static pressure. At such amplitudes there is already a danger of serious damage to some part of the water conduit.

Throughout the twentieth century, there have been several spectacular cases of failures of penstocks or power tunnels which have been documented in the

literature. Looking back, not all of them can clearly be associated with the auto-oscillation mechanism described here. Important cases have been described by Jaeger [11] and Wylie and Streeter [12]. The precise nature of the pressure oscillations, their mode shape, has in some cases been identified in retrospect, due to the damages observed in the water conduit. In plants having a pressurized tunnel and surge tank it was found that the location of the surge tank is crucial for development of an unstable mode of auto-oscillation. In particular, the pressure oscillation in the penstock and power tunnel must have a common pressure node (point where the pressure amplitude is very small) at the surge tank. Such modes may sometimes correspond to unexpected high frequency, with several half-waves distributed along the conduit in a suitable way. For instance, three stretches of the Kandergrund power tunnel [11] were damaged repeatedly in the early twentieth century, indicating that the auto-oscillation mode consisted of three half-waves between the headwater and surge tank.

In the case of Bersimis II [12], several auto-oscillation events have been observed in the early 1960s due to inadequate sealing pressure at the different ends of the penstock manifold. In this station, the oscillation modes have for the first time been identified by modern impedance analysis. Observations in Bersimis II also confirmed the occurrence of twice the static pressure, as explained in the previous section.

6.3.3 Countermeasures

Taking into account the large amplification of pressure, this phenomenon has to be taken very seriously. The use of well-proven valve designs, together with careful maintenance, is essential in order to avoid auto-oscillation.

If hydraulic resonance occurs in the water adduction for some reason, there is also an operational remedy possible which has already been proven effective. Starting a unit or opening a valve immediately creates a damping effect that helps to suppress the oscillation.

6.4 Pump and Pump-Turbine Instabilities

6.4.1 Pump Instability due to Excessive Head

Unstable pump operation is not acceptable and has to be avoided by proper pump layout for the given application. An operating condition is hydraulically stable if the difference of head between the steady-state characteristics of the water conduit (thin curve in Fig. 6.6) and the pump (bold curve) increases with increasing flow. In this case, any deviation from equilibrium will result in a system response
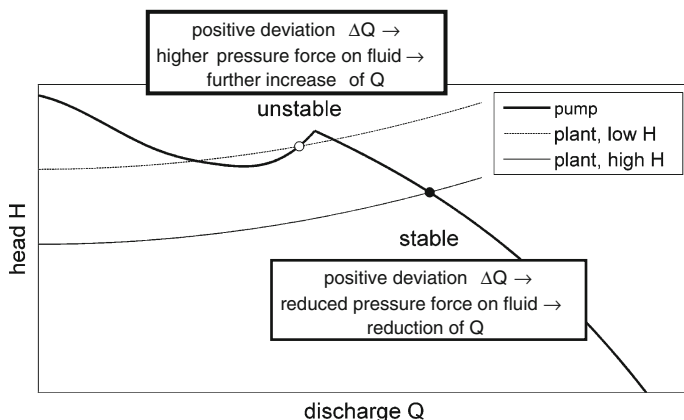
Fig. 6.6 Unstable and stable pump operation

counteracting the deviation (black marker). By contrast, in an unstable region of the characteristic (white marker), any slight deviation will be amplified, causing the operating point to run away or oscillate.

There are several fluid dynamic mechanisms which can lead to an unstable pump head characteristic exhibiting a region in which the head characteristic falls with decreases in flow, and these are described in detail by Gülich [13]. The mechanisms include rotating stall, inlet or outlet recirculation, or transitions between different flow patterns within the pump flow channels. Measurements on pump turbines at different guide vane setting angles have identified that the kink at the peak of the characteristic is often associated with the onset of rotating stall in the guide vanes, see Eisele et al. [14]. In a pump turbine model with low-specific speed, the rotating stall occurring at part load in pump operation has been studied by Braun in the Hydrodyna project [15]. Quite different from the rotating stall in turbine brake mode (Sect. 6.4.3), this stall pattern typically consisted of four stall cells and was rotating at a very low speed, only about two percent of the runner's speed.

The increased losses associated with the rotating stall cause a drop in the head characteristic. The unsteadiness of the flow is a local phenomenon causing a change in the operating characteristic but the unstable operation is a system response related to the shape of the characteristic.

If a pump operates close to the stability limit, this condition may be first noticed by the fact that the omnipresent small spontaneous fluctuations of line pressure start to increase significantly. The pump may still remain stable but the operation gets rough and noisy. Under these circumstances if the head is slightly increased, the discharge may drop temporarily, see Fig. 6.7 for an example. The figure shows a transient involving two pump turbines with a common penstock, one of them (unit 1) having an insufficient characteristic of pump head. In the beginning, only unit 1 is pumping; then unit 3 (cyan curves) starts pumping as indicated by the guide vane opening Y3 and power P3. The resulting slight upsurge of the common
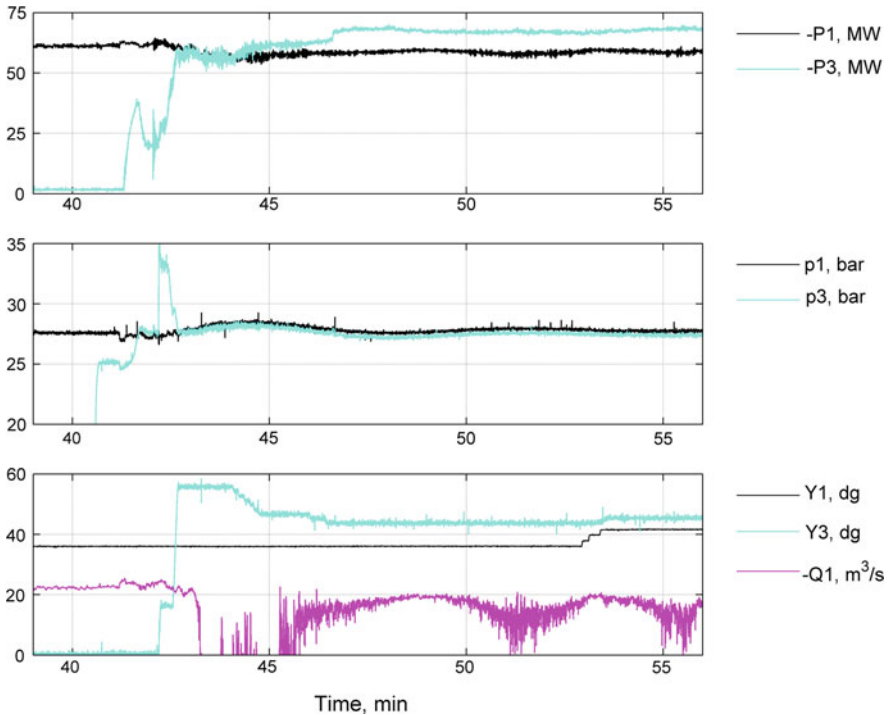
Fig. 6.7 Pump operation at the stability limit

surge tank makes the penstock pressure in the middle graph increase and unit 1 reaches the stability limit. The discharge Q1 (magenta) breaks down and the machine enters a condition with high vibration.

In case of regulated pumps or pump turbines, the useful head range depends to some extent on the setting of the guide vane opening. In some cases, the pump may come too close to the stability limit because the guide vane opening is not controlled in an optimal way. Typically, the guide vane angle may be too large as the high-head limit is approached.

6.4.2 Pump Turbine Instability due to S-Shaped Characteristics

Also, in turbine operation, a pump turbine may become hydraulically unstable. At high speed coefficients n_{ED}, the performance curves $Q_{ED}(n_{ED})$ for a constant guide vane opening angle α often have three different Q_{ED} values for a given n_{ED}, in particular for bigger guide vane openings. On the other hand, for a machine operating at constant speed, this means there are three possible values of discharge
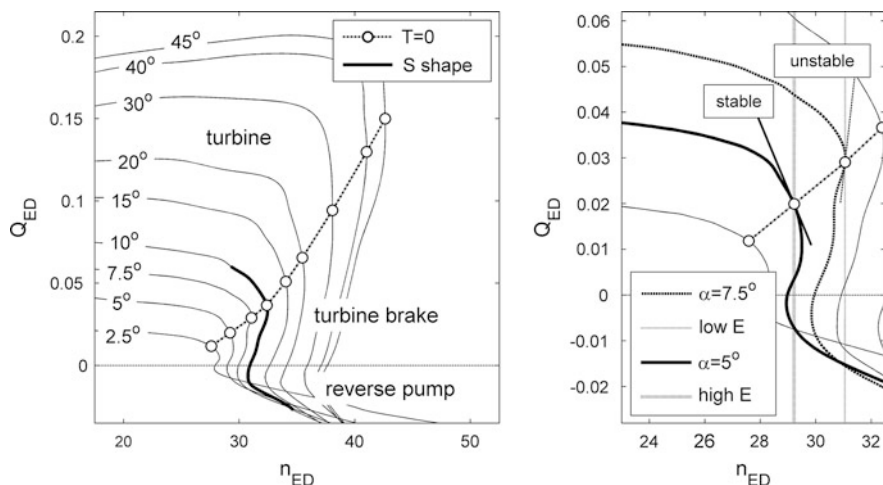
Fig. 6.8 'S shaped' characteristics near the runaway curve

Q for the same net head H. This behavior is called the S-shape characteristic, see Fig. 6.8.

Figure 6.8 shows the shape of the characteristic that may lead to stable or unstable behavior at speed-no load ($T = 0$ in the figure). Stability depends on the sense in which the performance curve intersects with the steady-state flow characteristic of the water conduit (indicated by the gray, almost vertical curves in the right-hand graph of Fig. 6.8). The logic of reasoning is the same as for stability in the pump mode, see Sect. 6.4.1, and in this case a positive slope of the flow versus head characteristic is stable because here we use a positive sign for flow in the turbine sense.

This issue of stability is mostly concerned with the starting process in turbine operation. The operation point of interest is the speed no load point for various values of operating head, or energy E (see Fig. 6.8). If this point is not stable, then the turbine is very difficult to synchronize because the ensuing oscillation of head and flow entails at the same time, also an oscillation of shaft torque and speed. A method how to estimate the period of the pulsation has been published by Martin [16]. In general, the risk of instability at speed no load increases with increasing guide vane opening, i.e., with decreasing head.

The difficulties with turbine control at synchronization already start at some distance from the hydraulic stability limit. There are basically three ways to improve stability in the S-shaped region. Two of them are described in [17], and in Sect. 8.3.2 of this book. If the turbine has to be started in the stable range close to the limit of stability, the speed governor function may be improved by using the penstock pressure as an auxiliary input in the turbine governor. This method enables satisfactory operation closer to the hydraulic stability limit, but not beyond.

The other method actually stabilizes the hydraulic system, using the main inlet valve as a damping device. At start-up, the valve is not opened completely but only partially, for instance to 20 % opening. At this opening, the start and synchronization in turbine mode is performed without any problem of instability. The explanation is that, if the turbine and valve together are regarded as an ensemble, then the discharge characteristic of this ensemble is stable; the variable head loss of the valve adds to the turbine head. This artifice indeed works perfectly well. However, this method is only acceptable if the unit does not have to be directly resynchronized out of a load rejection. Obviously, the main inlet valve must not close to a partly closed position because this would prevent its role as a safety device. Therefore, the stabilizing effect of the valve would not be available after load rejection, and instability would result if the unit is not shut down.

The third, and most universal way to overcome the instability is called the 'misaligned guide vane' method, originally described in [18]. Since its introduction around 1980, it has been used by several pump turbine suppliers as a method of last resort. Two guide vanes at opposite sides of the machine are first brought to a large opening while all the other guide vanes are used for regulation as usual. The two water jets entering the impeller through the channels of the over-opened vanes produce a stable behavior of the turbine over a sufficient range of guide vane openings. Some caution must be exerted because of possible increase of shaft vibrations at blade passing frequency. It may be necessary to counter this shortcoming by choosing vanes that are not 180° displaced from each other if the runner has an odd number of blades.

6.4.3 Numerical Simulation

The flow near no-load operation of turbines is highly irregular and dominated by backflow zones as well as vortex formations in all parts of the turbine (Fig. 6.9) so that numerical flow simulation is very challenging. Regions of recirculation reach from the vaneless space into both runner channels and guide vanes. Thus, the turbine runner acts partially as pump and partially as turbine. These flow patterns are time dependent in nature. Consequently, CFD methods need to be time dependent in order to provide a realistic flow prediction. Furthermore, grid resolution has to be very good in order to capture the details.

Staubli et al. [19] showed some first validation of CFD simulations of a pump turbine in turbine mode along the characteristic toward runaway. Experimental performance data obtained in a model test were used for validation. In a first step steady-state CFD simulations were carried out in order to limit the computational effort.

Although the strongly unsteady flow features are not taken into account, the CFD prediction for pressure coefficient follows the measurement well but with a considerable offset, see the circle symbols in Fig. 6.10. As expected, transient simulations lead to a better agreement between prediction and measurement data.
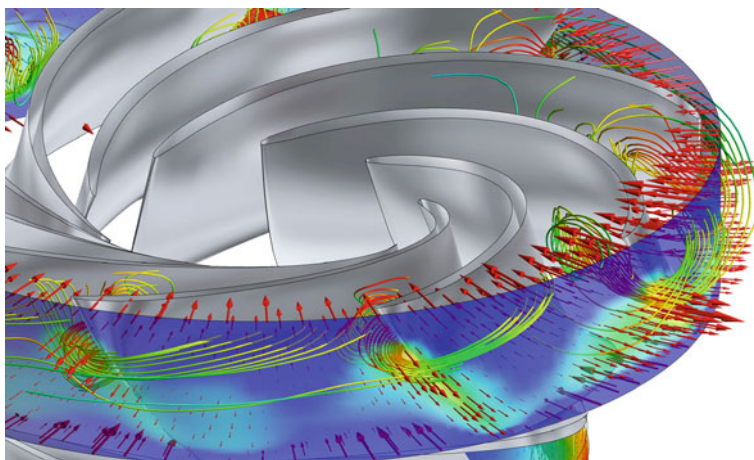
Fig. 6.9 Flow through a control surface between guide vanes and runner

In the case displayed, the CFD results do not reach sufficient stability in order to be directly compared to the steady-state measurements. This is certainly due to the unsteady nature of the flow and also due to the imperfections of the CFD model.

In an attempt to still evaluate the CFD results, the authors estimated a smoothed curve of the pressure coefficient ψ versus flow coefficient φ. The smoothed curve reveals a zone of 'unstable' (negative) slope of the characteristic curve near runaway ($\varphi_1 \cong 0.02$).

CFD prediction of operating conditions far away from design remains a very challenging topic for further research. Systematic studies of grid dependency, detailed validation of turbulence models and boundary conditions have still to be done as well as more detailed validation of CFD results versus pressure and velocity measurements. Here, the difficulty of obtaining good measurement data both in model and in prototype should be emphasized. As measurements of the unsteady pressure field in the runner and in the draft tube are difficult and very expensive to obtain, thorough validation of unsteady CFD simulations of the flow near no-load condition is a major task for research activities in the future.

6.4.4 Rotating Stall in Pump Turbines, Turbine Brake Quadrant

Apart from turbine instability, the S-shaped region of the pump turbines also has other peculiarities. In the 'recurrent', unstable branch of the S, where the speed factor n_{ED} is reduced with decreasing flow, many pump turbines exhibit a phenomenon of single-cell rotating stall. The lower inflection point of the S is typically at or close to the zero discharge condition. Below this point is what engineers call
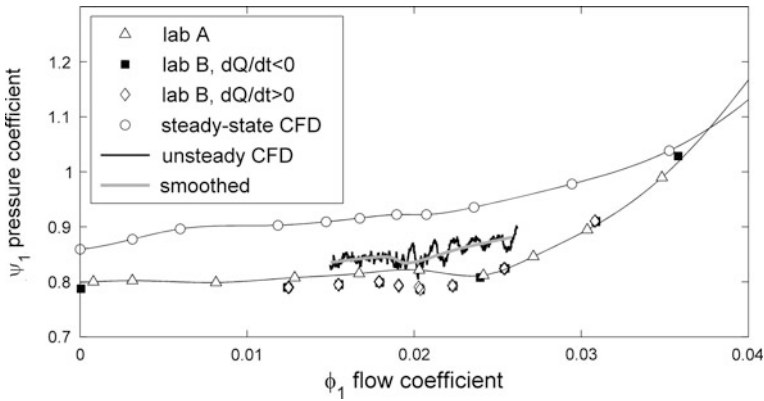
Fig. 6.10 Flow characteristic of a pump turbine near speed no load

the *reverse pump* area, see Fig. 6.8. The machine is pumping due to sufficient circumferential speed, but at the 'wrong' sense of rotation. Above the $Q = 0$ limit the overall flow is still in the turbine sense, but at the same time there are also zones of backflow at the outer runner diameter.

Figure 6.11 gives evidence for the occurrence of a rotating stall phenomenon. Two pressure transducers are used to measure pressure pulsation in the vaneless annular space between the guide vanes and runner of a low-head pump turbine. The sensors are displaced by 120° in the circumferential direction. The diagram shows test data obtained at a constant guide vane opening of 45°, as a function of the dimensionless discharge coefficient φ_1, focusing on the range of operation as a 'turbine brake' between zero discharge and zero torque. The flow characteristic of head coefficient ψ_1 versus. φ_1 is shown by the curve with 'diamond' markers; the shaded area where rotating stall occurs is also the range of strongly negative (unstable) slope of the flow characteristic. The curves of peak–peak pressure pulsation amplitudes, using average amplitude of the two sensors, are marked by triangles. The two curves differ by the frequency interval evaluated. The dominating pulsation component is the narrowband phenomenon Δp_{NB} (black symbols) with a frequency of 56–60 % of the runner frequency, whose peak-to-peak amplitude reaches about 50 % of the net head.

The phase shift between the two pressure signals corresponds well to their angular displacement of 120°. This means that a strong pressure disturbance travels along the annular space in the sense of runner rotation but only at 56 % of the runner speed. The same phenomenon also creates a periodic fluctuation of the guide vane torque; the torque signals from several guide vanes have the same frequency as the pressure signals, and their relative phase shifts are likewise equal to their difference in circumferential position. In a comparable pump turbine model, Staubli [20] detected a strong rotating radial force acting on the runner, in the same range of operation, and also rotating with the runner at approximately 60 % of runner frequency.
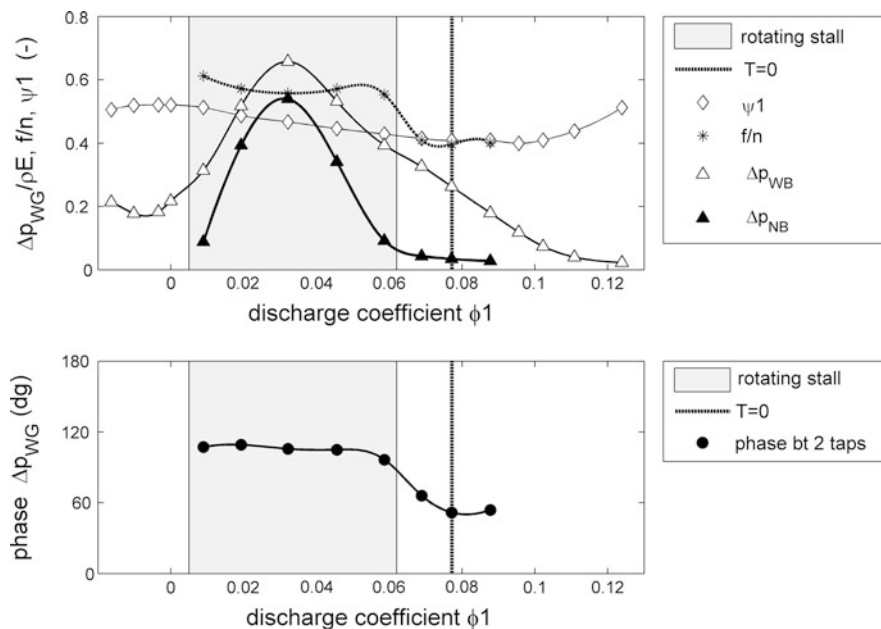
Fig. 6.11 Wicket gate pressure pulsation due to rotating stall

Tests on several models with different specific speed revealed that this phenomenon of rotating stall is quite typical in the turbine brake region, and is responsible for very high runner shaft vibrations in transient operation at high gate opening beyond the runaway point. For example, in a large high-head pump turbine, rotating stall has been identified during load rejection, as Pulpitel reported [21].

6.4.5 Pump Turbine Instability Influenced by Hysteresis

In addition to the S-shape of the turbine characteristic, there are other phenomena that may result in hydraulic instability. The runner blade profile of a radial pump turbine is largely dictated by the more difficult requirements of good performance as a pump—it is a pump impeller rather than a turbine runner. Therefore, the turbine behavior at high speed is not as perfect as in a Francis turbine, as can already be seen from Sects. 6.4.2 and 6.4.3.

A few pump turbines exhibit at high speed and low load a characteristic called hysteresis. If the point of operation (e.g., the transient discharge at given speed) is shifted along the characteristic for a particular, constant guide vane opening, the resulting transient head may suddenly leave the characteristic curve and switch over to a different one. As the flow changes further, the head remains on the new characteristic. If the direction of change is reverted, the point remains on the

changed curve until it switches back to the original characteristic. This switching back occurs at a flow different from that of the first change. Therefore, the back-and-forth changes describe a figure called *hysteresis*.

The existence of two different characteristics for the same flow indicates there are different flow regimes in the runner possible for the same discharge coefficient. A description of such a phenomenon has been given in the 1970s by Yamabe [22]. If the flow is decreased from a region of well-ordered flow patterns in the flow channels, with little separation and attached flow, then the transition occurs from non-separated flow to separated flow. In the reverse direction, the flow is already disordered and does not necessarily switch back to an ordered flow at the same discharge. It appears likely that the hysteresis phenomenon may produce unstable behavior in some cases. A case where this rare phenomenon showed up is described in the Sect. 8.3.3. The hysteresis at this particular pump turbine was not detected in the model test but appeared only out of the analysis of a 'strange' system instability with rather low frequency.

Some hints about how to deal with a hysteresis phenomenon in the development stage have also been given by Yamabe in a later publication [23].

6.4.6 Precautions Recommended for Commissioning

Experience has shown that stability prediction based on the shape of characteristic curves obtained in the model test is not absolutely reliable. In some cases, instability may only be detected on the prototype unit. To minimize any risk resulting from this uncertainty, it is recommended to perform a stability test in an early stage of commissioning. It is practical to split the test in two parts. First, hydraulic stability can be tested with the speed governor not active. The no-load behavior of the turbine shall be checked up to a certain speed

$$n_{\max} = n_{\max,\text{grid}} * \left(H/H_{\min,\text{transient}} \right)^{0.5} \qquad (6.1)$$

If this test has shown no instability, then it can be repeated with the speed governor activated.

Many pump turbines are used for network regulation, and are often operated in partial load. This means that, with the usual setting of the overspeed protection switch, a runaway condition starting from partial load may not be detected. In an ordinary reaction turbine, this would present no particular risk, but in a pump turbine it is possible that the runaway condition is unstable. In such a case, the machine would start oscillating between the turbine and turbine brake quadrants, as shown by Martin [24], with increased vibration in the time intervals with negative torque. It is even possible that a phenomenon like that described in Sect. 6.4.4 may occur—which is not likely to be detected in the model testing phase. Considering this uncertainty, it makes sense to protect the units against runaway from partial load.

This can be done using one of the usually two over speed triggers which are installed. It can be set at reduced speed (for instance, 110 %) and, in order to avoid a shutdown from occurring in case of any ordinary load rejection, this switch should be activated with a suitable delay (for instance, 20 s). Normally, the speed is restored within this time frame, and no shutdown is executed.

References

1. Lomakin, A. A. (1958). Calculation of the critical speed and the conditions to ensure dynamic stability of the rotors in high pressure hydraulic machines, taking account of the forces in the seals (in Russian). *Energomashinostroenie, 14*(4), 1–5, see also Brennen, C. E. (2011). *Hydrodynamics of Pumps*, Cambridge University Press, also as: Chapter 10 in http:// authors.library.caltech.edu/25019/3/pumbook.pdf.
2. Henry, L. F. (1991). *Some unusual vibrations in hydro machinery*. Waterpower'91, pp. 2224–2233.
3. Crawford, C. C., & Ruud, F. O. (1967). Self-excited vibration of a hydraulic turbine. *Journal of Engineering for Power, 31*, 573–576.
4. Pulpitel, L. (1982). Self-excited vibration of pump-turbine guide vanes. *IAHR section hydraulic machinery, equipment, and cavitation, 11th symposium, Amsterdam*, vol. 2, Paper 40.
5. Nennemann, B., & Parkinson, E. (2010). YiXing pump turbine guide vane vibrations: Problem resolution with advanced CFD analysis. *25th IAHR symposium on hydraulic machinery and cavitation, Timisoara*.
6. Ehrhart, R. W. (1979). Auto-oscillations in the Hyatt plant's penstock system. *Water Power and Dam Construction, 31*(4), 38–41.
7. Pérez, H. (1982). Resonant waterhammer: A case study. *Water Power and Dam Construction, 4*, 42–43.
8. Habán, V., Pochylý, F., & Fialová, S. (2009). The second viscosity of fluids. In *Engineering Mechanics 2009* (pp. 349–359), Prague, Czech Republic, Institute of Theoretical and Applied Mechanics, v.v.i. 2009.
9. Dörfler, P. K. (2011). Pressure wave propagation and damping in a long penstock. *IAHR work group on cavitation and dynamic problems in hydraulic machinery and systems, 4th international meeting, Belgrade, Serbia*.
10. Obermoser, H. (2011). Unexpected occurrences during rehabilitation work. In *Proceedings of Hydro 2011, Prague, Czech Republic*.
11. Jaeger, C. (1982). Resonance in hydropower systems. *Water Power and Dam Construction*, pp 20–22.
12. Wylie, E. B., & Streeter, V. L. (1965). Resonance in bersimis No. 2 piping system. *Journal of Basic Engineering, ASME, 87*(4), 925–931.
13. Gülich, J. F. (2008). *Centrifugal Pumps*. Berlin: Springer.
14. Eisele, K., Muggli, F., Zhang, Zh., Casey, M., Sallaberger, M., & Sebestyen, A. (1998). Experimental and numerical studies of flow instabilities in pump-turbine stages. *IAHR section on hydraulic machinery and cavitation, 19th symposium, Singapore*.
15. Braun, O. (2009). *Part Load Flow in Radial Centrifugal Pumps*, EPFL Thesis no. 4422, Ecole Polytechnique Fédérale, Lausanne.
16. Martin, C. S. (1986). Stability of pump turbines during transient operation. *5th international conference on pressure surges* (pp. 61–71), BHRA, Hannover.
17. Doerfler, P., Engineer, A. J., Pendse, R. N., Huvet, P., & Brahme, M. V. (1998). Stable operation achieved on a single-stage reversible pump-turbine showing instability at no-load. *IAHR section on hydraulic machinery and cavitation, 19th symposium, Singapore*, vol. I, pp. 430–440.

18. Klemm, D. (1982). Stabilizing the characteristics of a pump-turbine in the range between turbine part-load and reverse pumping operation. *Voith research and construction,* vol. 28e, Paper 2.
19. Staubli, Th., Senn, F., & Sallaberger, M. (2008). Instability of pump-turbines during start-up in the turbine mode. *Proceedings of Hydro 2008, Ljubljana.*
20. Staubli, T. (1987). Some results of force measurements on the impeller of a model pump-turbine. *IAHR work group on the behaviour of hydraulic machinery under steady oscillatory condition, 3rd meeting, Lille, P. 8,* 1–11.
21. Půlpitel, L., Kopřiva, M., & Zavadil, Z. (1996). Experiences from commissioning of 300 MW pump-turbines at Dlouhé Stráné pumped storage plant (in German). *9th International Seminar Hydropower Plants, Vienna.*
22. Yamabe, M. (1971). *Hysteresis characteristics of francis pump-turbines when operated as turbine*, ASME Paper No. 70-FE-D.
23. Yamabe, M. (1971). *Improvement of Hysteresis Characteristics of Francis Pump-Turbines When Operated as Turbine*, ASME Paper No. 71-WA/FE-28.
24. Martin, C. S. (2000). Instability of pump-turbines with S-shaped characteristics. In *Proceedings of the 25th IAHR Symposium on Hydraulic Machinery and Systems, Charlotte.*

Chapter 7
Model Tests, Techniques, and Results

In hydropower projects, model tests using a reduced-scale model are well-established practice regulated by international standards [1]. Measurement of unsteady phenomena, like pulsation of pressure or guide vane torque in the model is also widely used. Systematic comparison of test results from many projects in a physically sensible way has permitted 'generic' data describing the normal behavior of a certain type of machine to be established. Such data, which have not been publicly available before, are presented here to enable planners to formulate realistic specifications, and to make the assessment of measured pulsations more rational.

In some respects, the predictive value of a model test is not always absolutely clear because normally not all relevant laws of similarity can be fulfilled. These limitations are explained, and it is indicated which data are transferable from model to prototype and which are not.

7.1 Similarity Considerations

Kinematic similarity determines the model test conditions based on the steady-state performance. In order to reproduce the same energy change the blade speed and head has to be the same in both model and prototype so the rotational speed of the model should be increased in proportion to the size of the prototype relative to the model. As it operates at the same tip speed but is smaller the model has a smaller Reynolds number than the prototype so that even in terms of steady-state performance the fluid dynamic similarity is never exact. In fact the actual blade speed and head are often also scaled from those of the prototype so that the speed of rotation relative to the wave speed in the liquid (the Mach number of the flow) is also not dynamically correct. The effect of the difference between Reynolds number in the model and prototype is corrected by standards determined from experience. The effect of a change in Mach number has no marked effect on the hydraulic performance but is relevant to the pulsation behavior.

Since many decades, reduced-scale model tests have been used to examine, in addition to the steady-state performance, also their unsteady behavior. Since then, suppliers of hydraulic machines have also been concerned with questions of transferability between the model test results and the prototype machine [2, 3]. Model testing has important advantages. It is performed in an early stage of a project when improvements are possible at relatively low cost. Apart from that, visual observation of flow including the cavitation phenomena at the runner and in the draft tube, which are important for assessing the unsteady behavior [4] are only possible in a model.

For the correct reproduction of unsteady pulsations in the reduced-scale model, it is necessary, but not sufficient, to fulfill all the criteria that hold for testing the steady-state performance. It is necessary because the steady-state flow patterns are the basis on which the unsteady phenomena develop. It is, unfortunately, not sufficient for a number of reasons:

- Similarity of large cavitation zones, like the draft tube vortex, requires Froude similarity. In tests for very large prototypes, this would result in extremely low levels of net head and suction head that are not practicable.
- Propagation and interference of pressure waves inside and outside of the machine calls for hydro-elastic similarity (maintaining the ratio between the machine dimensions and the wavelength).
- If both model and prototype operate with the same working fluid, then the hydro-elastic and Froude similarity together would require 1:1 scale, in contradiction to the concept of a reduced-scale model.
- Some parts of the fluctuations inevitably interact with external systems connected to the model. The respective boundary conditions impose additional similarity requirements that are normally not fulfilled. Such external systems are the upstream and downstream water conduits of the test installation, as well as the brake or generator connected to the runner shaft.

This situation does not render dynamic model tests worthless but it is necessary to differentiate between items that are reasonably similar in model and prototype and others that are not. In a general sense, the transferable items are those directly linked with local flow variations, traveling with flow velocity or related to the blade circumferential speed. Examples are the asynchronous[1] and stochastic parts of draft tube pressure variation, the local pressure fluctuation between the runner and guide vanes caused by rotor–stator interaction, and the corresponding guide vane torque pulsation, and the fluctuation of any radial force acting on the runner, in particular in pump turbine models [5, 6]. These data are transferable to the prototype while others are not, as the following examples demonstrate.

The synchronous component of the draft tube pulsation is the result of an oscillation including the entire fluid column in the water conduit. The mechanism of this pulsation is explained in Sect. 1.4. Important features of the synchronous pulsation are, in the order of descending degree of similarity, the fluctuations of

---

[1] For explanation of the DTPP components, see Sects. 2.1.2, 7.2.1, 7.2.3.

- synchronous pressure in the draft tube cone
- axial thrust
- pressure pulsation in the turbine intake
- turbine discharge
- runner torque.

The potentially transferable quantity would be the pressure source Δp_{EX} forcing the synchronous pulsation, which from dynamic similarity can be scaled with the square of blade speeds in the model and prototype. But this quantity is normally not measured; it can only be extracted from measurements under certain conditions, an example discussed later in Sect. 7.2.3. The synchronous component of pressure in the draft tube cone often remains fairly transferable, namely, if the following conditions are fulfilled:

- Homology of the entire downstream conduit between runner exit and tail water, that is, they are geometrically similar apart from the scale.
- Constant pressure at the downstream end (large tank) in the test rig.
- Rather long intake pipe (i.e., intake impedance much higher than draft tube impedance).
- Test condition sufficiently different from draft tube resonance.

The same holds for the intake pressure, but to a somewhat lesser extent because the location—upstream of the turbine impedance—is already more sensitive to differences in the water conduit.

The pulsation of turbine discharge (and net head) depends very much on the configuration of the system. For frequencies lower than the first natural frequency of the upstream conduit, it is approximately inversely proportional to the intake impedance, i.e., doubling the pipe length approximately cuts the discharge oscillation into half (not quite, because the turbine impedance remains the same).

The pulsations of the runner discharge and runner torque are tightly coupled, via the turbine characteristic. Nevertheless, additional errors occur in the torque because it cannot be measured directly on the runner but rather somewhere else on the shaft. Due to the moment of inertia of the runner, the dynamic transfer function between the runner torque and the measured torque causes distortion starting from zero frequency. Such effects are normally not compensated because there is no similarity anyway. Due to these various effects, shaft torque pulsation in the model does not permit a direct prediction of prototype pulsation behavior and should only be measured for research purposes [6], taking into account the particular conditions of the test installation.

Another example where similarity is normally not granted, concerns the development of blade-frequency pulsation due to rotor–stator interaction in the stationary parts of the machine—guide vanes, stay ring, and spiral conduit. The frequencies f occurring in these effects are high and, consequently, the wavelength $\lambda = a/f$ is often of the same order as the machine dimensions. Important problems may result from the interference of waves, as discussed in Chap. 3.6. Similarity of these effects in a model test requires that the ratio between wavelength λ and machine size D is preserved between the model and prototype. If the wave speed a

is the same, then the product Df, and therefore also Dn, must also be the same; the model test must therefore be performed at the velocity level and head of the prototype. Except in special development tests (for example, as described by [7]), this requirement is normally not fulfilled. The blade-frequency pulsation in the casing and high-pressure conduit can therefore not be determined in a normal model test, as there is no degree of similarity. By contrast, the local pressure pulsation between the runner and guide vanes is not strongly affected by such interference. The usual measurement of this pulsation in Francis and pump turbine models is therefore sufficiently similar and transferable; the same holds for the fluctuation of guide vane torque at runner blade frequency including harmonics. Of course, the frequency response of the pressure taps must be adequate and the natural frequencies of the model guide vanes must be high enough to avoid dynamic distortion of results.

7.2 Francis Turbine Model Tests

7.2.1 Pressure Pulsation

Figure 7.1 shows the DTPP of a Francis turbine with high specific speed ($n_{QE} = 0.325$) as measured in the model test. The behavior of the two selected signals illustrates the descriptions given in Chap. 1.1, in particular, Fig. 7.2.

The pressure signals have been taken at the right- and left-hand sides of the draft tube cone. Four different load conditions are stacked in the same diagram using an arbitrary vertical offset. The division of the y axis is 10 % of the test head.

In Fig. 7.3, the four different load conditions from Fig. 7.1 are indicated by vertical cursor lines. The first example is just below the stability limit of the single-helix vortex, which for this design is close to $Q_{nD}/Q_{nD,opt} = 0.6$. The two pressure signals are hardly coherent and are composed of a wide spectrum of frequencies not much lower than the runner frequency. They stem from a multitude of vortices forming and decaying in the draft tube at random.

The second example ($Q_{nD}/Q_{nD,opt} = 0.67$) shows the well-developed single-helix vortex. The period of the pulsation is 4.33 runner revolutions, the relative frequency being $f/n = 0.231$. The phase shift between the two signals approximately corresponds to the 180° angular displacement between the two pressure taps. The amplitude at the left-hand side (p3) is slightly higher; this will be explained below, see Fig. 7.4.

The third example, taken at $Q_{nD}/Q_{nD,opt} = 0.80$, demonstrates the so-called '80 % pulsation' (see Sect. 2.2.5), in addition to the partial-load surge ($f/n = 0.314$) which is still present at that load. The spectacular high-frequency component comprises several narrow frequency bands differing by the multiples of the vortex precession frequency (see Fig. 7.2), the main component being $f/n = 2.61$, or 8.3 times the vortex precession frequency. This example has much similarity with the one investigated in detail by LMH/EPFL [9].
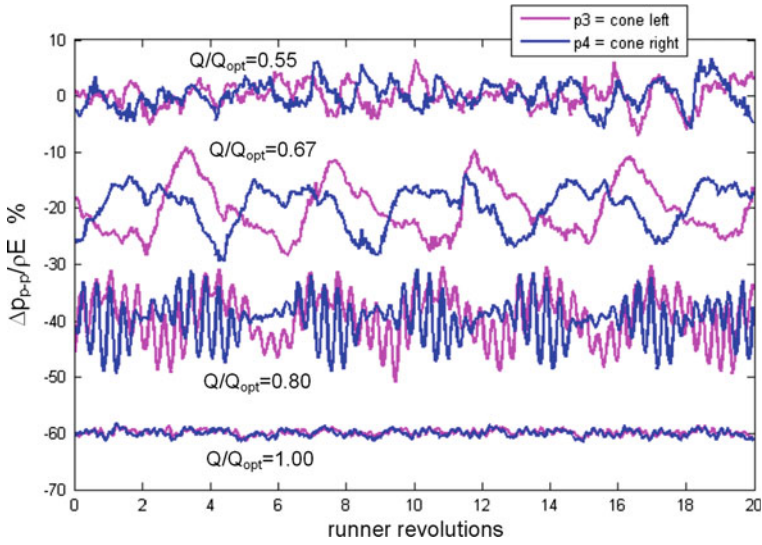
Fig. 7.1 DTPP time series
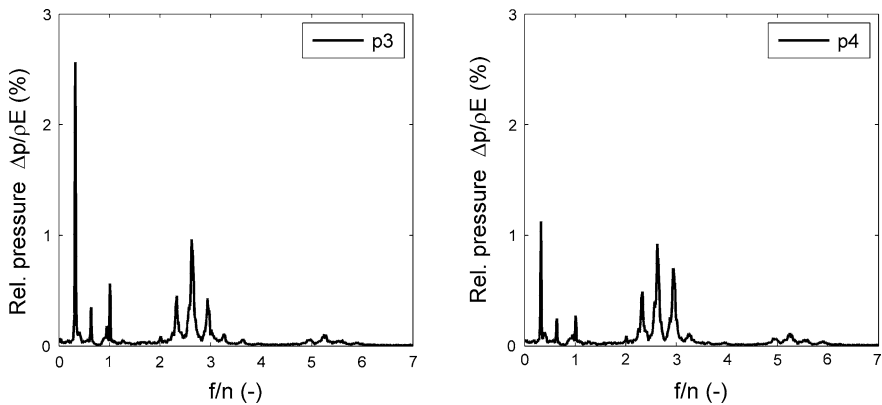
Fig. 7.2 DTPP spectra at $Q_{nD}/Q_{nD,opt} = 0.8$

The lowermost example (optimum efficiency flow, $Q_{nD}/Q_{nD,opt} = 1.00$) is from the swirl-free range where there are no significant fluctuations. The pulsation found is mainly due to small disturbances such as symmetry defects of the model runner, or the test circuit feed pump.

In Fig. 7.3 there are two more pressure signals shown in addition to the ones in the previous figures.

The four pressure taps are distributed around the draft tube cone in intervals of 90°. The colors were chosen in agreement between the figures. In the part-load
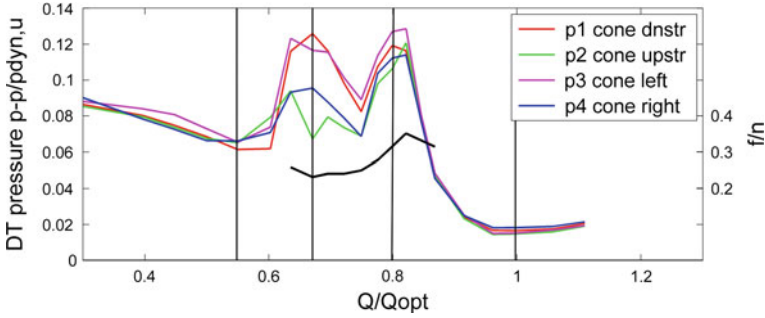
Fig. 7.3 DTPP amplitudes and frequency versus load

Fig. 7.4 Superposition of draft tube surge components
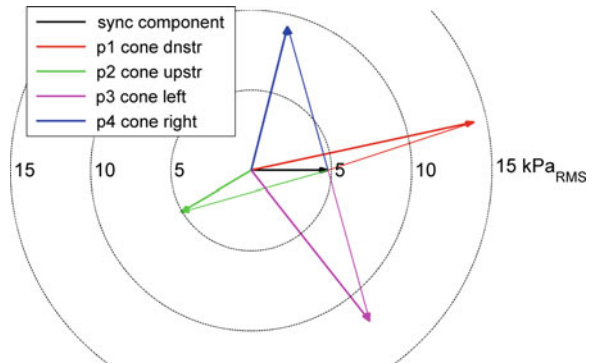
range, demonstrated by the point at $Q_{nD}/Q_{nD,opt} = 0.67$, significant differences may be observed between the amplitudes of the four signals.

The phase angle between the two partial processes of the half-load surge is not the same at the four locations. While the synchronous pulsation (black vector in Fig. 7.4, and black curve in Fig. 7.5) is the same for the whole circumference, the asynchronous pulsation, represented by thin vectors lines in Fig. 7.4, has a different phase due to the precession movement of the vortex rope. The phase vectors of two components have to be added in the complex plane, as shown in Fig. 7.4, and this explains the different amplitudes (i.e., the magnitudes of the bold-colored vectors).

The colors for the asynchronous components again correspond to the previous figures; the black arrow for the synchronous component holds for all four locations. At p1 at the downstream side of the draft tube, the two components are roughly in phase, therefore the largest pressure amplitude is very often observed in that area. By contrast, the synchronous and asynchronous (colored) components partly cancel out for p2, therefore the pressure amplitude is lower in the region opposed to the draft tube diffuser. This is where the draft tube adit and man door are located in many plants. It is even possible that the synchronous component increases due to partial resonance and the phenomena completely cancel out.
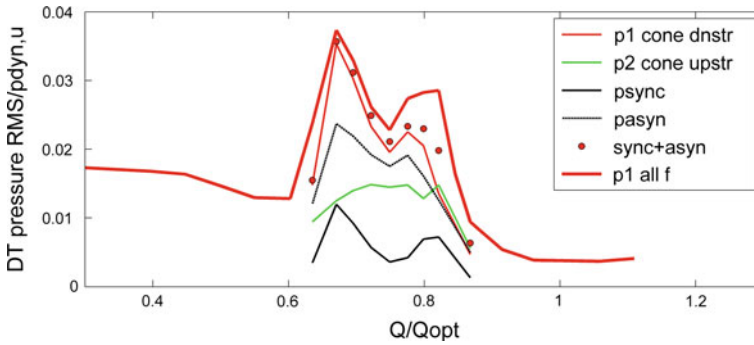
Fig. 7.5 Decomposition of draft tube surge at partial load

In such a case, the pressure amplitude for vortex frequency nearly becomes zero in a pressure tap at the man door but the surge may be perceived by the modulated noise.

The same decomposition of surge may be executed for all the points in the range of the partial-load vortex. The result is presented in a diagram similar to Fig. 7.3. This diagram (Fig. 7.5) uses a different definition of amplitude because it concentrates on the frequency band of the vortex only. Instead of the peak–peak amplitude we plot the rms amplitude integrated over the band of the basic vortex frequency, typically ± 5–10 %. This is necessary because the rest of the spectrum does not participate in the 2-components analysis.

In this diagram the scalar sum of the magnitude of the two basic components (psync and pasyn) is indicated using red dots; for every test point it is the maximum possible pressure amplitude of this frequency band occurring somewhere at the draft tube wall. The pressure at the downstream side (p1, thin red curve) corresponds more or less to this theoretical maximum, whereas p2 remains much smaller, as explained before. The total rms value of p1—including all frequencies—is also shown, by the bold red line, to demonstrate the relative importance of the surge frequency band. At the maximum (at $Q_{nD}/Q_{nD,opt} = 0.67$) the surge frequency band indeed makes up for nearly the whole intensity. Other frequencies make significant contributions at other load conditions, e.g., at $Q_{nD}/Q_{nD,opt} = 0.8$, where high frequencies are observed, as in Figs. 7.1 and 7.2.

From various studies [8, 9] it is known that the high-frequency components making up the 80 % pulsation exist only if the pressure level in the draft tube permits the vortex to cavitate. A comparison between amplitudes with and without cavitation of the draft tube vortex is given in Fig. 7.6 for a model turbine with specific speed $n_{QE} = 0.213$. The amplitudes shown are for the downstream side of the draft tube cone, like p1 in Fig. 7.1. At partial load, only the appearance of the 80 % pulsation increases the overall amplitude. In this range, the amplitudes would be in excess of the 'generic' behavior (the 'standard' behavior discussed on page 198 and following) if they could be reproduced in the prototype.
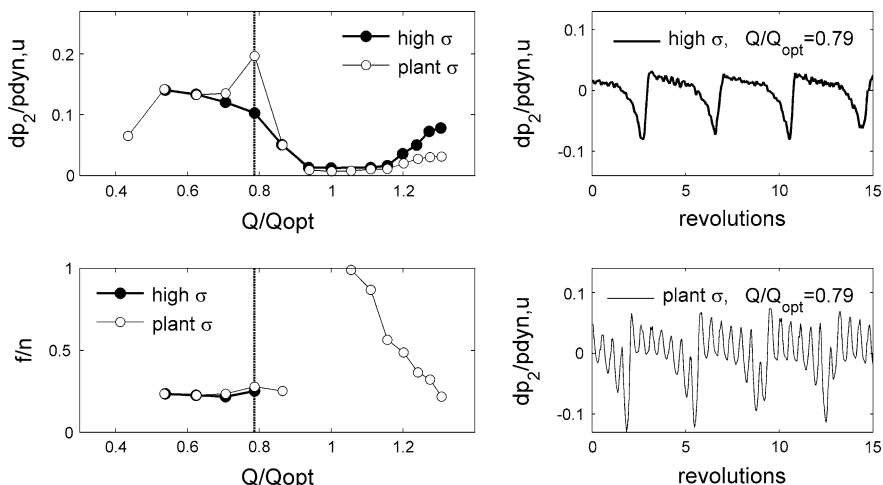
Fig. 7.6 Cavitation effects on DTPP

Another feature occurs at high load in the model test. Here, the cavitation in the model mitigates the pressure pulsation that would occur at plant sigma. The frequency characteristic at high load indicates the natural frequency of the draft tube; it is only applicable when vortex cavitation occurs, i.e., at plant sigma. At partial load only the frequency of vortex precession is shown, with but little effect of cavitation.

The dimensionless amplitude variables used in the previous figures require some explanation. In the pertinent international standard [1] there are also definitions of dimensionless parameters but these definitions are only intended to permit the comparison (or transposition of data) between a test condition in the model test and the corresponding condition at the prototype. Such a comparison is enabled by the conventional definition of a pressure fluctuation factor (in % or p.u.)

$$\tilde{p}_E = \frac{\tilde{p}}{\rho E} \tag{7.1}$$

where a pressure amplitude (rms, 0–peak, peak–peak, or the like) is divided by the pressure representative of the specific hydraulic energy. This definition is of course dimensionally correct and it permits the envisaged comparison.

The advantage of the definition is in its simplicity and the fact that engineers are familiar with it. However, with regard to the phenomena represented, this definition has some drawbacks; they may be avoided if variables that are more specific are used. Two aspects may be considered:

1. In a given turbine operating at fixed speed, the DTPP strictly depends on discharge but is almost independent of the net head (if conditions with equal discharge are compared).
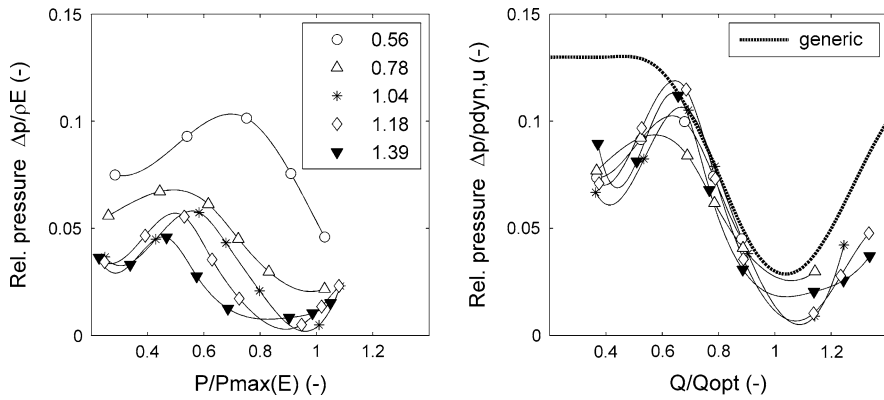
Fig. 7.7 Influence of head—various definitions of relative DTPP

2. If we want to compare turbines with different specific speeds, there is a systematic bias in favor of the machine with lower specific speed as these have higher heads relative to the flow.

Fact (1) has the consequence that the maximum pressure fluctuation factor at the lower head is always higher, compared to that at a higher head, while the maximum pressure pulsation (in kPa) may be the same. This means that the lowest prototype head is always critical if the simple and usual pressure pulsation guarantee is applied, using an overall limit for the pressure fluctuation factor. This is not logical because the same absolute amount of pulsation is not more disturbing if the net head is lower. More importantly, it is not possible to compare between different levels of operating heads because the inadequate reference variable E introduces a bias. This will be illustrated in Fig. 7.7. This bias could easily be avoided if the reference variable [the denominator in Eq. (7.1)] would be a constant pressure instead of a variable one.

Fact (2) is not important within the scope of a single project but becomes an obstacle if we try to utilize information retrieved from different machines. The DTPP phenomena are produced by the velocity distribution in the runner outlet on which the energy E has only a secondary effect. By contrast, a physically adequate reference pressure could be a velocity head based either on the circumferential blade velocity at the runner exit diameter D_2

$$u_2 = D_2 \pi n \tag{7.2}$$

or on the mean axial velocity

$$c_{m2}^2 = 4Q/(\pi D_2^2) \tag{7.3}$$

at a constant discharge, a suitable choice being the discharge at the point of best efficiency, Q_{opt}.

In the first case, the reference head would be

$$u_2^2/2g \;=\; H/\psi \qquad\qquad (7.4)$$

and in the second case it would be

$$h_{dyn,c} \;=\; c_{m2,opt}^2/2g, \qquad\qquad (7.5)$$

as already used in [10].

The development of DTPP versus load for different speed factors, i.e., for different values of prototype heads, is compared in Fig. 7.7. The legend in the left-hand graph indicates the relative head $E_{nD}/E_{nD,opt}$ of the various test series. This data set is from a model with $n_{QE} = 0.165$, for a power plant with an extreme ratio between the highest and the lowest operating head, $H_{max}/H_{min} \cong 2.6$. The conventional representation over the same range would be as at the left-hand side.

From the graph, it becomes immediately evident that with the given definitions, a separate DTPP guarantee and a separate test series is necessary for every specified operating head. On the other hand, if we use the relative discharge that is already used in the standard [1] together with a more suitable definition of relative amplitude, then the influence of operating head almost disappears even for this extreme range of operating head, as demonstrated in the diagram on the right-hand side. This property of the DTPP can be used for defining guarantees in a rational manner.

The question remains which draft tube velocity head—based on $c_{m2,opt}$ or on u_2 is the best choice for reference with respect to a general comparison of models. This question has been answered in an empirical way, by doing statistics based on both definitions. Test results from 90 different model Francis turbines are examined. The set of input data surveying more than two decades of development comprises a large number of different runners (~ 60) and draft tubes (~ 40). In some cases the same runner was compared with different draft tubes and vice versa. Sometimes the use of the 'same' model draft tube required some adjustments of the intake contour. The interesting questions are

(a) Is it possible to find a reasonable 'generic' representation for draft tube amplitudes?
(b) Is the suitable reference head $h_{dyn,c} = c_{m2,opt}^2/2g$, or rather $H/\psi = u_2^2/2g$?

The answers to the two questions have already been anticipated by Figs. 7.5 and 7.6, and now the proof will be given. For all of the 90 models we have determined the discharge factor φ_2 (at best efficiency point) as a very much reduced representation of the runner exit flow geometry, and the maximum DTPP amplitude in the draft tube cone. All data are taken from the data set closest to the optimum speed factor. All amplitudes are maximum peak–peak values in the partial-load range, using a 97 % confidence level in the histogram method suggested by IEC 60193.

Both references are tested in Fig. 7.8. In the graph on the left-hand side, $h_{dyn,c} = c_{m2,opt}^2/2g$, is used as a reference pressure for non-dimensionalizing the pressure pulsation. There is a clear trend of the resulting relative amplitude to
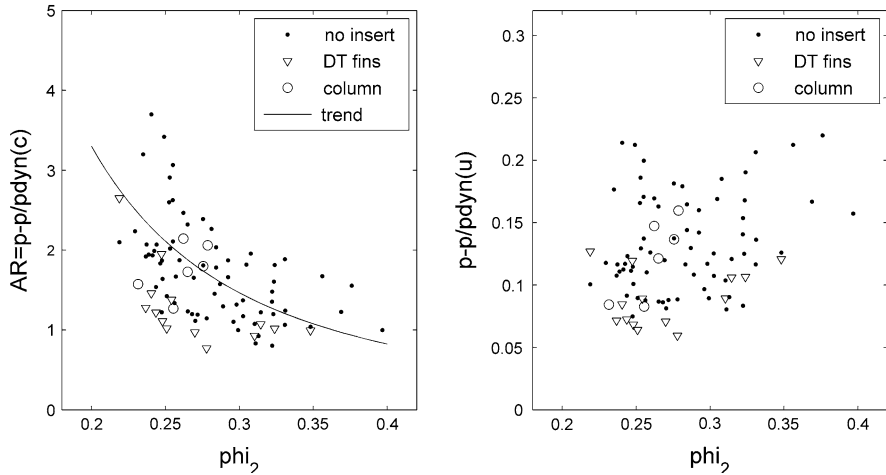
Fig. 7.8 DTPP amplitudes, test for best reference

decrease over the discharge coefficient φ_{opt} (=phi$_2$ in the figure), the trend line indicated is a function proportional to $1/\varphi_{opt}^2$

The alternative possibility, using the reference $H/\psi = u_2^2/2g$, as the reference for the pressure pulsation does not have such a trend, the probability distribution of the amplitudes ($\psi.p_{E,max}$) defined in this way is the same for all values of φ_2. This means that for all Francis turbines, independent of specific speed and discharge coefficient, a common 'generic' level of $\psi.p_{E,max}$ over Q/Q_{opt} may be expected. From the right-hand side of Fig. 7.8, however, one can see that there is still considerable scatter in the actual findings from the model tests. Several reasons are responsible for the differences. Apart from the different draft tube contours, there are also qualitative differences in the radial distribution of velocities in the runner exit. A very important influence hidden in the data cloud is the effect of draft tube pressure level. This effect is discussed in Sect. 7.2.3.

The generic curve has been established in an empirical manner, considering the measured curves of many models. It has already been used several times in the diagrams in Figs. 7.3, 7.4, 7.5, 7.6, 7.7. For an example, in Fig. 7.9 it is compared with model test results for a number of high-head Francis turbines. Some of them exceeded the pressure pulsations predicted by the curve quite significantly; it has to be recalled that every curve only shows the maximum DTPP for every load. If the curve is exceeded, then it is often due to unfavorable draft tube contour, or due to some cavitation-related resonance that may be suppressed by appropriate measures.

As may be seen in Fig. 7.9, the 'generic' curve does not represent an average behavior but has been established as a viable compromise for pulsation guarantees. It has to be higher than average by some margin because otherwise at least half of all models would become unacceptable. The designers of the plant (including the draft tube profile) and turbine must have some freedom which would disappear if
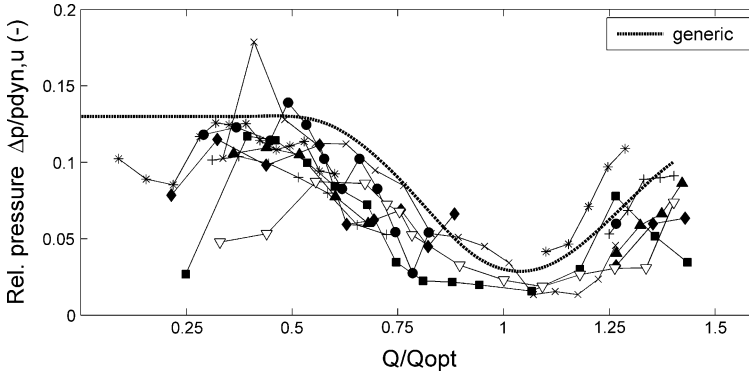
Fig. 7.9 Relative DTPP amplitudes of eight different high-head Francis models

extremely low amplitudes are given top priority. On the other hand, experience in many plants confirms that a prototype should operate sufficiently smooth with regard to draft tube pulsations if it stays within the 'generic' limit.

The four models in Fig. 7.9 with black markers have runners with splitter blades while the others have not; there is no systematic difference between amplitudes.

The dimensionless measure for draft tube pressure pulsations used in Fig. 7.9

$$\psi \cdot \tilde{p}_E = \tilde{p} \big/ (\rho u_2^2/2) \tag{7.6}$$

may be called a *pressure pulsation coefficient*, in order to avoid confusion with the pressure fluctuation *factor* $\tilde{p}_E$ defined in IEC 60193.

In a similar fashion to the amplitudes, the frequency of DTPP has also been subject to statistical studies. It is useful to know the frequency of partial-load surge in advance because objectionable power swings may result if the vortex frequency coincides with the natural frequency of the generator. This kind of resonance may reasonably be predicted, therefore the frequency is of interest.

As shown in the examples in Fig. 7.10, the relative vortex frequency f/n of a turbine at partial load may or may not be fairly constant versus load. It is not possible to predict precisely the frequency based on an earlier test with a given draft tube, as shown in Fig. 7.11; some scatter has to be accounted for.

The models of high-head turbines represented in the left-hand diagram have specific speeds n_{QE} between 0.06 and 0.10. All of them were tested, with minor adjustments, using the same rather deep draft tube 'A' typical of high-head plants. The low-head turbines (right-hand side), tested with a shallow draft tube 'B', have specific speeds $0.15 < n_{QE} < 0.20$.

There is a statistical dependency between the discharge coefficient φ of a turbine (at optimum discharge) and the relative precession frequency f/n. To exclude the influence of load, the comparison in Fig. 7.11 was made at the same relative discharge for all models. There is a positive correlation between the
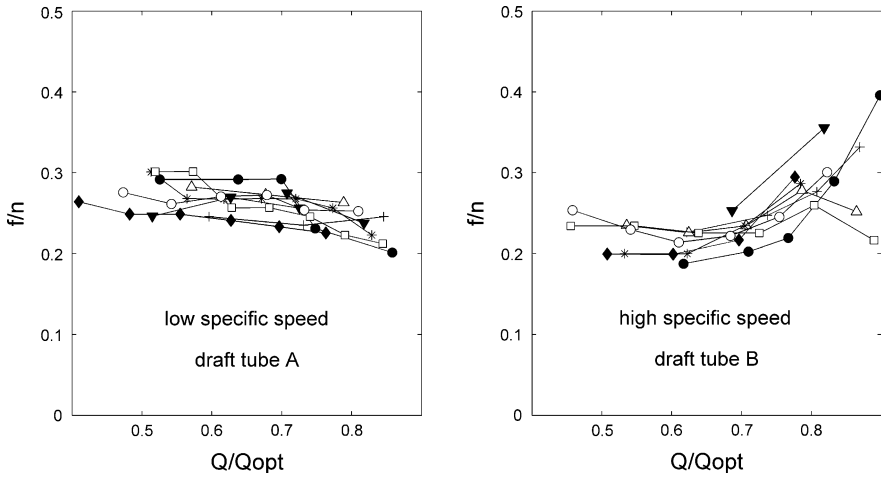
Fig. 7.10 Relative DTPP frequencies of Francis models
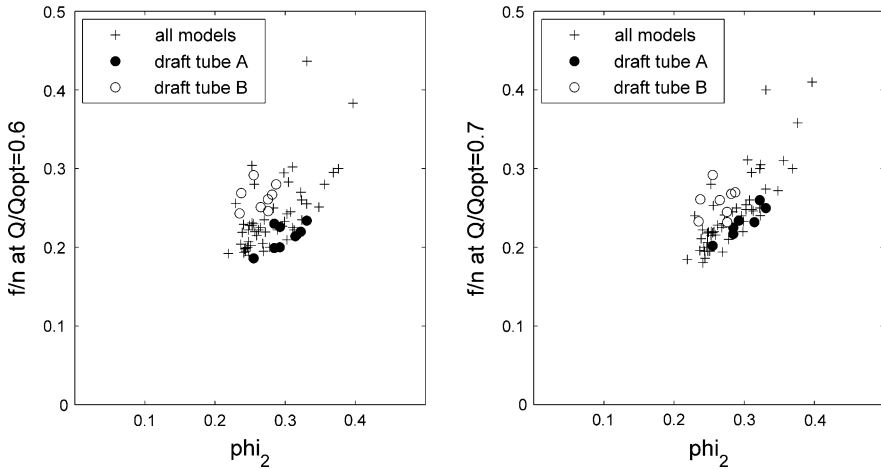
Fig. 7.11 Relative vortex frequency versus discharge coefficient φ_2

specific discharge and the precession frequency. At $Q/Q_{opt} = 0.7$, where the vortex is strong and well developed in all models, the dependency is approximately proportional, as shown in Fig. 7.12.

In the range of very low load, between speed-no load and the lower stability limit of the corkscrew vortex, intense random fluctuations from large-scale turbulence dominate the DTPP. Some fraction of wideband noise is present in the DTPP at all loads, however, these only become important at low part load.

Figure 7.13 shows the stochastic (random) component of DTPP as a curve with triangular markers. The conventional analysis for synchronous and asynchronous pulsation works only for discharge values above the lower limit of the 'organized'
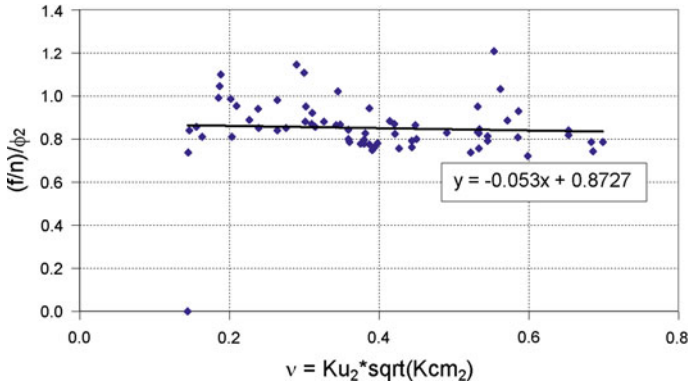
Fig. 7.12 Test for proportionality between $\varphi_{2,opt}$ and f/n, for $Q/Q_{opt} = 0.7$
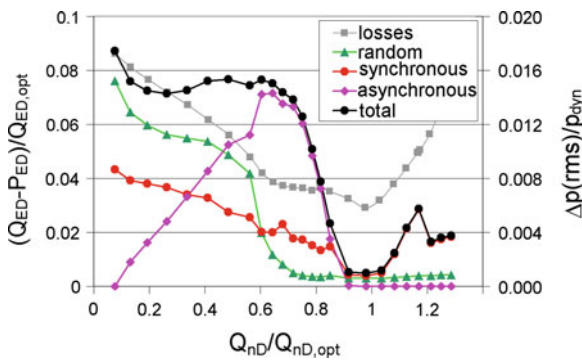
Fig. 7.13 Stochastic component of DTPP

part-load vortex, for $Q_{nD}/Q_{nD,opt} > 0.6$ in this model, where the random pulsation stays very low. Below the limit, the flow becomes more and more disorderly; the asynchronous movement gives way to pulsation without coherence between the various pressure taps in the draft tube cone. This transition comes together with a significant increase of the hydraulic losses (by grey curve, left-hand scale). For additional comments, see Sects. 2.2.2 and 4.2.2.

In addition to the draft tube, the pressure pulsation between guide vanes and runner is also sometimes examined. This makes sense only in high-head Francis turbines if any, because in low-head machines the increased distance between the two cascades renders their interaction quite unimportant. For some high-head models we have collected the test results and they are compared in Fig. 7.14. Unlike the DTPP, in this case the net head of the turbine is a plausible reference. The driving mechanism is the distortion of pressure field around the runner blades, which is closely related to the operating head.
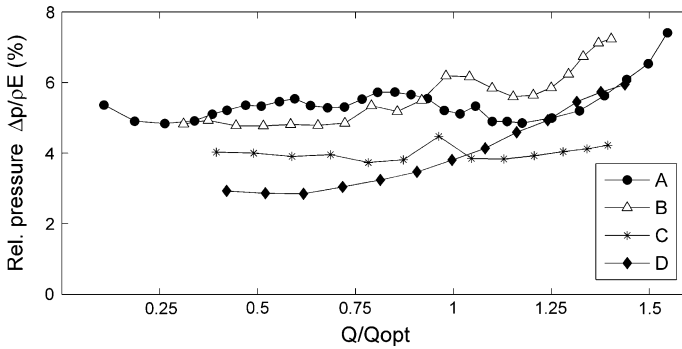
Fig. 7.14 Pressure pulsation between guide vanes and runner

Table 7.1 Francis models used for Fig. 7.14

Model	n_{QE}	D_z/D_1	Runner blades	Guide vanes
A	0.075	1.11	13 + 13	20
B	0.078	1.10	13 + 13	20
C	0.073	1.14	13	23
D	0.069	1.14	17	28

The most important component in the pressure pulsation downstream of the guide vanes is the runner blade passing frequency, with some contribution from the lowest harmonics. Other phenomena, such as the draft tube vortex, are also present but have smaller influence. There is often a tendency for the amplitude to increase at high load. This may at least partly be due to the decreasing radial clearance between the trailing edges of the guide vanes and the runner. Some information about the four models of Fig. 7.14 is given in Table 7.1.

7.2.2 Aeration Pressure

This section concentrates on aeration in the draft tube, which is the most frequent practice to reduce pressure fluctuations. Few data have been published concerning the air pressure required for draft tube aeration. A comprehensive discussion was given in [10]. Also, the earlier work published in [11] is interesting due to its focus on aeration through air pipes.

In connection with draft tube aeration there is often a question if admission of atmospheric air due to negative pressure in the draft tube will be possible, or else compressed air has to be provided. In the following the pressure difference between the foreseen air intake location x and the average pressure at the draft tube exit will be counted as positive in the case of suction:

$$\Delta H_x = -(p_{air}/\rho g + H_{sx}) \tag{7.7}$$

Fig. 7.15 Pressure definitions for aeration
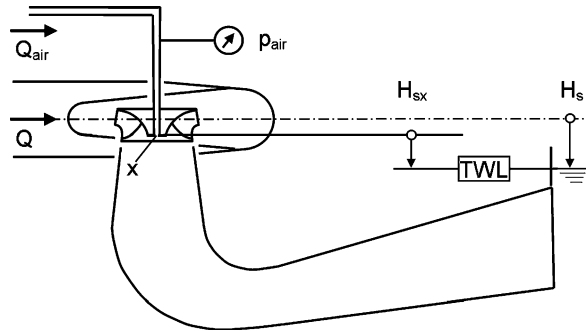
Measuring the required air pressure p_{air} as in Fig. 7.15 requires some caution because an undefined mixture of air and water in the connecting pipes or hose may spoil the result. A good compromise is to measure with a very small air flow rate in order to keep the duct clear of water, while at the same time avoiding a significant pressure bias due to high air velocity. A standard approach representing a relative pressure difference based on the net head, $\Delta H_x/H$, would require many measurements because for every prototype head a quite different characteristic would result [10], as shown in the upper diagrams of Fig. 7.16 (dH is the same as ΔH_x). The same would apply if output power was used as abscissa.

Even if one used the relative discharge proposed as an abscissa for pressure pulsation in the IEC 60193 standard, the suction numbers would still yield different curves [10] because the different values of net head used as reference are still distorting the result, as in the lower left-hand graph.

Systematic studies reported in [10] have shown that there is also a kind of generic behavior with regard to draft tube pressure, quite similar to the pressure pulsation amplitudes. The steady-state pressure distribution is also related to velocity head but not to net head, as observed in the draft tube surge amplitudes. The study reported in [10] showed that the draft tube velocity head based on the best efficiency discharge is a more suitable reference. Thus, a suction ratio SR is defined where the velocity head hdyn from Eq. (7.5) replaces the net head H as pressure reference:

$$SR = \Delta H_x / h_{dyn,opt} \qquad (7.8)$$

With such a representation, suction coefficients at all values of prototype head collapse into a single curve with acceptable accuracy (lower right graph in Fig. 7.16).

An additional benefit is that similar curves result even if the pressure in a comparable location is represented for a turbine with different specific speed. Figure 7.17 is an example from [10] that compares the pressure near the draft tube center for two turbines A and B described in Table 7.2.

The main difference between the suction ratios of the two turbines is a shift between the relative discharge areas where suction breaks down. This is due to the fact that the high-head model has the rope-free zone at a discharge below best
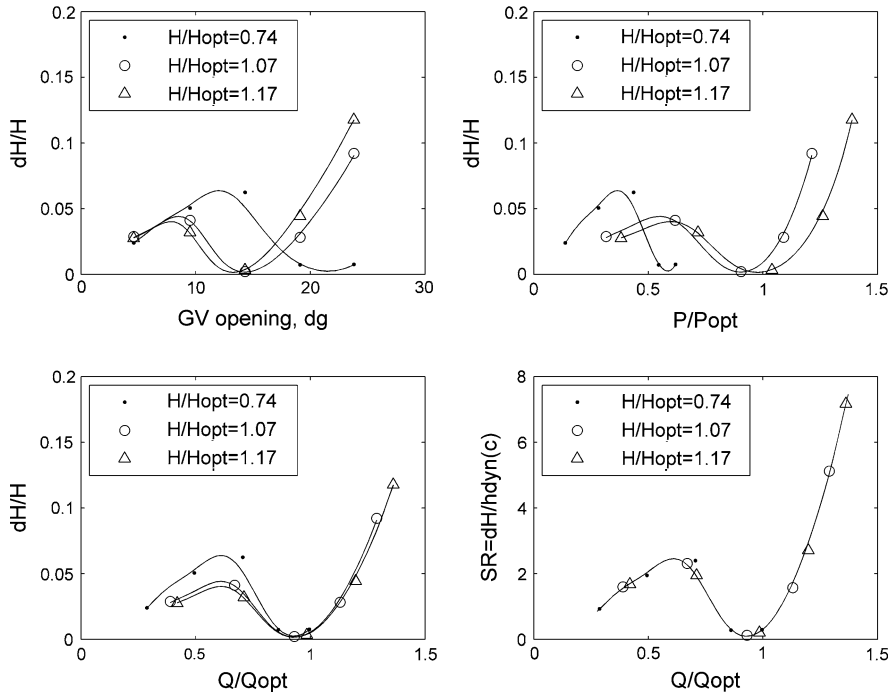
**Fig. 7.16** Uniqueness of flow-oriented DT suction coefficient SR
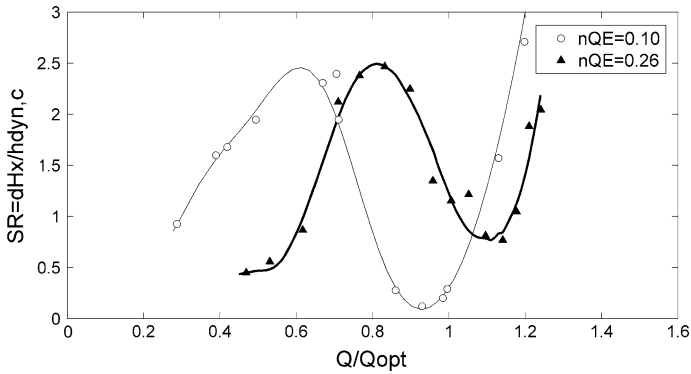
Fig. 7.17 Suction ratio SR at DT center, different specific speed

efficiency. However, the relative location of the zone with high suction ratio with regard to the zones affected by draft tube pressure pulsation is the same for both models.

At off-design values of discharge, the draft tube swirl creates a strong radial pressure gradient; for that reason the minimum pressure prevails in the center of

Table 7.2 Francis models used for Fig. 7.17

Model	N_{QE}	Runner blades	HP, mwc	Location
A	0.10	15	413	Surface of shaft
B	0.26	13	54	Bottom of hub
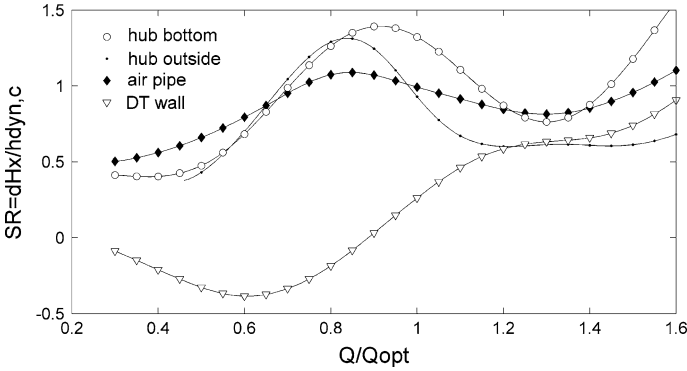
Fig. 7.18 Draft tube suction ratio SR for different locations

the draft tube. If for some reason aeration is to be done at the draft tube wall, this requires higher air pressure and often natural suction is not possible. Figure 7.18 compares the typical suction numbers to be expected in different locations of air entry. The figure presents conservative values, accounting for the fact that at plant sigma the suction rate SR is significantly lower than in case of non-cavitating draft tube flow [10].

The aeration types in Fig. 7.18 are the most frequently applied ones. In turbines with stabilizing fins mounted at the draft tube wall, it is desirable to aerate from the fin tips in order to suppress the secondary pulsation and potential wall erosion caused by the fin tip vortices. For two common types of fins, Fig. 7.19 shows the suction ratio at the lee side of the fin tip.

The results in the left-hand diagram are from a shallow draft tube with four short roof-shaped fins. The other diagram shows data from another concept using only two but much longer fins, as described in [12]. For both configurations, the 'generic' curve is an adequate estimate for the suction effect in the discharge range relevant for partial-load pulsation, i.e., between 50 and 85 % of Q_{opt}.

The results presented in this chapter have been obtained with models having approximately the same discharge coefficient ($\varphi_2 = 0.25$, or $Q_{nD} = 0.62$) at best efficiency point. Instead of using the velocity head $c_{m2opt}^2/2g$, it would have likewise been possible to use $u_2^2/2g$ as reference. Within the models compared, the ratio of reference pressures would have remained approximately the same, namely $(u_2/c_{m2opt})^2 = 1/\varphi^2 = 16$.

The available data source does not permit a safe conclusion if, in case of differing values of best efficiency discharge coefficient, $u_2^2/2g$ would be a better
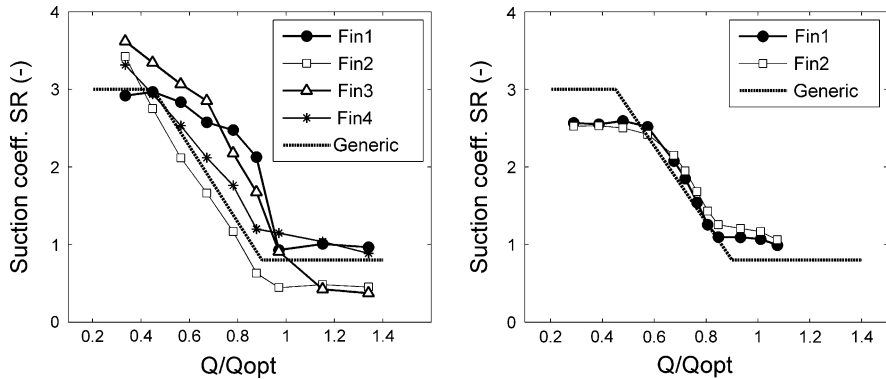
Fig. 7.19 Suction ratio SR measured at the tip of draft tube fins

reference—like in case of the part-load pressure amplitudes—or if $c^2_{m2opt}/2g$ should be preferred. The data in the last figure (Fig. 7.19), however, are from two turbines with very different discharge coefficient φ_2, namely, 0.25(left) and 0.35(right). Using $u^2_2/2g$ as reference would not support a common SR curve for both cases. In addition, the suction rate in the swirl-free condition is clearly defined by the diffuser effect, linking it to c_{m2} rather than u_2.

7.2.3 System Studies

Some model tests were dedicated to the study of the dynamic behavior of the Francis turbine within the hydraulic system. The purpose of such studies is to devise a simple analytical law describing the interaction between the turbine and the rest of the system. It is likely that different phenomena have to be described by different laws. For instance, the low-frequency pulsation at partial load seems to be governed by another law than the typical instability at high load.

The particular study discussed here [13] is only concerned with the draft tube surge at partial load (see Sect. 2.2.1), because this phenomenon is found in every Francis turbine, and because it is relatively easy to identify, being a pulsation with a simple forcing mechanism. Model tests were performed in order to validate a set of basic assumptions:

(1) Partial load surge is the sum of two phenomena occurring simultaneously
(2) Asynchronous pulsation is the local precession of the corkscrew vortex
(3) Asynchronous pulsation is limited to the draft tube
(4) Asynchronous pulsation is independent of cavitation number σ
(5) Synchronous pulsation is a one-dimensional forced oscillation of the entire fluid column
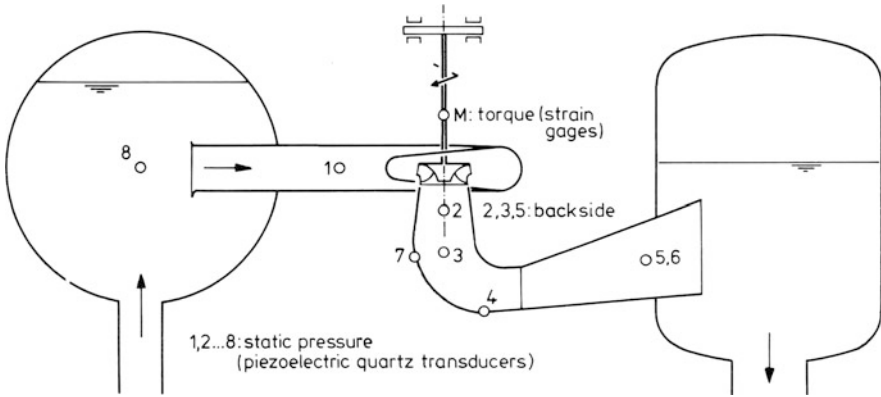
Fig. 7.20 Test arrangement for identification of half-load vortex parameters

(6) Synchronous pulsation is excited by a source at the draft tube elbow
(7) It is a pressure-type source and independent of σ
(8) Phase angle between pressure source and asynchronous pulsation is independent of σ
(9) Synchronous pulsation is σ-dependent due to cavitation compliance $C(\sigma)$.

The configuration of the test rig was very simple (Fig. 7.20). The model was tested in a closed test circuit, between two large tanks both having an ample air cushion to ensure a condition of zero pressure pulsation on either side. The intake pipe was straight and simple. Using the known hydraulic impedance Z_1 in the upstream point 1, the pulsation of discharge $q_1(j\omega)$ in the frequency domain could be determined from the pressure pulsation by the relationship $q_1 = p_1/Z_1$.

The separation between the asynchronous and synchronous pulsation was performed in a series of tests with different relative flow Q/Q_{opt}, the cavitation number being sufficiently high to suppress cavitation. In this condition the compliance parameter C_C is zero, and therefore exactly known. Together with assumptions (6) and (7), this permitted computation of the magnitude of the exciting pressure source, and with assumptions (4) and (8), the asynchronous pulsation could be separated.

The decomposition of the measured pressure pulsation vectors into the two partial phenomena is shown in Fig. 7.21a for the cavitation-free condition of a test point with intense pulsation. The main data of this test condition, together with some properties of the medium-specific speed turbine model used, are shown in Table 7.3.

Δp_{EX} in Fig. 7.21a is the vector of the excitation pressure source. The synchronous part of the pulsation (vector components drawn black) is approximately the same in all pressure taps at the draft tube cone. It is approximately equal to $-\Delta p_{EX}$ because for the draft tube cone, the downstream impedance is much smaller than the upstream impedance. The vectors of the asynchronous pulsation are drawn with thin lines, in analogy to Fig. 7.5 (Sect. 7.2.1). Adding the synchronous pulsation yields the total (measured) pulsation for every location.
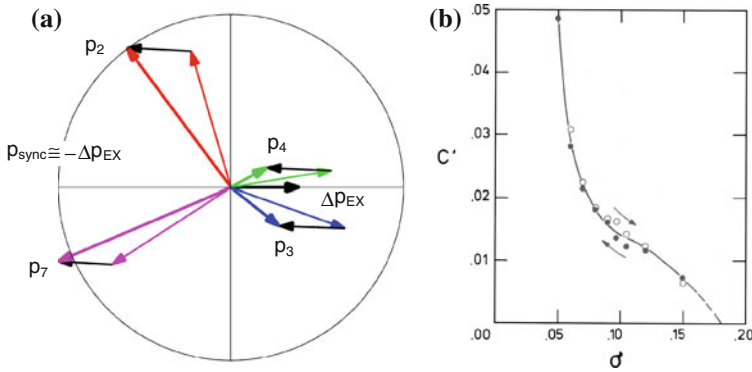
Fig. 7.21 Identification results at $Q_{nD}/Q_{nD,opt} = 0.68$. **a** Synthesis of pulsation vectors. **b** Cavitation compliance

Based on the cavitation-free parameters, the question was if the cavitating condition could be constructed only by changing the cavitation compliance C_C (which is 0 in the base case shown in Fig. 7.21a) as a function of the cavitation number σ.

For a sequence of comparable test points differing only by σ, the decomposition was made in reverse using the cavitation-free parameters and searching for the compliance value which achieved the best overall fit between measured and synthesized pressure pulsation. This procedure worked out well, except a small hysteresis between the test sequences with ascending and descending σ. The empirical dependency between σ and the cavitation compliance C_C resulting from this analysis is shown in Fig. 7.21b.

From the cavitation-free asynchronous pulsation, the synchronous pulsation computed using the cavitation-free excitation pressure and the best guess for the compliance (Fig. 7.21b) the vectors of pulsation in all locations can be resynthesized and compared with the measured values. For comparison of phase angles, the phase at pressure tap 1 (intake pipe) is used as a reference (zero). The dimensionless cavitation compliance used in Fig. 7.21b from [13] is defined as

$$C' = C_C \cdot H/D_2^3 \tag{7.9}$$

The turbine head is not a suitable reference for phenomena occurring in the draft tube, as explained earlier in Sects. 7.2.1 and 7.2.2; a different pressure reference ($u_2^2/2g$) would be more representative:

$$C^* = C_C \cdot (H/\psi)/D_2^3 \tag{7.10}$$

$$\sigma^* = \sigma \cdot \psi \tag{7.11}$$

For the example in Fig. 7.21, with $\psi = 1.92$, this would mean $C^* = 0.52 \cdot C'$.

Table 7.3 Francis model and selected test point

Runner exit diameter	m	0.30
$n_{ED, \, opt}$	–	0.325
$Q_{ED, \, opt}$	–	0.20
Test head $H_M = E/g$	m	40
Tested $E_{nD}/E_{nD, \, opt}$	–	1.00
Tested $Q_{nD}/Q_{nD, \, opt}$	–	0.68
Excitation $p_{ex}/(\rho E)$	% rms	0.40
Runner frequency	Hz	21.5
Vortex frequency	Hz	4.8

In Fig. 7.22, the amplitudes and phase angles computed in this manner for the individual locations are compared with the measured data. The vertical scale is logarithmic, covering two orders of magnitude.

The left-hand side of Fig. 7.22 is concerned with those variables where the asynchronous component does not appear, that is, the pressure pulsation in the turbine intake, and the pulsation of shaft torque. As the frequency remains approximately constant for the whole range of the cavitation number, the amplitude ratio and phase angle between the two signals must remain the same. For σ values above the limit of visual vortex cavitation (in this test point $\sigma = 0.19$), the cavitation compliance is zero, and everything remains constant and independent of σ.

In the other parts of Fig. 7.22, the σ-dependency is more complex, and it is different between the selected locations at the draft tube wall. In these signals, the asynchronous pulsation interferes with the synchronous one (which behaves similar to the casing pressure pulsation $\tilde{p}_1$). Due to the changing cavitation compliance, the phase angle between the synchronous and asynchronous component changes continuously with σ, and in three signals there is some condition where the two components are in opposite phases, thus producing a minimum amplitude. For the pressure pickup 7, at the upstream side of the cone, this happens near $\sigma = 0.075$, for location 3, at the right-hand side, at $\sigma = 0.14$, and for location 4, at the draft tube bottom, at $\sigma = 0.15$. The model also predicts a large shift of the phase angle with reference to casing pressure. Below $\sigma = 0.09$ the computed phase starts deviating from the measured phase (shaded areas). This is already outside of the range of prototype cavitation levels.

This early system study has confirmed that the notorious partial-load pulsation is a forced oscillation and the simplifying assumptions listed above are approximately correct. Later, a number of other Francis model turbines were examined using the same methodology. While some of them behaved in quite a similar way, there were also other tests where the expected resonance-like behavior was not clearly developed. The reason for the deviations has not been understood so far. It is possible that using the cavitation compliance as the only parameter for the vortex transmission behavior is too simplistic, and that a more complex model in analogy to the theory describing full load stability may be required. More specifically, in certain part-load conditions the mass-flow gain effect could contribute significant damping effects that could change the behavior and mitigate the resonance.
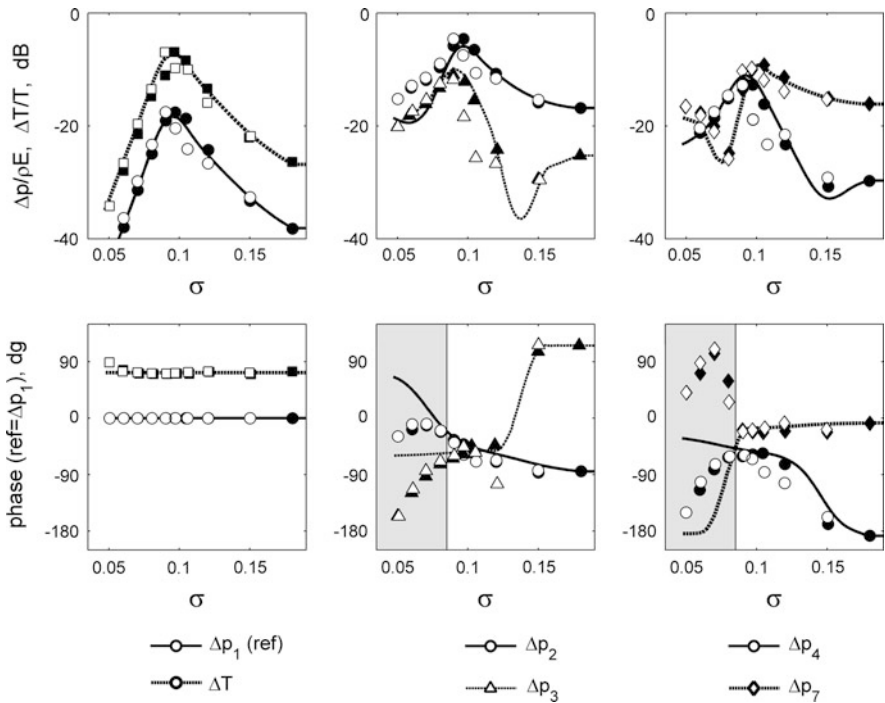
Fig. 7.22 Computed versus measured part-load pulsation of pressure and torque

So far, the theory described above [13] was never utilized nor contested by the hydro research community, except a later publication of the same theory by other authors [14]. There are very few alternative concepts to explain how pulsation test results from model tests should be transferred to the prototype turbine. The IEC 60193 standard says that the oscillation power radiated by the turbine into the penstock is the true transposable quantity; however, this statement is based on faulty reasoning [15] which does not account for the very important dissipation of oscillation energy in the turbine [16]. As a matter of fact, as of today there is no generally accepted practice of surge prediction that accounts for the systems aspect. It is hoped that the theory presented above will become accepted by the turbine community.

7.3 Pump Turbine Model Tests

7.3.1 Pressure Pulsation

The draft tube pressure pulsation (DTPP) in the generating mode of pump turbines has many similarities with Francis turbines. The clear dependency on $Q_{nD}/Q_{nD,opt}$ is also found in pump turbines. An example from a medium-head model with $n_{QE} = 0.133$ (for optimum efficiency in pump mode) is shown in Fig. 7.23.
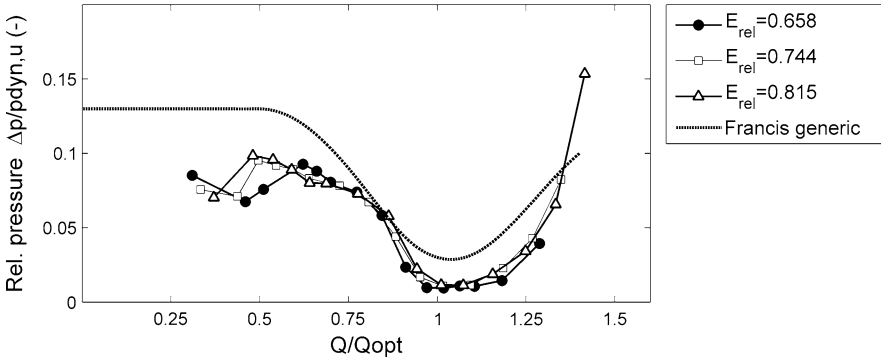
Fig. 7.23 DTPP in a medium-speed pump turbine, generating mode
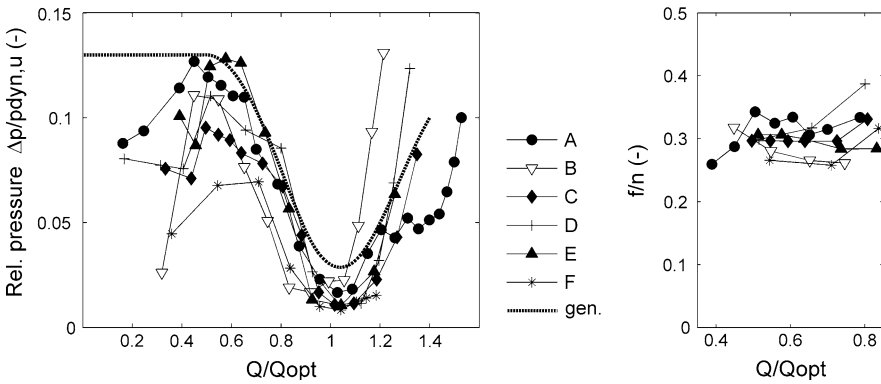
Fig. 7.24 DTPP amplitude in generating mode of model pump turbines

The 'generic' limit curve devised for Francis models is also suitable for DTPP of pump turbines in generating mode. At very high discharge, the pump turbines may have higher DTPP because the draft tube pressure level is higher; therefore the mitigating effect of vortex cavitation is not as effective as in Francis turbines. On the other hand, the high sigma normally prevents draft tube resonance in partial load, thus avoiding the increase of DTPP often occurring in Francis models.

The relative energy factor $E_{rel} = E_{nD}/E_{nD,opt}$ in the legend does not come close to unity because in turbine mode the pump turbine usually[2] has to operate at a relatively high speed, in order to permit satisfactory operation in pump mode.

The left-hand diagram in Fig. 7.24 compares the DTPP amplitudes from tests at six different pump turbine models whose data are summarized in Table 7.4. The ratio of runner diameters D_1/D_2 serves as indication for the specific speed.

---

[2] with the exception of variable-speed units.

Table 7.4 Pump turbine models used for Fig. 7.26

Model	n_{QE}	D_1/D_2	Runner blades	Guide vanes
A	0.108	1.72	7	20
B	0.133	1.52	7	20
C	0.166	1.43	7	24
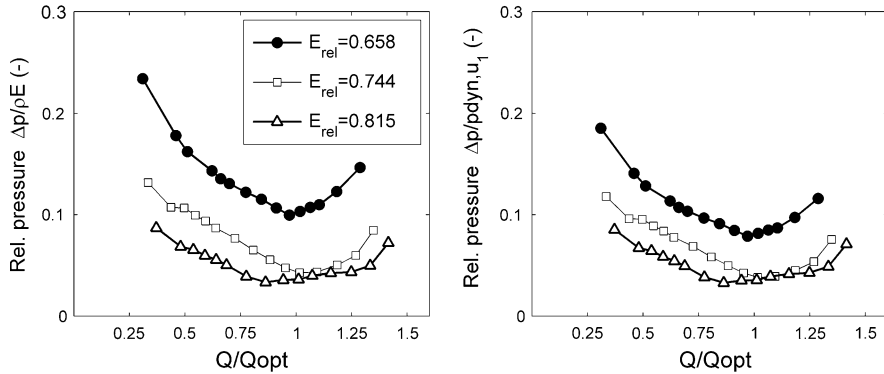
Fig. 7.25 GV pressure fluctuation factor in generating mode

The conventional amplitudes using the head as a reference would yield large scatter even for the same relative head E_{nD}/E_{nDopt} (standing for H/H_{opt}). The vortex frequency for the same models is given in the diagram on the right-hand side. The average frequency, shown on the right side of Fig. 7.24, is slightly higher compared to Francis turbines, probably due to higher average discharge coefficient.

Pressure pulsation measurement between the wicket gate and the runner is the standard practice in pump turbines. For a number of reasons the relative level of pulsation is higher than for Francis turbines. The runner blade number is often smaller, the runner blade profile has to be designed for good performance in the pump mode, and the operating head in turbine sense is, for systematic reasons, lower than at the best efficiency point. In addition, the radial gap between the wicket gate and the runner is typically smaller than in Francis turbines. This combines to give a more pronounced variation of pressure around the runner blades that results in an increased amplitude of the pressure pulsation in the stationary system.

The pump turbine model of Fig. 7.25 is the same as in Fig. 7.23, model B in Table 7.4. The increase in the relative amplitude at lower head (with actual turbine head as reference, left-hand side) is quite considerable, and not just a consequence of the lower reference. For comparison, using the circumferential velocity head at the runner intake D_1 would yield the result shown in the right-hand graph. The pressure pulsation level in turbine mode may seem high, but the pump turbine must anyway be designed for a pulsation level occurring in transient modes which is higher by roughly an order of magnitude.
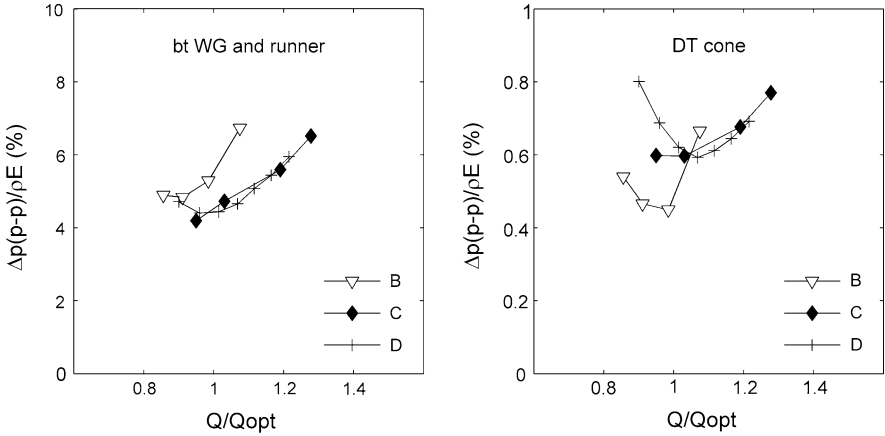
Fig. 7.26 Pressure fluctuation factor of three PT models in pump mode

Pressure pulsation in the pump mode depends on the pump head, on the impeller design, and on the guide vane adjustment for good efficiency. Of particular interest is the behavior when the pump is operated on the efficiency envelope, i.e., for every head the guide vane opening is set for best efficiency. Figure 7.31 shows the pressure fluctuation factor for three modern pump turbine models. In these two diagrams, the reference discharge coefficient Q_{nD} is for best efficiency in pump mode. Note the different scales used in this diagram—draft tube pressure pulsation is very low.

The pump turbines in Fig. 7.26 have different specific speeds, as described in Table 7.4. The specific speed $n_{QE,opt}$ is given for the pump optimum efficiency condition.

7.3.2 Guide Vane Torque

During network operation in pump or turbine mode, the fluctuation of the guide vane torque T_G is mainly caused by the passage of the runner blades. In the following we shall use the dimensionless variable defined for guide vane torque as in the model test standard IEC 60193 [1]. In the context of this standard, D is the runner exit diameter in the turbine flow sense. In terms of physics, this reference has nothing to do with the guide vanes, but at least it is the simplest possible definition:

$$T_{G,DE} = \frac{T_G}{\rho E D^3} \qquad (7.12)$$

The test series represented in Fig. 7.27 has been measured with the pump turbine model C in Table 7.4 at a constant energy factor, or pump head. The 'on-cam' condition for best efficiency at this head is $\alpha = 30°$.
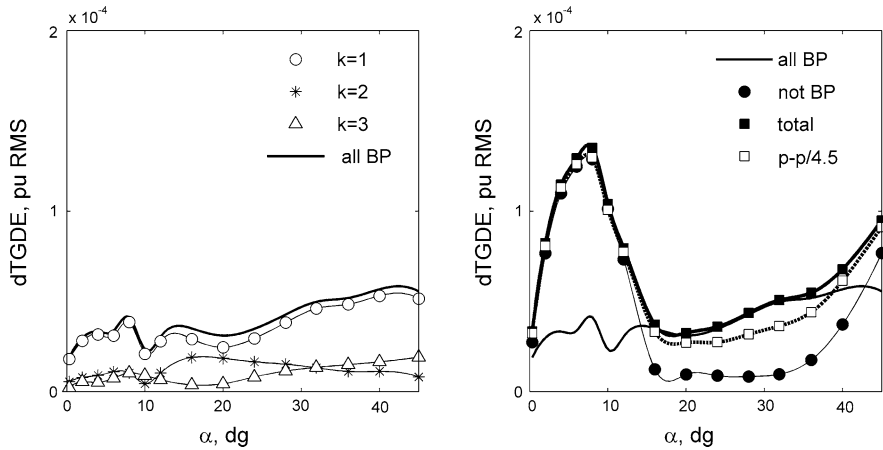
Fig. 7.27 Components of GV torque pulsation in pump mode

The rms amplitude of the guide vane torque pulsation is decomposed for its main spectral components. The blade passing frequency and its harmonics knZ_r contribute the component 'all BP', the first three orders are also shown separately on the left-hand side. The remainder of the pressure pulsation is shown as 'not BP'. Decomposition may only be done in terms of rms values, but the peak–peak amplitude for the overall signal is also shown (white markers, right scale), using the empirical transposition factor p-p/rms $\cong 4.5$.

Three ranges may be recognized in the diagram. For guide vane opening between $16°$ and $36°$ the pulsation is nearly periodic, the stochastic components are very small. For lower and for very high opening, the efficiency deteriorates and the losses are accompanied by increasing stochastic pulsation of flow, pressure, and guide vane torque caused by irregular backflow and large irregular vortex structures. Figure 7.28 illustrates the behavior in the three ranges. For the same model pump turbine, the guide vane torque pulsation in turbine mode has much lower amplitude, as shown in Fig. 7.29. This difference is very typical, it was also found in several other pump turbine models. The figure uses the same definitions as explained for Fig. 7.27. Unlike pump mode, the increase of amplitude at low opening is mainly due to an increase of the blade passage components.

As with the pressure pulsation, the fluctuation of guide vane torque is also much higher during transients compared to steady-state turbine or even pump mode. The differences are shown for a constant guide vane opening in Fig. 7.30. This figure combines all possible operating conditions—steady-state operation as well as transients—for a guide vane opening angle of $22°$. The shaded areas in the figure denote conditions with negative efficiency.

The flow variable X2 is a unique parameter explained in [17], derived from Suter's definition for pump characteristics [18] but adapted to single-regulated machines. The sign of X2 shows the sense of runner rotation—positive for turbine sense. X2 values of -0.5 or $+0.5$ denote the conditions of zero discharge.
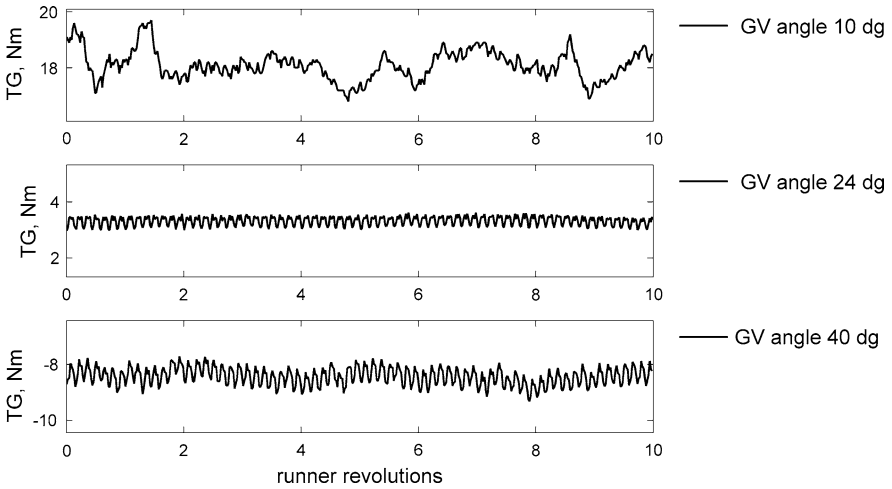
Fig. 7.28 Guide vane torque signal in pump mode
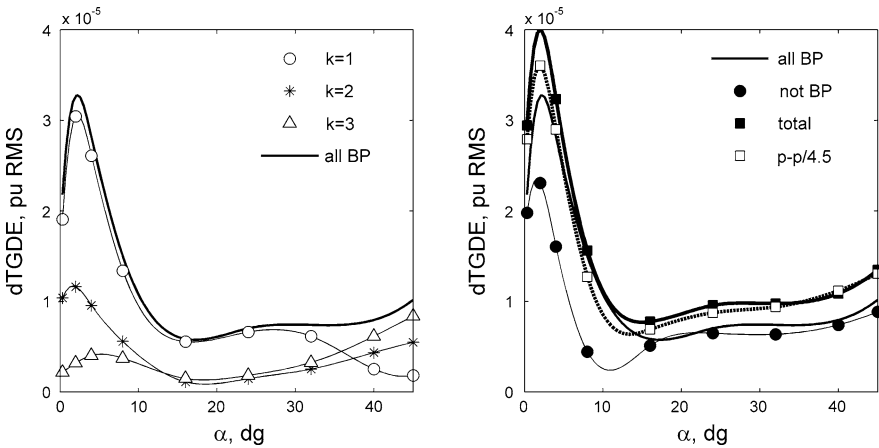
Fig. 7.29 Guide vane torque pulsation components in turbine mode

The steady-state operating conditions with good efficiency are close to the X2 values of −0.75 (pump) or +0.25 (turbine); it is there where the guide vane torque has the lowest pulsation level. The line signatures for the curves are like in the previous figures; to avoid confusion, the individual harmonics of the blade passing frequency are not shown. The values at X2 = 0 (zero speed) are interpolated because the blade-frequency component has a singularity in this condition.

The blade passing frequency makes up for most of the strong pulsation at low speed, while at low flow in pump rotation (−0.7 < X2 < −0.3) the stochastic pulsation ('not BP') dominates. For curiosity, there is a third 'optimum' with low
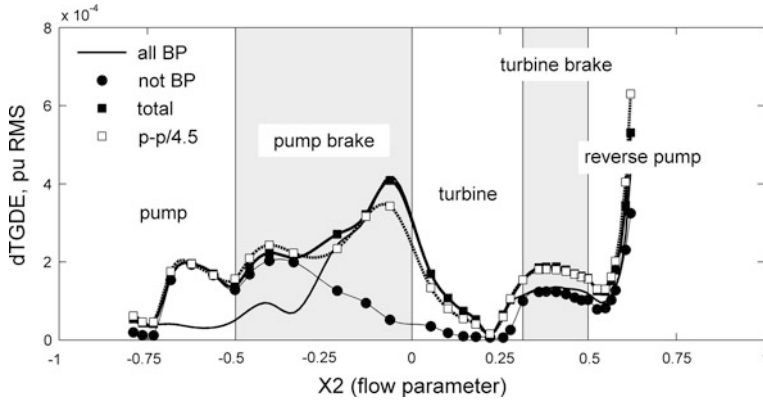
Fig. 7.30 Guide vane torque pulsation in four quadrants

pulsation at X2 ~ 0.6 in the region of reverse pumping (pump flow with rotation in the turbine sense).

7.3.3 Runner Forces

Both steady-state and unsteady forces and moments acting on the model runner have been measured in some pump turbine projects. A brief account on the technology is given in [6], from where Fig. 7.31 is reproduced.

The model must be equipped with a special shaft where combinations of strain gages are mounted whose output signals permit the separation of the three components of force and three components of moment. The radial components x and y are of particular interest.

In order to obtain the force components as seen from the stationary (casing) system, the x and y components must be processed using a transformation taking account of the angular position of the shaft.

The test point represented in Fig. 7.32 has been measured on model B from Table 7.5. It is a test point at partial load with a relative turbine head $E_{nD}/E_{nD,opt} = 0.659$ and relative discharge $Q_{nD}/Q_{nD,opt} = 0.618$, at the lower border of the single-helix region. The cursor line shows the location of this point in the next figure, left-hand graph.

The force and moment components in the stationary system (upper side of Fig. 7.32) are basically sinusoidal with the relative vortex precession frequency (28 % of the runner frequency, or, in model scale, 7.8 Hz) seen in all of the spectra. The measured phase of 90° between the x and y force components indicates that the corkscrew vortex produces a radial force (plus radial momentum) that rotates together with the pressure field; it is a product of the DTPP
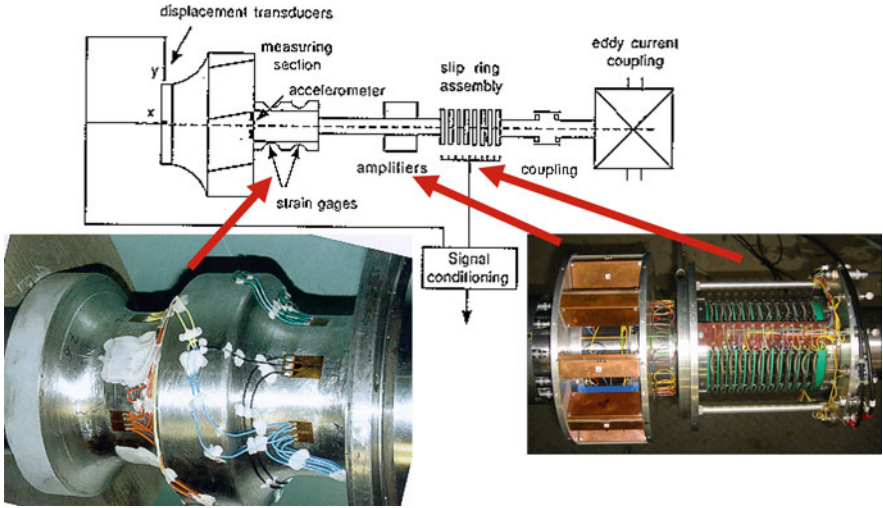
Fig. 7.31 Equipment for runner force measurement
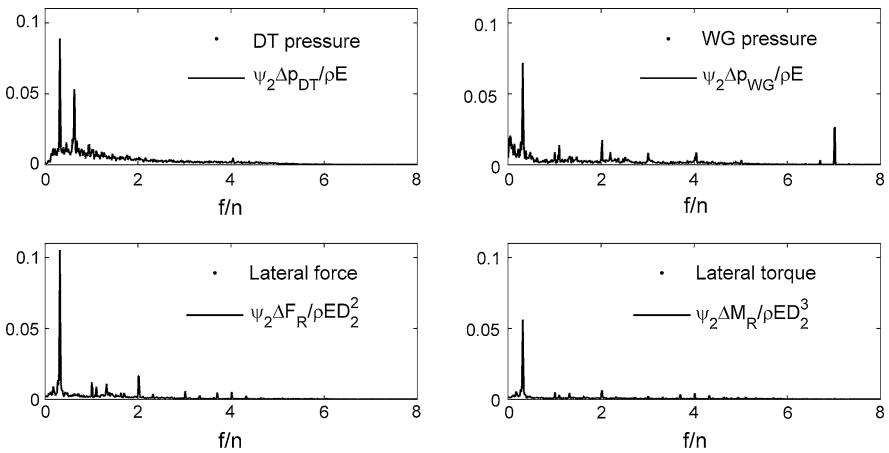
Fig. 7.32 Pulsation of pressure, runner force, and moment, at partial load

asynchronous part of the draft tube pulsation. The right-hand side of Fig. 7.33 shows, for the same load condition, the resulting x and y components of the radial force during a period of 25 runner revolutions. With the relative frequency $f/n = 0.28$, this translates to seven orbits of the vortex precession. The orbits are recognizable as large circular structures, with smaller movements at higher frequency superimposed. At lower load, the amplitude of radial forces F_x, F_y increases but the sinusoidal behavior gives way to random pulsations.

Table 7.5 Pump turbine models and test condition in Fig. 7.24

Model	A	B	C	D	E	F
D_1/D_2	1.722	1.722	1.519	1.431	1.388	1.080
Z_r	6 + 6	7	7	7	9	9
E_{nD}/E_{nDopt}	0.767	0.788	0.744	0.718	0.753	0.823
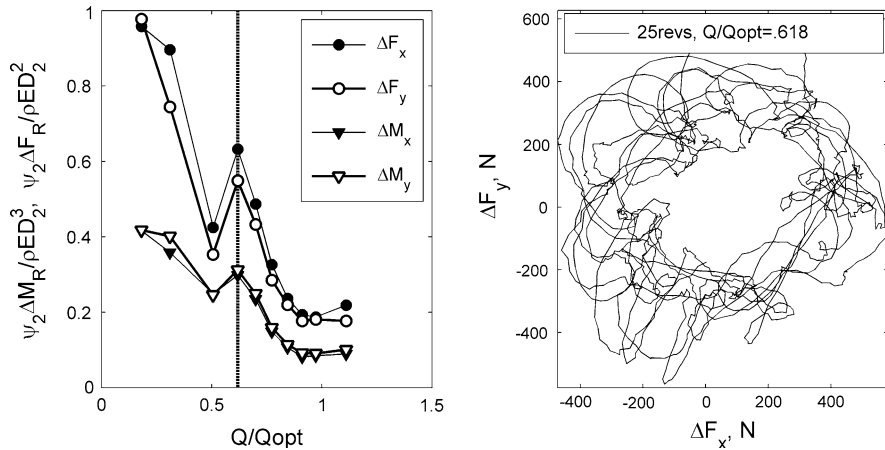
Fig. 7.33 Pulsation of runner force and draft tube pressure versus load

7.4 Axial Turbine Model Tests

Except for fixed-blade propellers, axial turbines are less prone to rough operation due to draft tube pulsation because they normally operate on-cam, that is the runner blade opening angle is adjusted to give approximately swirl-free runner exit flow at all discharges. Nevertheless, some pulsation is always present which may be subject to guarantee requirements.

7.4.1 Bulb Turbine Tests

Pressure pulsation (DTPP) has been measured in the draft tube of a model bulb turbine with a 4-blade runner. The pressure transducers were at a distance of one (1.0) runner diameter from the runner center plane. Only operating points close to on-cam condition were considered. It is important to distinguish between blade passage and the low-frequency DTPP. The frequencies of blade passage were not included in the evaluation whose frequency range terminated at the runner frequency. As with Francis turbines, there is no chance for a simple result unless we find a suitable measure for relative amplitude. Again, we use the peripheral velocity head based on blade speed as a reference. It turns out that this indeed
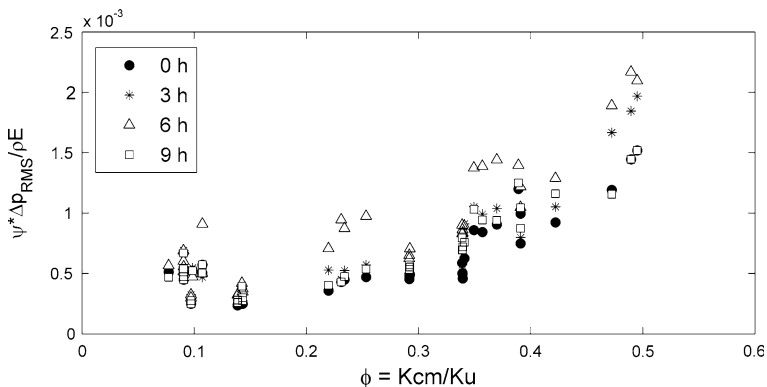
Fig. 7.34 Bulb turbine DTPP on-cam, without blade passage

reduces the scatter but the result depends on the runner blade opening, or discharge coefficient. It may be noted that this influence does not appear in Francis models (compare to the right-hand side of Fig. 7.8), but there we had to deal with effects of the corkscrew vortex which does not exist in on-cam operation.

The pulsation caused by blade passage was excluded because it depends so much on measuring distance from the runner that it has to be represented versus axial position (as shown in Sect. 3.4.3). The contribution of runner blade passage is important in bulb turbines because of the low number of blades.

The x axis in this diagram is proportional to the turbine discharge. The prototype operating head for the test points in the diagram extends over a large range from 3.0 to 11.2 m. Using the standard pulsation measure $\Delta p/\rho E$ for guarantees over such a wide range means that separate guarantees have to be given for many values of head. A more suitable measure like the one chosen for Fig. 7.34, or even a single-number guarantee in absolute pressure terms, would avoid that. On the other hand, a constant *relative* limit (in percent of head) will not be efficient because it will be either too high for high head, or cannot be fulfilled at minimum head.

7.4.2 Vertical Kaplan Turbine Tests

The model test results reported here concern a 6-blade turbine with a rated head of 26 m. Unlike the bulb turbine above, in this example we shall also deal with off-cam conditions.

Pulsation data in Fig. 7.35 have been measured for four different runner blade opening angles β; for every blade angle there is a different 'fixed-blade' hill chart whose best efficiency flow is approximately proportional to the blade opening angle. Measurements shown were made with various speed factors corresponding to prototype heads between 16 and 32 m. The reference flow $Q_{opt}(\beta)$ for every
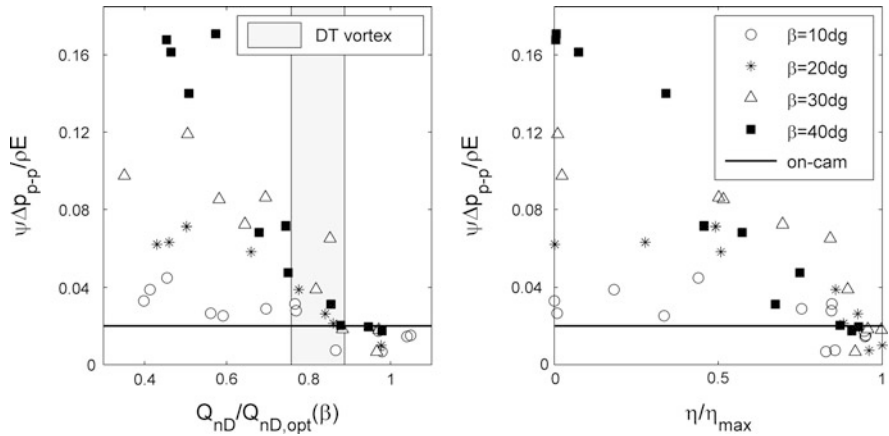
Fig. 7.35 Vertical Kaplan draft tube pressure pulsation

point in the figure is the individual optimum value for the respective β. The range of relative flow where the draft tube swirl is organized to a single-helix corkscrew with a well-defined frequency is for all runner blade positions between 75 and 88 % of the respective Q_{opt}. Compared to Francis turbines, this range is much narrower and closer to the best-efficiency condition. Another difference is that the pulsation amplitude at lower load continues to increase over the values in the single-helix range. In addition, the maximum amplitude strongly increases with runner blade opening.

As mentioned above, Kaplan turbines normally operate on cam, which means that relative discharge values inside the vortex range marked in the figure, or even lower, do not occur. Small deviations from the optimum runner blade opening for a given flow are possible without significant increase of pulsation. There is sufficient margin around $Q/Q_{opt}(\beta) = 1$ on the left-hand side of Fig. 7.35. The right-hand diagram shows the margin as a function of the deviation from on-cam efficiency.

The next figure (Fig. 7.36) concentrates on the draft tube vortex phenomenon in this turbine. Only the conditions located in the shaded area of Fig. 7.35 are represented. The DTPP amplitudes are smaller than the comparable ones for Francis turbines. The large dependence on the runner blade angle seen in Fig. 7.35 at lower discharge does not appear in the vortex range. Unlike the Francis turbines, much larger pulsation amplitudes occur at low partial load, and are due to irregular vortices.

The right diagram in Fig. 7.36 shows the vortex frequency increasing with the optimum discharge coefficient, for the four runner blade positions tested. This influence is, in a statistical sense, also found in Francis turbines, compared to Fig. 7.11. As in that figure, the relationship between φ_{opt} and f/n is approximately proportional, with the exception of $\varphi_{opt} \cong 0.1$ which does not occur in Francis turbines.
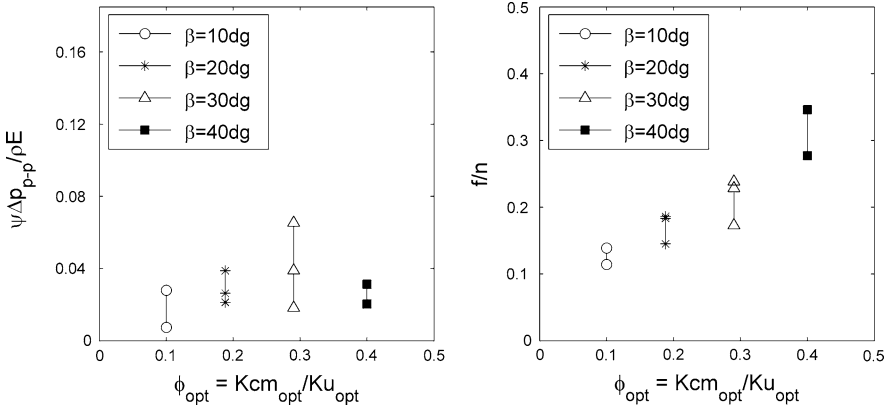
Fig. 7.36 Vertical Kaplan pressure pulsation, DT vortex amplitude, and frequency
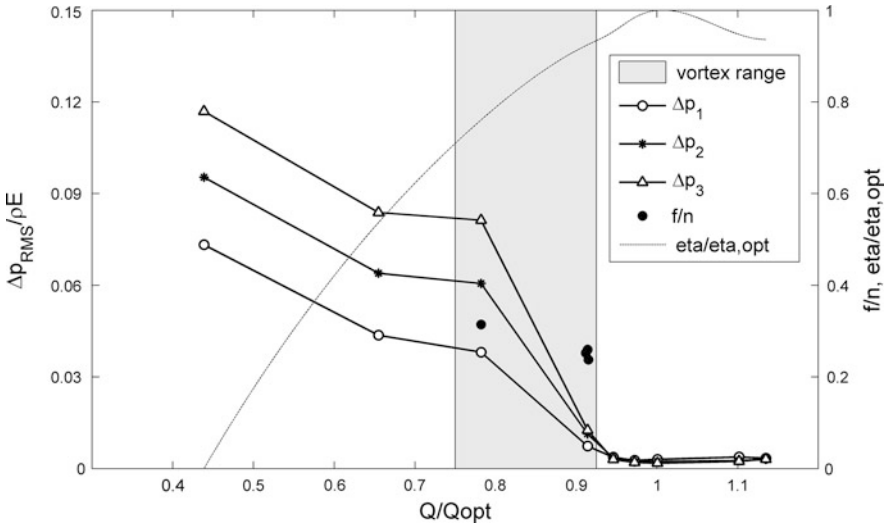
Fig. 7.37 Fixed-blade draft tube pressure pulsation

The 2 % limit, in this case corresponding to an admissible pressure pulsation of ±0.65 mwc, shown in Fig. 7.35 can only be applied for on-cam condition. There is however a sufficient margin with deviations up to ±10 % from the on-cam condition where pulsation is still low. The large variation of the vortex frequency does not represent a practical problem because the draft tube vortex does not appear in on-cam operation.

7.4.3 Vertical Fixed-Blade Turbine Tests

The behavior of the Kaplan turbine at a constant (large) runner blade opening, already shown in the previous chapter, is what we have to expect from a fixed-blade turbine. Operation 'off cam' is by definition unavoidable, and therefore much higher pressure pulsation occurs in steady-state operation at partial load.

Figure 7.37 is from the model test of a turbine with five runner blades, operating at a head of 11.5 m. The pressure taps are located at three circumferential positions in the draft tube cone. The two test points with a vortex frequency (black dots) show that the vortex range in terms of Q/Q_{opt} corresponds well with the test of the 6-blade Kaplan runner shown in Fig. 7.35 (left-hand side). The guaranteed range of operation begins just at the upper limit of the vortex region. From there upwards, the operation is very smooth.

The draft tube amplitudes in Fig. 7.37 are indicated as a percentage of the operating head, this makes sense because the operating head of the plant does not change significantly. It should be noted that the amplitudes shown are rms values; the peak–peak amplitudes would be higher by a factor of 4.5 approximately. Expressed in terms of runner velocity head, maximum peak-to-peak values of the same magnitude as in Fig. 7.35 would result, the pressure coefficient being $\psi = 2gH/u_1^2 = 0.34$.

References

1. IEC 60193. (1999–2011). *Hydraulic turbines, storage pumps and pump-turbines—model acceptance tests* (2nd ed.).
2. Lecher, W., & Baumann, K. (1968). Francis turbines at part-load with high back-pressure. *IAHR section hydraulic machinery, equipment, and cavitation, 4th symposium, Lausanne, Paper B-4.*
3. Fisher, R. K., Palde, U., & Ulith, P. (1980). Comparison of draft tube surging of homologous scale models and prototype Francis turbines. *IAHR section hydraulic machinery, equipment, and cavitation, 10th symposium, Tokyo,* Vol. 1, pp. 541–556.
4. Jacob, T., Prénat, J.-E., & Randriamamonjy, M. (1993). General survey of draft tube cavitation patterns in a medium specific speed Francis turbine. *IAHR work group wg1 (the behavior of hydraulic machinery under steady oscillatory conditions) 6th meeting, Lausanne.*
5. Egusquiza E., Mateos, B., & Escaler, X. (2002). Analysis of runner stator interaction in operating pump-turbines. *21th IAHR symposium on hydraulic machinery and systems, Lausanne, Switzerland, 9–12 September 2002.*
6. Doerfler, P., Lohmberg, A., Michler, W., & Sick, M. (2003). Investigation of pressure pulsation and runner forces in a single-stage reversible pump turbine model. *IAHR work group WG1 (the behavior of hydraulic machinery under steady oscillatory conditions) 11th meeting, Stuttgart.*
7. Tanaka, H. (1990). Vibration behaviour and dynamic stress of runners of very high head reversible pump turbines. IAHR *Section Hydraulic Machinery, Equipment, and Cavitation, 15th Symposium, Belgrade, Paper U2.*
8. Doerfler, P. (1994). Observation of pressure pulsations at high partial load on a Francis model turbine with high specific speed. *IAHR work group WG1 (the behaviour of hydraulic*

machinery under steady oscillatory conditions) *6th meeting, Lausanne 1993, also in: Hydro-power & Dams, January 1994*.

9. Arpe J., & Avellan F. (2002). Pressure wall measurements in the whole draft tube: steady and unsteady analysis. In *Proceedings of the 21st IAHR symposium on hydraulic machinery and systems, Lausanne, Switzerland*, September 2002, pp. 593–602.
10. Doerfler, P. (1986). Design criteria for air admission systems in Francis turbines. *IAHR section hydraulic machinery, equipment, and cavitation, 13th symposium* (*Montreal, 1986*), Vol. I, Paper 8.
11. Nakanishi, K., & Ueda, T. (1964). Air supply into draft tube of Francis turbine. *Fuji Electric Review*, Vol. 10(3).
12. Biela, V. (1998). Draft tube fins. *IAHR section on hydraulic machinery and cavitation, 19th symposium Singapore,* pp. 454–461.
13. Doerfler, P. (1982). System dynamics of the Francis turbine half load surge. IAHR *section hydraulic machinery, equipment, and cavitation, 11th symposium, Amsterdam*, Vol. 2, Paper 39.
14. Tadel, J., & Maria, D. (1986). Analysis of dynamic behaviour of a hydroelectric installation with a Francis turbine. *5th international conference on pressure surges, BHRA, Hannover*, Paper G1, pp. 169–176.
15. Jacob, T., & Prénat, J-E. (1996). Francis turbine surge: discussion and data base. *IAHR section hydraulic machinery, equipment, and cavitation, 18th symposium Valencia,* pp. 855–864.
16. Dörfler, P. K. (2009). Evaluating 1D models for vortex-induced pulsation in Francis turbines. In *Proceedings of the 3rd meeting IAHR workgroup on cavitation and dynamic problems in hydraulic machinery and systems, Brno, Paper F3*.
17. Dörfler, P. K. (2010). 'Neo-Suterian' pump-turbine characteristics and their benefits. *25th IAHR Symposium on Hydraulic Machinery and Cavitation, Timisoara*.
18. Suter, P. (1966). Representation of pump characteristics for calculation of water hammer. *Sulzer technical review research issue ,* pp. 45–48.

Chapter 8
Selected Field Experience

Measurement of vibration or pressure pulsation data on a prototype machine may be performed in order to verify compliance with guarantee, or in a monitoring process or, in some cases, to provide data for root cause analysis if the dynamic behavior is deemed unsatisfactory. It may occur that the nature of a problem is not immediately clear and testing has to check for several possible aspects. This chapter therefore presents a number of practical cases separated from the pertinent chapters. The logic of finding the facts and possible solution strategy based on the underlying physical phenomena is demonstrated.

The case studies reported here have been kept deliberately short and concentrated. Rather than giving too many details, it is intended to present the widest possible spectrum of experiences, with particular focus on successful solutions. Other experiences from prototype machines are included in the specialized chapters.

8.1 Francis Turbine with Forced Oscillation at High Load

In a power plant with 4 Francis units, unacceptable pulsation of draft tube pressure, penstock pressure, and active power at high load occurred during commissioning. Table 8.1 shows the main data of the turbine and water conduit. Every turbine in this plant has a separate penstock, with no surge tank.

During model testing for this project, a corkscrew vortex below the runner was visually observed at high discharge, similar to that which normally occurs at partial load, but in the opposite sense of rotation (counter swirl). The amplitudes involved, however, were not deemed critical.

The turbines have a deep and rather narrow draft tube, and no inserts in the draft tube. Stability at partial load is satisfactory. During commissioning of the first unit under a head of 151 m, power swings up to 8 MW p-p occurred. In addition, the dynamic axial displacement of the shaft was too high.

An erratum to this chapter is available at 10.1007/978-1-4471-4252-2_10.

Table 8.1 Main data of the generating unit and water conduit

Rated head	H_r	143	m
Rated output	P_r	138.5	MW
Runner exit diameter	D_2	3.39	m
Speed	n	214.3	rpm
Total flywheel effect	J	2770	$t \cdot m^2$
Penstock first natural frequency	$f_{n,u}$	1.70 … 1.25	Hz
Penstock inertia	$\Sigma L/A$	8.6 … 11.7	m^{-1}
Draft tube inertia	$\Sigma L/A$	1.84	m^{-1}
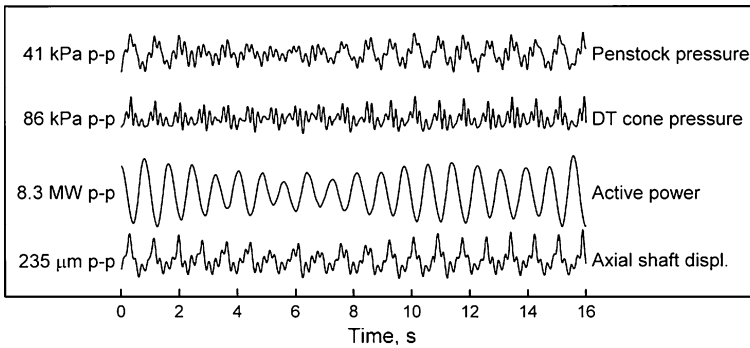
Fig. 8.1 Pulsation record, original condition

   A typical test result from the exploratory test campaign is shown in Fig. 8.1. The pressure fluctuations in the penstock and draft tube have the same main frequency, in the presented test point 1.23 Hz, with a component of higher frequency superimposed. The same behavior is also observed in the axial displacement of the shaft. The pressure amplitude in the draft tube is much higher than in the turbine intake.

   Detailed analysis in the frequency domain showed that three different phenomena were involved at the same time, combining to produce the undesired high amplitudes. The root cause of pulsation at high load was the precession of the draft tube vortex. Unlike the similar phenomenon at partial load, there is a strong dependency between the turbine discharge and the vortex precession frequency. At partial load, the swirl ratio increases while the discharge decreases—thus producing a fairly balanced frequency versus load. In the case of a forced oscillation at high load, the swirl number increases together with the discharge, thus producing a steeply increasing frequency characteristic of the precession frequency f_s, see Fig. 8.2.

   Due to the cavitation compliance of the draft tube vortex, there is also a hydraulic natural frequency f_h which, at high load, decreases with load, due to the increasing swirl intensity and diffuser effect. When the forcing frequency hits the natural frequency, the forced pressure pulsation is amplified, in a manner well

Fig. 8.2 Conditions
of resonance
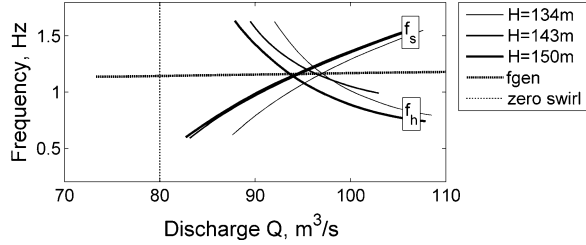
Fig. 8.3 Aeration influence
on frequency spectrum
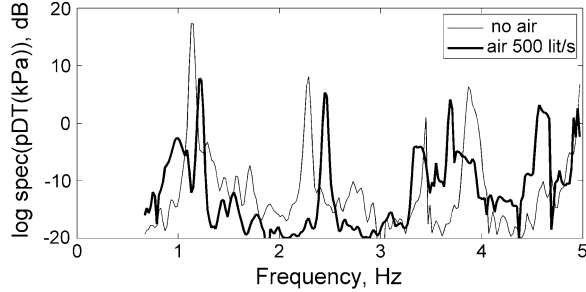
known from the classical partial-load pulsation. In this project, resonance occurred within the range of normal operation, where the f_h and f_s curves intersect.

Both frequencies can be identified from the frequency spectra of draft tube pressure, as in Fig. 8.3. This diagram is semi-logarithmic, the log scale for amplitude ranging from 1 to 100 mbar and the linear scale for the frequency. Two tests with the same constant load condition—115 MW at a head of 134 m—were done one after the other, one without aeration (thin line), and the other with compressed air injected through the runner (bold line). The spectrum with aeration shows the peaks for the natural frequency ($f_h = 1.00$ Hz) and the precession frequency ($f_s = 1.225$ Hz) separated. When no air is injected, the natural frequency is higher and the precession frequency is somewhat lower. In this case the two characteristic frequencies coincide at $f_s = f_h = 1.15$ Hz, and accordingly the forced hydraulic pulsation is in resonance, with the pressure amplitude becoming three times higher.

The typical effect of aeration on vortex rope frequencies as shown here is to reduce the natural frequency and to slightly increase the precession frequency, see also Fig. 8.4.

In the given case there is not only a hydraulic resonance amplifying the pulsation of pressure and turbine discharge, but unfortunately the frequency of 1.15 Hz is at the same time also the natural frequency of the generator, as shown in Fig. 8.2. Thus, in addition to the hydraulic pulsation and the axial shaft vibration, the pulsation of active power was further amplified. As already shown in Fig. 8.2, this condition persisted at different levels of net head.

While air injection is helpful in detuning the hydraulic resonance in the case shown above, it may also be harmful in other conditions. For instance, if the

Fig. 8.4 Hydraulic
resonance shifted by aeration
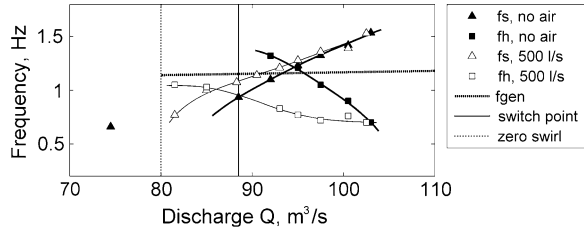
Fig. 8.5 Aeration influence
on power amplitude
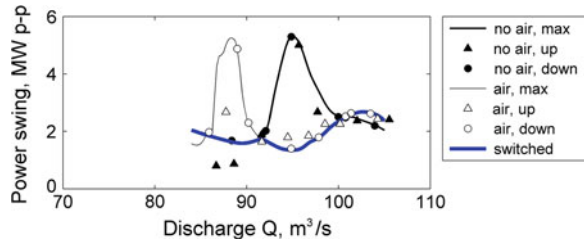
turbine discharge is about 86 m^3/s, the frequency of the pressure source f_s is lower, and aeration would reduce the natural frequency just as much as to provoke resonance. The same would also occur at partial load where the natural frequency without air is also higher than the precession frequency. It was necessary to determine a precise limit for the load range with aeration. For that purpose, test series with and without air were conducted for each unit. Each test series was conducted both with ascending and descending load, to account for possible delay effects.

Figure 8.5 shows how the switching point for aeration is defined for an individual unit. Differences between the units may be related to the different penstock length. The first natural frequency of the penstocks in this plant (Table 8.1) is also close to the frequencies discussed here, however the penstock influence on the natural frequency f_h is believed to be smaller than the draft tube cavitation influence. The amplitudes in Fig. 8.5 are 'equivalent peak-peak' amplitudes from rms values, the true peak−peak values being about 40 % higher. The switching point is slightly different from the intersection between the power resonance curves with and without air, because it is defined based on the pressure pulsation data with slightly shifted resonance 'humps'. The thin and bold lines indicate the behavior with and without injection of an air flow rate of 0.5 m^3/s. At lower load, the resonance produced by aeration would not be much behind the original problem encountered at higher load without air; thus an intelligent compressor control is of essence.

For aeration, the turbines of this plant have holes in the runner coupling bolts and an air pipe connected to the head cover. However, self-aspiration is not possible because the vortex is eccentric in this case, therefore no cavity can be tapped in the turbine axis. For this reason, compressors had to be used for aeration. A small hysteresis applies between switching on and off, in order to avoid unnecessary starting/stopping the compressors.

Table 8.2 Main data of the unit and water conduit

Rated head	H_r	148	m
Rated output	P_{max}	306	MW
Runner exit diameter	D_2	4.95	m
Speed	n	150	rpm
Total flywheel effect	J	13300	t· m^2
Penstock first natural frequency	$f_{n,u}$	2.0	Hz
Penstock inertia	$\Sigma L/A$	4.36	m^{-1}
Turbine fluid inertia	$\Sigma L/A$	1.96	m^{-1}
Draft tube inertia	$\Sigma L/A$	1.12	m^{-1}

Prior to the compressor tests, the approximate amount of air required was identified during a slow transient test using a variable, slowly decreasing amount of air provided from one of the pressure air tanks of the turbine regulators. Additional tests showed that resonance could also be avoided satisfactorily without using the full 500 l/s compressor capacity. In the final condition, three compressor sets were shared by the four units, one of them serving as a backup.

8.2 Francis Turbine with Self-Excited Oscillation at High Load

During commissioning of a vertical medium-head Francis unit, unacceptable pulsation of the draft tube pressure, penstock pressure, and active power was observed at high load. Table 8.2 shows the main data of the turbine. In this case, the pulsation was generated by a feedback mechanism between the size of the draft tube cavity and the turbine discharge. The mechanism was not well understood at the time. The solution had to be found on an empirical basis, but nevertheless the problem could be eliminated.

The draft tube of this turbine is deep and narrow but has a central pier. It is equipped with four draft tube fins. Operation at partial load is quite smooth. In this campaign, aeration also plays an important role. However, it was only after a long and difficult search for effective measures that the problem could be solved completely. The original concept for aeration through the runner hub is shown in Fig. 8.6.

The first observations were made during commissioning of the first unit when the turbine was operating under a head of 145 m. The condition of instability prevailed starting from 290 MW generator output until 320 MW output (full gate). In this condition, the first field measurements were performed in order to ensure proper understanding of the root cause. The pressure in the turbine intake and draft tube, the active power, and a number of mechanical vibrations were recorded and analyzed. Peak-to-peak power swings of 35 MW, and pressure oscillations up to 1.5 bar were recorded. The frequency of oscillations decreased steadily with
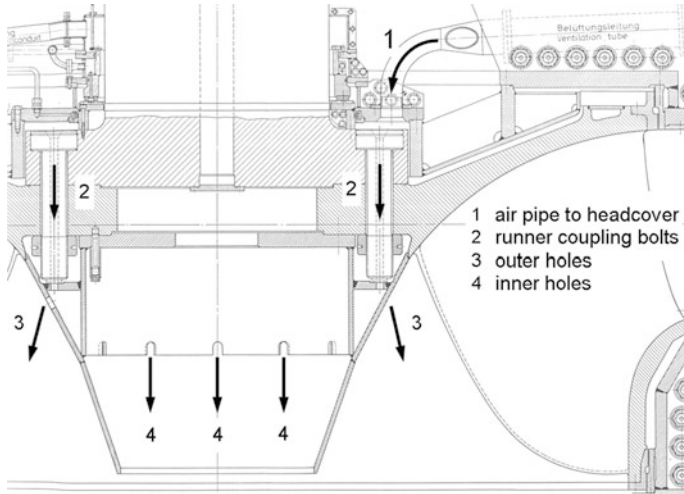
Fig. 8.6 Original condition of runner—no air aspirated

ascending load, from 80 to 20 % of runner frequency (part A of Fig. 8.7), the typical behavior of the self-excited full-load oscillation. In this turbine, the discharge at the best-efficiency point is 180 m^3/s. If the turbine discharge considerably exceeds this value, then an increasing amount of counter-rotation is produced in the flow exiting from the runner. The compressibility C_C of the cavitating core of this vortex increases together with the swirl. The pulsation frequency is the lowest natural frequency of draft tube flow which is approximately proportional to $1/\sqrt{C_c}$. Based on this feature it was possible to confirm the mechanism of the pulsation. The pulsation of penstock pressure and draft tube pressure had the same frequency as the generator output. Axial movement of the upper end of the shaft at the same frequency indicated that there was also a pulsation of axial thrust. Diagram (a) of Fig. 8.7 shows results of these tests in the original condition, both with ascending and descending load. The pulsation of pressure and power (see diagram) was equal for tests in both directions, and the turbine did not aspirate air in any test condition. To check for possible influence of the voltage control, additional tests were performed with the power system stabilizer (PSS) shut off. In these tests, the hydraulic oscillation remained the same while the power swing increased (diamond markers in graph (a)).

It was clear that the problem had to be solved on the hydraulic side, and steps were taken to make the turbine aspirate air. The original aeration holes in the hub were closed, and an air path to the center of the hub was built, in order to tap the expected vacuum. Figure 8.8a shows the modified hub. During tests with this configuration (part (b) of Fig. 8.7), and stepwise increasing load, the turbine started to draw air, but only at very high load. When the load was reduced, the turbine continued to aspirate air in the whole range affected by the pulsation. With the exception of a narrow zone, the pulsation was reduced to a low level. It was concluded that the location of the air
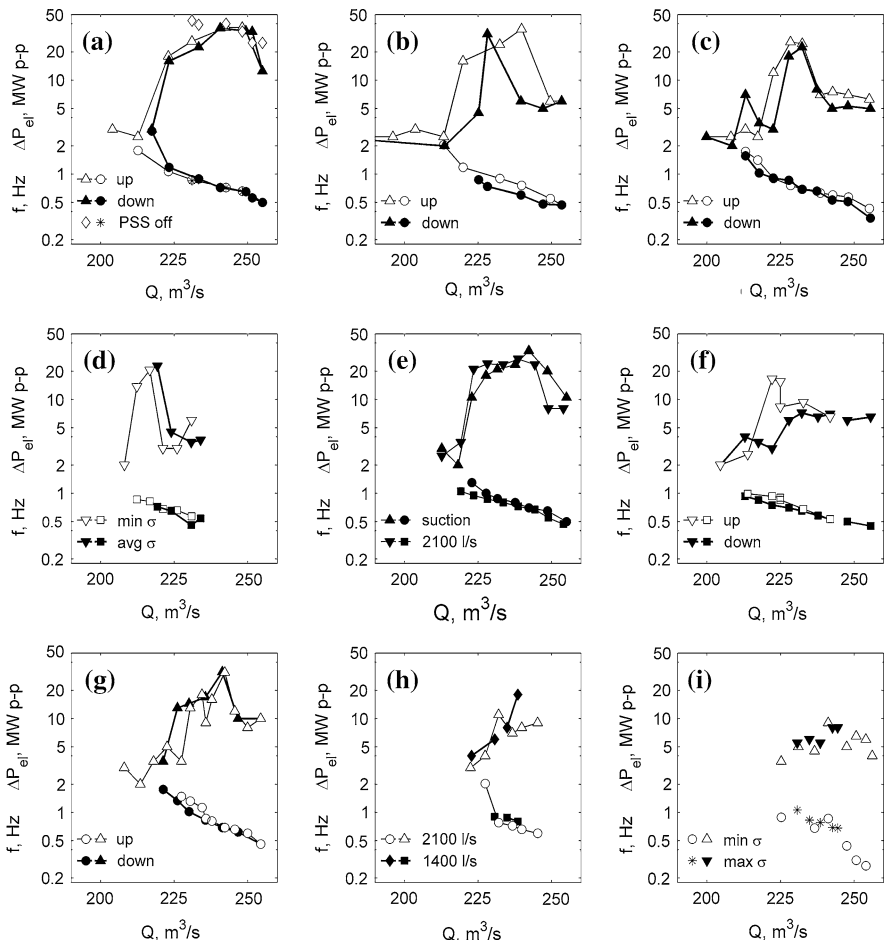
Fig. 8.7 Successive steps toward problem solution

outlet was not optimal because the turbine could only draw air once the hub was clear of water. A snorkel pipe was added in order to safely tap the vacuum below the runner as soon as the vortex develops, see right half of Fig. 8.8. As expected, the difference in behavior between ascending and decreasing load was eliminated. The turbine could aspirate air whenever the discharge exceeded 210 m^3/s. However, a residual pulsation remained near 230 m^3/s. With power swings in excess of 20MWp-p, further improvement was deemed necessary.

Aeration had provided stability in most but not all of the affected load range. Based on the idea that the effect of the naturally aspirated air flow was probably not sufficient, enhanced air flow was tested by means of three rotary piston compressors working in parallel, supplying a total intake air flow of 2.1 m^3/s. The increased air flow did not reduce the pulsation, see part (d) of Fig. 8.7.
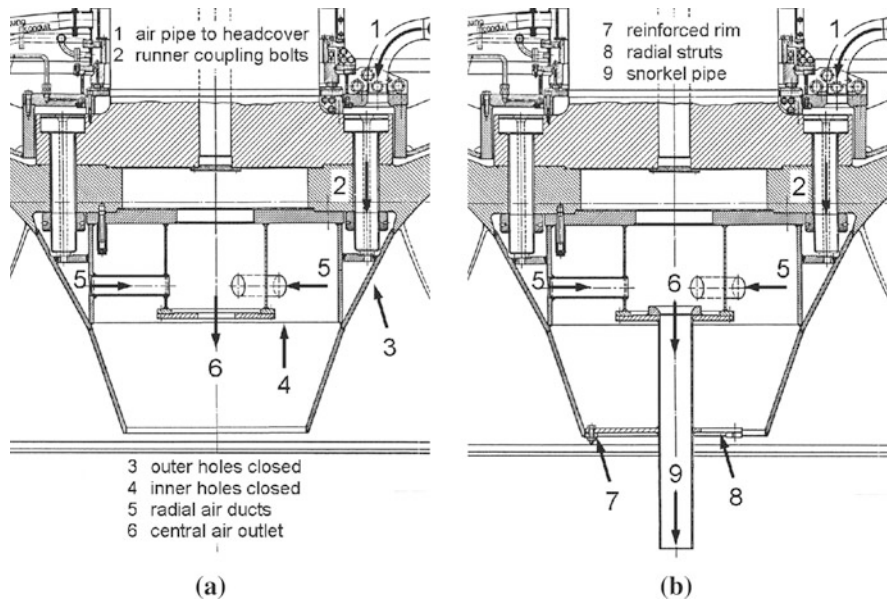
Fig. 8.8 Modifications of runner hub. **a** Step 1, **b** step 2

A new strategy had to be adopted, aiming for an improvement of flow conditions in the runner exit. To manipulate the negative swirl, a set of seven axial fins was mounted on the outer side of the hub. The test results, shown in the graph (e), proved this concept a failure, both with natural and forced aeration, and the fins were removed.

The design of this turbine comprised an annular chamber below the discharge ring, foreseen for additional aeration through the draft tube wall. As a next step, this chamber was activated, providing connection to the draft tube flow through a large number of circular holes. The admission of atmospheric air through the hub was combined with compressed air to the draft tube wall. This proved to be a step toward better stability (graph (f)), but in a small residual range, some power swing remained.

Another effort was then made to correct the runner exit flow. Based on CFD runner flow simulation (in 1988), the runner blades were cut back at the hub side of the trailing edges. With regard to steady-state performance, the CFD results were confirmed in a new model test. The pulsation in the prototype, checked in tests with natural air admission comparable to graph (c), was still there but slightly shifted toward higher load (part (g) of Fig. 8.7) and only slightly reduced when the central air flow was increased by compressors (part (h)).

In analogy to the combined aeration test of graph F, the joint aeration through the hub (atmospheric air) and draft tube wall (compressed air) was again tested and, together with the runner blade modification, was finally successful as shown in graph (i) of Fig. 8.7. In addition, field tests were done covering the entire range of tail water levels of the plant; the natural suction at the runner hub proved to work up to the maximum specified submergence of 7 mwc.
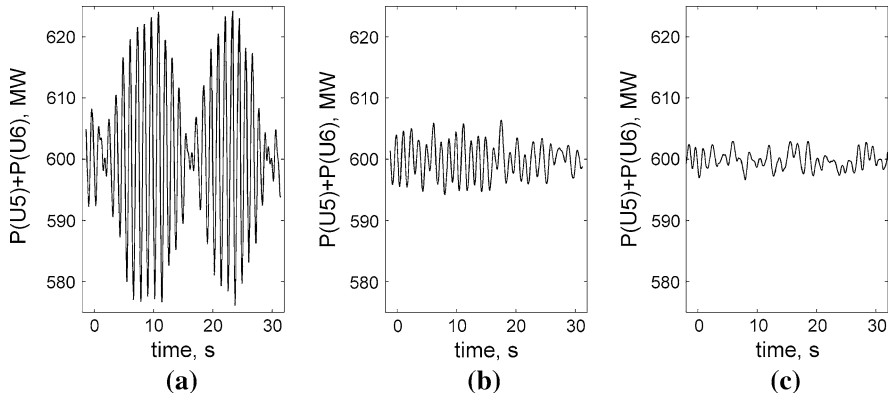
Fig. 8.9 Combined power stability of two units. **a** No air, **b** air to hub, **c** air to hub and wall

In a final test, the combined power stability of several units was tested. Figure 8.9 shows the total outgoing power of the station measured at the switchyard, for a test with two units operating at 300 MW each. With aeration shut off, both units produce the same magnitude of power swing (25 MW p-p) but with slightly different frequencies (0.82 and 0.89 Hz) because the underlying hydraulic pulsation is not coherent, resulting in a regular beat of the total power. With the atmospheric air admission activated, the power swing is already reduced; it could have been worse if load were somewhat different, due to the narrow remaining range of instability. With compressed air added, the power swing is finally reduced to a very moderate level.

8.3 Pump-Turbine Pulsation and Instability at Speed-No Load

A high-head single-stage reversible pump-turbine connected to a long penstock had various issues with pressure pulsation and instability at speed-no load condition, while the dynamic behavior in normal operation was without problems in both turbine and pump modes. The penstock has a total length of 1.6 km and an interior diameter from 3.7 to 3.3 m. The exposed pipe has a wall thickness between 20 and 25 mm (Table 8.3).

8.3.1 Penstock Vibration and High-Frequency Pulsation

Before the unit was connected to the network, vibration of the penstock was detected in speed-no load condition. Measurement of pressure pulsation in the turbine intake and draft tube showed that pressure pulsation with a frequency close

Table 8.3 Main data of the unit and water conduit

Rated head	H_r	485	m
Rated output	P_r	150	MW
Runner diameter	D_1	3.76	m
Speed	n	500	rpm
Total flywheel effect	J	625	$t \cdot m^2$
Penstock first natural frequency	$f_{n,u}$	0.17	Hz
Penstock inertia	$\Sigma L/A$	200	m^{-1}
Draft tube inertia	$\Sigma L/A$	10	m^{-1}

to 10 Hz was present in the draft tube as well as the turbine intake. The latter pulsation propagated upstream through the penstock and caused noticeable vibration of the cylindrical shell, at the same frequency. An area with rather high vibration was found 1.2 km upstream of the powerhouse where the design pressure was already low and the thin shell had several natural frequencies in the range excited by the turbine. The most affected area was between two anchor blocks of the exposed penstock having 3,500 mm inner diameter and a wall thickness of 21 mm, the internal pressure being 11.7 bar. The pipe is reinforced by ring girders every 16 m. Modal analysis of the fluid-filled penstock showed a natural frequency of 10 Hz pertaining to a mode shape with two nodal diameters (ovalization mode) and a half wavelength between adjacent ring girders. The shell vibrated basically according to this mode, with slowly varying amplitude, the peak−peak displacement sometimes attaining 4 mm in the vertical, and 3 mm in the horizontal direction.

Analysis of the pressure fluctuations in the no-load condition showed that mostly frequencies close to 10 Hz were present at both sides of the pump turbine. The left-hand side of Fig. 8.10 shows typical time histories measured at 96 % speed. The highest amplitude, denoted by MIV (main inlet valve) occurs at the turbine intake; the right-hand graph is a spectrum for this signal. The sharp peak close to 8.8 Hz coincides with a natural frequency of the water column in the penstock, in this case the 28th natural mode. Compared to the operating pressure of 52 bar, the intensity of the pressure pulsation is not alarming, but fluctuations are also present in the other parts of the penstock [1] including the region 1.2 km upstream (anchor block 16 N, AB16 N in the left-hand graph) where they cause the shell vibration.

The precise mechanism that generated the pulsation could not be clearly identified. It is likely that the turbine produces the ordinary wideband pulsation which is amplified near 9–10 Hz by the natural frequency of the draft tube and tailrace. Injection of air into the draft tube, however, was not effective in reducing the pulsation. It was finally not eliminated, the amplitude remaining always moderate. The vibration of the penstock was considered serious enough and a monitoring system was installed for surveillance of the pressure pulsation and vibration conditions at the penstock.
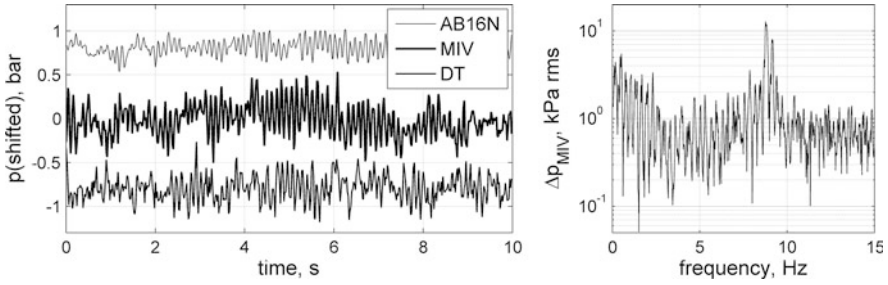
Fig. 8.10   Pressure variations and spectrum at 96 % speed, no load

Fig. 8.11   Oscillation close
to 100 % nominal speed
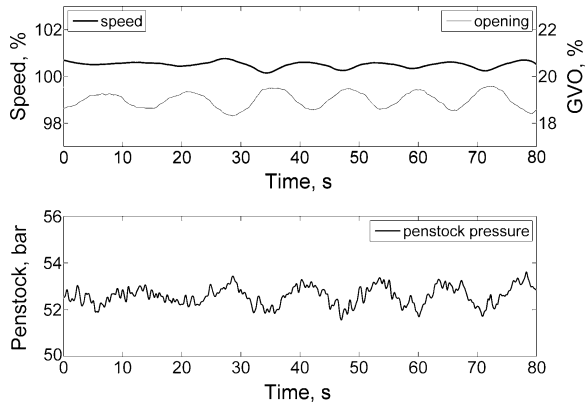
8.3.2 Instability at Speed-No Load

The performance guarantees for this particular pump turbine required that operation (and synchronization) must be possible at a speed and network frequency up to 103 % of the nominal value. It was discovered early that this value of speed could not be maintained in a stable manner. The speed, penstock pressure and, due to governor action also the guide vane opening,[1] oscillated with a period of approximately 15 s, as shown in Fig. 8.11. The reason was that at guide vane opening in excess of 16 % (3°) the speed-no load point became hydraulically unstable at the prototype turbine. This was not expected because in the model test the characteristic had a stable tendency. The question was how the problem could be overcome, and start and synchronization could be managed without any risk of instability.

The oscillation period of 15 s was in good agreement with an estimate obtained from Martin's approximate formula for the rigid water hammer case without speed

---

[1]   A 5 Hz low pass filter was used for the pressure history in this graph, as well as in Fig. 8.13 to avoid distraction by the 10 Hz component.
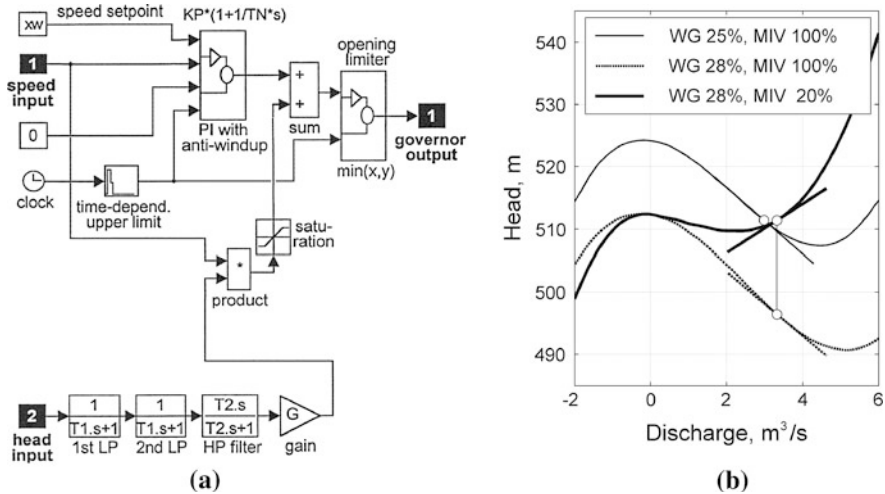
Fig. 8.12 Stabilizing measures. **a** Governor with pressure feedback, **b** throttling at inlet valve

regulation [2]. Indeed the speed governor responded to the variation of speed but did not significantly influence the oscillation, as shown in the upper graph of Fig. 8.11.

As a first step, a time-domain simulation model of the water conduit and pump-turbine unit including speed governor was built in order to thoroughly study the problem. The 4-quadrant transient characteristics of the pump turbine was slightly adjusted to represent the actual unstable behavior at speed-no load opening. A variety of possible speed governor concepts was simulated and the possibility of a governor-based solution was explored. An improved governor concept was identified that could ensure stability up to the limit of hydraulic stability but not beyond that limit.

Governor improvement consisted in adding to the PI governor a pressure feedback with appropriate filtering. The left-hand side of Fig. 8.12 is a flowchart of the modified speed governor. The pressure input is shown as input 2. The low pass filters minimize influence from spontaneous pulsations. The time constants T_1 and T_2 and gain G were optimized in a series of step response tests in speed-no load condition. The pressure feedback signal is subject to a speed-dependent weighting procedure; outside of the narrow range of speeds used for synchronization, it has to be suppressed because otherwise the pressure feedback would interfere with other vital governor functions during start or load rejection. The add-on pressure loop was valuable because it ensured safe operation in most conditions of head and network frequency. However it did not suffice to cover all of the specified n_{11} range.

The decisive shift of stability was obtained by the following artifice. The turbine was not started as usual with fully open main inlet valve (MIV), but the spherical valve was only partially opened and kept in a position of 20 % opening.

In this condition good hydraulic stability is achieved due to the throttling effect of the valve.

Figure 8.12b illustrates the principle of the stabilizing effect, for the no-load condition at 105 % speed. The root cause of instability is the negative slope of the original curve of head H over discharge Q in the zero-torque condition, in this case at a guide vane opening of 25 %. The partially closed position of the spherical valve—20 % valve opening—creates a head loss proportional to the square of discharge. A larger guide vane opening of 28 % is required to maintain speed due to the smaller net head seen by the turbine. At this opening, the turbine alone would still be unstable (dotted curve) but the ensemble of valve plus turbine has a stable characteristic according to the bold line, as shown by the positive tangent to this line in the new speed-no load point. The governor can then synchronize the unit very smoothly, and only afterwards the inlet valve is fully opened.

This unconventional procedure provided an effective solution. It was backed by a number of tests concerned with vibration at the valve and turbine [3], to prove that no new problems would arise due to the partly throttled valve.

This artifice can only be used in such power plants where, like in this plant, direct resynchronization after a rejection of load is not foreseen. It would not be acceptable to bring the main inlet valve to partially closed position when load rejection occurs because the valve would then lose its function as a safety device.

8.3.3 Medium-Frequency Pulsation

During the speed-no load tests in unstable condition, when the turbine was brought to even higher gate opening, an exotic pulsation phenomenon appeared. At 105 % speed, an almost periodic oscillation quickly built up whose period was 3.75 s. The onset of this pulsation, beginning from the rigid-column instability with 15 s period, is shown in Fig. 8.13. The pressure amplitude measured at the spherical valve was ±3.5 bar. It was suspected that higher amplitudes might have occurred in some reaches of the penstock because the fundamental frequency (0.267 Hz) was believed to be close to the first anti-resonance frequency of the penstock that, however, turned out to be 0.30 Hz. The near-periodic behavior and the good knowledge of the frequency response of the water conduit permitted an extraordinary analysis of the transient. The oscillation of all the important parameters was synthesized from the first 10 Fourier coefficients of the pressure upstream and downstream of the turbine, as well as the speed and wicket gate opening. The pulsation of flow Q was identified making use of the hydraulic impedance of the upstream and downstream sections of the water conduit which are known with good accuracy. The most surprising result of this synthesis is the dimensionless discharge diagram of the turbine shown in Fig. 8.14.

The diagram Fig. 8.14 below has been composed from the curves for discharge coefficient $\varphi(t)$ and head coefficient $\psi(t)$ synthesized from the Fourier spectra of the variables Q, H, and n. The pulsation of the wicket gate opening and of the

Fig. 8.13 Medium-frequency oscillation starts at 105 % speed
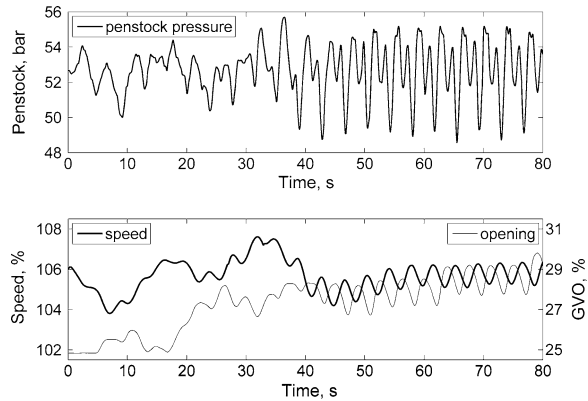
torque T was also determined. The x-axis (relative discharge coefficient) and the y-axis (relative head coefficient) are both shown as a ratio to the nominal values of the turbine. The relative coefficients in Fig. 8.14 remain the same if the standard coefficients Q_{nD} and E_{nD} are used instead of φ and ψ.

The transient operating point performs an oscillation cycle in the direction of the arrows in Fig. 8.14. The cycle will be explained starting at point 0 which corresponds to the minimum penstock pressure point in Fig. 8.13. In this point the discharge is quickly decreasing while the speed rises up to point 1 where the shaft torque T goes through zero. The trajectory follows the steady-state characteristics (gray curve) until point 2 where it starts to deviate abruptly; the following part from point 2 up until point 5 cannot be explained by the 4-quadrant curves measured in the model test. Point 2 is the minimum point of the discharge oscillation. At point 3 is the maximum deceleration of speed and at 4 there is a minimum of speed while the torque goes through zero. The kink at point 5 indicates that the trajectory comes back to the regular characteristic. The head shortly continues to drop, until (at 6—the higher minimum in the pressure curve in Fig. 8.13) the trajectory along the curve of constant opening angle reverses, and the cycle continues until another turning point (7). From here, the operating point follows the characteristic until the cycle is closed at point 0. The speed rises all the way from 4 to 1; the shaft torque passes through a maximum at point 8.

The reason for the 'forbidden' branch 2–5 of the trajectory is not known. The model test showed no deviation from the normal shape of characteristics. Obviously there is, in addition to the gray curve, an alternative flow regime in the turbine that appeared only in the context of this oscillation.

The pressure history along the whole penstock could be identified based on the discharge pulsation from this analysis. The pulsation had not attained the design pressure in any part of the water conduit during the transient. The unexpected pulsation was, however, not allowed to occur again. In addition to the effective stabilizing measures described in Sect. 8.3.2, the plant was equipped with a protection system monitoring pressure in several points of the penstock.
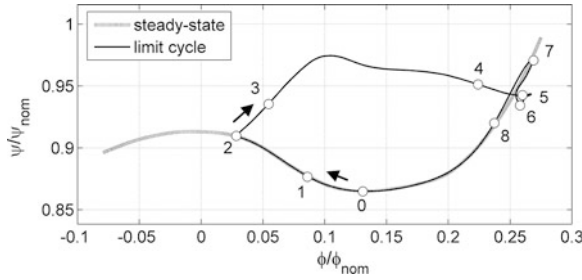
Fig. 8.14 Hysteresis loop during medium-frequency instability

Table 8.4 Main data of the unit

Rated head	H_r	27.4	m
Rated output	P_{max}	62.6	MW
Runner diameter	D_1	6.45	m
Speed	n	94.7	rpm
Number of guide vanes/stay vanes	Z_0	24	–
Number of runner blades	Z_2	6	–

8.4 Von Kármán vortex in Propeller Turbine Stay Vanes

The turbines in this plant were erected in the early 1960s. At commissioning of the first unit, high vibrations and 'bell-like noises' were observed in several locations of the unit and plant. Subsequent tests showed a pressure pulsation with a frequency of 38 Hz both in the scroll case and draft tube of the turbine. This phenomenon started when the gate opening exceeded 50 % and increased with load. At 100 % gate, the vibration was quite strong and could even be measured on the floor of the relay room (Table 8.4).

8.4.1 Cracking of Stay Vanes

Based on the measured intensities, the vibration was first classified as "slightly rough to rough—needs correction" but it was decided to keep the units operating and inspect them periodically. During one of these inspections, after 6 months of operation, cracks had developed in many stay vanes, in most cases starting from the welds at both ends of the trailing edge, as shown in Fig. 8.15. Some cracks also originated from the leading edge, and some of these cracks at the top end had already joined with the cracks from the trailing edge, and thus penetrated through the whole vane.
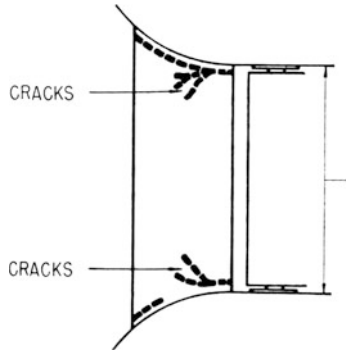
Fig. 8.15 Stay vane cracking pattern
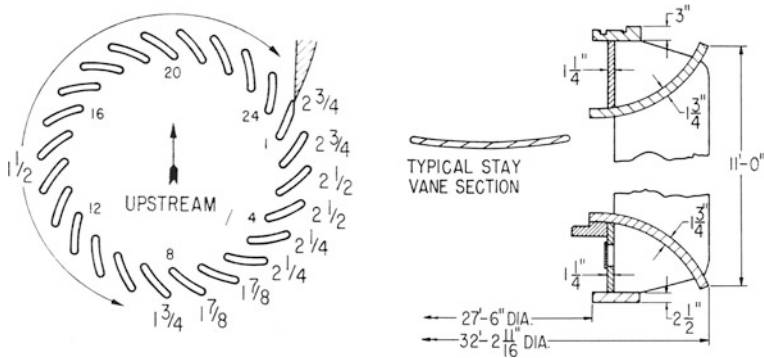
Fig. 8.16 Original condition of stay vanes

8.4.2 Analysis and Corrective Measures

The stay vanes had been manufactured from steel sheet by bending plates into a cylindrical shape, see Fig. 8.16. Stay vanes with five different values of thickness, from 2.75″ to 1.5″ were arranged along the circumference of the scroll case. Both the leading and trailing edges had a semi-circular profile.

It was noted that the 38 Hz vibration frequency was close to the so-called wicket passing frequency 24·94.7/60 = 37.89 Hz which is also a harmonic ($4nZ_2$) of the runner blade passing frequency. However due to the nature of the damages, the true cause of the problem was attributed to Von Kármán vortex shedding from the trailing edges of the stay vanes.

Some difficulty resulted from the fact of the large range of blade thickness. It was suspected that different modes of vibration may have been involved in the vibration. The four most simple modes were analyzed, which could be done—back in the 1960s—only in air. The results were compared to impact tests in air,
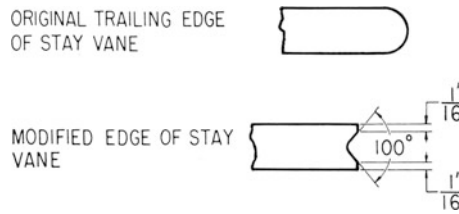
Fig. 8.17 Original and improved shape of trailing edge

Finite element mesh of the existing stay vanes

1st eigenmode of the stay vanes
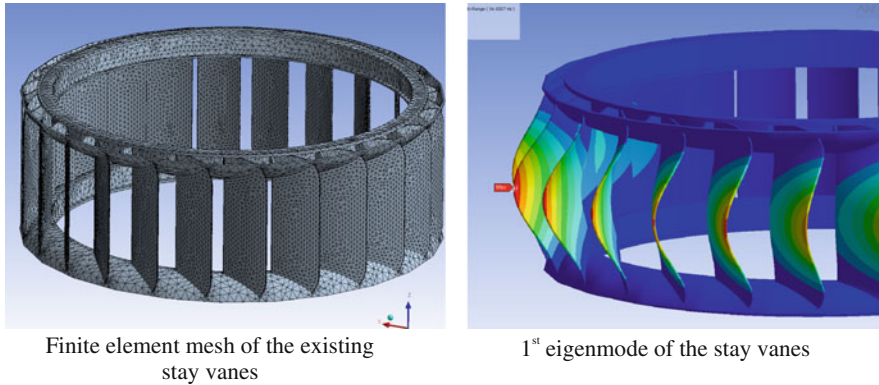
Fig. 8.18 Finite element model of the stay ring and first eigenmode of stay vanes (*right*)

showing fair agreement. The natural frequencies in water had to be estimated using a frequency reduction which at this time was believed to be some 27.5 %.

Research concerning the influence of trailing edge geometry on the formation of vortex streets was only newly available in the early 1960s, and it was recognized that the semi-circular profile of the trailing edge was quite unfavorable. The vanes were repaired and were given a better profile. A dovetail shape, as shown in Fig. 8.17 was chosen which had been shown to provoke much lower intensity of excitation force. Another reason for choosing this profile was its relative insensitivity to variations of the angle of attack between the different circumferential locations.

By 1968, the correction was still reported completely successful [4] as no more cracks had developed so far.

8.4.3 Later Development

Despite dramatic improvement regarding both vibration intensity and durability of the stay vanes, cracking still occurred in later years, however at a reduced rate.

The owner of the plant had another analysis made, with much more advanced technology after 40 years. It was now possible to compute the free oscillations of the mechanical structure coupled with the surrounding fluid, and thus obtain

precise results for the mode shapes (Fig. 8.18) and natural frequencies in water. It was even possible to simulate the process of vortex shedding at the trailing edges, and compare with a still better shape for the edge. Last but not least, it was possible to analyze the energy losses in the existing cascade of stay vanes and guide vanes and the efficiency improvement to be realized by mounting new stay vanes with a more suitable profile and angle of attack.

8.4.3.1 Natural Frequency

In order to find a sustainable solution both the mechanical structure and the time-dependent flow patterns were analyzed with great care. In the following two sections both the FEM-based modal analysis and the CFD-based flow analysis and their respective results are described in more detail.

8.4.3.2 Modal Analysis of the Stay Vanes

The eigenfrequencies of the stay vanes are determined by their shape and thickness and by the fixation of the stay vanes in the stay ring. Therefore, the complete polygonal stay ring was modeled and individual thicknesses of the stay vanes were taken into account.

The thickness of the stay vanes varied from 100 to 183 % causing a variation of natural frequencies. Moreover, the natural frequencies vary with the shape and order of the excited mode.

Due to the added mass effect of the surrounding water the natural frequencies are considerably reduced. In this investigation which was done in 2006 the reduction factor between natural frequencies in water and natural frequencies in air was determined by analytical considerations together with interpretation of the available measurement data [5]. It is worth noting that since 2009, the method of coupling the modal analysis with surrounding water has become well tested and would be an alternative way to analyze the natural frequencies in water.

Based on the modal analysis it could be decided that the seven lowest eigen-modes were potentially critical regarding Von Kármán excitation. Any structural change would have to lead to an increase of eigenfrequencies if the Von Kármán frequency was not altered.

Various possible alternatives of modifying the stay ring were identified and checked by modal analysis. One possible solution was to install a new, modern stay ring and guide vanes which would not only lead to an elimination of the vibration problem but also to an increase in power output due to loss reduction. One alternative was to stiffen the stay ring such that the hydraulic profile would not be considerably altered.

In both cases it could be verified by modal analysis that there would be no more resonance with Von Kármán vortex shedding. But this conclusion was possible only on the basis of sufficiently accurate knowledge of the Von Kármán frequencies.

Computational grid   **Computed vorticity**
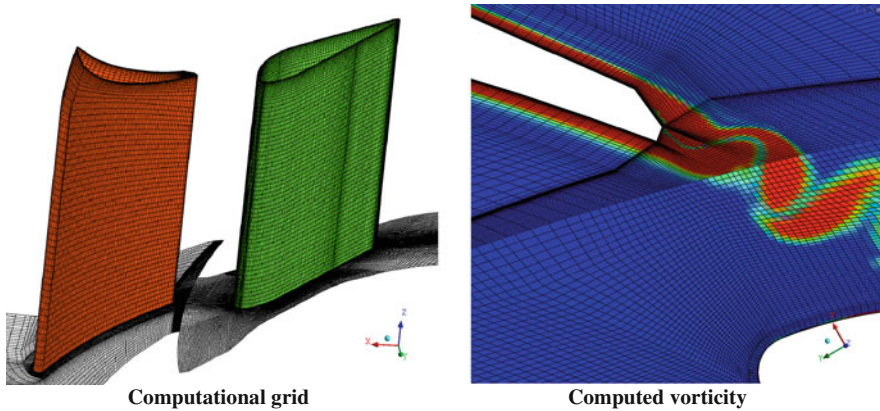
Fig. 8.19 Time-dependent CFD prediction of Von Kármán vortex street

8.4.3.3 Von Kármán Frequency

Von Kármán vortex shedding is a complex flow phenomenon which occurs both in nature and in technical applications where shear layers break into counter-rotating vortex streets. The shedding frequency f_A depends mainly on the flow velocity v and the thickness of the blade d. The frequency is then calculated according to the Strouhal law, $f_A = $ St·v/d with the non-dimensional Strouhal number S. According to experiments, St ranges between $0.18 <$ St < 0.24 depending on the specific geometry and Reynolds number.

It is assumed that the Strouhal number does not vary strongly neither with the position of the stay vane nor with the operating point because neither the flow conditions nor the geometry vary in a large way.

The Von Kármán vortex computations are based on the experience gathered in an extensive numerical parameter study of an elementary case. In the elementary case it was found that the computed Von Kármán vortex shedding frequency is about 20 % lower than the measured one [5]. The observation was independent of several tested numerical parameters like turbulence model or grid size. The same discrepancy could be observed between the numerical results and measurements in the presented case as well, where a frequency of about 33 Hz is computed for the existing geometry while the measured frequency is 38 Hz.

CFD simulations were carried out both for the original dovetail shape of the trailing edge and the Donaldson type modification of the blade geometry. Figure 8.19 shows the computational grid and monitoring points for one of these simulations.

As described in the literature [6–8], the Donaldson modification leads to a considerable reduction of the amplitude of the resulting force. This effect can be explained by a phase shift of the vortices which develop on each side of the blade rotating with opposite spin and thereby partly eliminating each other.
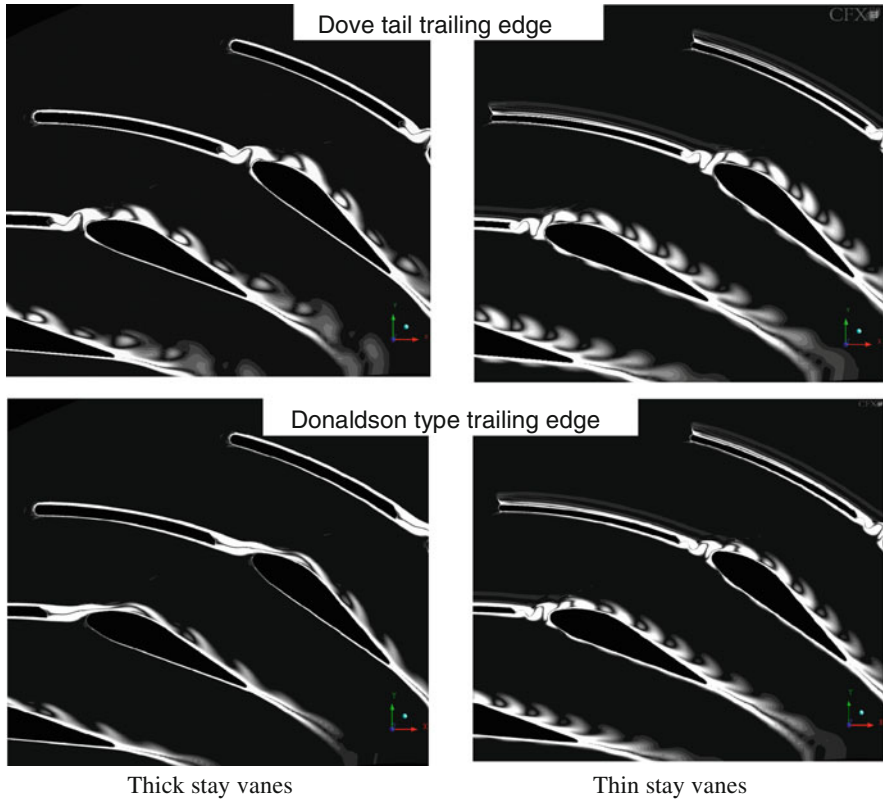
Fig. 8.20 Von Kármán vortex shedding visualized by vorticity

At full-load operation the CFD results for the Donaldson-like modification show a slight reduction of the amplitudes compared to the results for the dovetail-shaped trailing edge especially at the thick stay vanes where the shift between the two counter-rotating vortices leads to a nearly complete elimination of the resulting force (Fig. 8.20). At the thin stay vanes the interaction of the vortices is found to be less beneficial.

Most important, the CFD simulation shows that the vortex shedding frequency is not influenced by the shape of the trailing edge. Consequently, a change in the trailing edge shape would not be sufficient because the Von Kármán frequency remains in the range of the natural frequencies of the structure. Therefore, a refurbishment of the stay ring was proposed which would lead to an alteration of the natural frequencies of the stay vanes.

8.4.3.4 Loss Reduction

A possible solution to the vortex shedding problem was suggested to be a new stay ring with slightly thicker, hydraulically well-suited stay vanes whose natural

Existing stay vanes   Modern stay ring
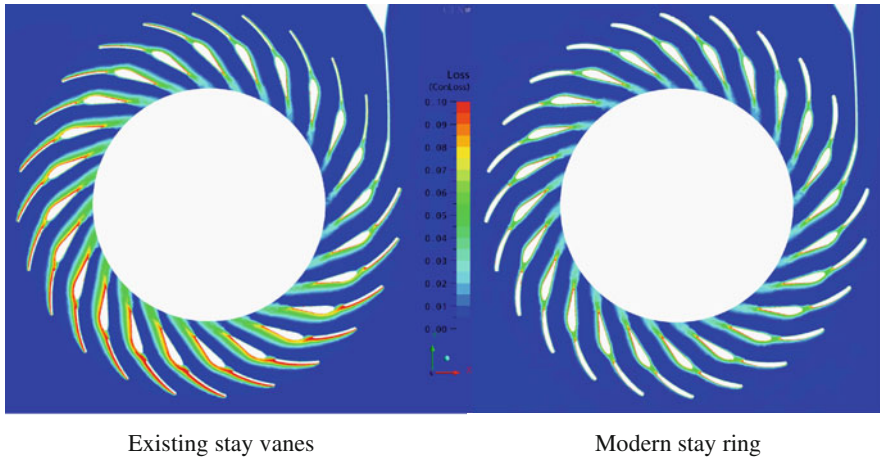
Fig. 8.21 CFD prediction of loss in the distributor at full load (*red* high loss, *blue* low loss), from [5]

frequencies are sufficiently far away from the Von Kármán vortex shedding frequency. CFD simulations of the flow through both the existing and the new distributor show an improved flow with less loss production in the modernized stay ring. As shown in Fig. 8.21, loss in the existing stay ring is mainly due to flow incidence at the inlet edges of the stay vanes in the first two-thirds of the distributor which causes flow separation, zones of high loss on the suction side of the stay vanes as well as unfavorable flow at the guide vanes leading edges. Thicker inlet edges of the stay vanes in the modernized stay ring guide the flow in a smoother way thus preventing flow separation and zones of high loss. Hence, with the help of CFD it could be demonstrated that a modern stay vane profile would not only be safe of cracking but also lead to a higher output of the turbine (Fig. 8.21).

8.5 Vertical Kaplan Turbine with Disturbed Intake Flow

An annoying phenomenon was observed in one out of four vertical Kaplan turbines of a block-type run-of-river power plant with four units. The turbines have a semi-spiral intake with two piers. Two pairs of units are of identical design. This section deals with the identical Units 2 and 4 (Table 8.5).

All four turbines of the plant were upgraded in the 1990s. The unit concerned—Unit 4—is the one located at the riverside end of the powerhouse, adjacent to the weir. It was anticipated that this unit would have precarious inflow conditions because in the absence of gate overflow the inflow from the bay enters with a large lateral velocity component.

Table 8.5 Main data of the turbine	Rated head	H_r	9.09	m
	Rated output	P_r	25.2	MW
	Runner diameter	D_1	7.20	m
	Speed	n	68.2	rpm
	Number of guide vanes	Z_0	24	–
	Number of runner blades	Z_2	4	–

Fig. 8.22 Simulated inflow to Units 2 and 4 1/3 of spiral intake shown

U4   U3   U2   U1
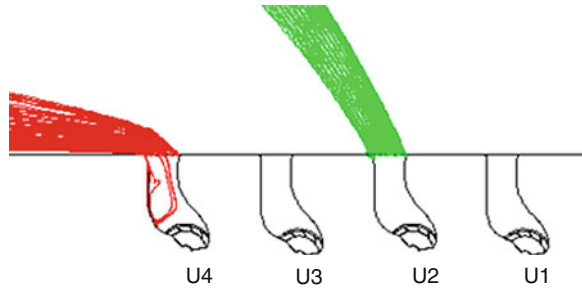
Figure 8.22 illustrates the very bad intake flow angle to the last unit. As an accompanying measure with the upgrading of the turbines it was necessary to provide more uniform inflow conditions to the stay ring close to the nose vane. To improve the situation, a stationary concrete vane had been inserted in the intake of Unit 4. A steady-state CFD study was made which concentrated on 1/3 of each intake adjacent to the nose vane (the other two-thirds between the other piers were replaced by sinks extracting the respective portion of discharge). A somewhat improved utilization of the intake region upstream of the stay vanes was obtained for Unit 4 (Fig. 8.23).

The study was later extended to study the interaction between the large-scale inflow and the internal flow conditions in the individual turbines.

8.5.1 Noise at High Load

At high head—in this plant this occurred with of low tail water level—it was observed that Unit 4 gets noisy if operated at high load. Unit 2, which is identical, continues to run smoothly at the same load. Initially, the character of the noise made the plant personnel assume that some rubbing or mechanical contact could occur with rotating parts.

The units have an inspection gallery all around the runner casing, this access was used to localize the annoying disturbance. It was found that there is a maximum of noise and also wall vibration slightly downstream of the guide vane located at the nose vane, in the sense of runner rotation. The maximum wall vibration occurred at an intermediate location between the wicket gate and the runner intake in case of fully opened runner blades.
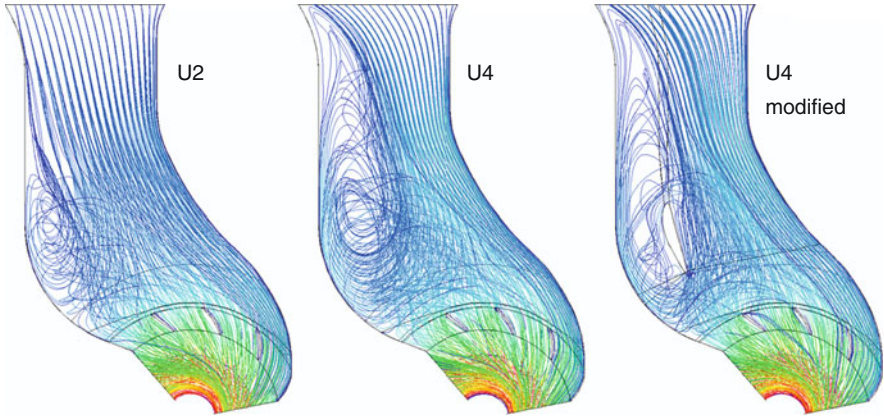
Fig. 8.23 Simulated spiral casing flow in U2 and U4
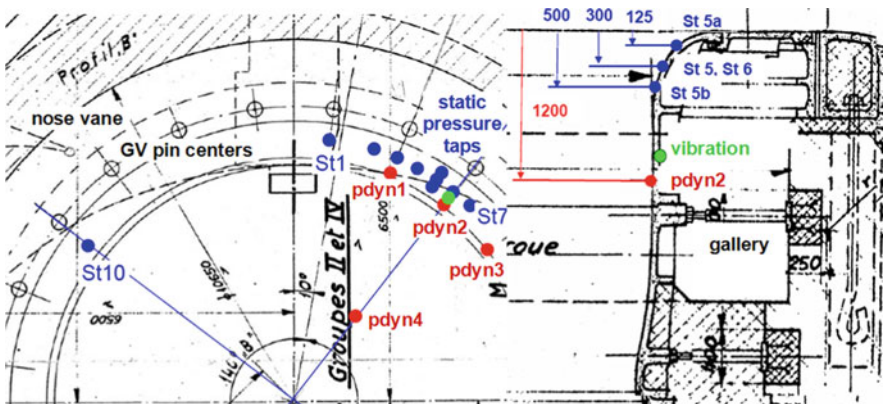
Fig. 8.24 Measurement locations

8.5.2 Root Cause Analysis

Inspection of the interior of Unit 4 did not confirm the suspected rubbing or mechanical collision between rotating and stationary parts.

To obtain quantitative data, a series of measurements was then performed on Unit 4. Pressure pulsation was measured at several points at the critical elevation, as shown in Fig. 8.24.

At the same time, the distribution of steady-state pressure was also measured in the area of interest between the wicket gate and runner. In addition, vibration of the wall and of the turbine shaft was recorded.

Fig. 8.25 Time histories of pressure, 24.1 MW, runner blade opening 86 %
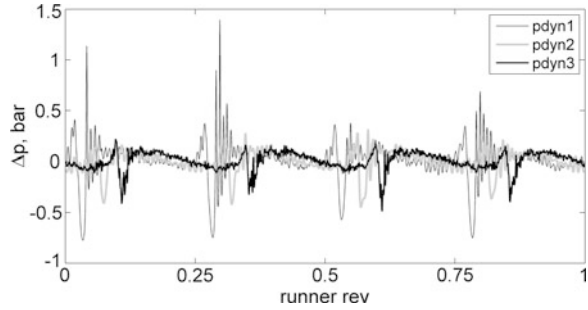
Fig. 8.26 Frequency spectra of pressure and vibration velocity
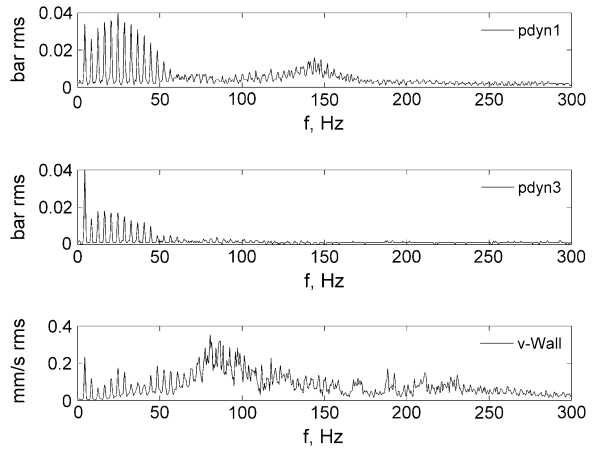
Steady-state pressure measurement locations are shown in Fig. 8.24 by blue symbols while red dots indicate the location of high-speed dynamic pressure sensors.

The intensity of pressure variation downstream of the wicket gate varied in much the same way as the perceived noise and wall vibration. The worst condition was found at maximum load. In this and all the other test points, the pressure pulsation clearly showed the period of runner blade passage (0.22 s) as shown in Fig. 8.25. Sensor pdyn1, where the strongest vibration was found, had also the maximum pressure pulsation, and this also showed some variation between successive cycles. The other sensors (see pdyn2 and shown in Fig. 8.25) had significantly smaller amplitude and better periodic behavior. Figure 8.26 shows that high harmonics made up for most of the pressure variation.

The spectrum of wall vibration, shown in the lowest graph of Fig. 8.26 has some similarity with the pressure spectra. It also has many harmonics of the runner blade passing frequency 4.55 Hz, and an important wide frequency band around approximately 100–150 Hz.

Fig. 8.27 Static pressure distribution in the stationary cascades

Unit 4   Unit 2
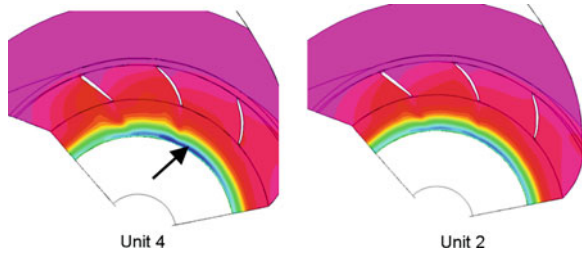
Fig. 8.28 Static wall pressure below guide vanes
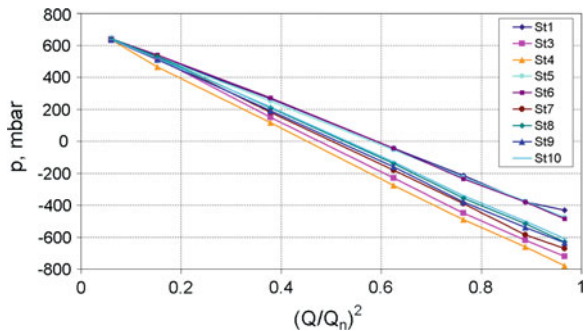
The reason for the large increase of pressure pulsation, noise, and vibration at the 'hot spot' downstream of the nose vane has been clearly identified by various phenomena. The inhomogeneous peripheral distribution of inflow creates a minimum pressure area in the region indicated in Fig. 8.27 by a black arrow. The runner blades rotate past this point and every blade experiences a local pressure variation. In a very short period a vacuum is generated at the minimum pressure spot which collapses a few milliseconds later, This collapse gives rise to a sharp pressure increase whose magnitude is sensitive to slight variations of the process. The area affected is somewhat above the runner. For this reason, and because the static pressure level decreases with increasing flow, the intensity of pulsation increases with the runner blade opening angle.

8.5.3 Possible Solution

Evaluation of the static pressure below the wicket gate in relationship to the relative turbine discharge is shown in Fig. 8.28. The curvature in the torus-shaped section creates a strong reduction of static pressure. It would be possible to use this vacuum to aspirate a small amount of air which would effectively mitigate the pressure shocks during blade passage. Air admission at this location has already been practiced in other, comparable turbines.

The static pressure readings represented in Fig. 8.28 are relative values (against atmospheric pressure), the location of the taps corresponding to Fig. 8.24.

After a review of the potential mechanical risks linked to the phenomenon it was concluded that the phenomenon was annoying but not critical with respect to mechanical safety. The main item reviewed was the runner blade which gets an impact once every rotation as the blade passes through the 'hot spot'. FE analysis accounting for both static and dynamic effects revealed there is an ample safety margin against fatigue strength. Based on this investigation, the owner of the plant decided to accept the condition and no corrective measure was executed.

References

1. Dörfler, P. K. (2011). *Pressure wave propagation and damping in a long penstock: Proceedings of the 4th Meeting IAHR Workgroup on Cavitation and Dynamic Problems in Hydraulic Machinery and Systems*, Belgrade.
2. Martin, C. S. (1986). *Stability of pump turbines during transient operation: 5th International Conference in Pressure Surges, BHRA, Hannover* (pp. 61–71).
3. Doerfler, P., Engineer, A. J., Pendse, R. N., Huvet, P. & Brahme, M. V. (1998). *Stable operation achieved on a single-stage reversible pump-turbine showing instability at no-load: 19th Symposium in IAHR Section on Hydraulic Machinery and Cavitation, Singapore* (Vol. I, pp. 430–440).
4. Goldwag, E. & Berry, D. G. (1967). Von Karman Hydraulic Vortexes Causes Stay Vane Cracking on Propeller Turbines at the Little Long Generating Station of Ontario Hydro, Journal of Engineering of Power, Transaction of the ASME, Paper No.67-WA/FE-40.
5. Lockey K. J., Keller, M., Sick, M., Staehle, M. H. & Gehrer, A. (2006). *Flow induced vibrations at stay vanes: Experience at site and FD simulation of von Kármán vortex shedding*, Hydro'06, Porto Carras, Greece, September 25–28.
6. Chen, Y. N. (1973). Durch die Nebensysteme erregte Schwingungen an den Kreiselpumpenanlagen, Teil 3: Strömungserregte Schwingungen an Platten infolge der Kármánschen Wirbelstrasse, (in German), Pumpentagung Karlsruhe, October 2–4.
7. Heskestad G. & Olberts D.R. (1960). *Influence of Trailing-Edge Geometry on Hydraulic-Turbine-Blade Vibration Resulting From Vortex Excitation*, Journal of Engineering for Power, Transaction of ASME, Paper No.59-Hyd-7, pp. 103–110.
8. Toebes G.H. & Eagleson P.S. (1961). *Hydroelastic Vibrations of Flat Plates Related to Trailing Edge Geometry*, Journal of Basic Engineering, Transactions of ASME, Paper No.61-Hyd-16.

Chapter 9
Practical Guidelines

In the successive stages of a hydroelectric project, the risk of flow-excited pulsations leading to problematic behavior of the plant should be accounted for by the various participants in a suitable manner. This starts with a good technical specification, and continues with a good design practice that avoids all kinds of possible pitfalls. The first physical test of the laboratory model has to be correctly assessed and finally the dynamic performance has to be correctly measured during commissioning of the machine, in some instances also in special tests, if improvements have to be found. Caution is required because results may be distorted under field conditions.

Some useful hints and guidelines to avoid the most common pitfalls are given in this chapter, but it should to be noted that any collection of suggestions for the wide variety of situations where pulsations can occur can never be complete. It is hoped that this collection includes those 25 % of the possible causes which account for about 75 % of the problems which may arise. The remainder of the cases will usually require expert advice or individual analysis.

9.1 Planning and Design

The planning and design of the power plant equipment has an enormous consequence on the risk of pulsations. We describe the aspects of planning (by the plant owner) and design (by the suppliers of equipment) in a common section because the common goal is more important than the formalities of the technical specification which really serves as an interface between the two parties.

An erratum to this chapter is available at 10.1007/978-1-4471-4252-2_10.

9.1.1 Influence of Plant Parameters

The influence of the main layout data of a hydroelectric plant on mechanical safety issues is directly concerned with its transient performance characteristics at design and off-design rather than with the pulsation phenomena of the machines. Nevertheless, there is also some direct influence of the plant layout parameters on the risk of pulsations. If the plant is equipped with Francis turbines or pump turbines, then the important factors for the behavior in off-design conditions comprise the length of the penstock, as well as the fluid inertia of the draft tube and tailrace, the turbine setting, and the variation of tail water level. Theories that would allow engineers to consider these parameters properly in the prediction of the pulsation behavior have not yet become standard. Any predictions which can be made have to be regarded with caution. While reflections concerning, for instance, the influence of the relative location of the powerhouse may be found in the literature [1], the underlying theories would have to be validated very thoroughly before they could reasonably be used in connection with plant layout.

    While it is not easy to give a clear-cut recommendation of quantitative data, the most important items influencing the dynamic behavior on the downstream side are clearly the inertia term

$$D_2 \int (dL/A) = D_2 I_2 g \tag{9.1}$$

between the runner and tail water, together with the relative variation of tail water level. A high value of the inertia term increases the risk of water column separation and hence reverse water hammer, and also lowers the lowest hydraulic natural frequency of the water conduit

$$\omega_{h,\min} \cong 1/\sqrt{I_2 C_{C,\max}} \tag{9.2}$$

which is critical for resonance conditions mentioned in Sects. 1.4 and 1.5. The resonance conditions are related to the risk of draft tube surges and power swings, and are the subject of the resonance check described in Table 9.1. Considering the cavitation influence on hydraulic pulsations explained in Sects. 2.2 and 7.2.3, the likelihood of hydraulic resonance or instability increases together with the possible variation of suction head.

9.1.2 Selection of Unit Data

The layout parameters of the hydroelectric units do have some influence on the probability for annoying dynamic phenomena to occur. If, for example, the power station will have Francis turbines with a speed of 300 rpm, then the draft tube pulsation at partial load will very likely occur at a frequency between 1.2 and 1.5 Hz, and thus be close to the generator's natural frequency and produce unwelcome

Table 9.1 Main resonance conditions in a Francis turbine

Exciter	Draft tube vortex	Runner unbalance	Runner passage	WG passage	Stay vanes Karman	WG Karman	Runner blade Karman
Frequency Nat. frequency	$0.2–0.4.n$	n, n_R	KnZ_r	$m.n.Z_S$	$St.v/d$	$St.v/d$	$St.v/d$
Water conduit	X1						
Shaft bending		X3					
Generator	X2						
Stay vanes			X8		X5		
Guide vanes			X9			X6	
Runner				X4			X7

power swings. This does not mean such units should not be built, but the predictable resonance should be dealt with in a rational way, as described in Sect. 9.1.4.

In a wider sense, in some projects it may be useful to first ask which type of machine would be best suited for the intended way of operation. There are intersecting ranges of head where a choice between either Kaplan or Francis turbines (30–70 m) or between Francis and Pelton turbines (200–700 m) may be made. While the Francis turbine has excellent peak efficiency and an advantage of lower cost, the double-regulated turbines may be preferable if operation at low load is intended for a large share of the operating time.

9.1.3 Pulsation and Vibration Guarantees

To ensure that a new or newly refurbished machine operates as smoothly as possible, quantitative limits for the level of vibrations or pressure pulsations are often stipulated as part of a technical specification. A few suggestions may serve to make such guarantees more efficient.

Pulsation guarantees—usually dealing with pressure pulsation—are left to the specific experience of the partners involved; there is no international standard providing a quantitative recommendation. At the same time, suppliers have, for about three decades, refrained from publishing such data. As a result, unrealistic requirements are quite common. The data presented in Chap. 7 of this handbook are intended to fill this gap.

It should be noted that possibilities to reduce the amplitudes of pulsations connected with the regular operation of hydraulic machines are limited. Also, the normal level of pulsation does not put the safety of a machine at risk. Therefore, the basis of a guarantee should be this normal behavior, and not some lower level of pulsation.

Much confusion results from the fact that guarantees for draft tube pressure pulsation (DTPP) are usually defined in percent of net head. As there is no systematic effect of net head on this amplitude, it would be more practical to guarantee in absolute units or for example as percent of rated head. The authors

recommend to define the draft tube pulsation guarantee as a peak-to-peak amplitude for the prototype, using the 97 % confidence limit as recommended in IEC 60193 [2], in absolute units of pressure, as a function of turbine discharge. To be of better practical value for the plant operator, this can easily be amended by charts where this guarantee is displayed as a function of power output, for the interesting values of operating head.

Other than for pressure pulsation guarantees, admissible levels of vibration are subject to international standards. ISO 10816/5 [3] sets limits for the rms vibration velocity measured at the radial bearings, while ISO 7019/5 [4] defines limits for the relative radial displacement of the shaft. The latter limit is a function of the speed of rotation. The rotating radial force occurring at partial load in Francis and fixed-blade Kaplan turbines as an unavoidable consequence of swirl is not accounted for, hence the radial shaft movement in such machines quite often exceeds the limit stipulated in the standard while operating in partial load.

To become efficient, a guarantee for shaft vibration would have to differentiate between operation at partial load and near design condition; a discharge-oriented criterion, changing at approximately 8–85 % of best efficiency flow, would be adequate. Above that flow value, a Francis or fixed-blade Kaplan turbine may be regarded as equivalent to a double-regulated machine operating on cam, and a vibration quality according to class A of the standard can reasonably be guaranteed. In the partial-load range below that limit, such a guarantee is sometimes counter-productive as it may induce the supplier to adjust a very low clearance at the guide bearings which may entail unnecessary high bearing temperature. Class B in ISO 7919/5 is therefore the best quality that makes technical sense in the partial-load range.

9.1.4 Resonance and Other Kinds of Trouble

A number of possible pulsation problems can be understood in terms of resonance, but many others cannot. For the case of a Francis-type turbine or pump turbine, Table 9.1 lists the most important pairs of forcing mechanisms (header line) and resonators.

The three rules explained in Sect. 4.1.3, in the context or Von Kármán vortex shedding, are also valid more generally for a range of problems. The rules are repeated here:

1. lower the forcing function caused by disturbances
2. avoid resonance
3. increase the damping

These rules are now discussed with respect to the pairs of forcing mechanisms in Table 9.1. As often stipulated in technical specifications, resonance should be avoided where this is possible (Rule 2), and this applies to each of the columns in this table.

For the interaction between the water conduit and the draft tube vortex, X1 in Table 9.1, the resonator is the fluid in the water conduit, not the draft tube and not the penstock. Its natural frequency is, however, mainly a function of the water inertia downstream of the turbine, I_2, and the cavitation compliance C_C, as discussed in Sect. 1.4. Depending on various influences, this natural frequency may be either lower or higher than the precession frequency of the vortex. So far the authors know no generally agreed way to determine the natural frequency of the water conduit and hence it is difficult to check for resonance X1 in advance.

The interaction between the generator and the draft tube vortex, X2, is series-connected with X1 because the fluctuation of shaft torque is roughly proportional to the pulsation of turbine discharge which in turn is the result of X1. X2 should be checked in any case because the vortex precession frequency is not altered by the resonance X1.

The avoidance of resonance X3 by means of critical speed analysis is a standard practice in rotating machinery.

The check for resonance X4 caused by runner-guide vane interaction requires more than just comparison of exciting and natural frequencies. Coinciding frequencies are dangerous only if the mode shape pertaining to a natural frequency is actually excited with the corresponding number of nodal diameters. The equivalent excitation with runner blade frequency (X8, X9) acts on the stationary components. The equivalent excitation with runner blade frequency (X8, X9) acts on the stationary components.

The frequency of Von Kármán vortex streets originating from the trailing edges at the three cascades (stay vane, X5, wicket gate, X6, and runner. X7), should not coincide with the natural frequencies of the respective blades. In the stay vanes, the velocity level is proportional to the discharge so it is sufficient to provide safety against resonance at maximum discharge, by assuring that the first natural frequency of the vane is higher than that of the associated vortex street. The velocity levels for the other blade rows vary over all load ranges and so coincidence between the Von Kármán frequencies and vibration modes cannot be checked or assured in advance. As may be understood from Sect. 4.1.3, freedom from resonance and vibration from the Von Kármán vortex streets is best obtained by weakening their effect (Rule 1). This is mainly limited by selecting a suitable trailing edge profile; this also holds for the runner blades. The authors recommend the use of a Donaldson type of trailing edge, or equivalent, for the wicket gates and the runner vanes.

A number of pulsations cannot be adequately handled in terms of the resonance scheme shown in Table 9.1. With regard to these phenomena, other means that may be summarized as 'good design practice' have to be taken to prevent damage caused by excessive pulsations—see next section.

One such class contains various types of fluid dynamic instabilities discussed in Chap. 6. In these cases, it does not make sense to deal with an instability by keeping apart the forcing and natural frequencies—the pulsation occurs by definition at natural frequency. On the other hand, in case of very wideband excitation, like for instance at very low load, there is no way to avoid resonance because the

continuous spectrum of pressure pulsations overlaps the natural frequencies of all the possible vibration modes of the main components. Robust design, with high inherent damping, is the only way to ensure the durability of the machines against this type of loads.

9.1.5 Good Design Practice

A hydraulic turbine or storage pump is a fairly complex object and at the same time, there are hardly two projects where machines of entirely identical design can be used. An element of uncertainty resulting from these facts cannot be avoided.

Unfortunately, there is no elegant single method to avoid at once all of the large variety of possible difficulties described in this book. One simply has to avoid each one of the pitfalls separately. Manufacturers who have supplied machines for many different projects may be expected to command an arsenal of design guidelines covering the various risks.

As a caution, Francis turbines should always be supplied with connections for admission or injection of air, regardless of the outcome of a model test or CFD study. It is always possible to encounter unexpected phenomena in a newly designed machine, even though surprises have become less frequent due to improved technology. It may become very costly if some pulsation must be acted on and there is no way to correct it by aeration.

9.2 Model Testing

IEC code 60193 is the international standard for model testing of hydraulic machinery for power plants. The code is quite detailed, which makes it easy to keep this section short. A few items may be improved, and indeed a maintenance round is taking place while this book is being written.

9.2.1 Test Conditions

Testing for pressure fluctuations should preferably be done on a test rig with simple boundary conditions. It is desirable to have a condition of zero pressure pulsation at the beginning of the high-pressure pipe connected to the hydraulic machine, as well as at the tail water side. The high-pressure pipe should not be very short, to provide some fluid inertia. This test configuration increases the chances to detect a tendency to high-load instability in the model.

The typical tests for DTPP at Francis models should preferably be executed with a Froude number equal to the prototype,[1] in other words, equal ratio H/D, as this ensures similarity with respect to the ratio between the dynamic pressures and gravity forces in the cavitation zone. For very large prototypes, this will not be possible. In such a case, the influence of gravity on the cavitation pattern of the draft tube vortex is not represented with similarity. As a compromise, it has been suggested to shift the reference elevation for the cavitation number σ halfway down the draft tube depth. Taking into account the diffuser effect, this correction is probably somewhat exaggerated. Quite likely, a degree of cavitation with comparable compliance will occur between the two extremes. For that reason, a variation of σ covering both the conditions should be tested for load conditions of particular interest.

9.2.2 Scope of Testing

In current practice, as mentioned in Sect. 9.1.3, an unnecessary amount of testing is sometimes spent because the standard definition of a dimensionless pressure pulsation factor makes the pulsation amplitude head-dependent. Using a physically sensible amplitude definition based on the exit kinetic energy, as in the pressure pulsation coefficient defined by Eq. (7.6), would reduce the necessary number of speed n_{ED} values tested, or permit the test effort to be applied for more useful investigations, for instance, variation of σ as described in Sect. 9.2.1.

Torque fluctuations at the model are very much dependent on the configuration of the test installation, and the same holds for the prototype. Similarity is normally not given, hence the results have no quantitative significance and the measurement of torque fluctuation does not reveal anything that is not already known from the DTPP results.

Measurement of hydraulic forces acting on the model runner is technically possible and the fluctuation forces, except those caused by the synchronous draft tube surge, may be regarded as similar. Within the scope of an ordinary model test for a commercial project, such measurements are an unnecessary complication because turbines and pump turbines are normally designed without specific new test data.

9.2.3 Interpretation

The results of model tests for pressure fluctuation must not be expected to be perfectly similar to the behavior of the prototype. As explained in Sect. 7.1, purely

---

[1] The standard IEC 60193 uses a Froude number definition $\mathrm{Fr} = \sqrt{(E/gD)}$.

local hydraulic phenomena may have better similarity compared to those which imply the response of the whole hydraulic system.

In model tests, high amplitudes are sometimes observed due to the 80 % pulsation (see Sect. 2.2.5) in the high partial load range. The value of these results is always questionable; normally, this phenomenon does not transpose itself to prototype. In case of large projects, much effort has been spent to obtain low amplitudes of the phenomenon in the model [5, 6], yet there seems to be no evidence that it actually occurs in the prototype.

Surges due to cavitation-related instability, i.e., full-load surge (Sect. 2.2.7) or low-load surge (Sect. 2.2.4) are particularly difficult to predict based on model tests. Several cases, like the ones discussed in Sect. 2.2.4 and 8.2 are known where prototype problems did not show in the model. Conversely, any indications for such phenomena in the model should be taken seriously because in some cases, for instance [7, 8] the prototype became hydraulically unstable at high-load and telltale signs of instability also showed in the model.

9.3 Field Testing

During commissioning of a hydroelectric unit, some amount of testing is usually concerned with the mechanical behavior, vibrations, and noise. The extent of such tests depends on the guarantees to be verified. Also, the supplier as well as the purchaser may seize the occasion to increase the knowledge base. Some guidance for such tests is given by the standard IEC 60994 [9].

The proper execution of dynamic tests is sometimes faced with practical limitations which have to be accounted for, as described in the following sections.

9.3.1 Measurement of Pressure Pulsations

The measurement of pressure pulsations requires suitable connections for the pressure transducers. It is advisable to foresee such connections as standard practice during design and construction. During commissioning, it may not be possible to procure additional pressure taps of good quality. The flexibility of testing is greatly enhanced if the foreseen connections are equipped with a shutoff device, like a ball valve, where transducers can be mounted and removed without dewatering of the unit.

The useful bandwidth of a dynamic measurement depends very much on the quality of the connection. The theoretical optimum would be to place the sensor flush with the wetted internal surface; but this is often impossible. It is imperative to minimize the length of the channel connecting the sensor to the flow, as this can seriously affect the pulsation measurements. Transducers connected by means of a pipe are often not capable of measuring the phenomena of interest because
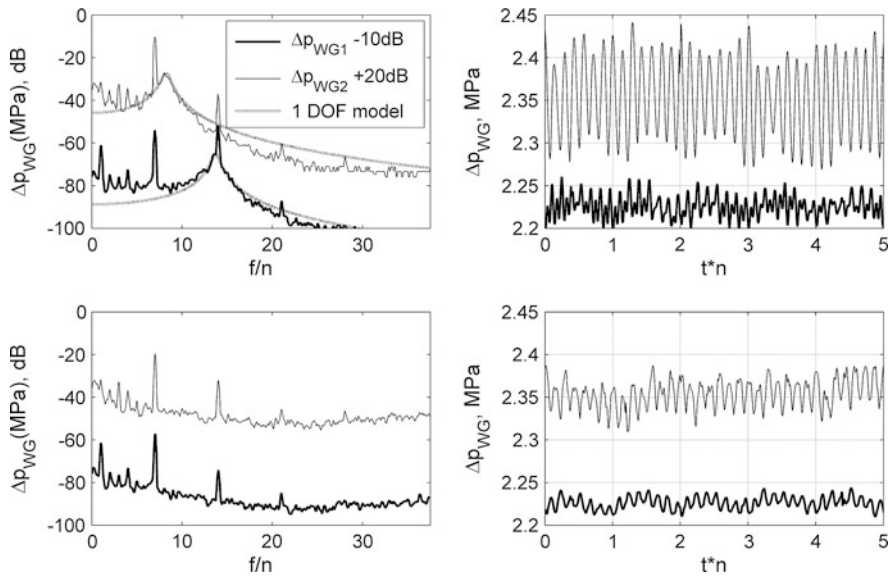
Fig. 9.1   Correction of distorted pressure pulsation signals using inverse FFT

hydraulic resonance inside the connection gives rise to unacceptable distortion of the signal. It is also important to avoid the combination of a narrow channel with a chamber at the sensor location; such an arrangement acts like a so-called Helmholtz resonator [9], a single degree of freedom oscillator with a resonance frequency defined by the water mass in the connecting pipe and the compressibility of the fluid in the chamber. The condition is even worse if traces of air are trapped in the chamber, or near the end of the connecting pipe. The added compressibility of entrapped air grossly reduces the natural frequency of the pressure tap, and therefore the available bandwidth for measurement. For that reason, a possibility to bleed air from the pressure tap prior to measurement should be provided at the sensor location. In pressure taps on the draft tube, this possibility sometimes does not work, due to the negative internal pressure relative to the atmosphere.

Theoretical estimates for the resonance frequency of a pressure tap are notoriously uncertain. It is recommended to check the frequency spectrum of the pressure signal to see if any frequency signal related to the pressure tap itself can be identified. The resonance frequency of the tap often appears quite clearly, as shown in Fig. 9.1. If the pressure tap cannot be improved, then the distorted part of the signal has to be removed by low-pass filtering. Only in exceptional cases may one recourse to signal conditioning as will be described further below.

This lack of bandwidth of the pressure tap is more of a problem if higher frequencies are to be investigated. The interesting low-frequency parts of pulsation in the draft tube are normally easy to measure, but the blade-passing frequency and its harmonics require very good connections. If such guarantees have to be verified, then the distortion due to inadequate pressure taps may produce large errors.

In some cases, the problem may be overcome by some post-processing which approximately removes the distortion. This can be done if the natural frequency of the tap is not too low compared to the frequencies of interest. As an example, Fig. 9.1 shows two pressure signals measured simultaneously between the wicket gates and the seven-blade impeller of a pump turbine. The natural frequencies of the pressure taps are clearly recognizable in the two spectra as shown on the upper left diagram. The dynamic transfer function distorting the signals may be esti- mated based on the wideband noise present between the harmonics $kZ_S n$ of runner blade passage. The unbiased signals, shown in the lower diagrams, can be approximately recovered in two steps. First, the complex linear spectrum of measured data is to be divided by the estimated complex transfer function [10], to obtain a corrected spectrum (lower left). Then, inverse Fourier transform of this spectrum yields the corrected signal in the time domain (lower right).

A procedure as described above may be the only way to arrive at useful results if the pressure transducer cannot be connected properly. It is, however, not very precise, and pressure taps of decent quality should of course be provided wherever possible. Nevertheless, it is always recommendable to check every test signal by inspecting its spectrum in the manner of the upper left diagram of Fig. 9.1, in an early stage of the test.

9.3.2 Vibration measurements

Vibration measurement is probably more a matter of routine, compared to pressure pulsation. Nonetheless, it also sometimes poses some problems.

Proximity sensors measure the distance between the sensor and the nearby surface of a ferrous component, like a shaft. They have the advantage of a large frequency range beginning at zero (steady-state value), but it has to be borne in mind that they measure only a relative distance. Quasi-absolute movements may be measured, but only if the absolute movement of the sensor can be safely avoided. Other types of sensors are capable of measuring absolute movements but they may also have some disadvantages.

Electrodynamic sensors measure absolute velocity. Their frequency range has a lower limit which may render the measurement at the frequency of partial-load pulsation (in large machines lower than 1 Hz) impossible.

Acceleration sensors also measure the absolute movement. Their signal has to be integrated in order to obtain the vibration velocity. This technique may be used to verify guarantees for casing vibrations, as stipulated in [3]; however, it requires experienced personnel and correct application. Inadequate insulation of the mea- surement chain has often produced faulty results because small signal errors are amplified in the integration process. This unwelcome problem may not be easily substantiated but has been proven on some occasions by comparing the results of parallel measurements.

9.4 Troubleshooting

The best starting point for improving an unsatisfactory condition in a prototype machine is to understand its physical cause. This statement should be self-evident but is sometimes hard to fulfill. An airtight root cause analysis is not always feasible, given the limited possibilities to carry out experiments in the plant. It is important to use all accessible information and compare it with possible scenarios, in the way physicians perform a differential diagnosis. There are a number of standard questions that should be considered at an early stage, in order to sort out possible explanations:

- What are the symptoms?
- Which components are concerned?
- In which mode of operation does the problem occur?
- At which head, output, gate, does the problem occur?
- Which frequencies have been observed?
- What kind of spectrum—periodic, narrow- or wideband?
- Does it happen at different levels of tail water?
- How does it respond to existing abatement measures (e.g, aeration)?

Starting from this information, it may be already possible to identify the root cause. Quite often, after this analysis the situation is not clear enough to identify a single cause and several possibilities remain. Some testing is necessary in such a case to narrow down the range of the possibilities. Tests have to be defined and conducted in a way, and with suitable parameters measured, to make sure the problem will be properly understood. The precautions for measuring pressure pulsation and mechanical vibration mentioned in Sect. 9.3 are also valid in this case. In addition, possible hazards arising in the test situation must be considered.

Digital recording of the test results is highly recommended. Multi-channel analysis may be very useful in order to examine for relationships between the various parameters measured. Coherent signals may permit possible mode shapes of an oscillation to be detected.

Once a likely explanation for a problem has been found, it is possible to define appropriate countermeasures. In this book, specific countermeasures have been mentioned in the chapters dealing with the various pulsation and vibration phenomena. In some cases, the foreseen countermeasure will be quite costly, and it is desirable to check the effectiveness of the countermeasure by means of a less expensive test, prior to the investment of resources for the correction.

For example, the permanent equipment for injection of compressed air into a turbine cannot be provided in a short term. It would, however, be reasonable to know in advance its effect, and the minimum effective air flow rate for the given case. This dilemma can often be resolved during commissioning if the plant has a suitable pressure tank—typically a regulator air accumulator—which can be used for the test. Using such a tank, a transient aeration test with duration of at least a few minutes can be performed, as illustrated in Fig. 9.2. The interesting dynamic

Fig. 9.2 Transient test for aeration influence (schematic)
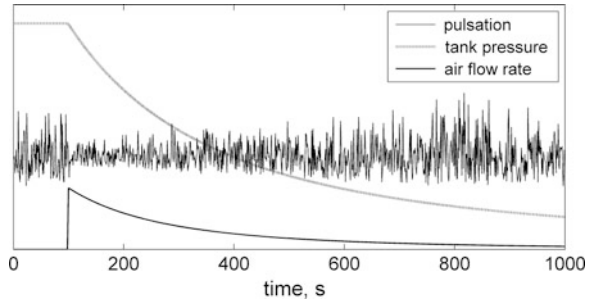
parameters (e.g., pressure signals) should be recorded together with the tank pressure. The development of air flow rate can be easily determined from the slope of the tank pressure. Due to the slowly decreasing tank pressure and air flow rate, together with the development of the dynamic variables, it becomes possible to determine an effective air flow rate for the aeration equipment. At the same time, the possible improvement is demonstrated in advance. This kind of test was used in the field test campaign described in Sect. 8.1.

It should be noted that sometimes the effect of a measure is not as expected. For instance, draft tube aeration may, instead of mitigating pressure pulsation, drive the condition toward resonance. This is quite possible in case of pump turbines where the aeration may be just sufficient to reduce the hydraulic natural frequency until it coincides with the vortex frequency.

References

1. Alligné, S., Nicolet, Ch., Allenbach, P., Kawkabani, B., Simond, J.-J., & Avellan, F. (2008). Influence of the vortex rope location of a Francis turbine on the hydraulic system stability. In *Proceedings of 24th IAHR, symposium on hydraulic machinery and systems, Foz do Iguassu, Brazil, 27–31 Oct 2008.*
2. IEC 60193. (1999). *Hydraulic turbines, storage pumps and pump-turbines—Model acceptance tests*, Ed. 2.0, 16 Nov 1999.
3. ISO 10816-1 Mechanical vibration—evaluation of machine vibration by measurements on non-rotating parts. *Part 1: General guidelines Part 5: Machine sets in hydraulic power generating and pumping plants*.
4. ISO 7919 Mechanical vibration—valuation of machine vibration by measurements on rotating shafts. *Part 1: General guidelines Part 5: Machine sets in hydraulic power generating and pumping plants*.
5. Billdal, J. T., & Holt, B. G. (2000). Three Gorges Project: Review of GE energy Norway's hydraulic design. In *Proceedings of the 20th IAHR symposium on hydraulic machinery and systems, Charlotte*.
6. Shi, Q. (2010). Hydraulic design of three gorges right bank powerhouse turbine for improvement of hydraulic stability. *25th IAHR symposium on hydraulic machinery and cavitation, Timisoara*.

7. Arzola, F., Azuaje, Z., Zambrano, P., & Gulbrandsen, G. (2006). Undesired power oscillations at high load in large Francis turbines. experimental study and solution. *23rd IAHR symposium on hydraulic machinery and systems, Yokohama*.
8. Alligné, S., Maruzewski, P., Dinh, T., Wang, B., Fedorov, A., Iosfin, J., & Avellan, F. (2010). Prediction of a Francis turbine prototype full load instability from investigations on the reduced scale model. *25th IAHR symposium on hydraulic machinery and cavitation, Timisoara*.
9. IEC 60994 *Guide for field measurement of vibrations and pulsations in hydraulic machines (turbines, storage pumps and pump-turbines),* Ed. 1.0 b:1991.
10. Bendat, J. S., & Piersol, A. G. (2000). *Random data analysis and measurement procedures* (3rd ed.). New York: Wiley.

Chapter 10
Errata to: Flow-Induced Pulsation and Vibration in Hydroelectric Machinery

Errata to:

Chapter 1: Basic Concepts, doi:10.1007/978-1-4471-4252-2_1
Chapter 3: Periodic Effects of Runner-Casing Interaction,
       doi:10.1007/978-1-4471-4252-2_3
Chapter 8: Selected Field Experience, doi:10.1007/978-1-4471-4252-2_8
Chapter 9: Practical Guidelines, doi:10.1007/978-1-4471-4252-2_9

Pages	Item or line	Corrections
25	Chapter 1	Replace X by χ (occurs three times)
90	Chapter 3	Replace Fig. 3.18 in second line under "Mechanical Effects" by Fig. 3.17
97	Chapter 3, Eq. 3.15	Replace $I = I_T/(1 - I_T/I_G)$ by $I = I_T/(1 + I_T/I_G)$
97	Chapter 3, inline equation in third paragraph	Replace $I = I_T/(1 - I_T/I_G)$ by $I = I_T/(1 + 2I_T/I_G)$
210	Chapter 8, Fig. 8.12a	Replace old Fig. 8.12a by new Fig. 8.12a
228	Chapter 9, third paragraph	Replace 8–85 % by 80–85 %

speed setpoint   KP*(1+1/TN*s)

xw

1
speed
input

opening
limiter

0

PI with
anti-windup   sum

1
governor
output

min(x,y)

clock   time-depend.
upper limit

satu-
ration

weighting   product

2
head
input $\frac{1}{T1.s+1}$ $\frac{1}{T1.s+1}$ $\frac{T2.s}{T2.s+1}$ G
1st LP   2nd LP   HP filter   gain

(a)

Index